The Influence of Propeller Position and Size on the Aerodynamics of Blown Wings

George Nicholas Hawkswell
Department of Engineering
University of Cambridge

This dissertation is submitted for the degree of
Doctor of Philosophy

Gonville and Caius College March 2024

Declaration

This thesis is the result of my own work and includes nothing which is the outcome of work done in collaboration except as declared in the preface and specified in the text. It is not substantially the same as any work that has already been submitted, or, is being concurrently submitted, for any degree, diploma or other qualification at the University of Cambridge or any other University or similar institution except as declared in the preface and specified in the text. It does not exceed the prescribed word limit for the relevant Degree Committee.

I undertook a Masters of Research in Gas Turbine Aerodynamics from October 2018 to August 2019 at the Whittle laboratory, which included a dissertation [35] on my proposed PhD research. Where work from this dissertation is used, it has been clearly referenced. Other than this dissertation, no work contained within this thesis has been submitted before for any degree or other qualification. This thesis contains fewer than 65,000 words including appendices, footnotes, bibliography, tables and equations and contains 150 figures.

Abstract

The drive to decarbonise the aviation sector is pushing aircraft designers towards more-electric propulsion architectures. One of the key benefits of electric propulsion is that multiple motors can be positioned around the airframe, without loss of motor efficiency. By placing many motors along the wing leading edge, each powering a propeller, increased lift can be achieved by blowing high velocity jets over the wing. This allows the wing to be reduced in size, decreasing its cruise drag, whist still maintaining the same lift during take-off and landing.

It is shown that the use of small diameter jets allows high velocity jets to be used for a fixed landing thrust, increasing the lift coefficient. It is also shown that the wing must be fully immersed in the jet to avoid premature stall. This is only possible by placing the jet below the wing centreline, due to the wings' up-wash. However, the use of small propellers placed below the wing centre-line requires many large nacelles, with a large associated drag. When the effect of nacelle installation drag is included, the optimum blown wing geometry to minimise drag is shown to be when the horizontal offset of the propeller is 25% wing chord in front of the wing leading edge, with no vertical offset of the propeller from the wing centre-line and with a jet diameter of 64% wing chord. This optimum is true for the wing and aircraft operating conditions studied in this thesis. This geometry achieves a 30% reduction in wing profile drag at cruise.

By comparing 2D CFD modelling methods to 3D CFD and experimental data, it is shown that the lift coefficient of a blown wing is primarily driven by two things: the jet thrust, and jet position relative to the wing. 2D modelling of the blown wing is therefore able to capture the lift and drag without the need to use more complex models. 2D models can also be modified to account for the effect of propeller spacing. It is found that the propeller spacing can be increased, with a minimal reduction in the blown lift, provided that the total thrust of the propellers remains constant. Increasing the propeller spacing reduces the number and hence drag of the nacelles.

The mechanism of blown wing stall when a flap is deployed is identified. It is shown that the flap stalls due to boundary layer diffusion resulting from a combination of the propeller jet and flap incidence. Moving the propeller down vertically increases the maximum lift coefficient, provided the jet does not pass below the wing, as the wing remains fully immersed in the jet up to higher flap angles. Increasing the propeller spacing leads to boundary layer separation at lower flap angles, however the growth of the separation with flap deployment is slowed when

compared to closely spaced propellers, as less of the flap is affected by the propeller jet; as a result, spacing the propellers out also increases the maximum lift coefficient. 2D modelling of the blown wing lift coefficient captures the trends in maximum lift coefficient with different vertical offsets, but is unable to capture the increased un-stalled flap angle range afforded by increasing the propeller spacing.

A power balance model for the aircraft shows that a blown wing can achieve a 12.2% reduction in power consumption in cruise if the leading edge propellers are stowed away after take-off. The optimum propeller position to achieve this is an axial offset of 25% chord upstream of the wing, a vertical offset of 5% chord below the wing chord-line and with a propeller diameter of 64% chord. If the leading edge propellers are not stowed away, and instead are also used in cruise, a 10.5% reduction in power consumption can be achieved. For this case, the propellers are positioned in the same horizontal location, but with no vertical offset from the wing chord-line and a larger diameter of 90% chord. Spacing propellers out offers a further 0.5% reduction in power consumption at cruise.

Acknowledgements

I would like to thank my supervisors Rob Miller and Graham Pullan for all their assistance with this project over the last four years. Their comments, ideas and enthusiasm have been invaluable. James Taylor, Sam Grimshaw, and Chris Clark at the Whittle lab for all of their assistance setting up and helping with the running of my experiments. Dave Fillingham and Herve Morvan from Rolls Royce plc. for their input into the project. Catherine, for all of your support whilst I finished writing and then correcting this thesis during those late nights after work, as well as putting up with me remaining a perpetual student over the last 5 years, and repeatedly extending my anticipated finish date. My parents, Ros and Andrew, for helping me when I came back to live and work on the PhD at home in North Yorkshire during lockdown. It was strange leaving the lab and the University to come home again, but a period I will treasure, and which, inadvertently, gave me an environment in which to produce much of the work, and many of the ideas which underpin this thesis. To my friends and teammates at Caius Boat Club, and Cambridge University Boat Club, whilst my involvement in rowing probably did not help with completing my thesis in good time, the memories and friends I have made along the way I will treasure for a lifetime. Finally to everyone at the Whittle laboratory. I could not have wished for a better environment in which to work on my PhD.

Publications

The following papers have been submitted for publication using work from this thesis.

[36] Hawkswell, G.N., Miller, R.J. and Pullan, G., "Selection of Propeller-Wing Configuration for Blown Wing Aircraft", AIAA Scitech, January 2022.

[37] Hawkswell, G.N., Miller, R.J. and Pullan, G., "The Effect of Propeller Spacing on the Performance of a Blown Wing Aircraft for an Electric Regional Aircraft", AIAA Scitech, January 2024. Relevant sections of this paper are reproduced in this thesis by permission of the American Institute of Aeronautics and Astronautics, Inc.

Nomenclature

Variables

A: Actuator Disk Area

A_p: Propeller Area

A_{jet}: Jet Area

A_R: Wing Aspect Ratio $= \frac{S^2}{A_{wing}}$

A_{wing}: Wing Area

$A_{throttle}$: Wind Tunnel Throttle Area

A_{fan}: Wind Tunnel Fan Exit Area

a: Axial Induction Factor

a': Tangential Induction Factor

B_p: Propeller Blade Number

C_D: Drag Coefficient $= \frac{D}{\frac{1}{2}\rho V_\infty^2 A_{wing}}$

C_F: Skin Friction Coefficient$= \frac{\tau_w}{\frac{1}{2}\rho V_\infty^2}$

C_L: Lift Coefficient $= \frac{L+T\sin\alpha}{\frac{1}{2}\rho V_\infty^2 A_{wing}}$

Δc_j: Excess Thrust Coefficient

C_p: Static Pressure Coefficient $= \frac{p_\infty - p}{P_{0,\infty} - p_\infty}$

C_{P0}: Total Pressure Coefficient $= \frac{P_0 - p_\infty}{P_{0,\infty} - p_\infty}$

C_P: Propeller Power Coefficient $= \frac{P}{\rho n^3 {D_p}^5}$

C_T: Propeller Thrust Coefficient $= \frac{T}{\rho n^2 {D_p}^4}$

C_x: Streamwise Force Coefficient $= \frac{D-T\cos\alpha}{\frac{1}{2}\rho V_\infty^2 A_{wing}}$

C_λ: Yaw Coefficient

C_τ: Pitch Coefficient

c: Chord

D: Drag

$D_{nacelle}$: Nacelle Diameter

D_p: Propeller Diameter

$\overline{D_p}$: Mean Propeller Diameter $= \frac{\pi D_p}{4}$

$d1_{fairing}$: Fairing Leading Edge Width

$d2_{fairing}$: Fairing Leading Edge Ellipse Length

$\dot{E}_{Induced}$: Kinetic Energy Lost in Tip Vortices

e: Span Efficiency Parameter

$e_{battery}$: Battery Specific Energy

F: Prandtl Tip Loss Correction

F_a: Axial Body Force

F_r: Radial Body Force

F_ψ: Tangential Body Force

F_x: Streamwise Body Force

F_y: Vertical Body Force

F_z: Spanwise Body Force

FF_{body}: Body Form Factor

f: Body Force per unit volume

g_n: Nth Load Cell Gradient

h: Actuator disk in-plane Vertical Height of Mesh Point

IF: Interference Factor for Nacelle Drag

J: Advance Ratio $= \frac{V_\infty}{nD_p}$

J': Jet Momentum

L: Lift

L/D: Lift to Drag Ratio

l/d: Nacelle Aspect Ratio

$l_{nacelle}$: Rear Nacelle Body Length

$l_{fairing}$: Fairing Length

M: Mach Number $= \frac{V}{V_s}$

$\dot{m}$: Mass Flow Rate

N_p: Propeller Number

n: Propeller Rotation Rate

P: Propeller Power

$P_{propulsor}$: Mechanical Power into System from Motors

P_0: Total Pressure

P_c: Propeller Power Coefficient $= \frac{P}{\frac{1}{2}\rho V_\infty^3 A_p}$

p: Static Pressure

Q: Propeller Torque

$\dot{Q}_{rig}$: Wind Tunnel Volumetric Flow Rate

q_∞: Freestream Dynamic Pressure $= \frac{1}{2}\rho V_\infty^2$

R: Radius

$R_{chamfer}$: Nacelle Chamfer Radius

R_e: Reynolds Number $= \frac{\rho V_\infty c}{\mu}$

r: radial coordinate

r_{tip}: Tip Radius

r_{hub}: Hub Radius

r': Non-dimensional Radius $= \frac{r}{r_{tip}}$

r^*: Normalised Non-Dimensional Radius$= \frac{r' - r'_{hub}}{1 - r'_{hub}}$

S: Wing Span

$\hat{S}$: Shape Space Parameter

S_{local}: Local Wing Span

S_{wet}: Wetted Area

S_{ref}: Reference Area

s: Propeller Spacing

T: Propeller Thrust

T_c: Thrust Coefficient $= \frac{T}{\frac{1}{2}\rho V_\infty^2 A_p}$

t: Wing Maximum Thickness

U_{fan}: Wind Tunnel Fan Tip Speed

V: Velocity

V_e: Boundary Layer Edge Velocity

V_{jet}: Propeller Jet Velocity

V_s: Speed of Sound

V_{stall}: Stall Speed

V_{wing}: Streamwise Velocity Upstream of Propeller

$V_{farfield}$: Velocity Downstream of Wing

V_{∞}: Freestream Velocity

V_L: Lift Load Cell Voltage

V_D: Drag Load Cell Voltage

W: Weight

W_p: Propeller Inflow Velocity

W_{wing}: Upwash Velocity Upstream of Propeller

W_{prop}: Upwash Velocity Downstream of Propeller

W_{tunnel}: Tunnel Jet Width

x: Wing Chord Direction Coordinate

x_p: Propeller Chordwise Position

x_{prop}: Propeller Width

y: Wing Normal Direction Coordinate

y_p: Propeller Vertical Position

y_s: Streamline Vertical Position

$y+$: Dimensionless Boundary Layer Thickness $= \frac{y\sqrt{\rho\tau_w}}{\mu}$

z: Spanwise Direction Coordinate

α: Angle of Attack

α_{mod}: Modified Angle of Attack

β: Propeller Twist

$\beta_{Patterson}$: Patterson Lift Multiplier

β_{jet}: Tunnel Jet Deflection Angle

Γ: Wing Circulation

Γ_w: Wing Local Circulation

Δ: Actuator Disk Thickness

δ: Shortest distance from Mesh Point to Actuator plane

ε_{wing}: Upwash angle upstream of propeller

ε_{prop}: Upwash angle due to propeller

$\hat{\zeta}$: Shape Space Co-ordinate $= \frac{y}{c}$

η: Propeller Efficiency $= \frac{TV_{\infty}}{P}$

η_{motor}: Motor Efficiency

θ: Propeller Inclination Angle

$\theta_{nacelle}$: Nacelle Boat Tail Angle

$\theta_{fairing}$: Fairing Boat Tail Angle

λ: Yaw

μ: Dynamic Viscosity

ρ: Density

σ: Tunnel Correction Factor

σ_{var}: Standard Deviation of Measured Variable

ς: Angle of Attack Correction Factor

τ_w: Wall Shear Stress

τ: Pitch

ϕ: Flap Angle

$\phi_{fuselage}$: Fuselage Boundary Layer Power Losses

$\phi_{empennage}$: Empennage Boundary Layer Power Losses

ϕ_{wing}: Wing Boundary Layer Power Losses

$\phi_{nacelle}$: Nacelle Boundary Layer Power Losses

ϕ_{froude}: Shear Power Losses in Jet

$\phi_{surfaces}$: Surface Boundary Layer Power Losses

ϕ_{blades}: Boundary Layer Power Losses in Blades

φ: Span Parametric Co-ordinate

ψ: In Plane Angle from Mesh Point to Vertical Axis

ψ_p: Propeller Inflow Angle

$\hat{\psi}$: Shape Space Co-ordinate $= \frac{x}{c}$

Ω: Rotation Rate

Subscripts

$blown$: A case with propellers in use

$unblown$: A case where the propeller blades have been removed

$clean$: Original wing

jet: A property of the propeller jet

max: Maximum value

$wing$: Referring to the wing only

$nacelle$: Referring to the nacelle only

$Induced$: Referring to the induced drag only

$aircraft$: Referring to the reference aircraft

$corrected$: Data corrected for Reynolds number effects

$nacelle\ body$: Referring to the main nacelle body of revolution

$fairing$: Referring to the nacelle fairing

$interference$: Referring to the interference between nacelle body, fairing and wing

$take-off$: Referring to take-off conditions

$cruise$: Referring to cruise conditions

$landing$: Referring to landing conditions

$safe$: Safety Limit

$approach$: Approach condition

∞: Freestream conditions

e: Boundary layer edge

Abbreviations

2D: 2-Dimensional

3D: 3-Dimensional

LE: Leading Edge

TE: Trailing Edge

CFD: Computational Fluid Dynamics

CAD: Computer Aided Drawing

HPC: High Powered Computing Service

RANS: Reynolds Averaged Navier Stokes

URANS: Unsteady Reynolds Averaged Navier Stokes

VLM: Vortex Lattice Method

DEP: Distributed Electric Propulsion

BEM: Blade Element Momentum Theory

MIL: Minimum Induced Loss

UDF: User Defined Function

STOL: Short Take-off and Landing

VTOL: Vertical Take-off and Landing

ESC: Electric Speed Control

PIV: Particle Image Velocimetry

Definitions

1. Whole Aircraft

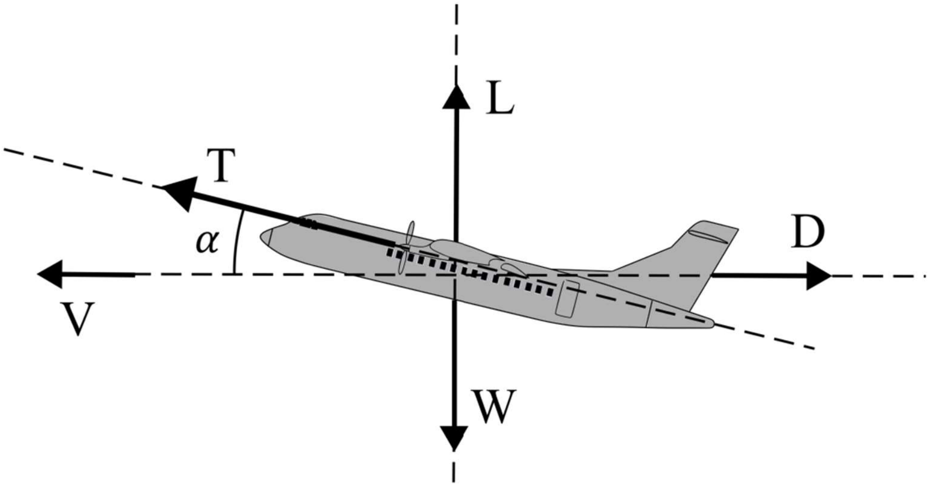

Definition of the force balance on an aircraft used in this thesis. The aerodynamic coefficients are decomposed into the forces parallel and normal to the freestream direction.

We define the forces on the aircraft as:

L: Wing Lift

D: Drag

T: Propeller Thrust

W: Aircraft Weight

Where needed for modelling, these dimensional values are given in tables in this thesis. Non-dimensionally, these quantities are expressed as,

$$C_L = \frac{L + T\sin\alpha}{\frac{1}{2}\rho V_\infty^2 A_{wing}} \quad . \quad (1)$$

$$C_D = \frac{D}{\frac{1}{2}\rho V_\infty^2 A_{wing}} \quad . \quad (2)$$

$$C_x = \frac{D - T\cos\alpha}{\frac{1}{2}\rho V_\infty^2 A_{wing}} \quad . \quad (3)$$

The component of thrust normal to the streamwise direction is included in the total lift of the aircraft. C_x is positive when the drag on the aircraft is greater than the component of propeller thrust in the streamwise direction. The drag value in C_x can refer to either the whole aircraft drag, or the wing drag. This is clearly stated when used. A_{wing} is defined below for the whole aircraft. For most calculations in this thesis, the 3D shape of the wing is ignored, and a straight local wing section is assumed. For these later cases, the area of the wing can be calculated by,

$$A_{wing} = c \times S_{local} \quad , \quad (4)$$

where S_{local} refers to the local span of interest, such that the wing area is equal to the area over which the forces measured (either computationally or experimentally) are acting. c is assumed to be the mean chord of the wing semi-span such that when multiplied by the aircraft wingspan, A_{wing} is recovered.

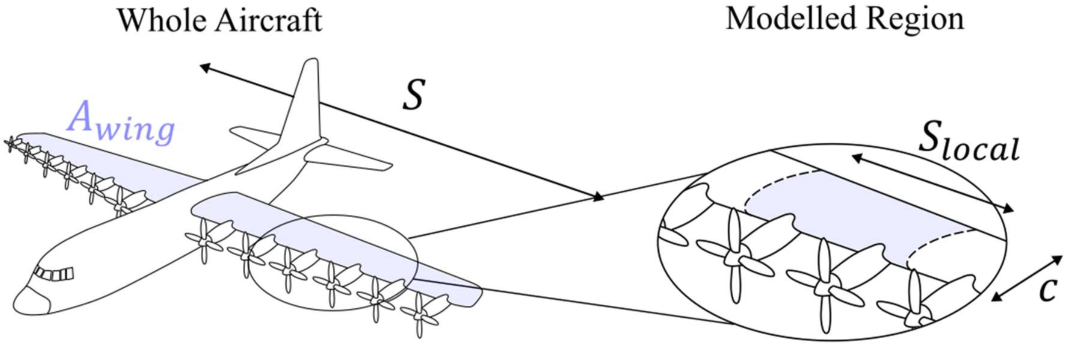

Aircraft wing geometric parameters at a whole aircraft level, and a modelled level. In this thesis, the aircraft blown wing is modelled with a local 2D wing section near the mid-span of the wing and the effects of wing taper and sweep are ignored.

2. Blown Wings in 2D

It is shown in Chapter 6 that it is possible to derive, from arguments of conservation of mass and momentum, an average jet height $\overline{D_p}$ for a circular jet given by,

$$\overline{D_p} = \frac{\pi D_p}{4} \quad . \quad (5)$$

This average jet height is used in both the previous literature discussed in Chapter 2, and the 2-dimensional modelling of Chapters 4 to 8. For two-dimensional calculations, we assume the disk is semi-infinite in the spanwise direction. For all references to two-dimensional jets in this work, the average jet height, $\overline{D_p}$ is used. The derivation of $\overline{D_p}$ is included in Appendix F.

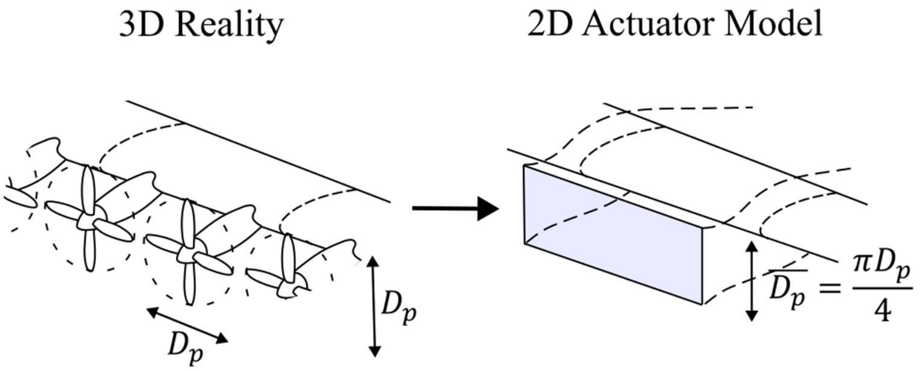

The change in definition of propeller diameter as we move from 3D to 2D simulations of a blown wing. The definition of the 2D propeller diameter is derived in Appendix F.

3. Blown Wing Geometry

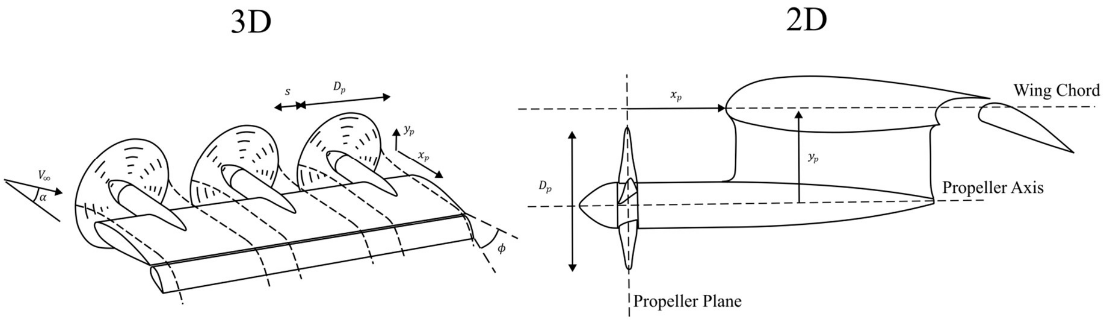

3D and 2D geometry parameters varied in this thesis.

The geometry definitions used in this thesis are shown above. All parameters are normalised by the wing chord, with the exception of the spacing between adjacent propellers which is normalised by the propeller diameter. x_p and y_p are aligned with a Cartesian coordinate system centred on the wing leading edge and measured to the propeller plane, and propeller axis respectively. The nacelle geometry parameters are defined in Appendix C.

4. Lift Definitions

The lift coefficient is defined in Eq. 1. Lift is always defined normal to the streamwise direction, and drag parallel to the streamwise direction.

For cases without blowing, either the subscript $unblown$ or $clean$ are used. $unblown$ refers to a wing fitted with the motors and nacelles for wing blowing, but with no thrust being imparted from the propellers. $clean$ refers to a plain 2D wing section consisting of just the aerofoil (and flap where relevant). For 2D calculations where the nacelles are not modelled, this distinction is irrelevant and the two terms can be used interchangeably (although $unblown$ is always referred to for these cases in this thesis). The ratio of $blown$ to $unblown$ lift, $C_{L,blown}/C_{L,unblown}$ is referred to as the lift augmentation achieved from blowing, and this term is the increase in lift from the propellers. Usually this is for a fixed geometry, however when quantifying overall benefits on the aircraft within the design, the flap angle or wing angle will change as blowing modifies the operating point of the aircraft.

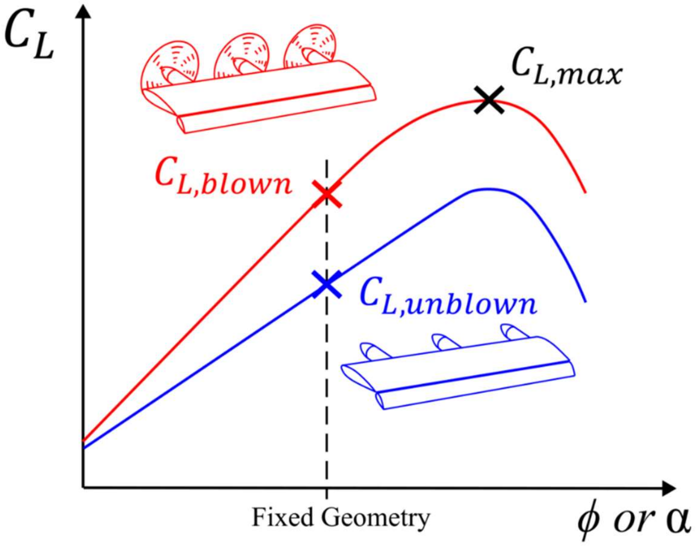

The definition of the lift coefficients used in this thesis.

The maximum lift coefficient, $C_{L,max}$, is defined as the point at which the first peak in the lift coefficient is reached. Beyond the angle at which this occurs, the wing is said to be stalled. It is important to state that this is the first peak, as for some numerical calculations, it was found that the wing lift could continue to rise after the stall angle.

5. Propeller Definitions

The design and modelling of propellers is explained in more detail in Appendix B. The key parameters used are,

$$T_c = \frac{T}{\frac{1}{2}\rho V_\infty^2 A_p} \quad . \quad (6)$$

$$J = \frac{V_\infty}{n D_p} \quad . \quad (7)$$

The advance ratio, J, represents a non-dimensional propeller tip speed. This parameter is a standard propeller performance coefficient and so has been retained in this work for cases where real propellers are used.

The thrust coefficient, T_c is applicable to both real propellers, and 3D actuator disks, in which case A_p refers to the disk area (ignoring the loss of disk area at the hub due to the nacelle). For 2D calculations, the disk area is given by the mean jet height, $\overline{D_p}$ and T is then the thrust per unit span. The loss of disk area associated with the nacelle is ignored for 3D cases as this allows propellers with the same diameters and total thrusts to retain the same thrust coefficient, irrespective of if the nacelle is modelled.

6. Aerodynamic Coefficients

$$C_p = \frac{p_\infty - p}{P_{0,\infty} - p_\infty} \quad . \quad (8)$$

$$C_{P0} = \frac{P_0 - p_\infty}{P_{0,\infty} - p_\infty} \quad . \quad (9)$$

Static and total pressure coefficients, note the sign convention of C_p which has been chosen for convenience in plotting pressure distributions.

Reynolds number is based on wing chord, unless stated otherwise.

$$R_e = \frac{\rho V_\infty c}{\mu} \quad . \quad (10)$$

Contents

1. Introduction

2. Literature Review

3. Methodology

4. The Design and Operating Space of a Blown Wing

5. Installation Drag

6. Real Propulsor Effects On-Design

7. Real Propulsor Effects Off-Design

8. Overall Aircraft Performance with a Blown Wing

9. Conclusions

11. Appendices

1. Introduction

1.1 Overview of Blown Wings with Electric Propulsion

Electric propulsion offers the potential to change the size and number of propulsors on an aircraft. This is because electric motors retain their efficiency down to small scales whereas gas turbines do not. This offers the opportunity to move from a small number of large propulsors to a large number of small propulsors, allowing the propulsors to be distributed around the aircraft. There are many possible configurations for these propulsors, however, one that shows particular potential is to mount the propulsors along the wing leading edge to blow the wing. Blown wings deflect part of the high velocity slipstream down during take-off and landing, increasing lift. This allows smaller wings to be used, which create less drag during cruise [56].

Photo of Rolls Royce concept aircraft with distributed propulsion [64]. Removed for copyright reasons. Copyright holder is Rolls Royce plc.

(a)

Photo of ATI FlyZero concept aircraft [41]. Removed for copyright reasons. Copyright holder is the Aerospace Technology Institute.

(b)

Photo of Leonardo Clean Sky concept aircraft with distributed propulsion [43]. Removed for copyright reasons. Copyright holder is Leonardo S.p.A.

(c)

Photo of NASA X-57 aircraft with distributed propulsion [42]. Removed for copyright reasons. Copyright holder is NASA.

(d)

Figure 1.1: Concept aircraft incorporating leading edge distributed propulsion to blow the wing. (a) Rolls Royce Distributed Open Rotor Aircraft [64]. (b) ATI FlyZero Regional Aircraft [41]. (c) Leonardo EU Clean Sky Hybrid-Electric Distributed Propulsion Concept [43]. (d) NASA X-57 Maxwell [42].

The aim of this thesis is to study the optimum position and size of these propulsors along the wing leading edge in terms of the wing lift increase, wing drag reduction and overall power consumption in cruise.

Leading edge distributed propulsion can be used in two ways. The first way shown in Fig. 1.1 (a), (b) and (c) is to operate the propellers throughout the flight of the aircraft. The increased propulsive area improves the propulsive efficiency of the aircraft. The lift of the wing is also increased by the propellers. The second way, shown in Fig. 1.1 (d) is to only operate the propellers during take-off and landing and pack them away during cruise. This allows the propellers to be optimised for high lift, with smaller, more highly loaded propellers which would otherwise be inefficient at cruise. Cruise thrust is produced by tip-mounted propellers. This thesis will study both approaches and determine which is best for use in different types of aircraft operation.

Most modern aircraft already incorporate high lift devices in the form of flaps and slats to increase wing lift. These high lift systems are typically limited to maximum lift coefficients, $C_{L,max}$, of 3.5 [70] whilst blown wings have been shown to increase $C_{L,max}$ to up to 10 [3] without generating any net forward thrust. This additional lift allows smaller wings to be used, with reduced wetted area and hence drag whilst still meeting adequate take-off and landing performance. This can be understood by considering Eq. 1.1,

$$C_{L,max} = \frac{W}{\frac{1}{2}\rho V_{stall}^2 A_{wing}} \quad . \quad (1.1)$$

For a given aircraft weight W, and regulatory stall speed, the wing area can only be reduced if the maximum lift coefficient, $C_{L,max}$, is increased.

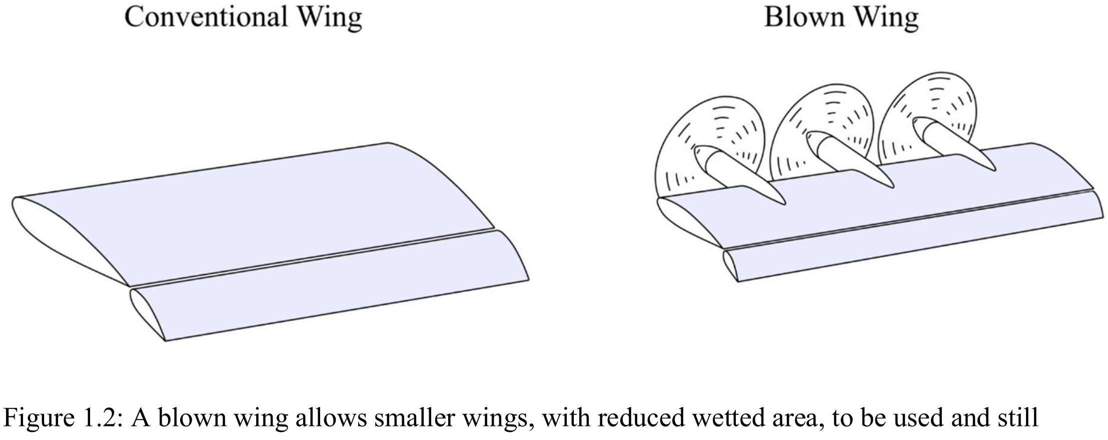

Figure 1.2: A blown wing allows smaller wings, with reduced wetted area, to be used and still maintain the required design performance at low speed.

In this work, the benefit of the blown wing is assessed for a region near the mid-span of the wing, as shown in Fig. 1.3. By doing this the added complexity of modelling the wing taper, and wing root and tip interactions can be ignored initially in order to make progress exploring the design space. The flow in this mid-span region is still 3-dimensional, due to the effect of the propeller swirl and circular jets, but assumed to be periodic between adjacent propellers. The complexities of real 3D wing design are reintroduced later in this thesis.

Within this mid-span view of the blown wing design, the performance of a blown wing is limited by the thrust from the propellers and the maximum lift coefficient of the wing.

Whilst blowing increases wing lift by deflecting the propeller slipstream, the majority of the jet momentum still creates a streamwise force on the aircraft. If this streamwise force exceeds the total drag, the aircraft will accelerate and will be unable to land. An upper limit therefore exists on the maximum thrust that can be applied by distributed propellers.

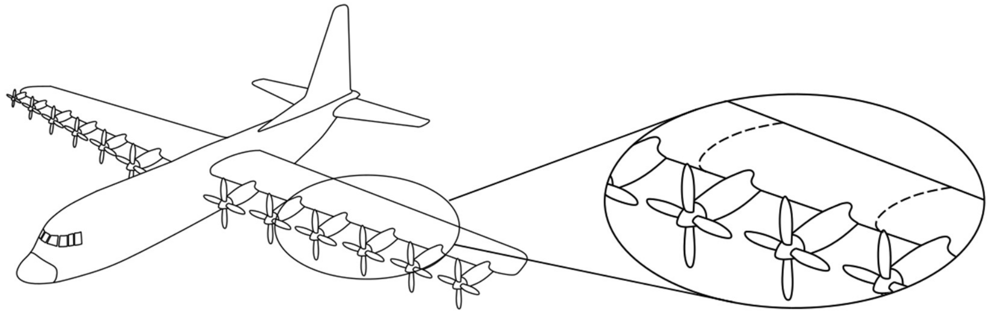

Figure 1.3: This work investigates the blown performance of the mid-span region of the wing.

The maximum lift generated by a blown wing is dependent on its mechanism of stall. The jet from the propeller affects the loading of the wing, and the swirl from the propeller changes the local wing incidence causing 3-dimensional boundary layer separation. This can lead to premature stall if an unsuitable blown wing geometry is chosen by the designer.

The design space is broad for the full aircraft wing design with the choice of propeller geometry and location influencing the wing lift and streamwise force. By focusing this study on the mid-span performance only, the choice of design parameters can be limited to a minimum viable set, labelled in Fig. 1.4. This is a manageable number of parameters to be tested, giving insight into the trade-offs within the design space.

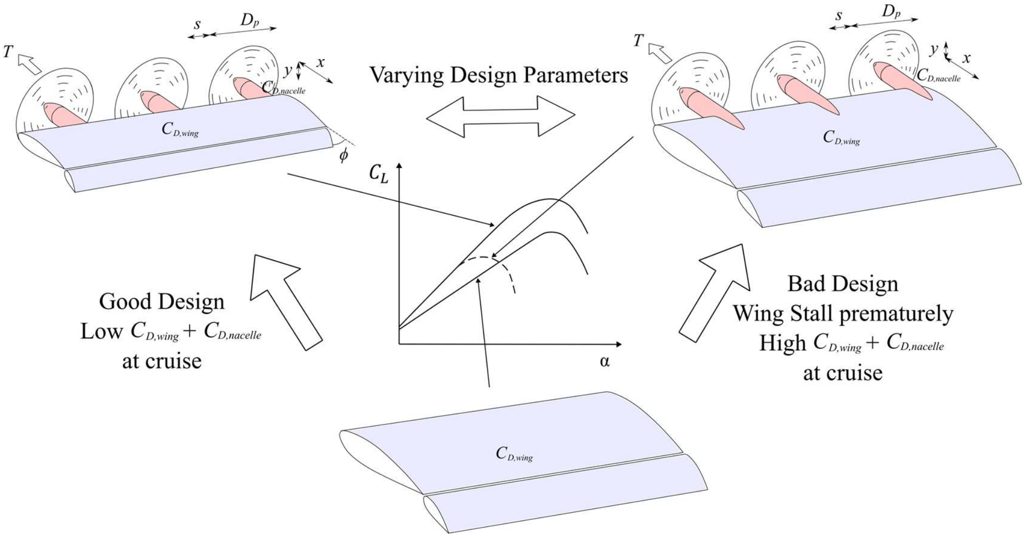

Figure 1.4: Blown wing performance is sensitive to the design geometry. A low maximum lift coefficient increases the area of the wing, and hence its drag during cruise. A high maximum lift coefficient reduces the area of the wing, and hence its drag during cruise. Exploring this space is one of the aims of this work.

The best modelling techniques for preliminary design, the achievable design space of a blown wing, and the stall mechanism of the wing when fitted with multiple upstream propellers are not well understood. Designers and researchers wish to know if there is sufficient benefit from distributed blowing to warrant the extensive work required to fill these gaps in knowledge and see the technology through to implementation on an airframe. Whole aircraft models have been developed previously to calculate the aircraft benefit with blown wings fitted. As the number of design variables with distributed blowing is high, these optimisation codes rely on the simplest available blown wing models in order to reduce computational time. These models are usually inaccurate near wing stall, an area that is essential to predicting maximum lift performance. Experimental data is sparse for distributed blown wings, and whilst 3D CFD codes are known to accurately model the blown wing, these codes are computationally expensive and cannot be integrated into design codes.

1.2 Thesis Questions

This work will attempt to answer four questions:

1. How should a blown wing with distributed propulsion be sized to maximise the lift of a real aircraft and minimise the total drag of the wing? This question is answered in Chapters 4 and 5.

2. Can a 2D model of the blown wing correctly predict the on-design, and off-design performance of a blown wing? This question is answered in Chapter 6.
3. What is the mechanism by which a blown wing stalls? This question is answered in Chapter 7
4. How should a blown wing with distributed propulsion be sized in order to minimise the power requirements of a real aircraft, and what is the overall benefit of a blown wing on performance? This question is answered in Chapter 8.

1.3 Thesis Contributions

This work makes a number of new contributions to the field of blown wings.

1. The design space is mapped out for both on-design, and off-design performance near stall. This allows the optimum blown wing design for maximum wing lift increase, and minimum wetted area to be found, with a wing profile drag reduction at cruise of up to 50% if the propellers are folded in cruise.
2. The complexity of the blown wing modelling is built up from a 2D actuator disk model, to 3D actuator models with varying complexities of propeller jet model, and finally a blown wing experiment that correctly captures the real distributed propeller jet effects on the wing. This progressive fidelity increase allows simple 2D blown wing models, capable of being used in design optimisation, to be developed, with an understanding of their limitations.
3. Designers might wish to reduce the streamwise force on the wing by using smaller propellers. However, it will be shown in this thesis that this approach can lead to excess nacelle drag at cruise which offsets any benefit from reduced wing area. It is shown in this thesis that a well-designed blown wing can reduce wing profile drag (including nacelle drag) by 30% during cruise.
4. The stall mechanism for the flap of a blown wing is identified and the effect of propeller vertical offset and spacing on the stall angle explained.
5. Increasing propeller spacing and the disk loading of the blowing propellers is identified as a useful trick designers can play to reduce the nacelle drag, and complexity of their blown wing system whilst still maintaining high lift through blowing.
6. A whole aircraft model is constructed which predicts a 12.2% reduction in cruise power requirement with distributed propulsion when folding the high lift propellers away

during cruise. If the propellers are not stowed away, the power consumption increases by 1.7%. These stated performance benefits are relative to a non-blown wing aircraft with the same maximum take-off weight.

1.4 Structure of the Thesis

The questions posed in Section 1.2 will be further refined in Chapter 2 following a literature review. Chapter 3 discusses the methods used in this thesis. The results of this thesis are split into five chapters.

Chapter 4 investigates the design space of a blown wing. The optimum location and size of the propeller relative to the wing is determined in order to maximise wing lift, and minimise the wing drag at cruise when propellers are folded away. The modelling is undertaken using a 2D actuator disk in CFD, shown in Fig. 1.5. The simplicity of the actuator disk allows a large design space to be rapidly explored.

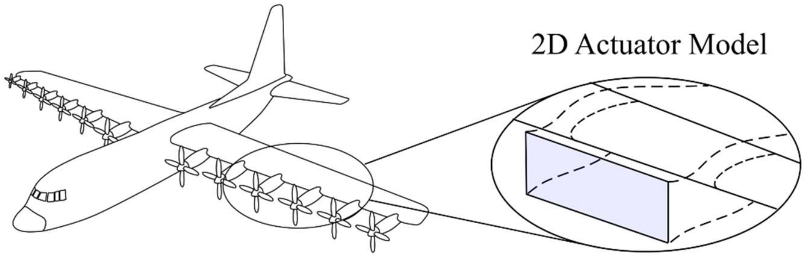

Figure 1.5: The design space is explored in Chapter 4 with an 2D actuator disk model, removing the complexities of the real 3D flow due to the propeller swirl. This allows the effect of propeller position and diameter to be quantified for a range of geometries and operating points.

Chapter 5 investigates the installation drag of a blown wing at cruise when the propellers are folded away. A model for the nacelle drag is developed using experimental data in order to quantify the installation drag impact. It is shown that the optimum location and size of the propeller relative to the wing changes from that reported in Chapter 4 if reducing the overall drag of the wing and motor nacelles at cruise is the design objective. The modelling ignores the presence of the propeller, as shown in Fig. 1.6.

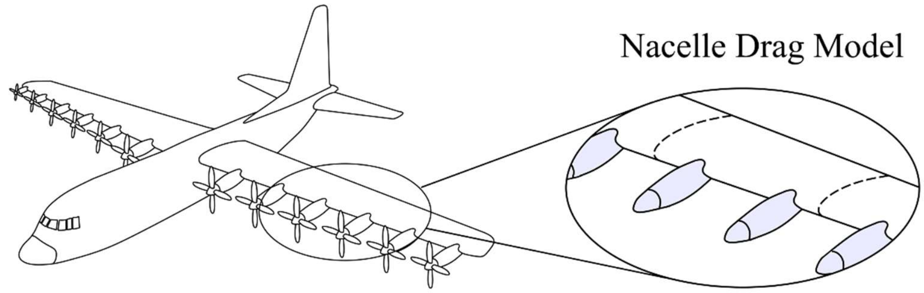

Figure 1.6: The installation drag from nacelles is modelled in Chapter 5 using a low-order model built on experimental data. It is shown that the nacelle drag is significant and needs to be considered when assessing the performance of the blown wing.

Chapters 6 and 7 use a combination of 3D actuator disk models, and experimental data from a low Reynolds number test rig for a range of test geometries. This approach is shown in Fig. 1.7.

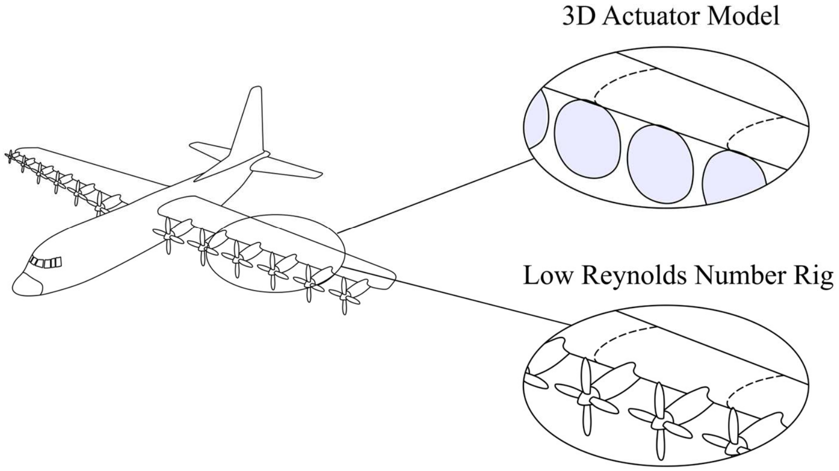

Figure 1.7: The 3D effects of propeller jet wakes and position are modelled with 3D Actuator disk CFD and a Low Reynolds number experiment in Chapters 6 and 7. It is shown that good agreement can be achieved away from stall between 2D models, 3D CFD and the experiment.

Chapter 6 investigates the effect of real propeller jets on the on-design performance of the blown wing. The propeller spacing, a parameter not modelled in 2D, is also investigated using a combination of 3D actuator disk CFD models and experiment. The 2D actuator model for the blown wing is found to accurately capture the on-design performance of the blown wing. It is shown that the propeller spacing can be increased without adversely impacting the blown wing lift, but does reduce the nacelle drag contribution.

Chapter 7 investigates the effect of real propeller jets on the off-design performance of the blown wing. The 3-dimensional stall mechanism of the flap is explained, and it is shown that 2D actuator disk modelling is able to capture the trends in maximum lift coefficient with propeller position and size. The 2D modelling always under-predicts the true maximum lift coefficient. It is shown that increasing the spacing between propellers extends the pre-stall flap operating range. Modelling of the flap stall is done with a combination of CFD and experiment.

Chapter 8 estimates the reduction in cruise power consumption possible by fitting an electric regional aircraft with distributed propulsion. The relative benefits of deploying the blown wing during take-off and cruise or packing the propellers away in cruise are quantified. The benefit of increasing propeller spacing on the blown wing performance is also quantified. The optimum propeller location and size to minimise cruise power consumption is stated. This analysis uses the design space exploration work of Chapters 4 and 5, as shown in Fig. 1.8.

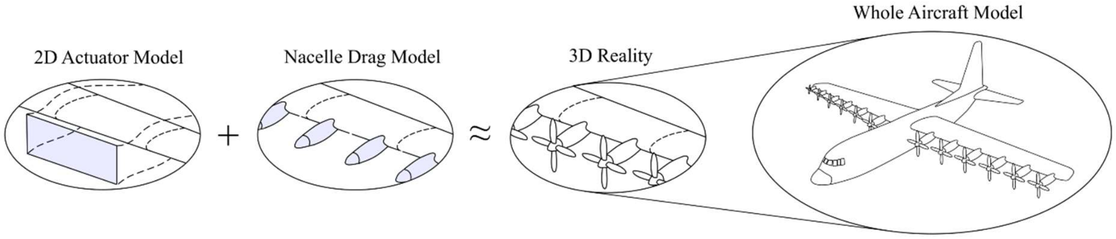

Figure 1.8: In Chapter 8, the modelling results of Chapters 4 and 5 are combined to estimate the performance benefit of an aircraft fitted with a blown wing compared to an aircraft of the same take-off mass but fitted with a conventional propulsion system.

2. Literature Review

2.1 Introduction

In this chapter, the previous work on blown wings will be examined in relation to the four questions posed in Chapter 1. The first section looks at the optimal design of blown wings, the second different modelling fidelities which can be used, the third the fluid mechanism responsible for the 3D stall of a blown wing and the fourth the overall aircraft benefit that can be achieved by using a blown wing. By doing this, the questions posed in the introduction can be refined.

2.2 Optimum Blown Wing Design for Maximum Wing Lift

In this section the current understanding of the optimum location to position blown wing propellers, and how to size them to maximise the lift of the blown wing is examined. Figure 2.1 shows part of this design space.

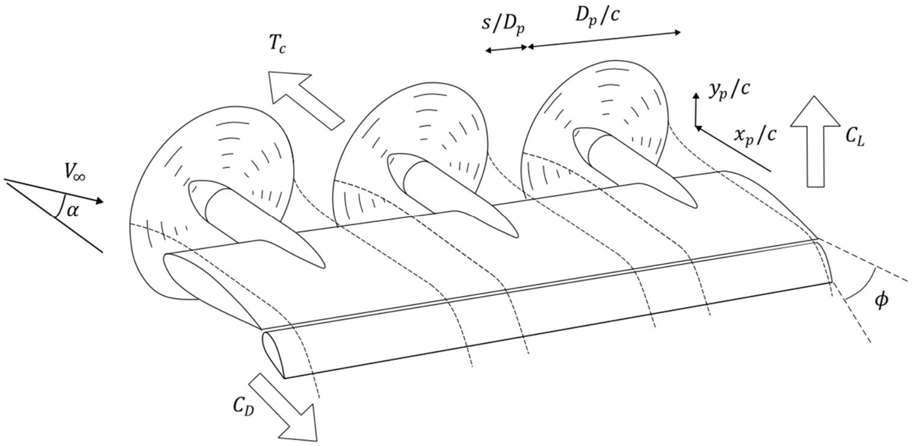

Figure 2.1: The blown wing design space at its simplest. The propeller position in relation to the wing is defined by its horizontal and vertical offset. The spacing between propellers is uniform and the diameter of the propellers is uniform along the span. The wing operating point is defined by its flap angle and angle of attack, and the propeller operating point is defined by its thrust coefficient.

Barnhart et al. [10] performed an analysis of the available experimental data on distributed blown wings at the time of publication (2021). 705 data points were found for a range of configurations. 20 variables were investigated with a principle component analysis, and it was found that the wing lift coefficient was mostly sensitive to propeller thrust coefficient, and wing flap angle.

This result is to be expected. To a first order, and assuming incompressible flow, the lift of a blown wing can be calculated from Equation 2.1 [56]:

$$C_{L,blown} = C_{L,unblown}\left(\frac{V_{jet}}{V_\infty}\right)^2 \quad . \quad (2.1)$$

This equation applies if the jet from the propeller is large and uniform. The wing then acts as though it is immersed in a flow with a higher dynamic pressure, and the lift scales accordingly. The unblown wing lift is primarily a function of its incidence (flap angle or wing angle), and the propeller thrust controls the jet velocity, hence the dependencies found by [10]. It is unlikely, however, that propeller jets will be large and uniform for a distributed blown wing, and, in practice, propeller jet profile, size and position are also important for blown wing lift.

2.2.1 Propeller Jet Profile

The effect of a single propeller slipstream on the lift distribution of a wing can be split into two components: an increase in lift due to the higher dynamic pressure in the propeller jet, and a spanwise variation in lift due to the propeller swirl changing the local angle of attack [77]. These two effects are shown schematically in Figure 2.2. The lift scales with dynamic pressure, as shown in Eq. 2.1. However, Patterson [60] showed for finite jets that the lift augmentation (ratio of blown to unblown lift) does not increase linearly with jet dynamic pressure. In practice, the blown lift is attenuated at high thrust coefficients, with less lift being generated than predicted by the model. In another work, Patterson [58], postulated that a uniform jet would produce more lift than a conventional propeller jet profile, with peak axial velocities around 70% of the propeller span. This assumption was not validated experimentally, however the designs proposed produced the same average axial velocity with 11% less thrust and 15% less power.

Whilst the wing reacts to the local variations in jet dynamic pressure and angle of attack caused by the propeller swirl, this response is generally smaller than would be predicted by a 2D analysis. Kroo [47] found that the wing acts a stator, helping to recover the swirl generated by the propeller and increase the propulsive efficiency by up to 7%. Veldhuis [77] argued that this improvement was due to local tilting of the lift vector in the thrust direction (effectively reducing induced drag). To account for this effect, a swirl recovery factor, which reduces the swirl strength of the propeller in the presence of a wing, was applied in order to get adequate results from low order models.

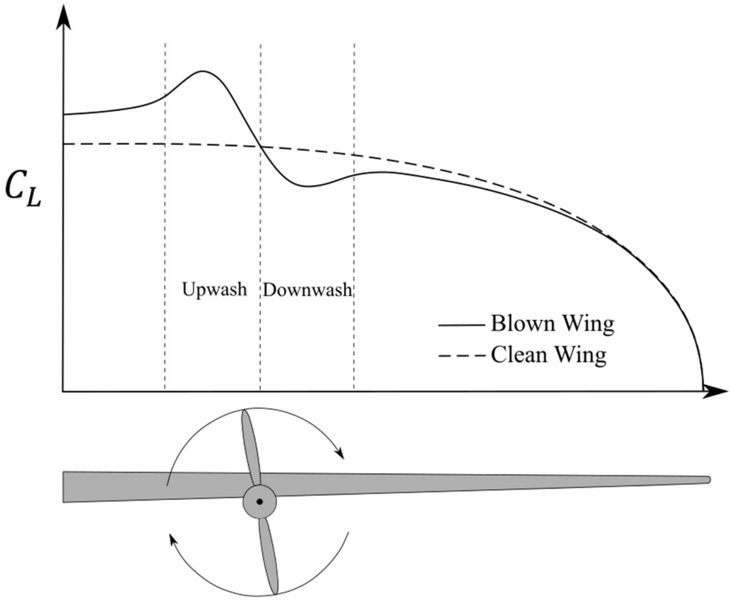

Figure 2.2: The effect of a tractor propeller on wing loading. The presence of propeller swirl locally changes the loading on the wing. The dynamic pressure of the propeller jet increases the average lift of the wing. Redrawn from [77].

2.2.2 Propeller Spacing

The effect of the propeller swirl extends well outside the disk area of the propeller, typically up to 3 propeller radii [2]. For multiple propeller systems, the neighbouring jets will interact. When the propellers rotate in the same direction, the swirl will cancel at the boundary between the propellers [34] whereas for propellers rotating in opposite directions, the swirl will superimpose [73]. De Vries et al. [79] looked at the performance of a propeller with additional propellers either side of it. The presence of the additional propellers modified the inflow velocity field, reducing the efficiency of the propeller by 1.5%. Figure 2.3 shows plots of section lift coefficient multiplied by local chord against span, and iso-surfaces of vorticity for a dual propeller system both rotating inboard up [8].

The loading for the dual propeller system is not the linear combination of the single propeller systems shown in Figure 2.3. The addition of the outboard propeller jet has no noticeable effect on the wing loading downstream of the inboard propeller. Downstream of the outboard propeller, the loading decreases with both propellers operating. In the region between the two propellers, the tip vortices from the propellers pass over the wing surface, changing the wing loading. This interaction between adjacent propellers has been exploited to increase wing L/D ratios by 21% [83]. As well as the propeller tip vortices, vortices are also formed by the nacelle.

Plot of wing loading for three propeller-wing configurations, inboard propeller only, outboard propeller only, and inboard and outboard propeller [8]. Removed for copyright reasons. Copyright holder is High Performance Computing Research Centre, USAF Academy, Colorado.

Plot of surface pressure distributions for the CFD simulation of a wing with two upstream propellers [8]. Removed for copyright reasons. Copyright holder is High Performance Computing Research Centre, USAF Academy, Colorado.

(a) (b)

Figure 2.3: The effect of two, closely spaced, tractor propellers on wing loading (a) and vortical structures (b) showing the isolated effect of each propeller and their interaction. Redrawn from [8].

Kuhn [48] defines a thrust recovery factor as a metric for assessing how much of the propeller momentum is successfully deflected by the wing to generate lift. Results show that placing two propellers next to each other restricts the expansion of the jet in the spanwise direction. Best performance is achieved by placing the propellers overlapping such that their fully contracted slipstreams are adjacent. The optimum spacing, s/D_p is therefore a function of propeller thrust and streamwise location. By using distributed propulsion with closely spaced propellers, a 10% increase in wing lift was achieved with the same streamwise thrust with overlaps $s/D_p = 0.208$, [34].

2.2.3 Propeller Location

Veldhuis [77] conducted a parametric study on propeller vertical position and angle relative to the wing. High propellers positions above the wing of 25% propeller diameter gave an increase in lift coefficient 56% higher than propellers positioned on the wing chord line. This is due to a higher proportion of the jet momentum moving over the wing suction surface, where the majority of the wing lift is created. However, it has also been found that propeller positions below the wing improve the stall performance of the wing, which may be more important for blown wing design [33]. This effect is similar to a leading edge slat, [70].

Tilting the propeller axis by 20° to blow air upwards onto the wing increases the wing angle of attack, increasing lift and improving L/D by 20% relative to an installation angle of 0°. However, increased loading will lead to earlier wing stall. It has also been found that in-board up rotation is best to maximise lift [51] as the chord is largest near the wing root. Moving the propeller upstream increases wing lift due to additional contraction of the propeller slipstream [68]. 85% of this contraction occurs within one propeller diameter of the disk [23] and so blown wing designers typically place the propellers ~1 propeller diameter upstream of the wing leading edge as a compromise between aerodynamic and structural considerations.

2.2.4 Propeller Diameter

To maximise the wing lift whilst minimising propeller thrust, the designer may be motivated to go for very small jets with a high jet velocity. However, it is well established both experimentally and theoretically, that for small jets, like high thrust coefficients, the lift augmentation effect decreases. Ting et al. [76] found analytically that for 2D jets with a diameter less than two chord lengths, the lift of a flat plate started to decrease for a fixed jet velocity. The threshold diameter increases as the thrust coefficient increases. This effect was also found experimentally by Smelt and Davies [23] when they tested single small propellers. Patterson also observed this effect for 2D RANS simulations of a wing immersed in a finite jet [56].

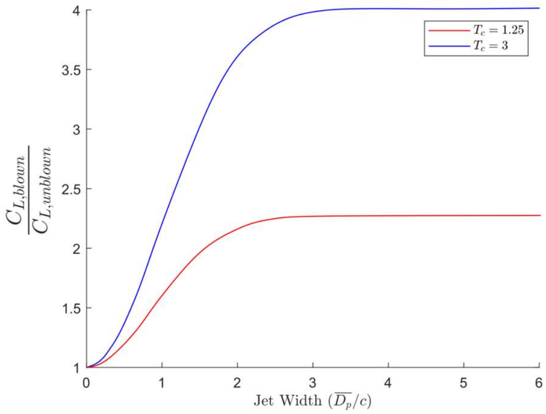

Figure 2.4: The 2D effect of propeller jet width on blown lift, modified from [56]. Decreasing the propeller jet width reduces the lift coefficient of the wing, for the same propeller thrust coefficient.

Whilst the blowing effectiveness decreases with smaller propeller diameters at fixed jet velocity, the total thrust also decreases in proportion to the propeller area. Courtin et al. [22] found in flight testing of an STOL aircraft that reducing the propeller diameter to chord ratio D_p/c from 0.5 to 0.39 increased the lift coefficient in steady flight for a fixed streamwise force coefficient, as shown in Fig. 2.5.

Graph of lift coefficient against streamwise force coefficient with flaps deployed to 36° [22]. Removed for copyright reasons. Copyright holder is Christopher Courtin.

Graph of lift coefficient against streamwise force coefficient with flaps deployed to 34° [22]. Removed for copyright reasons. Copyright holder is Christopher Courtin.

(a)

(b)

Figure 2.5: Lift and streamwise force measurements in flight of a blown STOL aircraft [22]. D_p/c=0.5 in (a) and D_p/c =0.39 in (b). Δc_J is defined in Eq. 2.4. Reducing the propeller diameter increases the wing lift coefficient for the same streamwise force.

Although the measured aerodynamic coefficients for the larger propeller diameter shown in Fig. 2.5 (a) occurred at a higher flap angle of 36°, the lift coefficient is lower for a given streamwise force coefficient. Δc_J is defined in Eq. 2.4 in the next section and can be treated as analogous to the thrust coefficient. The smaller propeller diameter allows a higher thrust coefficient to be used for the same streamwise force, increasing the lift. This effect was also found by Taylor [75] for tilt-wing aircraft. Whilst larger propellers were beneficial for cruise efficiency, small propellers required less power for a given lift coefficient, improving the power consumption during the transition from vertical take-off to horizontal flight. In the next sub-section, it is shown that the total thrust on the aircraft is the key metric when sizing for landing.

2.2.5 Limitations on Blown Wings in Landing

Regulation changes for small aircraft mean that the stall speed during landing may now be defined as that during powered flight, i.e. with distributed propulsion utilised, rather than that for unpowered flight. This allows a higher maximum lift coefficient to be defined [57]. In addition, the new regulations require only an appropriate stall speed safety margin to be implemented. Current requirements are that the aircraft landing speed is 30% higher than the stall speed. This gives an operating wing lift coefficient 41% lower than the maximum lift coefficient of the wing for a fixed wing area. Patterson and Borer [57] argue that applying this traditional safety margin to blown wings does not make sense as the maximum lift coefficients generated are much higher. A blown wing with a maximum lift coefficient of 5 would have a C_L margin of 2.05, greater than the maximum lift of most unblown wings.

To meet the new legislation, Patterson and Borer [57] suggest an absolute lift coefficient margin in the range 0.61 to 0.82, typical of most unblown wings. By using an absolute C_L margin equal to that of the unblown wing, a higher wing angle may be employed than if a 41% safety margin was applied. This approach to the safety margin for landing is discussed further in Chapter 4. It is clear that, even for blown wings, the maximum useable lift coefficient of the wing is still dictated by the maximum lift coefficient.

During landing, the aircraft drag must exceed the blown wing thrust to enable the aircraft to slow down to its landing speed [57]. NASA propose to use tip propulsors to generate drag. This technology may not be used on all blown wing aircraft and so it is important to consider other drag generating devices. While air brakes etc. could be used, these are not desirable in case of an aborted landing when the drag devices would need to be folded quickly [56]. A conventional drag generating device used by pilots is deployable flaps. For larger blown wing aircraft, the angle of attack will be fixed, and lift controlled with a flap. Patterson and Borer [57] calculated different aircraft approach profiles during landing, considering the total streamwise force on the aircraft. To maintain adequate stall margins whilst not accelerating, a linear increase in lift coefficient due to blowing and a linear increase in lift coefficient due to wing incidence as the aircraft decelerates was found optimal, and unlikely to require wind-milling tip propellers to generate sufficient drag.

An alternative, simpler approach to modelling the thrust constraints in landing uses a power loading constraint diagram, as shown in Fig. 2.6. This method was developed by de Vries et al [81] for hybrid aircraft studies. A force balance in the x and z directions produces two equations of motion. Constraint curves can be plotted for each axis. The locus of points produced when these two curves intersect for different flight speeds is shown as the hatched boundary. The addition of distributed propulsion allows higher wing loading with lower drag (and hence thrust) to be used. Additional constraints can be added to account for wing stall loadings and constraints imposed by take-off and landing requirements.

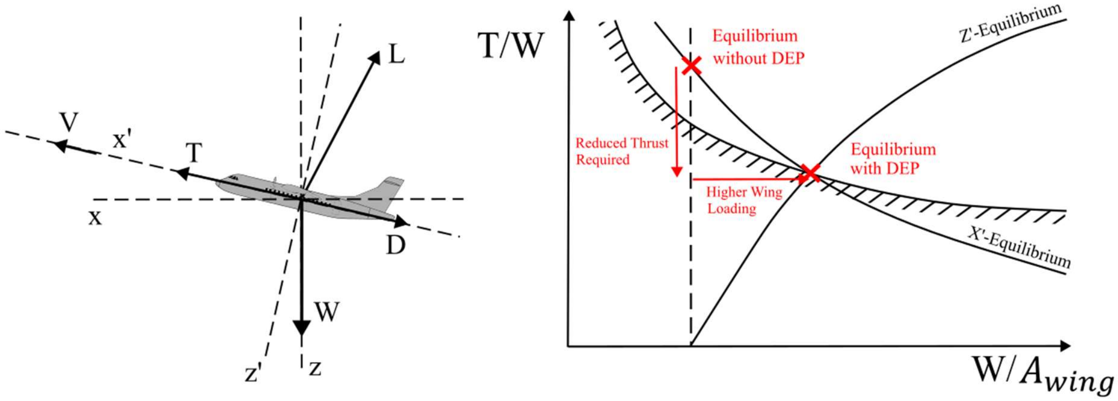

Figure 2.6: Constraints on the aircraft for take-off and landing showing maximum allowable wing loadings for a given aircraft thrust to weight ratio. Redrawn from [80]. Blowing the wing allows higher wing loadings, reducing the thrust in cruise.

Agrawal et al. [3], considering the problem of high blown lift without excessive thrust, developed an experimental set up consisting of four propellers upstream of a wing with flap attached to a load cell. By directing the propeller jets upwards onto the wing pressure surface, and using the flap to deflect the slipstream downwards (shown schematically in Fig. 2.7), they were able to generate zero net thrust. They define a parameter called the excess jet momentum coefficient to quantify the effect of the propeller thrust:

$$\Delta c_J = \frac{J' - \rho {V_\infty}^2 \overline{D_p}}{\frac{1}{2}\rho {V_\infty}^2 c} \quad , \qquad (2.2)$$

where

$$J' = \rho {V_{jet}}^2 \overline{D_p} \quad . \quad (2.3)$$

and V_{jet} is the velocity of the fully developed propeller jet at ambient static pressure assuming no loss of total pressure. Δc_J is related to the propeller thrust coefficient by,

$$\Delta c_J = 2\frac{\overline{D_p}}{c} T_c \quad . \qquad (2.4)$$

The results of Agrawal et al. [3] are shown in Fig. 2.7 with the streamwise force coefficient, C_x defined as:

$$C_x = \frac{D - T}{\frac{1}{2}\rho {V_\infty}^2 A_{wing}} \quad , \qquad (2.5)$$

and ϕ is the flap angle. Sweeps were measured for fixed flap angles at different wing angles and thrust settings. The excess jet momentum coefficient was fitted through the data points, and curves of constant Δc_J in increments of 0.5 from 0 to 4.5 are plotted in the Figure. Values of C_x greater than zero indicate a net force on the aircraft in the streamwise direction (net drag). Values of C_x below zero have excess thrust. As the flap deflection increases, the drag from the flap increases, moving C_x closer to zero. At a flap deflection of 40°, exceptionally high lift coefficients of ~8 can be achieved with zero net thrust. However, a rake traverse placed downstream of the wing showed upper surface flow separation. The suction surface boundary layer separation of this geometry is discussed in Section 2.4.

Graphs of lift coefficient against streamwise force coefficient with flaps deployed to 0°, 20°, and 40° for a blown wing in a wind tunnel [3]. Removed for copyright reasons. Copyright holder is the American Institute of Aeronautics and Astronautics, Inc.

Figure 2.7: Plots of lift against streamwise force for a range of thrust coefficients [3]. The propeller is inclined downwards, blowing high speed flow onto the underside of the flap an enabling lift coefficients of up to 10.

2.2.6 Summary

The results of this section detail some of the effects of propeller positioning on the lift and streamwise force coefficients of a wing. Optimum lift can be achieved with propellers positioned above the wing centreline, with large diameter to chord ratios, positioned as far in front of the wing leading edge as possible. However, reducing the propeller diameter increases the wing lift for a given thrust and it has been observed that low propeller locations have a higher maximum lift coefficient. It is clear that the blown wing is limited in its performance by the propeller thrust and the maximum lift coefficient of the wing. Different methods exist to account for this in aircraft modelling. The correct propeller position and size to maximise blown wing performance within these constraints is not yet understood.

2.3 Current Propeller-Wing Modelling Techniques

An optimum propeller location will exist for a blown wing design. However, the benefits quoted in the previous section for blown wings with different propeller positions are sensitive to the modelling approach used. In this section, we look at what models exist currently to predict the blown wing performance, and how they compare to experimental data. Models range from low order approaches able to carry out rapid design space explorations, to more computationally expensive CFD. As a result, the impact of geometry is usually modelled with either a low order code for multiple geometries, or a higher order CFD simulation limited to a few geometries.

Experimental data for blown wings with multiple propulsors is currently sparse. 33% of the 705 points used by Barnhart et al. [10] came from a single study, the one shown in Fig. 2.7. Validation data is therefore not always available for these different models. In this section, we examine the available modelling techniques, and how well they are able to capture the mechanisms of the blown wing interaction.

2.3.1 Analytical Models

Analytical models have been developed for the propeller-wing interaction using lifting line and lifting surface methods. Jameson [44] considered early V/STOL aircraft and developed a lifting line model for the blown wing lift. The model assumed a uniform jet and that the jet was not deflected by the wing. Cases where individual jets merge to form a single elliptical jet with foci at each of the wing tips could be solved analytically. The model showed that the effect of blowing was to change the aspect ratio of the wing, increase the lift curve slope according to Eq. 2.1 and introduce additional induced drag. The increase in induced drag is also equal to the ratio of dynamic pressure in the jet to the freestream. Figure 2.9 compares this model to experimental data.

2.3.2 Low Order Methods

A number of other low order methods have also been proposed to model the influence of a propeller jet on a wing [2, 11, 21]. These models use panel methods or vortex lattice methods to discretise the propeller and wing. Free wake methods use iterative schemes to find the location of the jet in relation to the wing. Good agreement between experiments and these low order models has been achieved for single propellers away from the stall point. These models are capable of modelling both the interaction of the wing with the propeller, and the upstream effect of the wing potential field on the propeller. However, these methods do not include a model for viscous drag or wing stall, and are computationally expensive for multiple propellers. A simpler method, known as one-way coupling, calculates the jet profile of a propeller from blade element momentum (BEM) theory and impose this wake as a boundary condition on the wing, which can be modelled from experimental data or a lifting line [12, 78]. This approach does not allow the interaction between propellers or the influence of the wing on the propeller to be modelled. In these models, the performance of each 2D wing section along the span is calculated from a look-up table of measured aerodynamic coefficients at different angles of attack and Reynolds number. A 3D analysis of the wing boundary layer is not possible.

2.3.3 2D Computational Fluid Dynamics

For distributed propellers, few parametric studies similar to those discussed in Section 2.2 have been conducted so far. Patterson, as part of NASA's ongoing efforts to design the X-57 aircraft, generated a surrogate model to predict the effect of the propeller jet size, location and velocity, on wing lift [60]. The model used an inviscid 2D CFD solver with an actuator disk free to move in space upstream of the wing. This approach uses Jameson's assumption that the discreet propeller jets merge upstream of the wing to form a uniform jet. Patterson proposed the use of a factor, $\beta_{Patterson}$, as a lumped parameter to correct Eq. 2.1 to model the effect of finite jets. In the limit as the jet width tends to infinity, $\beta_{Patterson}$ is equal to 1. With this modification, the lift of a wing is augmented by a jet according to,

$$C_{L,blown} = C_{L,unblown} \frac{\left(\beta_{Patterson}\left(V_{jet} - V_{\infty}\right) + V_{\infty}\right)^2}{{V_{\infty}}^2} \quad , \quad (2.6)$$

where $C_{L,unblown}$ is the unblown wing performance, V_{∞} the aircraft speed and V_{jet} is the velocity of the fully developed propeller jet at ambient static pressure assuming no loss of total pressure.

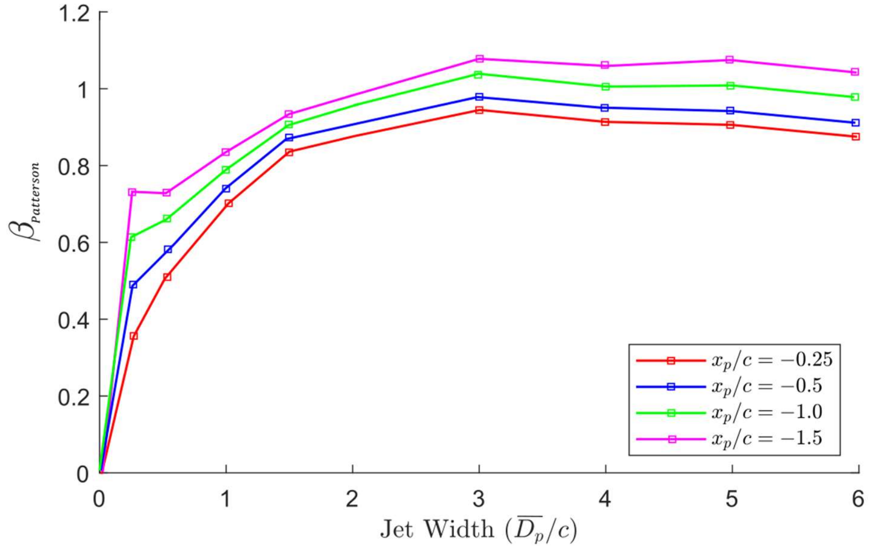

Figure 2.8: A 2D inviscid RANS model of the blowing effectiveness, $\beta_{Patterson}$ of a propeller jet for different jet heights and positions in front of the wing leading edge, modified from [60].

Figure 2.8 shows a plot of $\beta_{Patterson}$ for different upstream positions and jet diameters at an angle of attack of 1°. For wide jets, the jet velocity can be used to obtain a new reference dynamic pressure and $\beta_{Patterson}$ approaches 1. Moving the jet upstream increases $\beta_{Patterson}$ as the jet contracts further. The simulations were validated against RANS CFD actuator disk calculations, and experimental data and compared to the analytical models of Smelt and Davies [23] and Jameson [44], the results of which are shown in Fig. 2.9.

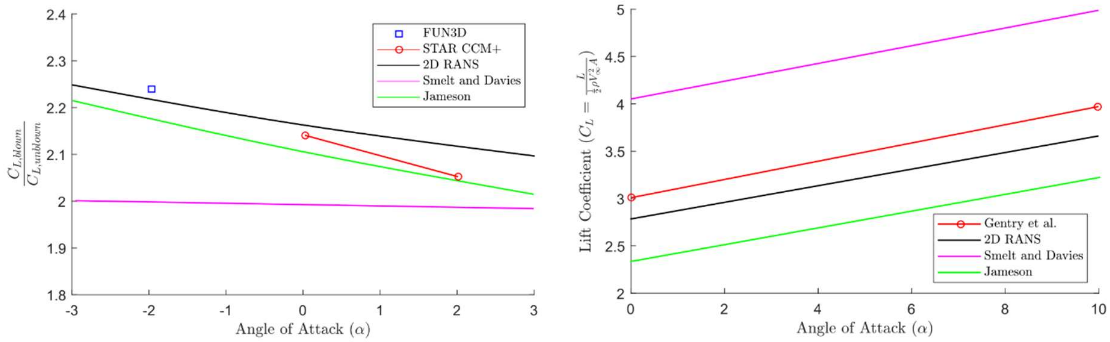

(a) (b)

Figure 2.9: Comparison of Patterson's 2D model [60] to the models of Jameson [44] and Smelt and Davies [23]. Also plotted are the RANS CFD results of the Leaptech DEP blown wing [55] in (a) and experimental data from Gentry et al. [30] in (b).

Fig. 2.9 (a) shows the lift augmentation for a narrow range of angles of attack predicted with the different models. The 2D RANS model better captures the 3D RANS than either the experimental curve fit of Smelt and Davies (which is too general to capture the details of propeller location) or the model of Jameson, whose assumptions about the wing being immersed in an elliptical jet are inadequate. Gentry et al. [30] tested a single propeller whereas the LEAPTech aircraft has a DEP blown wing. The accuracy of Jameson is sufficient for the closely spaced propellers, but breaks down for isolated propellers.

Using the 2D CFD data, Patterson generated a surrogate model for wing lift prediction that has been employed by other authors conducting whole aircraft analyses of distributed propulsion benefits [59, 81]. However, there are several drawbacks of the work. The practical lift of a blown wing is dependent on its stall point, and its net streamwise drag during landing, both of which requires viscous effects to be considered. The model does not account for vertical position which is known to influence wing lift [3, 79]. Finally, the model only considers a plain wing whereas real wings employed in blown systems will likely have flaps.

2.3.4 3D Computational Fluid Dynamics

A number of studies have been published which investigate the propeller wing interaction using 3D CFD simulations. Stoll et al [72] compared two RANS codes with different turbulence models to a vortex lattice method and experimental data for the NASA LEAPTech aircraft. The vortex lattice method (VLM) used an actuator disk for the propeller with prescribed axial and radial velocities. The VLM produced a lift curve with a slope twice the gradient of the RANS models. The RANS was able to correctly capture the lift curve slope of the experiment, which consisted of a wing mounted to a truck. There was uncertainty at the time of publication on the upstream conditions due to the truck, and the ground plane effect of the truck bed. Given these uncertainties, the agreement between the methods was promising.

Actuator disks offer the ability to capture the one-way interaction of the propeller on the wing if the propeller loading is known and assumed to not change due to the wing potential field. Cao et al. [17] found that an actuator disk model was able to predict the averaged aerodynamic coefficients of a blown wing to within 3% of that predicted by a URANS calculation, using only 3.4% of the computational time. Casses et al. [18] compared an actuator disk implementation and a full URANS calculation for the geometry in Fig. 2.7. They found that the actuator disk accuracy dropped relative to the URANS due to the strong up-wash ahead of the wing due to its low positioning in relation of the wing, violating the one way assumption.

Roosenboom et al. [65] used Particle Image Velocimetry (PIV) to validate the use of URANS for modelling multiple propeller slipstreams interaction with a wing. The result for one plane is shown in Fig. 2.10. The authors claimed good agreement was achieved between the CFD and PIV as the CFD was able to capture the location and magnitude of the vortices shed by the propeller. It was noted however that the velocity in the propeller jet was higher in the CFD and this was attributed to inviscid modelling of the propeller blades. An overprediction of the viscosity in the Spalart-Allmaras turbulence model [71] was identified as the cause of discrepancies in the breakdown of the propeller wake vortices.

Image of experimentally measured PIV contours of vorticity and CFD contours of vorticity for the same geometry consisting of a wing with two upstream propellers and a downstream flap [65]. Removed for copyright reasons. Copyright holders are Airbus SAS and DLR, The German Aerospace Centre.

Figure 2.10: PIV vs. CFD for a propeller slipstream [65]. The unsteady CFD simulation is able to capture the position and magnitudes of the propeller wakes interacting with the wing.

Several authors have used 3D URANS as a benchmark from which to assess the performance of lower order codes. Ahuja and Litherland [4] compared an unsteady panel method code to a 3D URANS simulation of a single propeller upstream of a wing. The panel method took 10 minutes to converge whilst the URANS required 50-60 hours of HPC wall clock time. The methods agreed for low to moderate angles of attack, but diverged for high angles of attack up to and beyond stall. Casses et al. [18] also found that a blade element model performed well for on-design cases, compared to URANS, but was unable to capture the 3D localised stall on the wing flap.

2.3.5 Summary

A range of modelling approaches are available to the designer, from computationally cheap vortex lattice methods, and 2D actuator disk RANS models, to more expensive 3D CFD models using either an actuator disk or an unsteady fully resolved propeller calculation. 3D URANS is generally accepted to capture the flow-physics of the propeller-wing interaction well and correctly predicts aerodynamic lift and drag coefficients. Actuator disk models have been compared to URANS, and experiment and found to agree well provided that the distortion at inlet to the actuator disk plane is small.

For preliminary design of the aircraft, where the overall configuration is being decided, only the simplest analytical models and low order codes are available to the designer due to the range of possible designs, and high solution times associated with higher order methods. Patterson attempts to bridge the gap between the cheap low order models, and the validated actuator disk approach by moving to a 2D RANS solver. The 2D RANS solver was shown to predict both 3D actuator disk simulations, and experimental results for a few isolated cases. Further validation is required, however, and viscous effect need to be included.

Currently, high-fidelity CFD and experimental data sets that exist are only for a few specific geometries. The agreement between URANS, Actuator disk 3D CFD and experiment is encouraging however the transition to lower order models, and the loss of accuracy in the process is still under investigation. Patterson's 2D CFD approach offers a useful compromise. Chapters 6 and 7 will expand on this work to establish the 3D effects not captured by the 2D model, and the errors this introduces. Many geometries have been tested at a lower fidelity, but these results are uncertain around the stall point. A better understanding of the design space around the stall point is still required.

2.4 Blown Wing Stall

It was shown in Section 2.2.5 that accurate prediction of the maximum wing lift coefficient is essential for predicting the blown wing performance during landing. The maximum lift coefficient occurs at the point where the benefits of increased loading due to wing incidence are offset by the separation of the flow on the wing suction surface. This is defined as the stall point in this work. Stall behind a blown wing can lead to violent aircraft buffet due to the higher dynamic pressure of the jet [33]. In this section, we look at what is known about the mechanisms governing the blown wing stall point.

2.4.1 The Effect of the Propeller on the Wing Stall Point

As propeller thrust increases, the stall wing angle of a blown wing increases. As the wing angle increases, the propeller introduces a component of flow perpendicular to the freestream direction. This reduces the incidence seen by the wing, allowing higher geometric angles of attack to be achieved for a given flow angle. The effect was widely used on tilt-wing aircraft in the 1950's and 60's to allow transition from high angle of attack take-off configurations to low angle of attack cruise configurations [53]. Fig. 2.11 shows the predicted stall angle from a low order model [15] compared to experimental data [75] for a tilt wing. The model over-predicts the stall angle for high thrust settings, but wing angles of 40° can still be achieved experimentally without wing stall.

Plot of wing stall angle for different propeller thrust coefficients comparing a model from [15] with an experiment from [75]. Removed for copyright reasons. Copyright holders are K. Butler, K. Huang and L Goland, U.S Army Aviation Material Laboratories.

Figure 2.11: Experimental [75] and model data [15] showing the change of stall angle with thrust coefficient. Redrawn from [15]. The propeller jet rotates the slipstream and delays stall to higher geometric angles of attack.

2.4.2 The Effect of the Propeller on the Wing Boundary Layer

As the thrust from the propeller increases, the velocity over the wing goes up, increasing the local Reynolds number. Increasing the Reynolds number thins the boundary layer, and allows it to tolerate greater diffusion. It has also been reported that by blowing the wing, the centre of pressure can be made to move rearward depending on the streamline curvature produced [14]. For low Reynolds number blown wings, it has been found that the propeller slipstream promotes early transition of the wing boundary layer and a decrease in the chordwise extent of the separation bubble upstream of this point, [5, 6]. This reduces drag and makes the boundary layer less susceptible to trailing edge separation. For single propeller tractor configurations, the propeller's influence extends well outside its wake region [5], reducing the drag of the unblown wing. Veldhuis [77] showed that for these low Reynolds number wings with laminar flow, the wing locally transitions from laminar to turbulent at the blade passing frequency within the propeller wake.

2.4.3 Separation Location Downstream of the Propeller

For practical blown wings fitted to regional aircraft, it is likely that the wing boundary layer will be fully turbulent. In this section, we investigate the separation patterns seen for blown wings with turbulent boundary layers.

The rotation of the propeller slipstream leads to a spanwise variation in boundary layer growth across the wing. At higher incidences (either wing angle or flap angle), this non-uniform boundary layer growth can lead to locally separated regions on the wing suction surface, creating a complex 3-dimensional flow field [35, 85, 86]. Figure 2.12 shows the flow visualisation results from a range of wing angles and propeller advance ratios for a plain wing downstream of three distributed propellers at a Reynolds number of 170,000 [84]. The propeller swirl causes the wing separation to move rearward in the region of propeller downwash where the incidence decreases, and moves upstream in the region of propeller upwash, causing a leading edge separation. Leading edge separation was also observed by Ahuja and Litherland for a 3D URANS simulation of a single tractor propeller upstream of the wing [4].

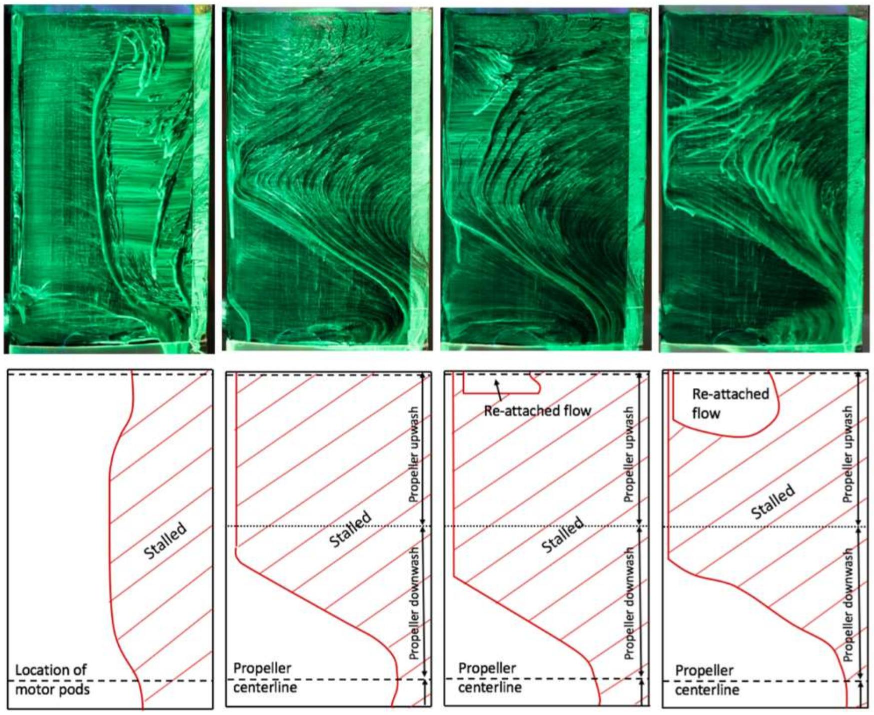

(a) (b) (c) (d)

Figure 2.12: Three-dimensional separated flow structure over the suction surface of a blown wing [84]. In (a), angle of attack, α=15°, advance ratio J=∞, in (b), α=20°, J=0.575, in (c), α=30°, J=0.378, in (d), α=20°, J=0.307.

For plain wings fitted with large propellers, the wing separates first on the up-wash side of the propeller due to the higher local angle of attack of the wing. However, for blown wing geometries with flaps, the location of the separation is not well understood. Cao et al. [17] found that the flap behind a single propeller stalled when no jet from the propellers passed through the flap slot to re-energise the flow. Goodson [32] in their testing of a 4-propeller tilt-wing aircraft conducted tuft experiments on a full-scale model of the XC-142A. The onset of stall was noted from the tufts to occur at the boundary between the closely spaced overlapping propellers, near the trailing edge. The propellers rotate inboard down and show the largest region of separated flow to exist behind the outboard propeller, where the propeller swirl will be decreasing the flow angle seen by the wing. This effect was also observed by Deere et al. [24] using actuator disks to model the propellers. It is interesting to note that the stall pattern for many propellers is the same as that between just two propeller. Neither author commented on the location of the separation or offered an explanation as to its cause. Chapter 7 attempts to provide an explanation for the stall location and how it can be delayed.

Schematic of the flow over the wing of an XC-142A aircraft with separated regions of the wing are shaded. Removed for copyright reasons. Copyright holders are K. W. Goodson [32].

CFD simulation of a wing with multiple upstream propellers showing the shear stress on the wing surface. Separated regions of the wing are shown. Removed for copyright reasons. Copyright holders are NASA and Joby Aviation [24].

(a)

(b)

Figure 2.13: Results of tuft experiments for a full-scale XC-142A aircraft [32] at the point of stall, with the stalled region shaded (a), and Actuator disk CFD [24] of a distributed blown wing with stalled flap regions hatched out (b). Both experiment and CFD show stalled flow on the flap downstream of the propeller downwash region.

The spanwise variation in flap stall was also observed by Courtin et al. [22] for flight test results of the geometry shown in Fig. 2.7. Again, the tufts show periodic reversed flow downstream of the downwash region of the propeller. The outboard propeller has been left to windmill in this test. The authors suggested that the spanwise variations in the stall point were likely to be due to variations in the velocity field around the wing, but offered no further explanation.

Image of a model aircraft in flight showing tuft flow measurements on the flap near stall. Removed for copyright reasons. Copyright holder is Christopher Courtin [22].

Figure 2.14: Location of separations on the flap of a distributed blown wing during a test flight. [22]. The test flight shows stalled flow on the flap downstream of the propeller downwash region.

2.4.4 Summary

Limited work has been done on the stall mechanisms for a distributed blown wing. For large propeller diameters, without a flap, it is generally accepted that the additional upwash onto the wing caused by the upward rotation of the propeller leads to premature leading edge stall of the wing. At high angles of attack, the jet from the propeller can actually decrease the average upwash onto the wing by modifying the direction of the flow. For smaller diameter propellers, especially when interacting with a flap, the stall mechanism has not been investigated. Multiple authors observe spanwise variations in boundary layer separation location along the span on the flap, but as yet no explanation has been given. In Chapter 7, the stall mechanism for a blown wing with distributed propulsion is explained, and used to extend the operating range of the wing.

2.5 Optimum Blown Wing Design to Maximise Overall Airframe Performance

For conventional aircraft, an experienced designer can quickly move from the conceptual to the preliminary design phase with an intuitive understanding of the effects of engine size and position on the airframe performance. Such an intuitive understanding does not yet exist for the sizing of distributed propulsion systems and both the designer and the researcher rely on whole aircraft models and optimisation software to choose the best design, often incorporating simple blown wing models to size an aircraft. In this section, we look at some of the modelling approaches taken to predict the benefits of a blown wing aircraft.

2.5.1 Integration of Distributed Electric Propulsion into Aircraft Models

De Vries et al. [80] conducted a detailed study of the performance of several aircraft configurations with, and without, distributed propulsion. The airframe considered was similar to the ATR-72, with a mission range of 1528km and a payload of 7500kg. This is one of few studies to consider a large, regional aircraft design. The modelling considered a number of different hybrid-electric powertrains, focusing on a conventional powertrain, a serial powertrain (where the gas turbine is used as a generator, powering electric motors) and a partial turboelectric powertrain (where the gas turbine produces thrust as well as powering electric motors).

A representative flight mission was assumed for the aircraft. The results found that, compared to the conventional airframe, the distributed propulsion increased the wing L/D by 6%. For the serial hybrid, the power consumption increased by 40% due to the increased take-off weight of the aircraft. For the partial turbo-electric power train, the power consumption only increased by 3%. The higher weight for the serial powertrain is due to the increased motor mass needed to produce take-off thrust. It is clear from this study that the effect of motor weight, and power requirements of the possible motor configurations must be accounted for in a whole aircraft analysis.

The modelling of the blown wings in [80] was limited in several ways. First, the benefits of increased blown area on the propulsive efficiency were not captured. Second, the wing was scaled on a constant aspect ratio. This increases the induced drag as the wing cruise lift coefficient increased. The NASA X-57 work scales the wing on a constant chord, producing thinner more efficient wings. This later approach is used in this thesis when predicting blown wing benefits. Finally, no optimisation of the propulsion system geometry was conducted and only specific geometries were considered. The modelling of the blown wing employs the 2D actuator disk model developed by Patterson [56] for use on the X-57. As discussed previously, this model is limited by the lack of viscous effects.

Clarke et al. [20] considered two general aviation aircraft: a 2 propeller configuration, and an 8 propeller configuration. A representative flight cycle was specified and the distributed propulsion was found to reduce the energy of the flight from 57.96kWhr’s to 37.57kWhr’s, a 35.2% reduction. The distributed propulsion was modelled with a vortex lattice method which was found to correctly predict experimental wing loadings at low incidence to within 2%, but at an angle of attack of 10°, near the wing stall point, the predictions began to diverge by up to 10%. Only the two geometries were considered, and no optimisation of the propeller number, or spacing was investigated.

Flanagan [29] pointed out that the work of Clarke et al. [20], like the work of de Vries et al. [80], was limited due to the lack of appropriate optimisation of the airframe. Flanagan developed an optimisation code coupled to an aircraft model to predict the performance of various aircraft sized for different mission requirements. The optimiser showed that the design space for aircraft with distributed propulsion is very lumpy, with local peaks and troughs in performance as it moved around the high-dimensional design space. The modelling employed a blade element model for the propeller and wing which Flanagan acknowledged did not capture the maximum lift coefficient of the wing well. As the design space is lumpy, it is likely that the optimum geometry could change considerably depending on the distributed propulsion modelling.

Whilst the optimisation routines discussed in this section are useful, and necessary to ultimately design DEP aircraft, an understanding of what the available design space is for a blown wing is needed, and more accurate blown wing models with stall performance included is required.

2.5.2 Installation Problems with Blown Wings

Little is discussed about the installation of blown wings in the open literature. For single tractor propellers, the optimum propeller location: large propeller placed above and well in front of the wing, is not possible due to the structural requirements of designing the nacelle to achieve this [78]. For distributed blown wings, multiple nacelles are required, each generating drag and requiring structural support, adding weight to the airframe. Patterson acknowledges that, for some blown wings, this drag may exceed any benefit from the blowing [56]. Work is undertaken in this thesis to address the impact on the wing aerodynamics of fitting multiple nacelles, although the weight of the nacelles is neglected.

2.5.3 New Approaches to Quantifying Propulsor-Airframe Benefits

The models of Clarke et al. and Flanagan discussed previously use drag book keeping in order to estimate the change to the airframe performance with distributed blowing. De Vries et al.'s work employs a power balance analysis. This method [25] calculates the power consumed by different parts of the airframe during cruise, such as losses in the boundary layer, kinetic energy in propulsion wakes etc. Moving within the design space then allows the modification to each power term to be analysed. This method is useful for closely integrated propulsion and airframe components, such as boundary layer ingestion, and is also relevant for blown wings, where benefits of reduced dissipation in the wing boundary layer may be offset by increased kinetic energy losses in the propeller wake.

2.5.4 Summary

Reports that detail the blown wing benefit are typically limited to full aircraft design systems. These codes use the simplest blown wing models possible due to solution speed which often poorly capture the wing performance near stall. The reports of blown lift benefit vary from 500% with the NASA X-57 to negligible or worse than the baseline aircraft in the case of de Vries. A framework in which to compare geometries fairly, and assess whole airframe benefits, is required. The full design space needs to be mapped out with enough complexity to capture the key physics, but simply enough to be done in a sensible time frame. For integrated systems, this is challenging but one approach, power balance, offers the ability to quantify individual component effects.

2.6 Conclusions

In this chapter, the previous work on blown wings has been examined in relation to the four questions posed in Chapter 1. We can now be more precise about the questions to be answered in this thesis.

The first question in Chapter 1 asked, "how should a blown wing with distributed propulsion be designed in order to maximise the lift of a real aircraft?" Designers do not yet have an intuitive understanding of where to position the propellers in a blown wing, how to size them, and what the realisable benefit of including the blown wing is. Both the on-design and off-design performance of the blown wing needs to be considered in order to maximise the practical lift coefficient of the blown wing during take-off and landing. By maximising the wing lift, the wing profile drag can be minimised, the key objective of the blown wing. Constraints on the sizing due to landing should be included, and the effect of wing stall modelled. The installation drag of the blown wing is also unknown and requires modelling. A more precise first question, answered in Chapter 4 and 5 is, therefore:

1. What propeller position and diameter should be used to minimise the drag of a blown wing whilst constrained to still give adequate performance in landing, and by how much can the wing drag be reduced?

The studies presented in Chapters 4 and 5 report the drag saving of the blown wing at cruise due to the reduced wing area enabled by distributed blowing on a regional aircraft with electric propulsion onboard. The propellers are assumed to be folded during cruise, and only deployed during high lift situations such as take-off and landing. Changes in drag due to the installation weight of the blown wing are not considered, however the drag due to the wetted area of the nacelles is modelled.

The second question in Chapter 1 asked, "can a 2D model of the blown wing correctly predict the on-design, and off-design performance of a blown wing?" The 2D approach of Patterson [59] is attractive as it ignores the complexities of spanwise flow variations for initial design. Provided that this approach is able to correctly predict the overall aerodynamic performance coefficients of the wing, the local 3-dimensionl flow-field can be initially ignored. Previous work has compared different fidelities of modelling, but the full range of complexities, from 2D modelling to experiment has not been considered. A more precise second question answered in Chapter 6 is, therefore:

2. What are the limitations of 2-dimensional actuator disk modelling for a blown wing and by how much does the performance prediction change as the fidelity of the modelling is systematically increased from 2D modelling to experiment?

The third question in Chapter 1 asked, "by what mechanism does a blown wing stall?" Whilst the stall mechanism for large single propellers on a plane wing is well understood, the stall on a blown flap with multiple small propellers has been observed but not explained. Delaying the stall of the wing to higher angles of attack is important to increase maximum lift. How well the 2D modelling captures the real, 3D stall is also important in order to assess if the model under-predicts or over-predicts the maximum lift coefficient in preliminary design. A more precise third question, answered in Chapter 7 is, therefore:

3. What is the mechanism by which the flap of a blown wing stalls? How does the position of the propeller in relation to the wing affect the stall point? Can 2D modelling capture this behaviour?

The final question in Chapter 1 asked, "how should a blown wing with distributed propulsion be sized in order to minimise the power requirements of a real aircraft, and what is the overall benefit of a blown wing on performance?" Current work estimating the overall performance of a blown wing uses simplified models with inadequate prediction of the blown wing performance. With access to validated 2D modelling of the full design space, and experimental data for specific blown wing geometries, the performance benefit of blown wings could be predicted with greater confidence. The benefit of folding propellers away during cruise vs. continuous deployment has not yet been considered for larger regional aircraft. A more precise final question, answered in Chapter 8 is, therefore,

4. What is the performance benefit of using distributed blowing over conventional propulsion layouts and how should the blown wing be configured to maximise this benefit?

This question is answered by comparing a regional aircraft with distributed propulsion to a regional aircraft fitted with a more conventional propulsion system with two propellers. Both aircraft are assumed to have electric propulsion onboard provided by either a hybrid-electric system or fully electric powertrain, and the maximum take-off weight is assumed constant. This allows the aerodynamic benefits of fitting a blown wing to an aircraft with electric propulsion to be assessed, without the complexity of a full aircraft weight convergence study such as the ones performed by deVries [80] and Clarke et al. [20].

3. Methodology

3.1 Introduction

This chapter is split up into two sections. The first section describes the computational fluid dynamics modelling methods used in this thesis. These consist of both two-dimensional and three-dimensional actuator disk simulations of a blown wing. The second section describes the low Reynolds number experimental test rig (developed for the same geometry as the numerical simulations) consisting of a configurable 2D wing section with propellers mounted in a wind tunnel.

3.2 Computational Fluid Dynamics Modelling Methods

This section describes the development of a computational fluid dynamics (CFD) set-up to model a blown wing using actuator disks. The solver chosen was ANSYS Fluent (v17.0) [7] which can implement both two-dimensional (2D) and three-dimensional (3D) Reynolds averaged Navier-Stokes models (RANS) of an aerofoil downstream of an actuator disk.

3.2.1 Mesh Generation

To conduct a design space exploration for two-dimensional and three-dimensional blown wings, rapid meshing software was required due to the large number of cases to be tested, each with a different geometry. Pointwise v18.3 [61] was used as the meshing software. Automation is achieved with a Glyph meshing script. The script is edited using MATLAB [52] and controls the locations of nodes, the number of mesh points and their spacing. A combination of structured and unstructured mesh regions are used to resolve the flow, as shown in Fig. 3.1. Pointwise's TRex functionality uses in-built algorithms to calculate the growth of tetrahedral cells into the freestream regions of the mesh. The boundary layer region around the wing uses a structured mesh with a y+ of 30 and a growth rate of 1.1.

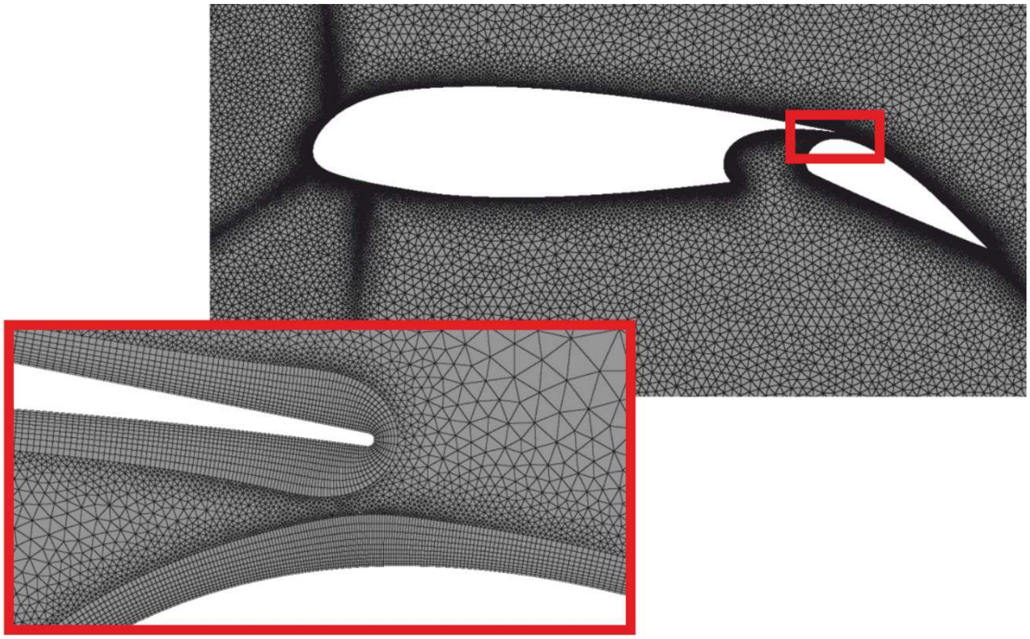

Figure 3.1: Meshing approach used for 2D and 3D CFD simulations [37]. The red box shows a close-up of the mesh in the gap between the wing and flap. The boundary layer region consists of a structured mesh, with unstructured cells in the far-field.

Figure 3.2 shows the overall mesh structure for 2D and 3D actuator disk cases. The solver uses a hybrid unstructured mesh between the actuator disk and wing to join up the complex geometries. A structured mesh is used around the wing boundary layer, and in the streamwise direction around the actuator disk. The structured mesh around the actuator disk was necessary to ensure continuity in the calculation, as the body force implementation (see Section 3.2.3) required the actuator disk boundary to be defined. As a result, a new mesh was required for each actuator disk position. Separate Glyph scripts were written for 2D and 3D meshing, as well as scripts to add the flap into the mesh (not shown in Fig. 3.2). 2D meshes can be generated in ~90 seconds, and 3D meshes can be generated in ~5 minutes. $1\text{x}10^5$ cells are used for a 2D simulation and $4\text{x}10^6$ cells for a 3D simulation. The mesh size was determined with a mesh independency study of the lift and drag coefficient for the wing without a flap or propeller. The mesh was deemed sufficiently refined when the measured lift and drag coefficients varied by less than 0.1%. The mesh density around the actuator disk was determined by the requirement that the polytropic efficiency of the actuator disk be greater than 99.9%.

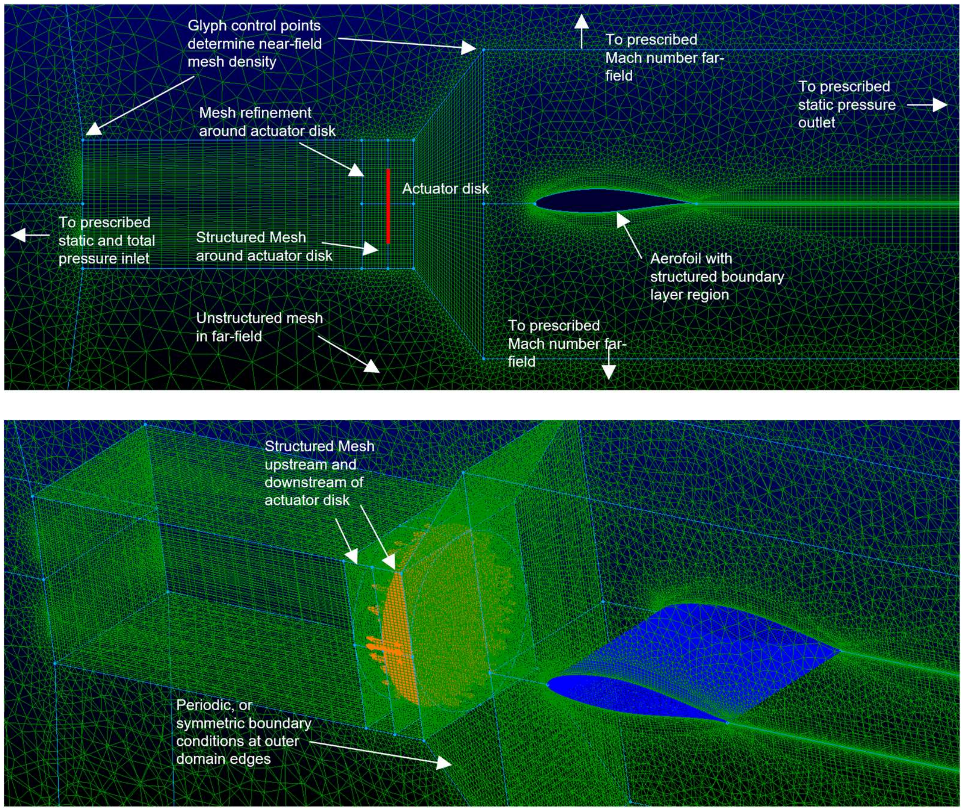

Figure 3.2: Mesh structures for 2D (top) and 3D (bottom) CFD simulations. The wing is shown in blue, and the actuator disk in orange. Control points are added in the mesh to allow for refinement of the mesh near the wing and actuator disk.

3.2.2 ANSYS Fluent Solver

The ANSYS Fluent v17.0 CFD solver [7] was chosen to model the propeller-wing interaction with an actuator disk. The solver has a well-documented user-defined-function capability that allows users to include custom body force models in the solver. This allowed the actuator disk model, described in the next section, to be implemented quickly. The pressure based solver was chosen due to its greater stability over the alternative density based solver.

The Spalart-Allmaras turbulence model [71] was chosen. The model was originally developed for use with external aerodynamic flows and being a single equation model, is quick to solve. Wall functions were used to model the boundary layer around the wing. A mesh domain of 20 chord lengths by 20 chord lengths was used to ensure the wing did not influence the freestream boundary conditions, with the wing placed at the centre of the domain. The boundary conditions of the simulations consisted of a specified total pressure, static pressure and flow angle at the inlet to the domain, giving control of the freestream velocity and angle of attack. The downstream outlet had a specified static pressure, set to zero gauge pressure, and the upper and lower outer domains had specified flow angles and Mach numbers. For the 3D solutions, a periodic boundary conditions was applied at the spanwise outer boundaries of the mesh for cases with co-rotating flow, and mirror boundary conditions for counter rotating (or no-rotation). This allows the solver to model an infinite series of propellers.

To improve convergence speed, simulations were run on the Cambridge University High Powered Computing Service, using 72 cores [16]. Simulations typically converged within 20 minutes for a 2D case, and between 12 and 24 hours for a 3D case depending on the complexity of the geometry. For runs of a single geometry at multiple thrust settings, the results of a previous simulation were used as an initial guess. To calculate total lift and drag, a control volume approach was used around the domain. Comparisons between the control volume method and a surface integral approach around the wing found a 0.3% discrepancy in lift, and 3-5% discrepancy in drag. The skin friction extracted from the solver is calculated from the gradient of the velocity across the first cell. As a wall function has been used, this shear stress was typically out by up to 20% [45] leading to the discrepancy, hence the control volume approach was used to calculate forces on the wing.

3.2.3 Actuator Disk Implementation

To model the effect of swirl, and non-uniform pressure rises across the actuator disk, a user-defined-function (UDF) was developed to integrate with the Fluent software, capable of modelling the actuator disk as a body-force momentum source [74]. This was initially developed in 2D, then expanded to 3D to include a radial and tangential momentum source to model swirl.

Figure 3.3 shows the geometry used to calculate the contributions of axial, radial and tangential force to the x, y, and z-components of the body force. The actuator disk is treated as a thin disc over which the force acts. The UDF loops through the mesh during each iteration, determining the value of δ, r and ψ. If δ is less than the thickness of the disk and r less than the radius of the disk, the solver applies a force per unit volume to the cell. The components of the body force are calculated as:

$$F_x = F_a \cos\theta + \left(F_r \cos\psi + F_\psi \sin\psi\right) \sin\theta \quad , \quad (3.1)$$

$$F_y = F_a \sin\theta - (F_r \cos\psi + F_\psi \sin\psi) \cos\theta \quad , \quad (3.2)$$

$$F_z = F_r \sin\psi - F_\psi \cos\psi \quad . \quad (3.3)$$

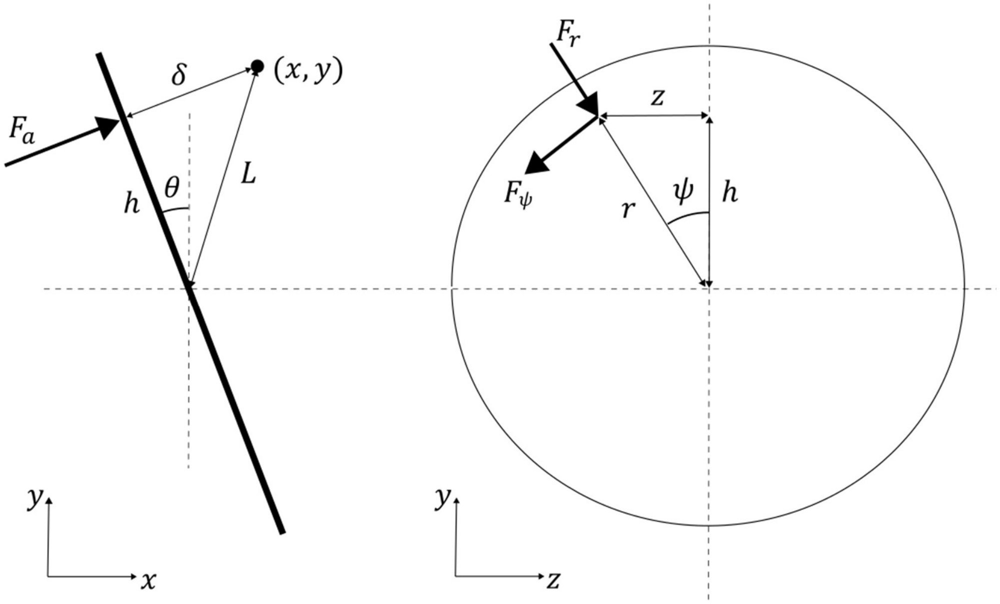

(a) (b)

Figure 3.3: Diagram showing the calculation of geometric quantities used by the Fluent UDF to model the body forces applied in 2D and 3D actuator disk simulations.

F_r is set to zero for a propeller. For the 2D simulations, z, ψ and F_ψ are also equal to zero. As well as introducing a momentum source into the flow, the UDF calculates an energy source equal to the product of force and local velocity to model the work done by the disk.

Figure 3.4 shows contour plots of pressure and velocity around a 2D actuator disk. For 2D simulations of an actuator disk, a uniform axial momentum source is applied at the actuator disk plane, leading to a uniform step change in the static and total pressure. The total momentum applied is used to define the thrust coefficient of the actuator disk. An actuator disk thickness (δ) of 1% diameter was used for all simulations. The fluid contracts as it accelerates through the disk, as shown by the streamlines. The curvature of the streamlines leads to the pressure gradients outside of the jet streamtube. Within the jet streamtube, the static pressure drops upstream of the disk, has a step increase at the disk, then return to atmospheric conditions leading to an acceleration of the jet. In the downstream wake, mixing of the wake with the freestream velocity occurs. The solver uses the ideal gas model for the fluid properties. Step changes in pressure and total temperature, due to the energy source, lead to a small step increase in density, and a corresponding step decrease in velocity at the disk to ensure mass continuity.

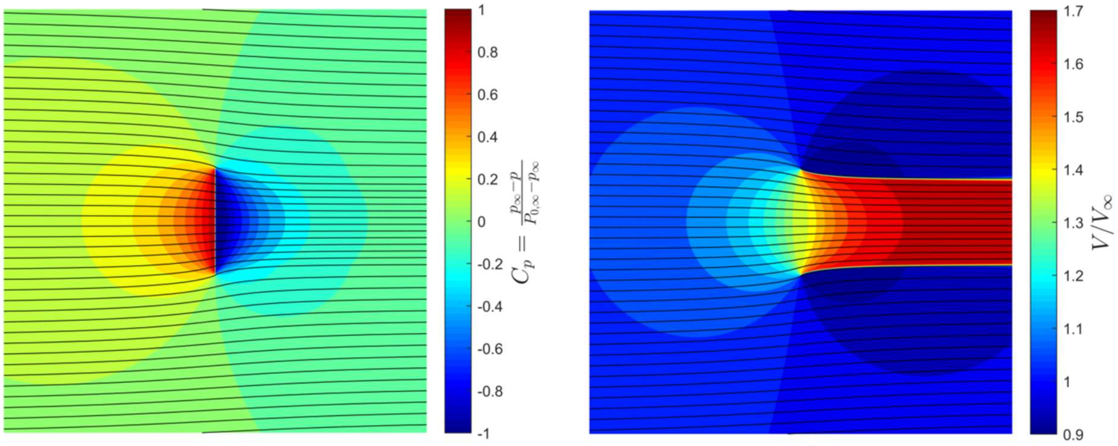

(a) (b)

Figure 3.4: Contour plots of the pressure (a) and velocity fields (b) around the 2D actuator disk generated in Fluent with a UDF. The thrust coefficient is set to T_c=2, and the angle of attack is zero.

Typical pressure and velocity distributions for a 2D blown wing with a uniform jet are shown in Fig. 3.5. The pressure rise is fixed across the jet width. Because the actuator disk experiences the local flow perturbation due to the potential field of the wing, the exit of the disk is non-uniform.

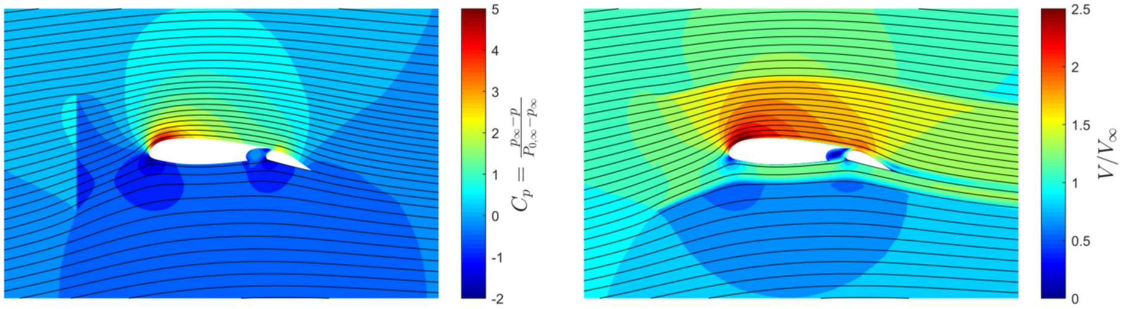

(a) (b)

Figure 3.5: Plots of the pressure (a) and velocity (b) fields around a 2D blown wing actuator disk simulation. The geometry is x_p/c=-0.5, y_p/c=0 and D_p/c=0.8 at a flap angle, ϕ=23°, a thrust coefficient, T_c=1, and an angle of attack of 3°, typical of the simulations used in this thesis.

For real propeller geometries, F_ψ and F_a are both functions of radius. To model the radial variation of axial and tangential force, the Goldstein propeller distribution was used [63]. This distribution gives an analytical expression for the distribution of axial and tangential force needed to give a minimum induced loss (MIL) design. Expressions for this distribution are given in Appendix A.

3.2.4 Model Parameters

All blown wing simulations in this thesis are carried out at the landing operating point. The model parameters used in the CFD simulations are included in Table 3.1. The wing geometry used was the NACA 43018 aerofoil section. This geometry was chosen as it comprises the root section of the ATR-42's wing [40].

Model Parameter	Value
Reynolds Number	$4.3\text{x}10^6$
Mach Number	0.18

Table 3.1: CFD Model Parameters used in this thesis.

A Fowler flap was designed for the NACA 43018 aerofoil using the process described by Howe [38]. 2D CFD simulations were run for a range of flap geometries to optimise the design for maximum wing lift. The flap geometry was parameterised using shape space [49]. Different wing and flap angles were tested in order to find an optimal geometry over a range of incidences up to stall. For each wing and flap angle, the optimum flap position relative to the main wing was found in order to maximise the lift of the wing and flap at that incidence. A 4-bar linkage to deploy the flap was designed such that the flap is located at its optimum position at each deployment angle. The 4-bar linkage was chosen based on practical flaps described by Rudolph [66, 67], so that the flap design could also be deployed in the experimental test rig of Section 3.3.

For the 2D simulations, a uniform thrust coefficient, defined by,

$$T_c = \frac{T}{\frac{1}{2}\rho V_\infty^2 \overline{D_p}} \quad , \quad (3.4)$$

was applied at the actuator disk. $\overline{D_p}$ is the two-dimensional height of the jet and T the thrust per unit span.

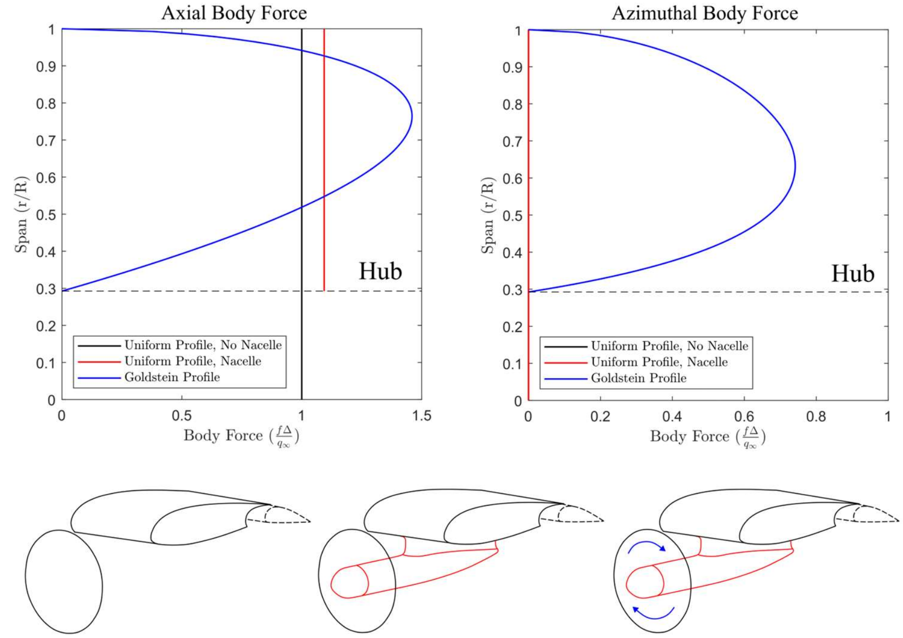

Figure 3.6: Plots of the input 3D actuator disk body forces applied in the simulations presented in Chapter 7 and 8..

For 3D simulations, a combination of uniform jets and Goldstein distribution jets (see Appendix A) were used. The axial and tangential body force profiles for a thrust coefficient, T_c=1 are shown in Fig. 3.6. The radial body force is always neglected. For each thrust coefficient, the total torque is calculated using the propeller design code described in Appendix B.

3.3 Experimental Methods

3.3.1 Introduction

In this section, the set-up of the experimental test rig developed for this work is explained. Figure 3.7 shows a photograph of the propeller-wing test used in this work. The test rig consists of a 2D NACA 43018 aerofoil mounted vertically in a 0.674m x 1.08m open jet wind tunnel. A Fowler flap is mounted to the wing, with a sliding mechanism at either end to control its angle. The wing chord is 0.212m without flap extension, the aspect ratio of the wing is 3.15. With flaps deployed, the aspect ratio of the wing drops to 2.74. Secondary flows, discussed in Section 3.3.7, reduce the aspect ratio of the clean section of the wing to 2.55. The diameter of each of the 6 propellers is 50% wing chord and the minimum spacing between adjacent propellers is 5% of propeller diameter. The wing is mounted on turntables allowing the wing angle of attack to be varied from -90° to +90°. The flap can be deployed up to 50°. The test rig Reynolds number based on wing chord is 3×10^5 [37]. A family of nacelle geometries was created, and is discussed further in Appendix C.

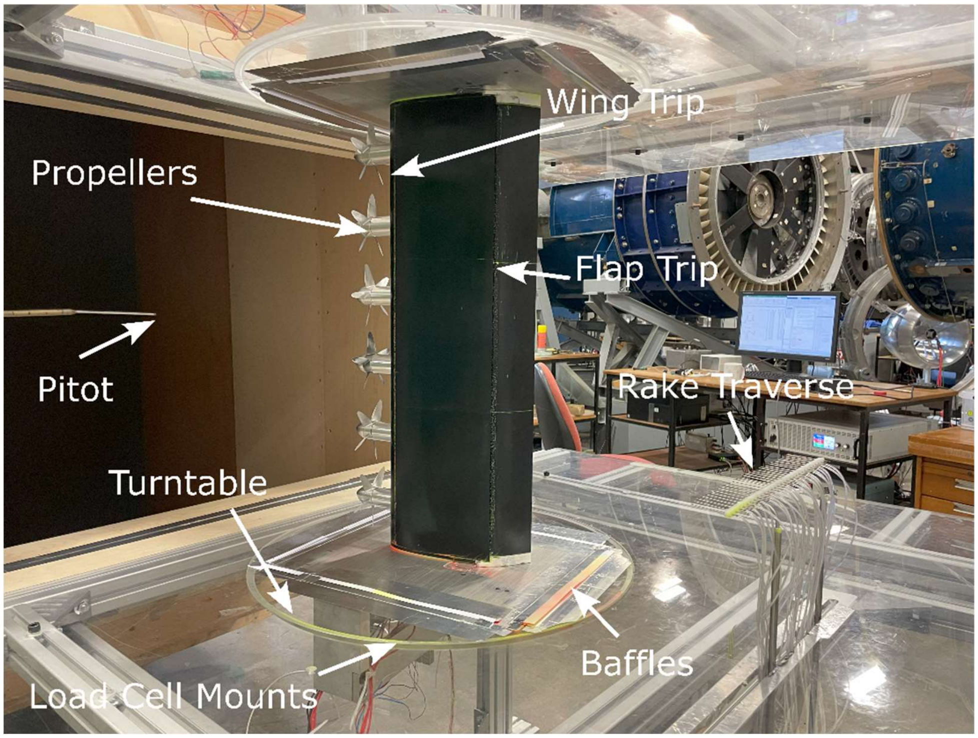

Figure 3.7: The blown wing experimental test rig [37]. A 2D wing section is mounted vertically in an open jet wind tunnel with up to 6 propellers attached.

A traverse of the tunnel showed that the inlet flow was uniform to within 1% across the span. The boundary layer thickness is 5mm at the tunnel exit, giving a blockage fraction of 0.015. The wing and flap are both tripped using glass beads with a diameter of 0.0017% chord. This diameter was chosen by increasing the trip size until separation bubbles were no longer visible in either flow visualisation or IR camera images. The wing is tripped at 10% chord. Lift and drag load cells are mounted to the top and bottom of the wing. These are attached to the wing via ball and socket joints to alleviate bending moments. Rotation is constrained via a 5th load cell mounted at the rear of the wing which allows the moment to be measured. Baffles are attached to the wing end plates to eliminate leakage in the air gap between the tunnel wall and the wing end plate.

The propellers used in this study were designed with a Minimum Induced Loss (MIL) philosophy, as described by Adkins and Liebeck [1]. Details of this method are given in Appendix B. The target thrust coefficient was 1.2 at an advance ratio of 0.7 and test rig Reynolds Number of 1.55×10^5 based on propeller diameter. The propellers were machined from aluminium with a special collet designed to clamp each propeller to the motor shaft. Motor speed is controlled via a feedback loop which measures the signal from the electric speed control (ESC) unit, passes this through a Fourier transform to identify the rotation speed and adjusted the ESC signal accordingly. Turnigy XK2845-1980kv in-runner motors were used to power each propeller. The speed controller unit was developed by a Masters student [85] and communicates with the users laptop via a Raspberry Pi. This speed controller is accurate to within 0.3%.

The 2D wing section is built from 3D printed plastic, with steel strengthening rods through the centre. The surface was lightly sanded and built up with spray paint to eliminate the printer steps. The nacelles were also 3D printed, and a new geometry set could be printed within 12 hours. The nacelles are attached to the wing with screws into brass inserts, the screw heads being covered by putty.

The main advantages of the test rig are:

- The 3D-printed components make the test rig versatile, allowing geometries to be changed quickly to try new ideas.
- The angle of attack of the wing, and flap angle can easily be changed.
- A load cell gives quick readings for the total lift and drag of the wing, avoiding timely surface and wake pressure measurements.

3.3.2 Sizing of the Test Rig

Key to a good experiment design is the sizing of the test rig itself. Figure 3.8 shows the geometry parameters sized before the test rig design work was commenced.

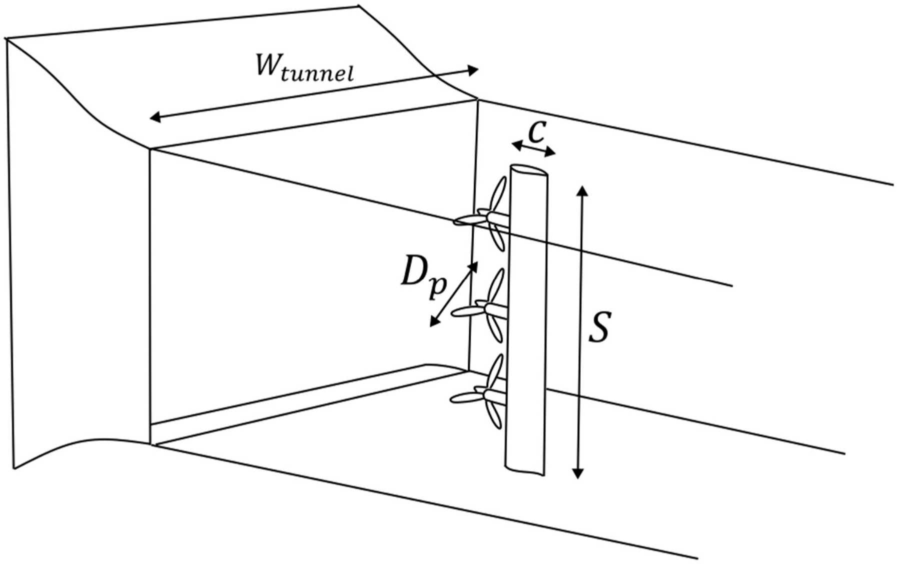

Figure 3.8: Parameters to be fixed in the test rig initial design work.

A contraction was built to fit onto the Rhoden tunnel in the Whittle laboratory, allowing several choices of jet width, W_{tunnel}. An earlier version of the test rig, developed by masters students [84, 85] was found to be a convenient size for working, and fitted into the space around the Rhoden tunnel. It was decided to use the original frame, and end plates from the earlier experiment, fixing the span, S, at 0.674m. The velocity of the tunnel is set by the choice of jet width, and the Reynolds number of the test rig by a combination of the tunnel velocity and the wing chord, c. For a given chord, the propeller diameter, D_p, is then fixed by the test geometry. Based on initial studies of the optimum geometries found in Chapter 4 and 5, it was decided to use a propeller with a diameter to chord ratio, D_p/c=0.5.

Figure 3.9 shows a plot of the total pressure rise against volumetric flow rate measured for the Rhoden Tunnel in the Whittle laboratory. The Rhoden is an open circuit wind tunnel. This tunnel has a 350bhp motor and is the most powerful wind tunnel available in the laboratory. Assuming static conditions at tunnel exit, and knowing the fan tip speed of the tunnel for different motor settings, it is possible to use this tunnel characteristic to extract the jet velocity for a given throttle setting and test section area.

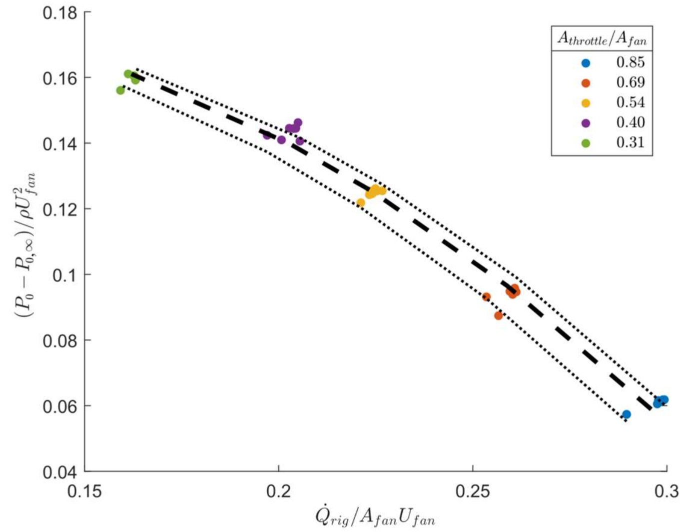

Figure 3.9: Fan characteristic of the Rhoden wind tunnel used to size the experiment.

Whilst tempting to reduce the size of the jet width to increase the tunnel velocity, and hence the Reynolds number, the accuracy of the test decreases as the jet width to chord ratio decreases (see Section 3.3.10). As the jet width to wing chord ratio decreases, the gradient of the lift slope decreases [31]. A correction exists which allows the original lift curve gradient to be recovered.

Defining, σ as,

$$\sigma = \frac{1}{3}\left(\frac{\pi c}{4W_{tunnel}}\right)^2 , \quad (3.5)$$

and,

$$\varsigma = (1 + 2\sigma)^2 + \sqrt{12\sigma} , \quad (3.6)$$

then the original lift curve can be recovered by applying the correction,

$$\alpha_{mod} = \frac{\alpha}{\varsigma} . \quad (3.7)$$

This correction factor, ς, accounts for the reduction of the wing angle of attack due to the curvature of the jet. The correction factor is extended later in this chapter for wings immersed in jets. Because the jet curvature varies locally around the wing, the angle of attack of the wing and propeller will be different. Finite jets therefore reduce the accuracy of the experiment, and it is preferable to reduce the finite jet effects of the wind tunnel by minimising ς.

To estimate the power requirements of the motors, the minimum induced loss propeller design code described in Appendix B was employed. A design speed limit of 8,000rpm was placed on the motors to stay well away from possible blade failure. A stress calculation found that yield stresses first occur around 20,000rpm. A nacelle diameter to wing chord ratio of $D_{nacelle}/c$=0.14 was used to match expected real engine geometry based on motor sizing results presented in Chapter 5. The upper limit on the motor diameter was therefore set to be 2mm less than $D_{nacelle}/c$ to give sufficient material to provide a wrapper to contain the motor housing. Figure 3.10 shows commercially available motor diameters and maximum rated powers. To avoid overheating, experienced with the earlier version of the test rig, the continuous power requirements of the motor should be less than 50% of the maximum rated power. The Turnigy XK2845-1980kV brushless in-runner motor was ultimately chosen for its high power and low diameter.

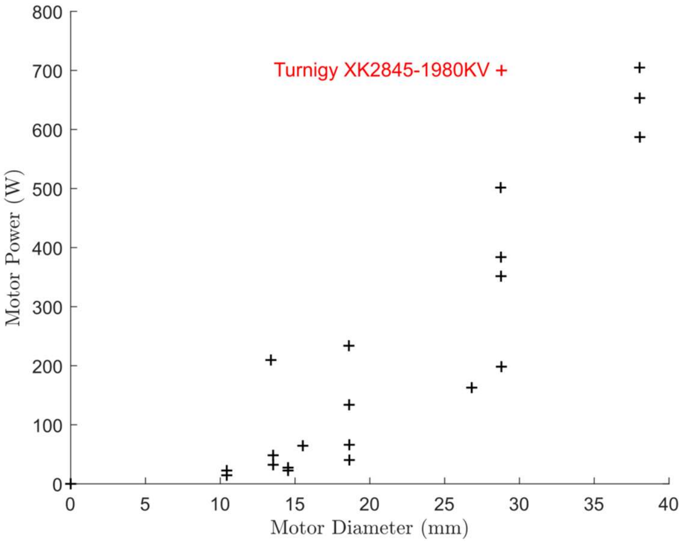

Figure 3.10: Motor power for commercially available motors with different diameters.

Figure 3.11 shows contours of finite jet correction, ς, for different combinations of jet width and wing chord. Values have been normalised by those used in the earlier version of the test rig ($W_{current}$=0.7m, $c_{current}$=0.125m). As the propeller speed was limited to 8,000rpm, the propeller code crashes below a certain propeller diameter due to the blade sections stalling. This places a limit, shown in red, on the test rig geometries that can be used due to propeller operation. Increasing the propeller speed would extend this region to smaller wing chords and jet widths with correspondingly higher jet velocities, but at the cost of safety.

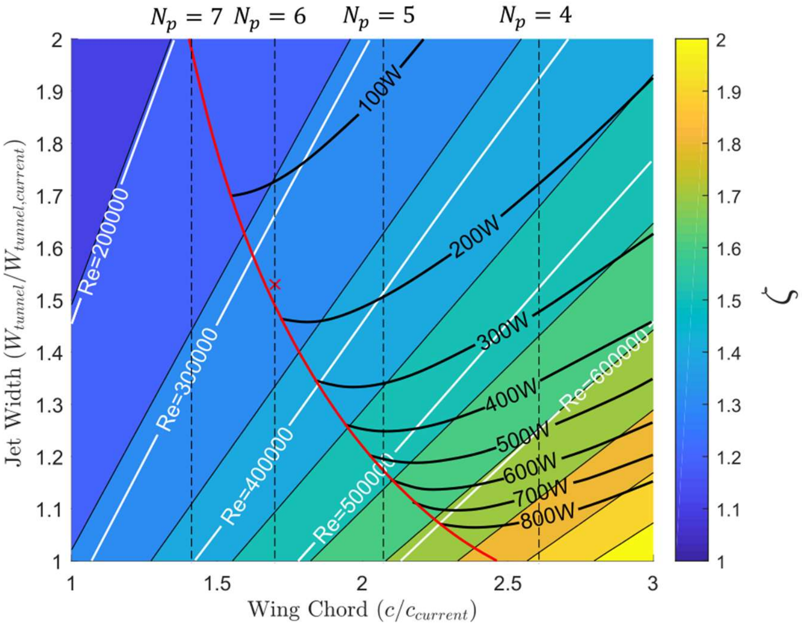

Figure 3.11: Tunnel sizing constraints with the final test rig design marked. Values have been normalised by the test rig designed in [84]. The correction factor for finite tunnel jets is plotted as a contour plot for different tunnel widths and wing chords. Overlaid is the predicted wing Reynolds number, and power requirements of the motors.

As an integer number of propellers must fit along the wing span, the choice of geometry is further limited. These integer propeller numbers, N_p, are also marked on the figure. To maximise the aspect ratio of the wing, 6 propellers were chosen to cover the wing span. Each propeller has a 5% of diameter gap to its neighbouring propeller. The maximum width of the jet, dictated by the size of the Rhoden tunnel is 1.07m. The chosen design point is marked on the figure with a red cross. A wing chord of 212mm and a jet width of 1.07m was used. This gave a value for ς of 1.34 and a Reynolds number of 320,000. The maximum power requirement of the motor is 168W and the nacelle diameter is 0.031m which can easily accommodate the Turnigy 2845-1980 brushless in runner motor. With this choice of wing chord, the wing aspect ratio is 3.15 using 6 motors, the maximum that can be achieved within the design space shown.

3.3.3 Propeller Design

Having sized the test rig, the propeller design can then be finalised. A design thrust coefficient of 1.2, and diameter to chord D_p/c=0.5 was chosen, based on optimal designs found in an earlier version of the study presented in Chapters 4 and 5. The propeller is a high lift propeller, and assumed to fold away in cruise. Therefore the propeller is primarily designed to give high thrust coefficients at low speed, rather than achieve efficient thrust generation. A tip diameter of 0.106m and a hub diameter of 0.031m was used to match the motor diameter. The propeller was designed using the blade element momentum theory code described in Appendix B. The propeller operating point was set to the design tunnel speed of 23ms^{-1} and the maximum rpm of 8,000. Figure 3.12 shows the distribution of blade chord and twist along the span.

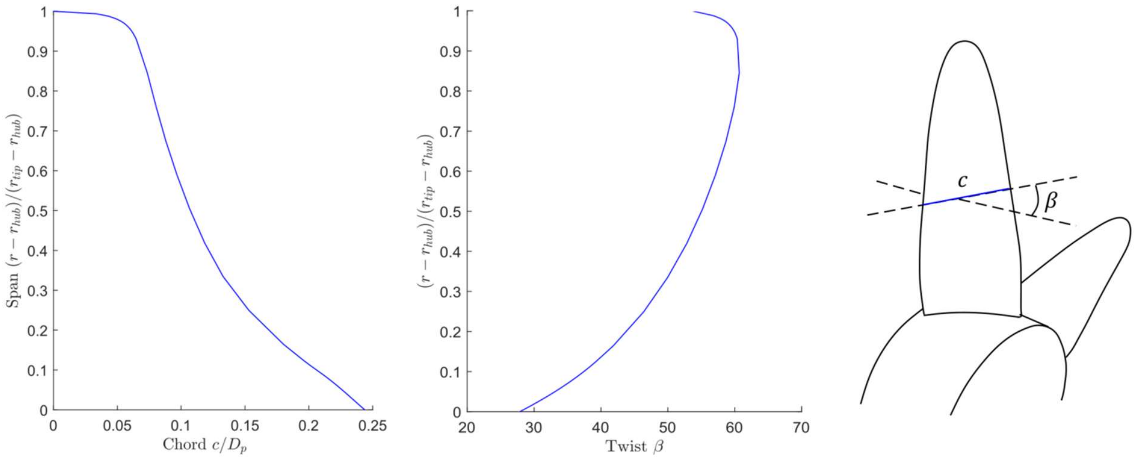

Figure 3.12: Propeller geometry used in the test rig.

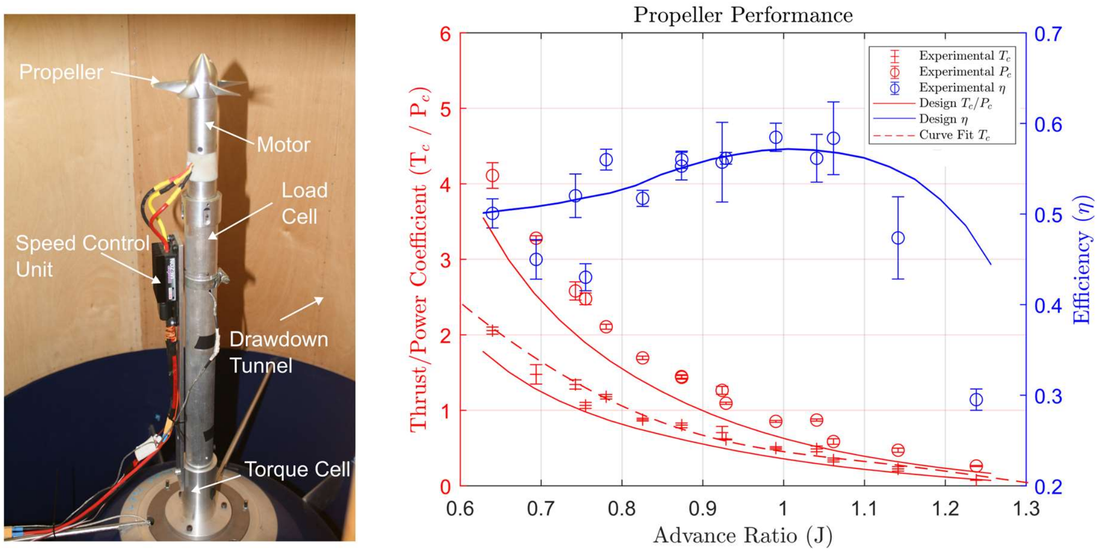

Figure 3.13: Characteristic measured for the propeller used in the test rig [37]. The measured performance of the propeller is plotted, along with the design performance from the blade element model. Although the model under predicts the thrust of the propeller at a given advance ratio, the propeller can reach the design thrust coefficient of 1.2. A curve fit, also plotted, is used to determine the experimental thrust coefficient from the known advance ratio for propeller-wing integrated tests.

The NACA 4415 aerofoil was used as the blade section geometry. Figure 3.13 shows the measured propeller performance characteristic, without a wing, using a draw-down wind tunnel in the Whittle laboratory and dedicated propeller test stand. The theoretical design characteristic using blade element momentum theory is also shown on the plot. Discrepancies between the model and measured values may be due to a combination of uncertainty in the measured thrust and power coefficients, included as error bars in the figure, and the blade element model struggling to capture the low Reynolds number of the root sections. Whilst the propeller generates more thrust than predicted for a given advance ratio, it is capable of producing the design thrust coefficients of 1.2. To estimate the thrust coefficient from the measured rpm of the propeller when mounted in front of the wing, a 7th order polynomial curve fit, plotted on Fig. 3.13, was used.

The nose cone geometry was created using shape space [49] with a third-order Bezier curve fitted to the shape space function extracted from the NASA nosecone [50] used on the X-57 folding propellers. Details of this geometry are given in Appendix C. A collet was used to secure the propeller to the motor shaft. By tightening the nose cone to the propeller, the tapered section of the collet is pulled down onto the motor shaft. It was found that grub screws placed on the collet shaft were also required to avoid slip between collet and motor, and dowels were positioned between the collet and propeller to avoid slip at that interface. The nosecone, propeller and collet were made from aluminium.

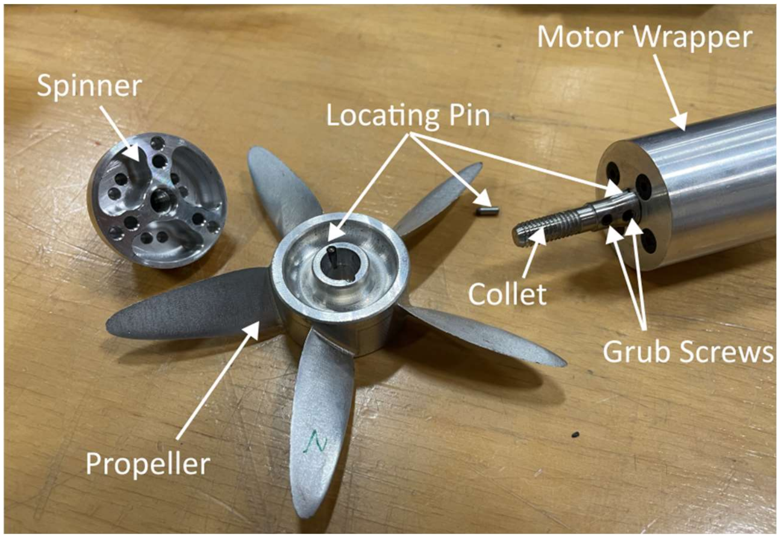

Figure 3.14: Collet, nosecone and propeller assemblies dismantled.

3.3.4 Flap Deployment Mechanism

The CFD design of the flap is described in Section 3.2.4. To generate the deployment path specified in the design, the flap needed to be secured at either end of the wing by means of the 4-bar linkage designed for the flap. Figure 3.15 shows the chosen flap deployment system with flap tracks to model a 4-bar linkage path and locking nuts to fix the flap position for testing.

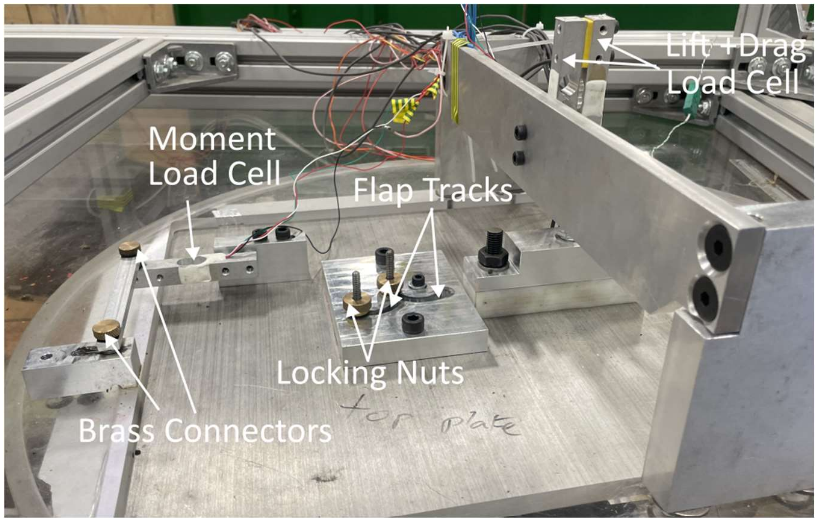

Figure 3.15: Flap deployment and load cell systems for the test rig.

3.3.5 Load Cell System

The load cell mounting points are shown in Fig. 3.15. To calculate the wing loads, the load cells were calibrated with a known weight. Interference between the lift and drag load cells were measured to give a calibration matrix for each of the top and bottom load cells, given by,

$$\begin{bmatrix} L \\ D \end{bmatrix} = \begin{bmatrix} g_1 & g_2 \\ g_3 & g_4 \end{bmatrix} \begin{bmatrix} V_L \\ V_D \end{bmatrix} \quad , \quad (3.8)$$

where V_L and V_D are the measured voltages on the lift and drag load cell. Two matrices are calculated, one for each end of the wing, and a further gradient, g_5 is measured for the moment load cell. Error RMS values of 0.99 were achieved between the measured loads and the straight line fit through the measurements.

3.3.6 Boundary Layer Trips

Figure 3.16 (a) shows a plot of the pressure distribution around the NACA 43018 aerofoil at zero incidence for two Reynolds numbers, 210000 and 6000000 representative of typical tunnel and aircraft landing conditions respectively. Whilst sharp kinks in the C_p distribution, characteristic of laminar separation bubbles, exist at the test rig Reynolds number, these kinks are considerably less well pronounced at higher Reynolds number, and occur further upstream. To remove this low Reynolds number effect, a trip was required for the wing. In this section, the size and position of trip is explained.

XFOIL was used to establish the boundary layer properties for the wing at low Reynolds number. Figure 3.16 (b) shows a plot of the location of the separation bubble at different wing incidences.

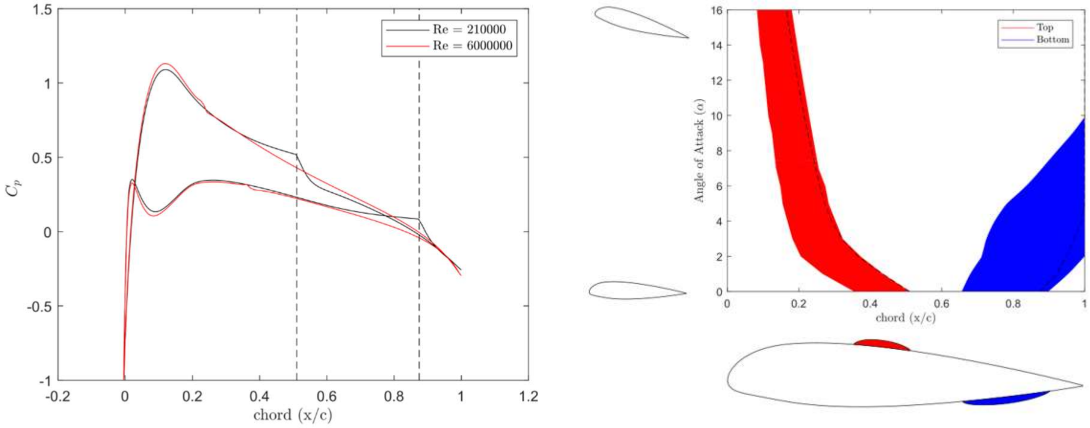

(a) (b)

Figure 3.16: Wing boundary layer study in XFOIL. The pressure distribution is plotted in (a) at two Reynolds numbers representative of the test rig and aircraft conditions at an angle of attack of 0°. The extent of the suction and pressure surface separation bubbles is plotted in (b) for different wing angles at a Reynolds number of 210000.

As the wing incidence increases, the point of peak suction on the suction surface moves upstream, closer to the leading edge and the point of laminar separation moves with it. The wing stalls at around 16° and so to ensure transition always occurs at all operating points, the grit was chosen to start at x/c=0.1 with a thickness of 2% of chord. The pressure surface bubble is much larger in size, but as it’s furthest upstream extent is at $x/c = 0.65$, and the cut off point on the real wing for the flap is at 67% chord, it was felt that a pressure surface trip was unnecessary. In practice, a trip on the pressure surface would be tricky to employ as the nacelles that attach to the wing would need to avoid damaging the trip each time they were installed.

Figure 3.17 shows flow visualisation of the suction surface bubble at four flap angles at zero incidence. The maximum upstream position of the suction surface bubble is 12% chord at the highest incidence, which further justifies the decision to place the trip at 10% chord.

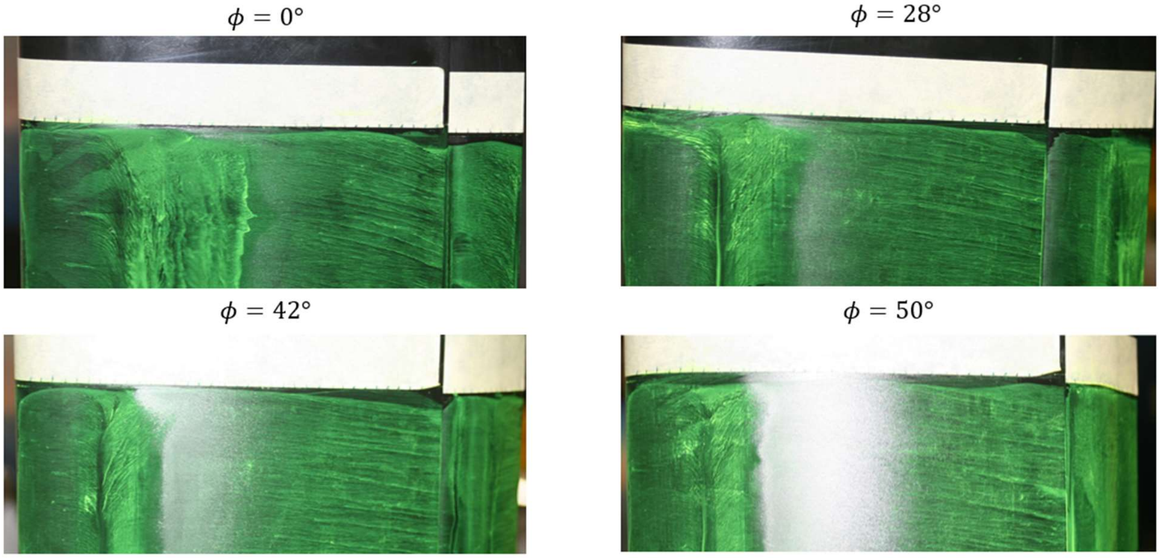
$\phi = 0°$

$\phi = 28°$

$\phi = 42°$

$\phi = 50°$

Figure 3.17: Flow visualisation of the suction surface bubble at four flap angles. The wing angle of attack is 0°.

The Rig 150 methodology [19], developed at the Whittle Laboratory, was employed to choose the trip. Three trip types were available; a chevron tape, a straight tape, or grit. Chevron tape produces streamwise vorticity which delays boundary layer separation, affecting the measured stall characteristics. The separation bubble may not close at high incidence with straight tape giving a leading edge separation. The grit method avoids these two issues, but does introduce parasitic grit drag which is undesirable. It is therefore required to minimise the size of the grit to still achieve transition, without excessive drag. Work [13] in accelerating flows has provided correlations on which to base the sizing of grit to achieve transition. In decelerating flows, the disruption to the boundary layer required by the grit is less severe, and so a smaller grit size can be used, of the order of the momentum thickness. A range of grit diameters were tested on the wing, as shown in Fig. 3.18. Both flow visualisation paint, and IR camera images were used to confirm that the separation bubble was removed with a grit diameter greater than 250-300μm. It was found that the paint could artificially trip the flow, or modify the bubble location, hence the use of IR cameras to validate the effectiveness of the trip. A trip height of 300-350μm beads was chosen for the final trip.

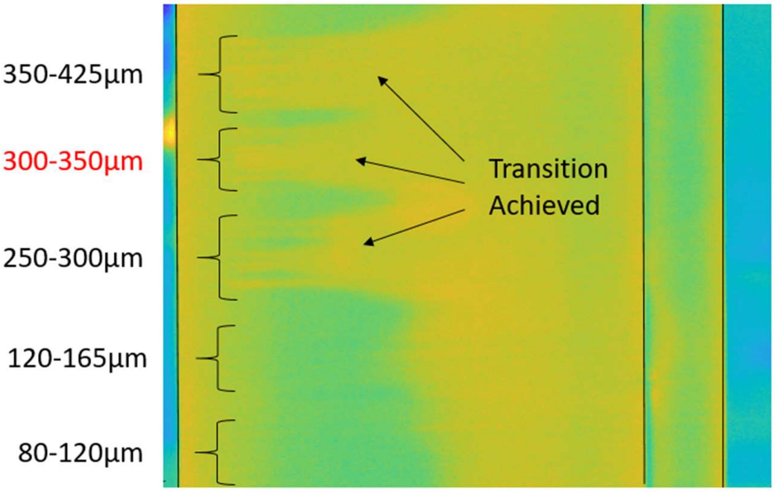

Figure 3.18: IR camera results showing effectiveness of boundary layer trip for different grit sizes. The 300-350μm grit diameter was selected for the rig to ensure the boundary layer transition is achieved.

A trip was also applied around the leading edge of the flap. The flap trip had a width of 10mm, 15% of the flap chord, in order to catch the boundary layer before the bubble at all flap deployment settings. The trip also had grit with a diameter of 300-350μm.

3.3.7 Corner Flow Treatment

In the blown wing test facility reported by [3] at MIT, it can be observed that corner separations are occurring for the flapped wing both with, and without propeller blowing and the size of the separation increases with the propellers in position. It was found, when commissioning the test rig, that similar corner separations exist at high flap angles near to the start of flap trailing edge separation, as shown in Fig. 3.19. The corner separations lead to an increase in wing drag of 0.01. Attempts to suppress the corner flows through smoothing of the flap attachment lugs, and introducing a small gap at the end-wall to reduce the flap loading were both unsuccessful. More intrusive methods, such as blowing the flap boundary layer in the corner to reattach the boundary layer, will modify the lift coefficient by an unknown amount, and were therefore discarded. The flap was therefore left as designed.

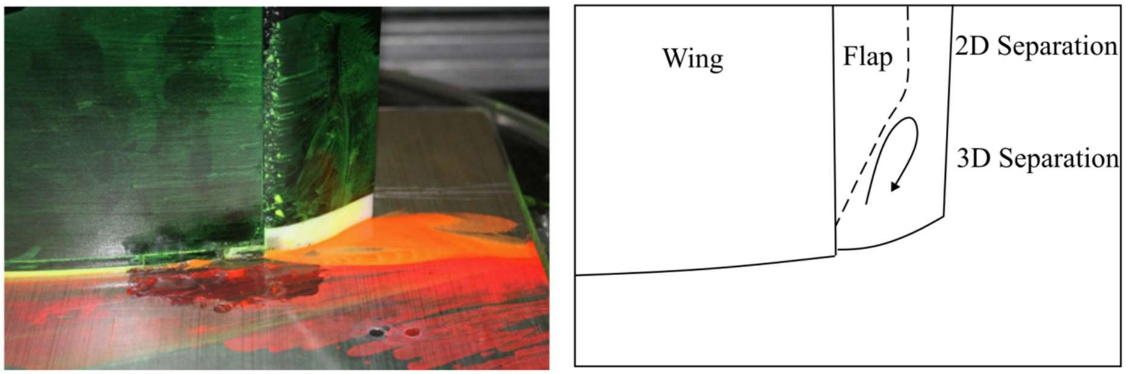

Figure 3.19: Flow visualisation of the wing-end plate joint showing a corner separation at high flap angles. Junction flows, due to the roll up of the vorticity in the end-plate boundary layer around the wing were also observed.

3.3.8 Rake Traverse

The corner separation accounts for up to 7% of the flap area. A non-intrusive method to quantify the drag effects of the corner separation is to measure the mid-span region of the wing, away from the separated wakes, using a traverse. A rake traverse allows the total-pressure to be measured quickly, enabling a full operating sweep to be calibrated for corner separation drag. The rake traverse, shown in Fig. 3.7, was placed 1.5 chords downstream of the wing, to allow the static pressure to return to ambient conditions. This separate measurement was conducted over 3 of the middle 4 propellers and used to calculate a correction factor for the load cell drag data. Two DSA's, each with a sampling time of 2.5 seconds was used to measure the pressures. The drag coefficient can be approximated as:

$$C_D \approx \frac{1}{c}\int\left(\frac{P_0 - p}{P_{0,\infty} - p_\infty}\cos^2\beta_{jet} - 1\right)dy \ , \qquad (3.9)$$

where the jet deflection angle, β_{jet}, is estimated in Section 3.3.10. Equation 3.9 assumes that the static pressure at the traverse plane is uniform, and the local perturbations in flow angle in the wing and jet wakes are small. Two rakes could be interchangeably fitted, each with 30 probes, at spacing's of either 5.3mm or 10.6mm, which were used for measuring the nacelle drag, and propeller thrusts respectively These spacings were found to be sufficient to reconstruct the flow field and estimate drag to within 1% of a finer traverse taken with a 5-hole probe, provided a spline was fitted to the measured date. The coarser rake was required to capture the full wake of the propeller and wing in a single traverse.

3.3.9 Error Analysis

In Chapter 5, error bars are included for all experimentally measured lift and drag values from both the load cells and rake traverse. For the rake traverse, the dominant source of error originates in the location of the jet edge. It was found that the best way to identify the jet was to choose the jet edge location manually, as shown in Fig. 3.20. To estimate the error in the measurement, this value was perturbed by 5% of the jet width on either side of the jet. The possible drag coefficients for each perturbation at every measurement station are also plotted in Fig. 3.20. The total drag is calculated from the integral of the section drag over the span. The error in total drag is taken as half the difference in total drag, ΔC_D measured with the minimum and maximum section drag values.

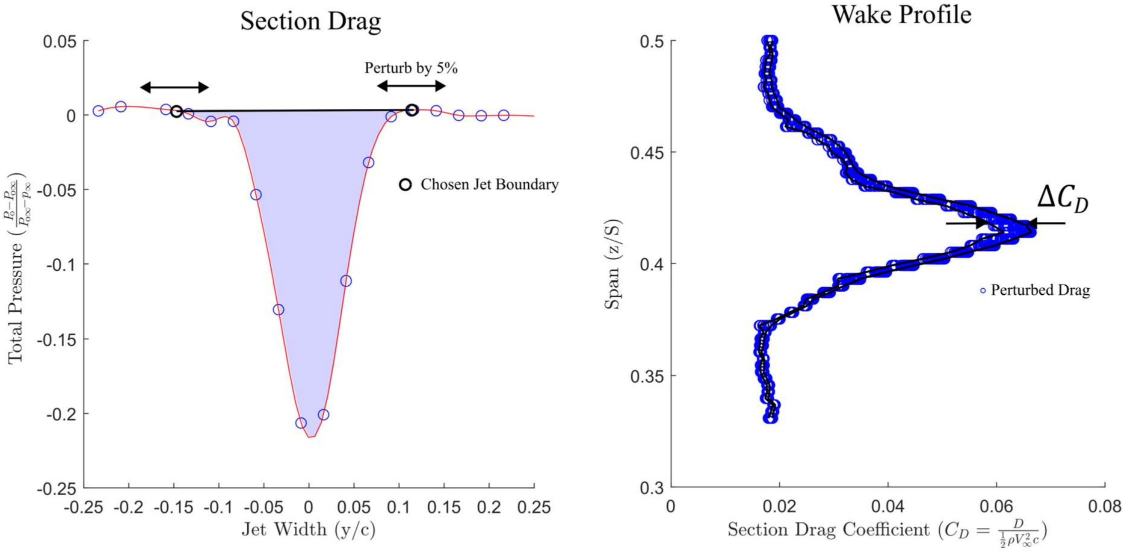

Figure 3.20: An example of extracting drag measurements, and corresponding errors from the traverse of a wake downstream of the aerofoil without propellers fitted. The wing angle of attack is 0° and it is assumed the jet deflection angle, β_{jet} = 0° and the static pressure has returned to ambient.

A standard error analysis is applied to the load cell lift and drag values. The error in the measured lift coefficient can be calculated as,

$$error = \sqrt{\sum \left(\frac{\partial C_L}{\partial var}\right)^2 {\sigma_{var}}^2} \quad , \quad (3.10)$$

where var refers to each variable contributing a source of error to the measured lift coefficient, C_L. The lift coefficient is calculated as,

$$C_L = \frac{L}{q_\infty A_{wing}} \quad , \quad (3.11)$$

where q_∞ is the dynamic pressure measured from the pitot tube, the area, A_{wing}, of the wing is fixed, and the lift, L, is measured from the load cell. The loads are calculated from the matrix in Eq. 3.8 and can be expressed as,

$$L = \sum g_n V_n \quad , \quad (3.12)$$

where n refers to each of the load cells required for the relevant vector (lift or drag). Combining Eq. 3.10 with Eq. 3.11 and Eq. 3.12, the error in lift can be calculated as,

$$error = \sqrt{\frac{1}{q_\infty A_{wing}}\left(\sum {g_n}^2 {\sigma_{V,n}}^2 + \sum {V_n}^2 {\sigma_{g,n}}^2\right) + \left(\frac{C_L}{q_\infty}\right)^2 {\sigma_{q_\infty}}^2} \quad . \quad (3.13)$$

The error in the load cell gradient, $\sigma_{g,n}$, is estimated using the MATLAB polyfit functionality to calculated a 95% confidence interval for the gradient. Errors in the voltage reading, $\sigma_{V,n}$ were taken as twice the standard deviation of the mean. 40 readings per test point were found to provide a good trade-off between speed and uncertainty. The same approach was used for the DSA pressure readings which has additional internal averaging of 10 measurement points over a period of 150ms for every reading of the load cell.

The analysis has been applied to the lift coefficient in this section. The same approach was applied to the drag readings. The analysis presented has avoided the complexity of moving the lift and drag measurements from the load cell reference frame to the tunnel reference frame. For reported errors in Chapter 5, this transformation was performed.

3.3.10 Jet Deflection Correction

The effect of a finite tunnel jet is to reduce the angle of attack of the wing within the test section [9, 31]. The lift from the wing deflects the jet by an angle β_{jet}, as shown in Fig. 3.21, leading to a reduction of the angle of attack by $\beta_{jet}/2$ [37]. The correction derived from momentum theory is:

$$\beta_{jet} = \frac{1}{2} C_L \frac{c}{W_{tunnel}} + \frac{\pi}{6} C_L \left(\frac{c}{W_{tunnel}}\right)^2 . \quad (3.14)$$

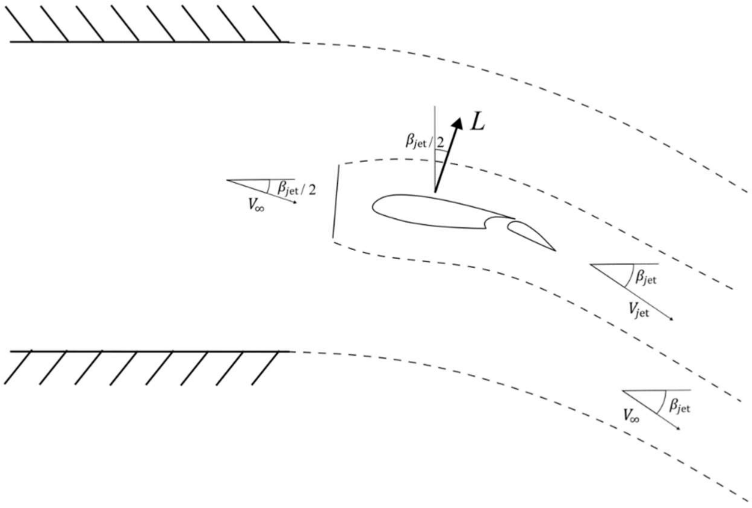

Figure 3.21: Diagram of tunnel jet deflection due to the presence of a blown wing [37].

The first term accounts for the jet deflection angle whilst the second term accounts for expansion of the jet. This correction is applied in Fig. 3.22 to the lift and drag curves for the plain NACA 43018 section in the experiment and shows good agreement pre-stall with both XFOIL solutions, with a trip applied at 10% chord, and ANSYS Fluent running fully turbulent at the test rig Reynolds number. This change in reference of the wing leads to an induced drag term,

$$C_{D,induced} = C_L \frac{\beta_{jet}}{2} , \qquad (3.15)$$

measured by the load cell, in addition to the viscous drag generated. This additional drag term is not measured by the wake traverse which only measures the viscous terms due to losses of stagnation pressure [37].

Whilst Eq. 3.14 works well for plain 2D wing sections, the correction does not account for the additional momentum produced by the propeller jets in the test rig. Applying actuator disk momentum theory, Eq. 3.14 can been modified below to account for this extra momentum.

$$\beta_{jet} = \frac{1}{2} C_L \frac{c}{W_{tunnel}} \left(\frac{1}{1 + \frac{1}{2} \frac{A_p}{W_{tunnel} S} \left(T_c + \sqrt{1 + T_c} - 1 \right)} \right) + \frac{\pi}{6} C_L \left(\frac{c}{W_{tunnel}} \right)^2 . \quad (3.16)$$

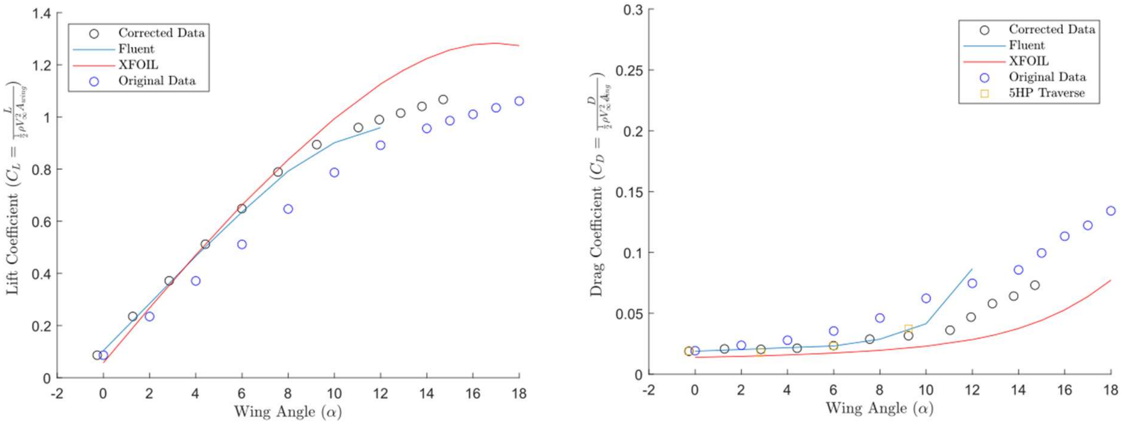

(a) (b)

Figure 3.22: Tunnel measurements of the lift and drag coefficients for a NACA 43018 aerofoil, corrected for wind tunnel deflection [37]. Experimental results are compared to XFoil [88] and ANSYS Fluent [7] simulations of the wing.

Equation 3.16 assumes that the propeller jet leaves at the same angle as the tunnel jet. Small angle approximations have been used for cases where the propeller is placed at incidence. The discrepancy due to propeller incidence is found in the analysis to be small up to 20° propeller angle. Equation 3.16 was validated by running 2D CFD simulations for a finite tunnel jet.

Figure 3.23 shows the exit velocity and flow angle for a typical simulation. Due to artificial viscosity in the simulation, non-zero flow speed of the order 3% of the tunnel speed is registered outside the jet. Within the tunnel jet, the exit angle is uniform to within 5%, validating the assumption of uniform exit angle used in deriving Eq. 3.16. The deflection angle for different angles of attack (and hence lift coefficients) is also plotted in Fig. 3.23. The agreement is improved from a 10% error to a 2% error using the new, modified correction factor [37].

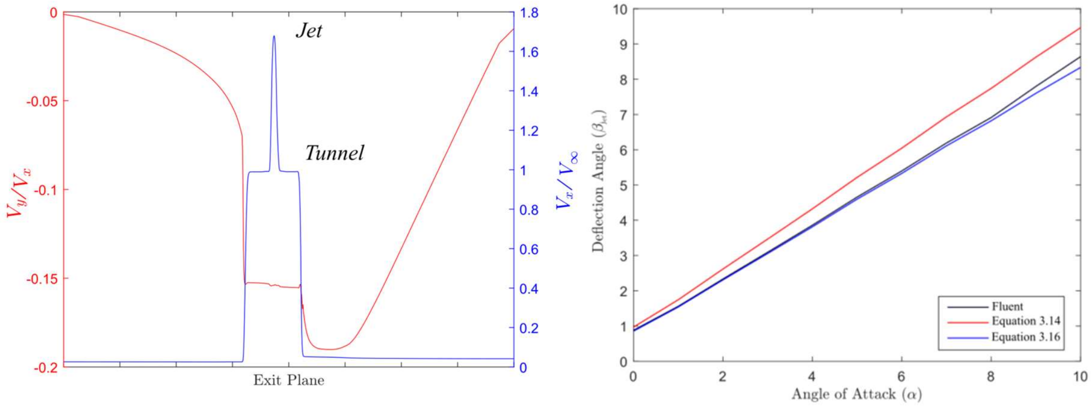

(a) (b)

Figure 3.23: CFD model of wind tunnel exit profile (a) and both analytical and CFD predictions of the tunnel exit angle (b) [37]. The tunnel jet deflection angle is uniform in the jet, and the modified correction presented in Eq. 3.16 reduces the error in predicted jet deflection angles from 10% to 2%.

Figure 3.24 shows the results of correcting a blown wing with a thrust coefficient of 2 and a 2D diameter of 50% chord over a range of angles of attack. From the figure we can see that the finite jet drag increases, due to the rotation of the lift vector. The corrected drag force is accurate to within 1%, and the corrected lift is accurate to within 5%, an improvement on the 10% error produced by using Eq. 3.14 [37].

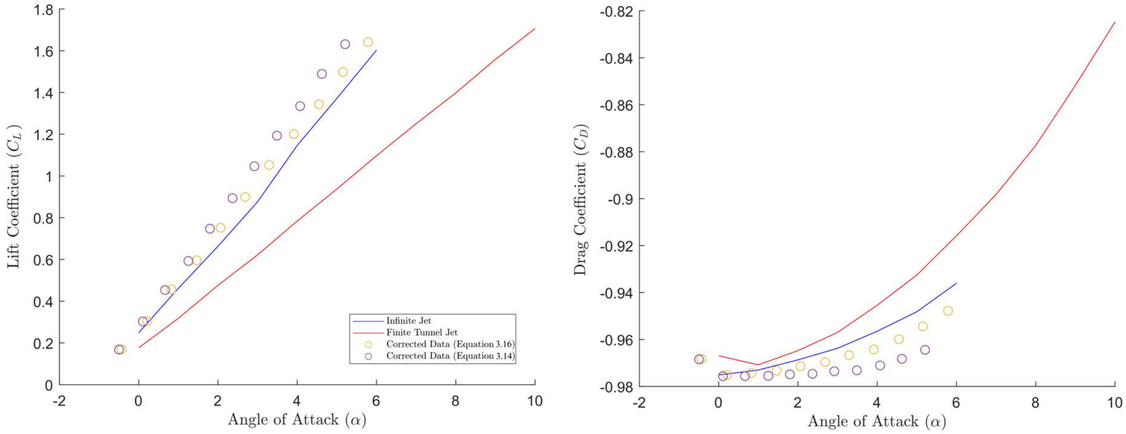

(a) (b)

Figure 3.24: CFD model of the corrected wind tunnel lift (a) and drag (b) coefficients with blowing compared to a CFD model of blown performance in a wide jet [37].

3.3.11 Reynolds Number Corrections

The lift and drag of the wing and flap vary with Reynolds number. The rate of growth of the boundary layer increases as the Reynolds number drops, as shown for the NACA 43018 aerofoil at 10° incidence in Fig. 3.25. Plotted in Fig. 3.25 (a) is the boundary layer displacement thickness for the suction surface of the aerofoil at two Reynolds numbers, Re=2.6x10^5, representative of the test rig, and Re=4.15x10^6, representative of the aircraft during final approach to landing. The boundary layer thickness doubles between the two cases. The result of this additional growth is shown in Fig. 3.25 (b). The loading on the wing drops, due to the reduction in the curvature of the flow. The effect on the lift curve is shown in Fig. 3.25 (c). The lift coefficient drops at a given incidence due to the reduced curvature of the flow. Despite this, the stall angle does not increase, and so the maximum lift coefficient of the wing also drops.

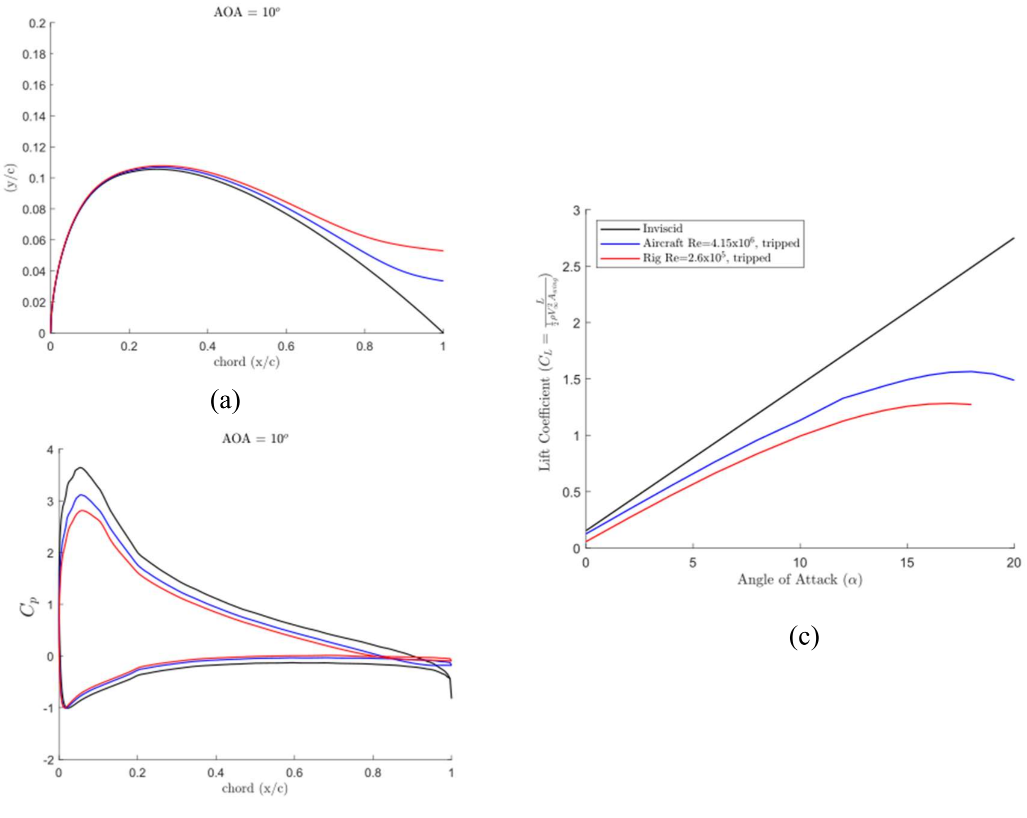

(a)

(b)

(c)

Figure 3.25: Reynolds number effects on the wing boundary layer growth and lift coefficient. Plotted is the boundary layer displacement thickness in (a), pressure distribution (b) and lift coefficient for different angles of attack (c) for three Reynolds numbers: Re = 2.6x10^5, Re = 4.15x10^6 with a trip applied, and an inviscid simulation from XFoil [88].

The results of Fig. 3.22 showed that good agreement can be achieved between the Fluent CFD, the experiment, and XFOIL at low Reynolds numbers. The flow-field around a wing is extensively validated for aerofoil sections, the trip on the wing is small compared to the wing chord, and the Spalart-Allmaras turbulence model is able to correctly predict the growth of the turbulent boundary layer. Because the trip is small compared to the wing, the additional jump in boundary layer height that it causes (not modelled by XFOIL or Fluent) is negligible and does not affect the solution.

As discussed in Section 3.3.6, the trip on the flap occupies 14.7% of the flap chord, with a height of 0.5% of the flap chord. The height of this trip is 3 times larger than the wing trip when taken as a fraction of the chord. The trip width is 7.5 times larger as a fraction of the chord. As modelling the Fowler flap involves capturing the complex recirculating flow in the cove, the viscous-inviscid coupled approach of XFOIL is not applicable, and a RANS solver is required. Figure 3.26 (a) shows plots of the lift curve slope from the experiment, and Fluent. Plotted are solutions from Fluent for a y+ of 30, the methodology used throughout this thesis, and a y+ of 1. The smaller y+ value is required as, at the low Reynolds numbers of the test rig, the number of cells in the gap between the wing and flap is too low to resolve the flow if a y+ of 30 is used. This leads to the differences in the lift curve slope. The Fluent solver is unable to predict the lift curve slope of the experiment, as the additional boundary layer growth due to the trip is now a significant fraction of the total boundary layer thickness [37]. When using the experimental data to provide insight into models for blown wing lift increase, it is the ratio of blown to unblown lift that needs to be captured, and the ratio of blown to unblown maximum lift coefficient. Despite the thick boundary layer at low Reynolds number, the experiment should be able to capture these ratios.

A methodology is therefore proposed to map the experimental unblown lift onto the CFD solution for the unblown wing at the aircraft Reynolds number. The uncorrected data, and the mapped “corrected” data are shown in Fig. 3.26 (b). The correction can be broken down into two components, a reduction in the experimental flap angle (from real to equivalent) of 33%, and an increase in the lift coefficient of 10.7% at each incidence. These two scaling factors map the experimental lift at test rig Reynolds number to the CFD at aircraft Reynolds number [37]. Because the aerofoil is tripped, the boundary layer will be turbulent, and any modifications to the boundary layer due to blowing in the test rig will be capturing real physics that should be present at aircraft Reynolds number.

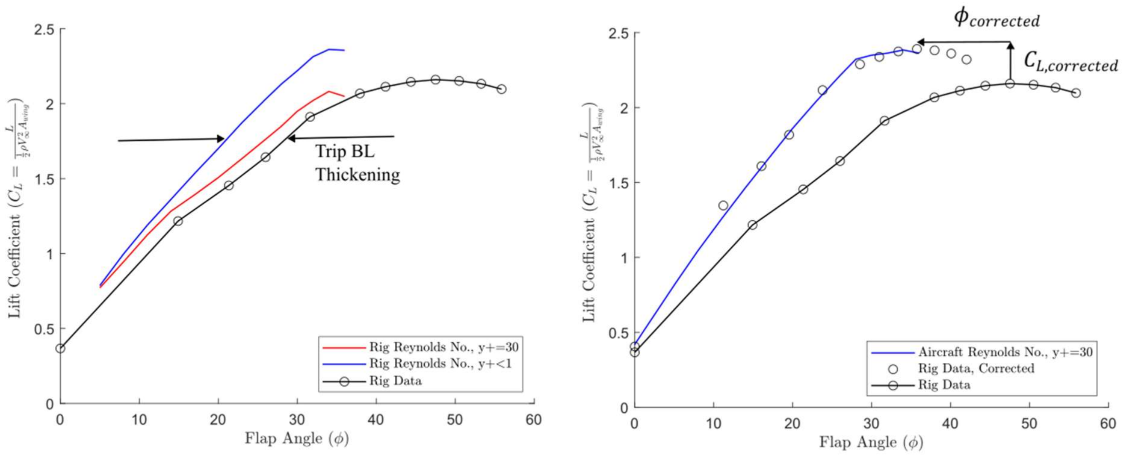

(a) (b)

Figure 3.26: Correcting measured lift slopes in the test rig for Reynolds number effects using 2D CFD calculations of the wing with a flap at the aircraft Reynolds number [37].

These two corrections can be expressed as,

$$\phi_{corrected} = 0.752\phi_{rig} \quad . \quad (3.17)$$

$$C_{L,corrected} = 1.067C_{L,rig} \quad . \quad (3.18)$$

For the experimental lift and drag coefficients reported in Chapters 6 and 7 in this thesis, $C_{L,corrected}$ and $\phi_{corrected}$ will always be quoted for cases with deployed flaps.

Whilst the lift coefficient decreases with Reynolds number, the drag coefficient increases due to the additional thickness of the boundary layer [37]. Plotted in Fig. 3.27 is the CFD drag coefficient at aircraft Reynolds number, and the experimentally measured drag coefficient at test rig Reynolds number, with C_D plotted against $\phi_{corrected}$.

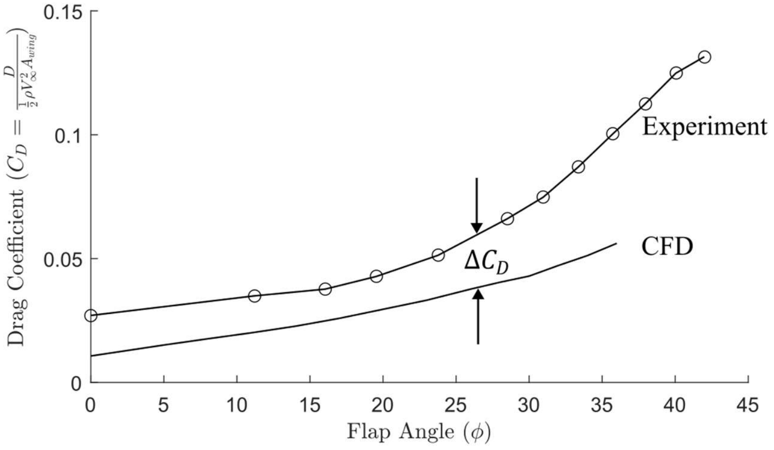

Figure 3.27: NACA 43018 aerofoil drag coefficient at test rig and aircraft Reynolds number measured in the test rig and calculated from CFD respectively [37].

The discrepancy in drag, ΔC_D between the test rig and aircraft cases is a function of the flap angle, ϕ. To a first order, drag of the wing scales with the square of the freestream velocity. With propellers present, the drag scales with the square of the local velocity on the wing surface instead. This local velocity is related to the freestream velocity by,

$$\frac{V_{jet}}{V_\infty} = \sqrt{1 + T_c} \quad . \quad (3.18)$$

The corrected drag coefficient is therefore calculated as,

$$C_{D,corrected} = C_{D,Experiment} - (1 + T_c)\Delta C_D \quad . \quad (3.19)$$

As with the lift coefficient, all drags reported in Chapters 6 and 7 are the corrected drag [37].

3.3.12 5-Hole Probe Traverse

As well as a rake traverse, and load cell system, a 5-hole probe traverse gear was also built for use with the test rig. Fig. 3.28 (a) shows a diagram of this traverse gear in operation. A probe with a diameter of 1.75mm was used. The overall length of the probe was 520mm, allowing the traverse gear to be mounted well away from the wing. The probe was calibrated [87] with flow angles of ±45° in both yaw and pitch directions. Due to the high incidence range, non-standard coefficients were used to extend the range of the map,

$$C_\lambda = \frac{p_3 - p_2}{p_{max} - p_l} \quad , \qquad (3.20) \qquad C_\tau = \frac{p_4 - p_5}{p_{max} - p_l} \quad , \qquad (3.21)$$

$$C_{P0} = \frac{P_0 - p_1}{p_{max} - p_l} \quad , \qquad (3.22) \qquad C_p = \frac{P_0 - p}{p_{max} - p_l} \quad , \qquad (3.23)$$

where,

$$p_{max} = 0.666p_l + 0.334p_h \quad , \qquad (3.24)$$

$$p_h = 0.5(p_{1st} + p_{2nd}) \quad , \qquad (3.25)$$

$$p_l = 0.5(p_{3rd} + p_{4th}) \quad , \qquad (3.26)$$

with p_{1s} the highest of the 4 outer pressures and p_{4th} the lowest [27].

The location of each hole and definitions are shown in Fig 3.28 (b). Through a sweep of yaw, it was found for the settling time of 2s and measurement time of 2.5s, the yaw and pitch could both be calculated to within 0.5°.

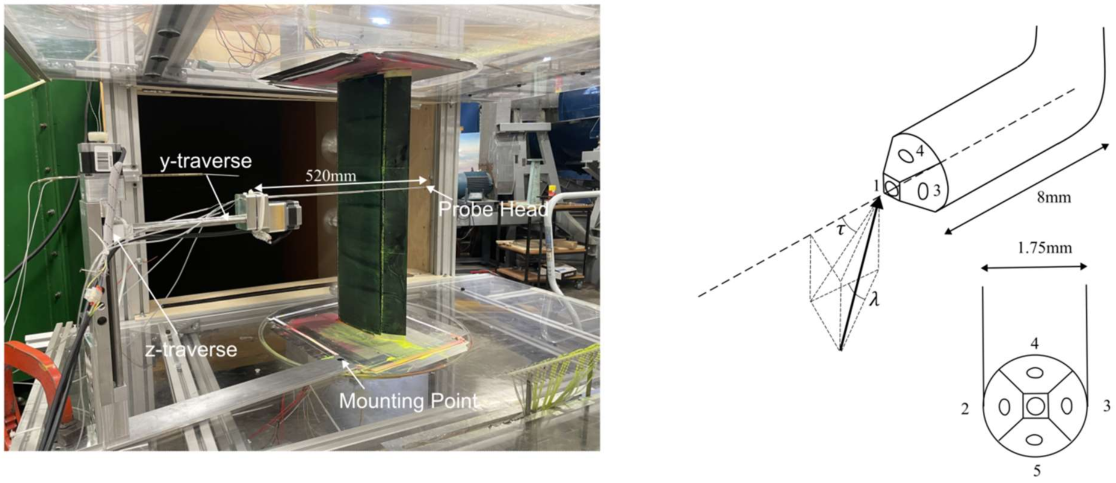

(a) (b)

Figure 3.28: 5-hole probe traverse set up in the test rig. Traverse planes just downstream of the wing trailing edge are shown in this thesis.

3.4 Aircraft Model Parameters

In Chapter 4 and 5, the reduction in the profile drag of the wing with distributed propulsors fitted is reported. The aircraft chosen as a reference is the ATR-42, parameters for which are shown in Table 3.2. The drag benefits reported are for an aircraft at its cruise condition. The wing area reductions possible are calculated for the aircraft in the landing condition. In Chapter 8, the reduction in power consumption of an electrified aircraft at cruise, with the same maximum take-off weight as the ATR-42, is reported. Parameters for these calculations are also shown in Table 3.2.

Parameter	Value
Take-off Speed (ms^{-1})	67
Initial Climb Rate (ms^{-1})	9.4
Aircraft Mass (kg)	18600
Fuselage Length (m)	22.67
Fuselage Diameter (m)	3
Cruise Altitude (m)	7630
Cruise Speed (ms^{-1})	152.8
Airport Altitude (m)	0
Landing Speed (ms^{-1})	62.2
Wing Span (m)	24.57
L/D in Take-off/ Landing	8
Unblown Wing L/D in Landing	61.2
Unblown Wing C_L	1.47
Stall Margin ΔC_L	0.83
ATR-42 Propeller Diameter (m)	3.94

Table 3.2: Aircraft model parameters used to assess the aerodynamic benefit of a blown wing when fitted to an aircraft. Data taken from [40] with missing information estimated [28].

4. The Design and Operating Space of a Blown Wing

4.1 Introduction

This chapter quantifies the wing profile drag reduction that can be achieved by employing blown wing technology, and the geometry required to achieve this. The effect of blowing on the lift and drag of a wing is modelled using a 2D actuator disk which captures the effects of propeller diameter and location, but removes the complexities of spanwise variations in the flow. The actuator disk diameter, and streamwise and vertical positions of the actuator disk are varied in this chapter, as shown in Fig. 4.1.

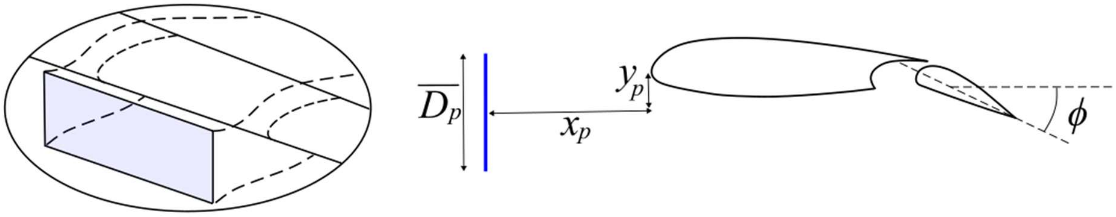

Figure 4.1: In this chapter, a 2D actuator model is used to determine the effect of propeller position and size on the performance of a blown wing.

The use of 2-dimensional models is an attractive option for the preliminary design of an aircraft as it allows the designer to neglect spanwise variations in the performance of the wing, and consider only the first order effects of propeller diameter and location. The spanwise variations in wing loading inherent to the real swirling circular jets produced by propellers, and the 3D effects on the wing they generate, will be quantified in Chapters 6 and 7 and shown to be of second order importance compared to the 2D propeller diameter and location of the actuator disk. A 2D mean propeller diameter, $\overline{D_p}$, is used for this chapter. The relationship between the mean propeller diameter, and propeller diameter are described in Chapter 6.

Patterson et al. [59] derived a surrogate model for the lift of a 2-dimensional blown wing as a function of jet streamwise location, jet thrust and jet diameter. This model provides a useful reference for predicting blown wing performance. However, because the calculations used were inviscid, the model is only valid for low incidence away from stall. It is shown in this chapter that, whilst blowing provides an extra degree of freedom to the pilot when landing, the performance of the wing is still limited by the stall point of the wing, and thus a viscous solver is essential for predicting the limits of blown wing performance. The effect of propeller diameter, and propeller location, on the performance of the blown wing are first considered separately. We then calculate the limits on the operational thrust and wing angle for a safe landing with a blown wing. These limits are used to compare different blown wing geometries in order to establish the optimum blown wing geometry for maximum wing drag reduction, and quantify the drag saving possible, thereby answering the first question of Chapter 2.

4.2 The Effect of Propeller Diameter on the Performance of a Blown Wing

In the limit as the propeller diameter becomes large compared to the wing chord, the lift of the blown wing is given by the relationship,

$$C_{L,blown} = C_{L,unblown} \frac{{V_{jet}}^2}{{V_\infty}^2} \quad , \qquad (4.1)$$

where V_∞ is the freestream velocity, and V_{jet} is the velocity of the propeller jet in the far-field once the pressure has returned to ambient. This model assumes the wing is fully immersed in the jet, the effect of finite jet diameters can be ignored, and the lift increase is due to the increased dynamic pressure seen by the wing, as shown in Fig. 4.2.

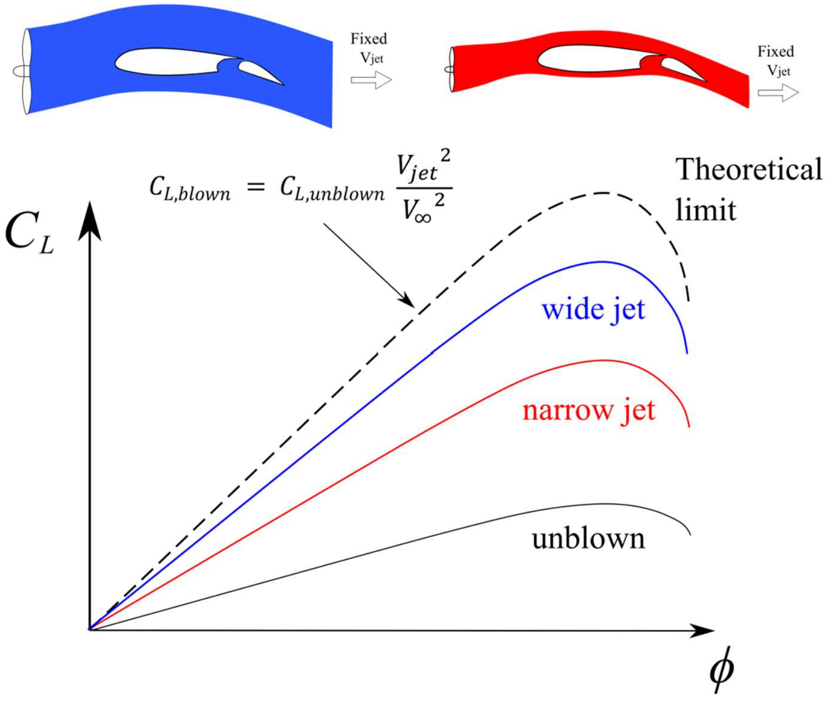

Figure 4.2: Theoretical and actual lift slopes for a wing immersed in a finite jet of varying width. Reducing the width of the propeller jet reduces the slope of the lift curve.

In the limit as the jet becomes large (typically with a propeller diameter to chord ratio greater than 1), the vortex sheet at the jet boundary does not affect the performance of the wing (provided the boundary is not close to the wing) and the change from the unblown lift curve to the blown lift curve is modelled by Eq. 4.1. For narrower jets, with a diameter less than the wing chord, the lift curve slope reduces as the deflected jet momentum decreases.

During descent and landing, the thrust of the propulsion system must not exceed the aircraft drag if the aircraft is to decelerate. Because the total thrust of the blown wing, T, is fixed by this constraint, the jet velocity is fixed by the jet area (for 2D cases, the area of the jet, $A_{jet}=\overline{D_p}$) according to,

$$\frac{V_{jet}^2}{V_\infty^2} = 1 + \frac{T}{\frac{1}{2}\rho V_\infty^2 A_{jet}} \ , \quad (4.2)$$

where V_{jet} is the velocity produced by the propeller. Substituting Eq. 4.2 into Eq. 4.1, and ignoring the effect of propeller diameter on the lift of the wing, as the jet area is reduced, the lift coefficient of the blown wing rises for the same total thrust. This relationship is shown as the dashed line in Fig. 4.3 for two different aircraft lift-to-drag ratios, a high landing drag for the jet to push against (and hence high thrust) with L/D=5 and a low drag configuration with L/D=10. Figure 4.3 indicates that a small propeller diameter is beneficial in raising the maximum lift coefficient of a blown wing for a given span. This approach is only possible through the use of distributed propulsion, and would likely necessitate the use of folding propellers, to avoid the low propulsive efficiency of the smaller propellers at cruise.

Also overlaid onto Fig. 4.3 are the results of a surrogate model for blown wing lift, from Patterson et al. [60]. This model quantifies the effect of propeller diameter on the lift of a blown wing. The model shows that an optimum propeller diameter exists which maximises the lift for a given thrust. Below this propeller diameter, the lift coefficient of a real blown wing falls. This is because in the limit as the propeller diameter goes to zero, and jet thrust to infinity, the wing will be unable to react to the jet and the lift increase due to the propeller jet drops to zero. It will be impossible to achieve the condition that the jet edge is far from the wing surface and the wing will now no longer be fully immersed in the jet. This section has shown that an optimum blown wing propeller diameter exists for maximising lift under the constraint that the total thrust of the system is fixed, and that this optimum diameter occurs at very small propeller diameters.

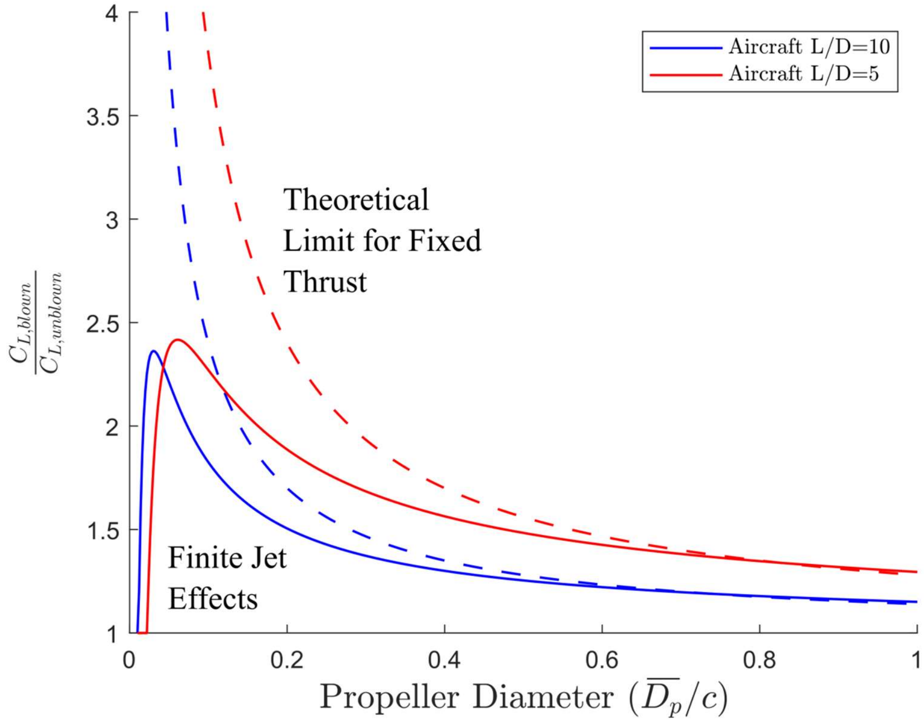

Figure 4.3: The effect of finite propeller size on the lift of a blown wing. Dashed lines represent the lift calculated from Eq. 4.1 and 4.2. The solid lines show the lift predicted by the surrogate model of Patterson et al. [60].

4.3 The Effect of Jet Location on the Performance of a Blown Wing

In this section, the effect of jet location is investigated. As the jet area becomes small, the likelihood that the wing is not submerged in the jet increases. To investigate this, viscous RANS simulations were run for the NACA 43018 aerofoil over a range of incidences up to stall for three different vertical offsets of the actuator disk. The red line in Fig. 4.4 shows the propeller in the highest position (y_p/c=0.05), the middle position (y_p/c=0) is in green and the lowest position (y_p/c=-0.05) is in blue. The jet has a diameter, $\overline{D_p}$/c, of 0.5, and a streamwise location of x_p/c=-0.5. The boundary of the jet is marked for each propeller position at the incidence at which the wing stalls.

At low incidence, moving the jet down reduces the lift coefficient. This effect is widely reported [78], and is due to the reduction in the amount of jet passing over the wing suction surface, the side of the aerofoil that experiences the most flow turning at positive angles of attack. However, bringing the jet down below the wing centreline increases the stall angle of the wing, leading to a higher maximum lift coefficient, $C_{L,max}$. This effect was observed by Kirby and Hassell [33] as early as 1966 who noted that the descent angle at which wing stall first occurred for a tilt-wing aircraft could be increased by positioning propellers well below the wing centreline. In this instance, moving from y_p/c=-0.05 to y_p/c=0.05 increases $C_{L,max}$ by 40%. It can be seen from the jet boundary streamlines in Fig. 4.4 that the wing stall, in all three cases, occurs at the point where the jet first moves above and no longer fully immerses the wing.

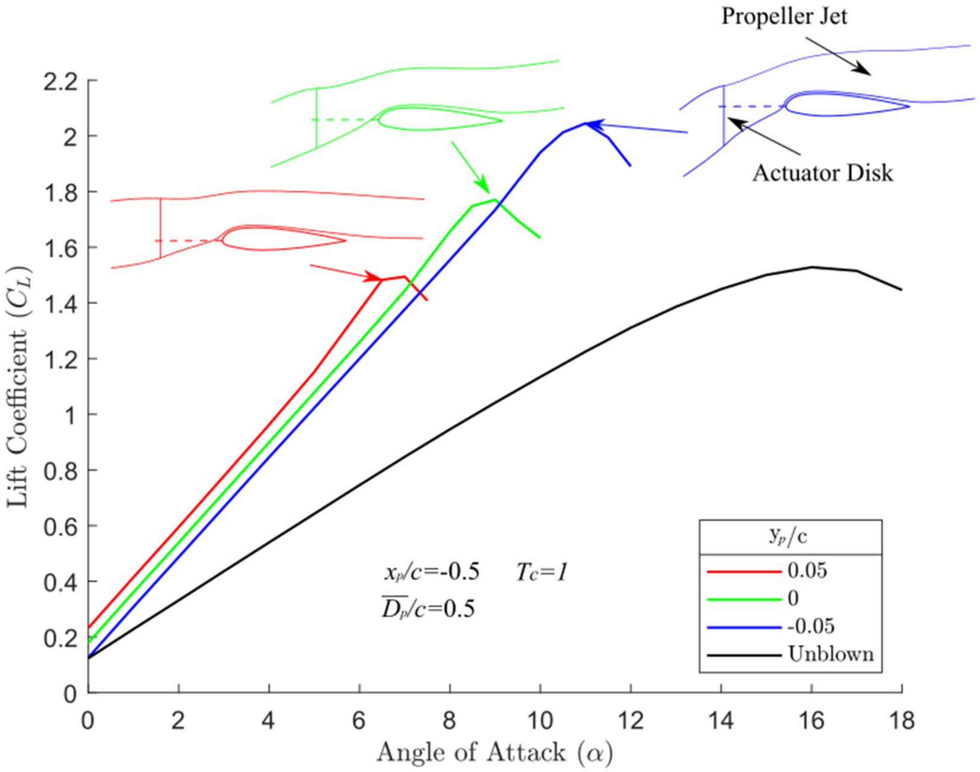

Figure 4.4: The effect of propeller vertical position on stall incidence (T_c= 1, x_p/c=-0.5, $\overline{D_p}$/c=0.5). The unblown wing is shown in black along with three blown wings shown in blue (y_p/c=-0.05), green (y_p/c=0), and red (y_p/c=0.05).

To gain more insight into the physics responsible for the change in stall angle with jet position, inviscid simulations were run for the NACA 43018 aerofoil with an actuator disk placed at two different vertical offsets of y_p/c=-0.05 and 0.05. The propeller has a diameter, $\overline{D_p}$/c, of 0.5, a streamwise location of x_p/c=-0.5 and the simulations were run at an angle of attack of 8°. Figure 4.5 shows plots of the wing suction surface velocity distribution.

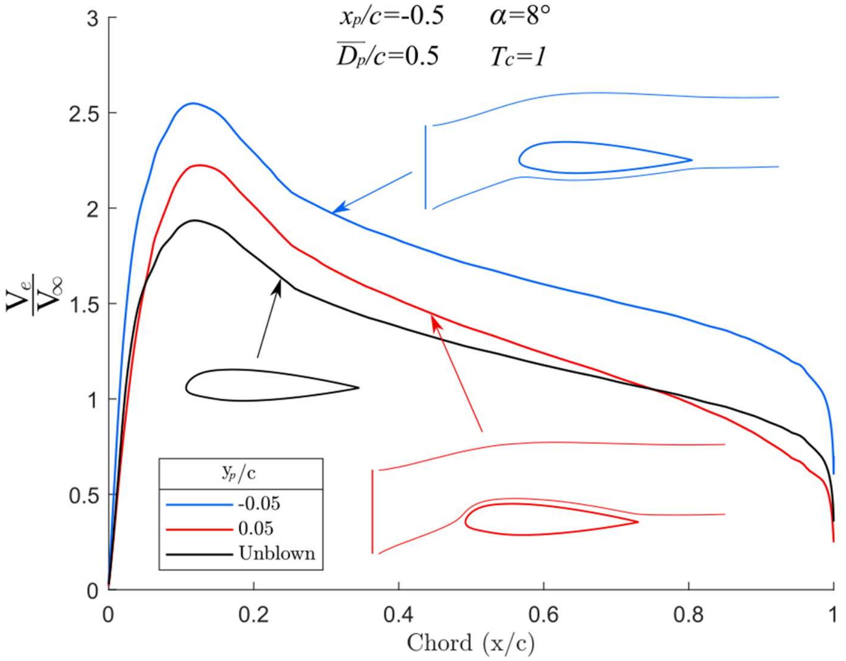

Figure 4.5: The effect of jet location on the aerofoil suction surface velocity distribution (inviscid cases shown). Moving the jet from fully immersing the wing (blue) to only passing above the wing suction surface (red) increases the suction surface boundary layer diffusion compared to the unblown wing (black).

The black line shows the aerofoil with no jet. The blue line shows a case in which the vertical position of the jet has been set so that aerofoil is fully submerged in the jet. The red line shows the case in which the vertical position of the jet has been set so that it just misses the aerofoil and passes above the suction surface. Comparing the black and blue lines it can be seen that even when the wing is only just submerged in the jet, the velocity distribution around the wing behaves as if the wing is fully submerged, causing the wing lift to rise. Comparing the blue and red lines, the drop in velocity from the peak velocity to the trailing edge has increased by 16%.

To explain the increased diffusion of a jet passing above the wing, let us consider a blown wing with the jet passing above the suction surface, illustrated schematically in Fig. 4.6. If the jet is to follow the freestream flow, the wing has to turn the momentum of the jet around the suction surface, as shown. This leads to an increased pressure gradient from the far-field to the wing surface for the blown case compared to the unblown case. The increased pressure gradient is given by,

$$\frac{\partial p}{\partial r} = \rho \frac{{V_{local}}^2}{r} \quad . \quad (4.3)$$

where V_{local} is the local velocity of the jet above the wing. The peak suction pressure in the blown case, $p_{peak,blown}$ is lower than the equivalent unblown peak suction pressure. However, the total pressure of the flow in the region between the jet and the wing is equal to the freestream total pressure, $P_{0,\infty}$ for both the blown and unblown case. The reduced peak suction pressure leads to a higher peak suction surface velocity for the blown case. This explains the increased peak suction velocity, of the case shown in red in Fig. 4.5 compared to the unblown wing, shown in black. As the jet moves further away from the wing, the radius of turning of the jet will decrease, allowing the loading on the wing to return to its unblown value.

We now consider the wing trailing edge. The Kutta condition requires that the velocity at the trailing edge of the wing must be equal on both the pressure and suction surface in order for the trailing edge circulation, Γ_{TE} to be zero. The pressure surface is not blown in either case considered, giving a low trailing edge velocity.

Because of the high peak and low trailing edge velocity, the diffusion is higher when the jet passes above the wing, than when there is no jet at all.

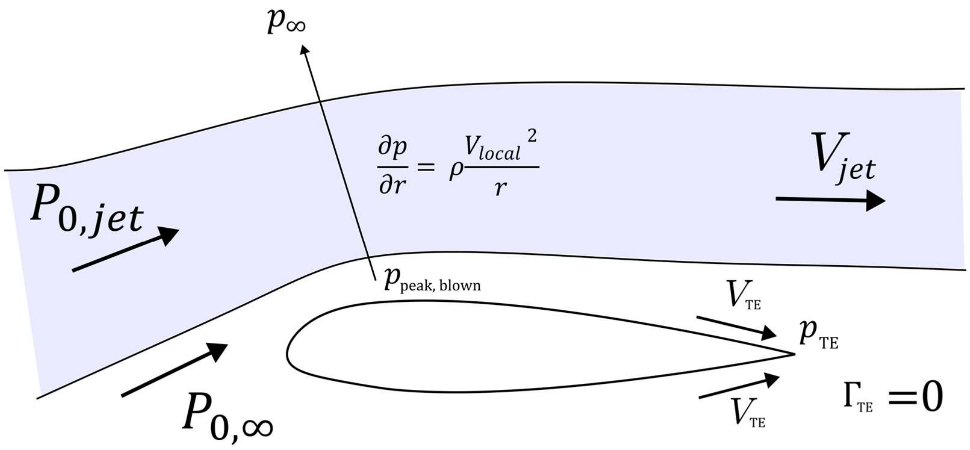

Figure 4.6: Schematic of a wing with the jet passing above the suction surface. The pressure gradient caused by turning the additional momentum of the jet leads to an increased boundary layer diffusion relative to an unblown wing.

If we now consider the case where the wing is fully immersed in the jet, as shown in blue in Fig. 4.5, although the peak suction pressure is lower than the unblown wing for the same reasons outlined above, the trailing edge velocity is higher as both the pressure and suction surfaces are immersed in the high speed flow of the jet. As a result, the diffusion factor is low and close to that of the unblown wing. The effect of the sudden rise in suction surface diffusion as we move from the case with the jet immersing the wing to the case with the jet passing above the suction surface is to produce a premature stall of the wing.

To avoid premature stall the wing should therefore be fully submerged in the propeller jet at all operating points. This implies that the range of incidences over which the wing remains un-stalled is a strong function of the size and position of the propulsors. Figure 4.7 shows two propulsors of different size and location but which both achieve an un-stalled wing at the incidence shown. This is due in both cases to the wing being fully submerged in the propulsors' jet.

To ensure the jet fully immerses the wing at any given incidence we can therefore say that,

$$\frac{\overline{D_p}}{2} - y_p \geq f(x_p) \quad . \qquad (4.4)$$

where $\overline{D_p}$ is the propeller diameter, y_p is the vertical coordinate of the centre of the propellor and $f(x_p)$ is the equation for the vertical coordinate of the stagnation streamline. This simple equation will be shown later to be useful in interpreting the propeller wing design space.

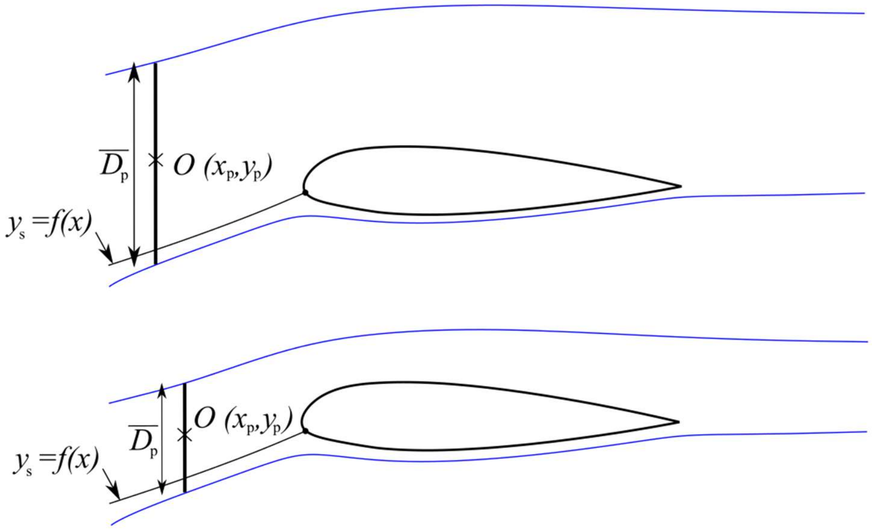

Figure 4.7: The streamline pattern for two jets of different size and position around a blown wing. To avoid premature stall, the propeller jet should intersect the wing stagnation streamline.

4.4 The Effect of Introducing a Flap on a Blown Wing

So far this analysis of the blown wing has only considered the simple case of a plain wing. However, high lift can be achieved with a range of leading and trailing edge devices, namely slats and flaps, which are fitted to most conventional aircraft. The aim of this section is to understand how the introduction of a flap affects the findings of the previous section. The important difference with a flap is that the incidence of the main wing remains fixed and the flap is deployed at the wing trailing edge. This allows the aircraft to remain level during landing, and increases the lift possible from the wing. It was shown in Chapter 2 that the use of a flap in a blown wing also allows high lift coefficients to be achieved, without creating excess thrust.

The ATR-42, which is used as a reference aircraft in much of this thesis, employs a Fowler flap in order to generate high lift coefficients during take-off and landing. A Fowler flap was designed by the author for the NACA 43018 profile, the method for which is described in Chapter 3.

Figure 4.8 shows a comparison of the lift coefficient generated with different levels of blowing by deploying the Fowler flap at a fixed angle of attack of 3°, and by pitching the wing with the flap retracted over a range of angles of attack. The lift coefficient for two different geometries, y_p/c=-0.2 and y_p/c=0 is shown. The actuator disk horizontal distance, x_p/c=-0.5 and $\overline{D_p}/c$=0.5.

Moving the jet down below the wing centreline delays blown wing stall. For y_p/c=-0.2, the stall angle is nearly constant for both wing angle and flap angle sweeps. This is because the wing is always immersed in the jet from the actuator disk, and stall occurs from progressive separation of the wing trailing edge due to the high incidence, as occurs for the unblown wing, and not due to the stall mechanism identified in the last section. However, for y_p/c=0, the stall mechanism identified in Section 4.3 does apply for both the plain wing and the wing with a flap, leading to sharp stall at low wing/ flap angles. Whilst the wing angle is fixed for Fig. 4.8 (b), the deployment of the flap increases the wing circulation, generating an upwash which pulls more of the jet over the wing suction surface. Eventually, the flap is deployed sufficiently to distort the shape of the streamlines such that the criteria in Eq. 4.4 is met and the flap stalls.

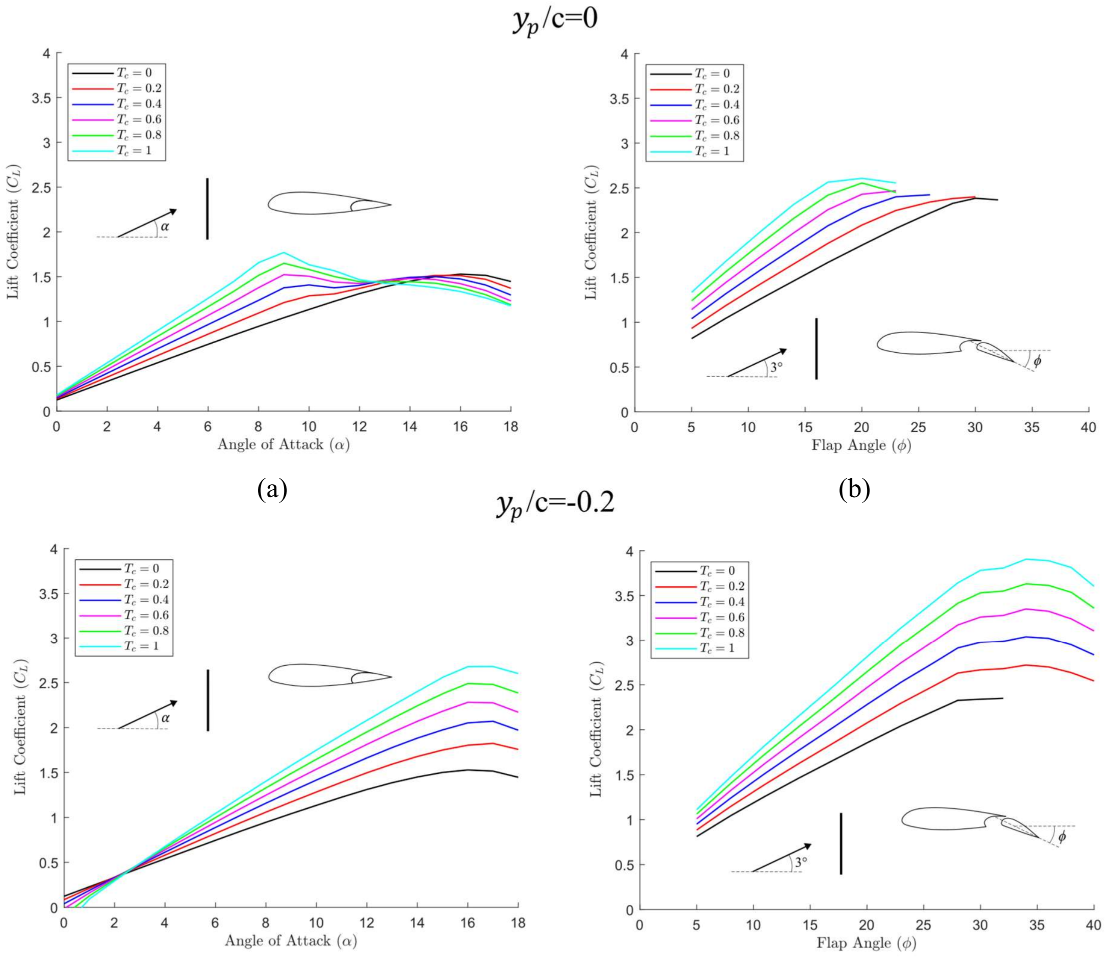

(a) (b) (c) (d)

Figure 4.8: Comparison of the lift curves for blown wings at a range of angles of attack with the flap retracted ((a) and (c)) and at fixed angle of attack of 3° with flap deployed ((b) and (d)) for two different vertical offsets of the actuator disk, y_p/c=0 ((a) and (b)) and y_p/c=-0.2 ((c) and (d)).

This is shown using contours of velocity in Fig. 4.9. Rather than the wing stalling at the point the jet lower boundary moves above the wing stagnation streamline, the criteria shifts to the flap stagnation streamline instead.

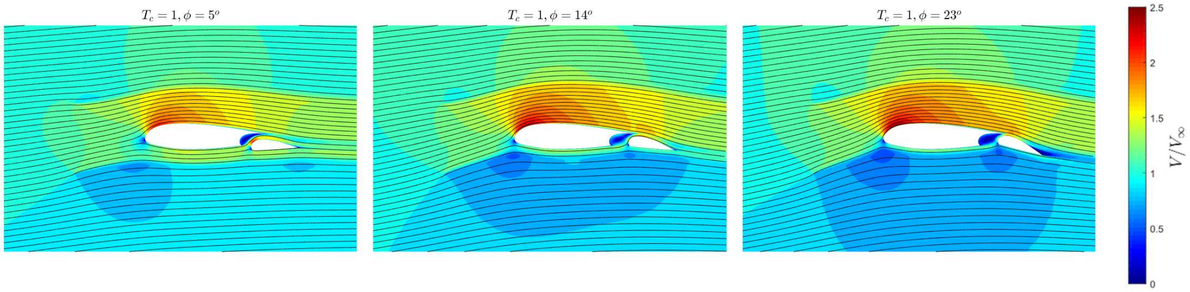

Figure 4.9: Flowfield around the wing for x_p/c=-0.5, y_p/c=0 and D_p/c=0.5 at three flap angles, ϕ=5°, 14° and 23°. As the flap is deployed, the wing circulation accelerates the jet over the suction surface, stalling the wing.

Another example of the role of the wing circulation on jet distortion when the flap is deployed is shown in Fig. 4.10. The figure shows a case where the actuator disk is placed well below the wing centreline at x_p/c=-0.5, y_p/c=-0.5 with a diameter, $\overline{D_p}$/c=0.5. For moderate flap angles up to 25°, the jet passes below the wing and the lift is unaffected by the blowing. However, above a critical flap angle, which is dependent on the thrust coefficient, the circulation of the wing is sufficient to accelerate part of the jet over the wing suction surface. At this point, the lift of the wing increases sharply to the blown lift of the wing, and the drag increases. The fact that the wing does not lose lift due to the jet passing below the wing and reducing its circulation could not be explained, and should be studied further.

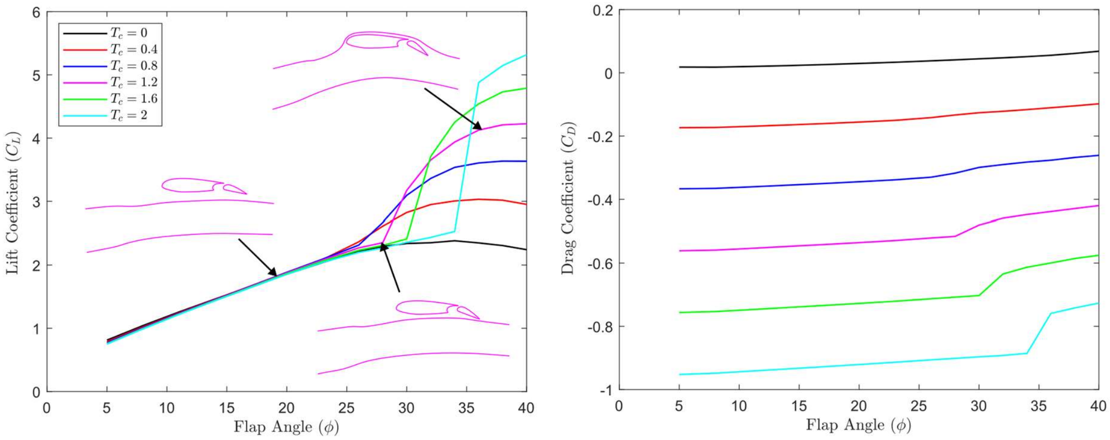

Figure 4.10: Lift and drag polars for a jet placed well below the wing centreline. The wing angle of attack is 3°. As the jet moves from passing below the wing to immersing the wing suction and pressure surface, the lift increases.

The jet location is shown schematically for three flap angles of interest, ϕ=20°, 28° and 36° in Fig. 4.10. Contours of the velocity field at these angles are shown in Fig. 4.11.

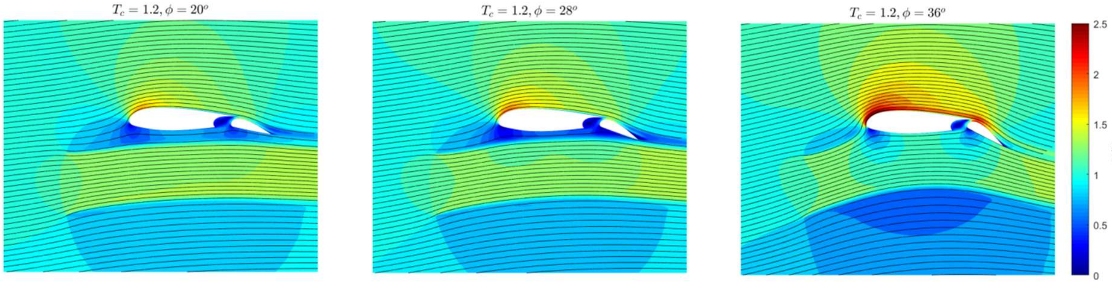

Figure 4.11: Contours of the flow-field for an actuator disk placed below the wing centreline at x_p/c=-0.5, y_p/c=0, with D_p/c=0.5 at three flap angles, ϕ=20°, 28° and 36°.

To generate augmented lift, the blown wing must therefore be immersed in the jet at all operating points. The useful design space can be carved up, as shown in Fig. 4.12 into three regions, defined by,

$$\pm\frac{\overline{D_p}}{2} - y_p \geq f(x_p) \quad . \quad (4.5)$$

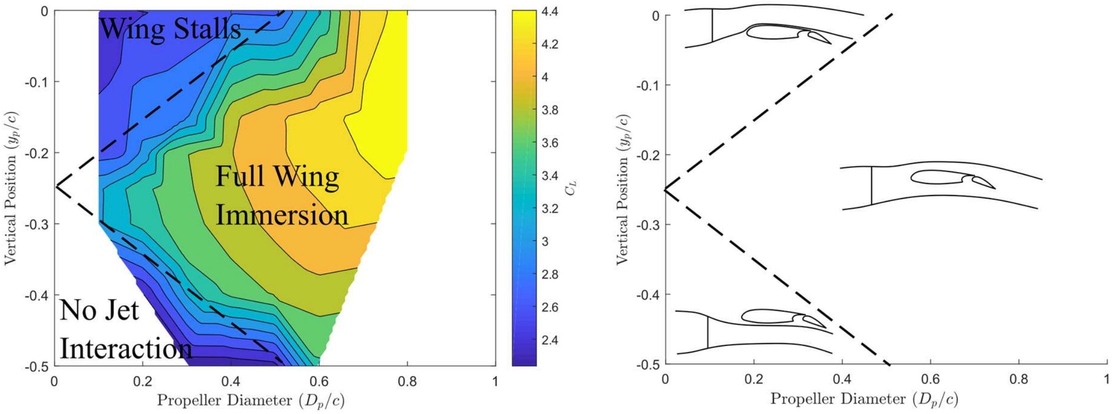

Figure 4.12: Regions of the design space which should be avoided due to poor propeller positioning. The thrust coefficient, T_c=1.5, the flap angle, ϕ=28°, and the wing angle is 3°.

The left hand side of Fig. 4.12 shows the lift coefficient generated at a flap angle of ϕ=28°, and thrust coefficient, T_c, of 1.5 for a range of actuator disk diameters and vertical locations, with x_p/c=-0.5. The boundaries marked out by Eq. 4.5 can be seen on the contours of lift coefficient. A fixed value for $f(x_p)$=-0.26 has been used (taken from the stagnation streamline of the unblown wing at ϕ=28°). This is an approximation, as blowing changes the circulation of the wing, affecting the value of $f(x_p)$. Despite this approximation, Eq. 4.5 predicts the optimum regions of the design space to place the actuator disk.

4.5 The Blown Wing Operating Space

We have learnt in Section 4.3 and 4.4 that the lift of a blown wing with a flap is sensitive to the position of the jet in relation to the wing, and the thrust and flap angle settings. Reducing propeller diameter was shown in Section 4.2 to increase blown wing lift, for a given thrust; however, reducing propeller diameter also reduces the range of acceptable positions for the jet that do not lead to either premature stall, or no blown wing benefit. The optimal thrust and flap angle for a blown wing is different for each geometry, due to the changing maximum lift coefficient and total streamwise force. In order to find the optimum propeller size and position, which is presented in Section 4.6, a robust method for identifying the optimal blown wing thrust and flap angle is presented in this section. We focus on the blown lift during landing, as this is the critical condition where the propeller thrust is limited.

Figure 4.13 shows schematically the operating space of a blown wing. The performance of the wing on landing is primarily limited by two requirements: that the wing be a safe incidence range away from its stall lift coefficient, $C_{L,max}$, and the thrust from the blowing propellers must not exceed a critical value such that the aircraft can slow down and land on the runway (C_x=0, see Eq. 4.6). The wing flap angle must be set a safe distance away from the stall point to maintain a safety margin during landing. A safety factor, ΔC_L, developed for blown wings is described in Appendix D.

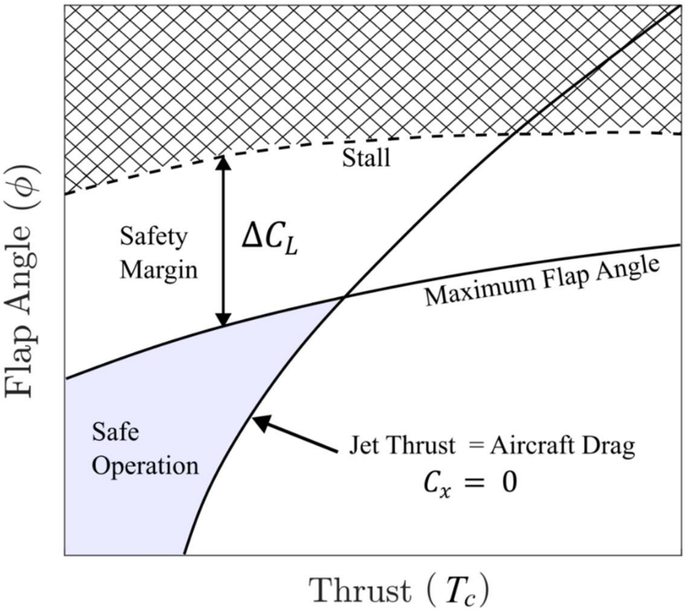

Figure 4.13: The operating space of a blown wing is limited by jet thrust and wing stall. A safe operating zone, demarked by these limits, is available for the pilot to operate within.

Using either an analytical approach, or the 2D actuator disk modelling presented in the previous section, it is possible to construct the operating space shown in Fig. 4.13. The maximum lift of the design is the point within the Safe Operation region producing the greatest lift. A reference aircraft, in this case the ATR-42, is used to provide realistic sizing of the wings, and airframe drag during landing. Details of the ATR-42 are given in Table 3.2.

To account for the airframe drag, the reference aircraft modelled in this study was assumed to have a fixed airframe L/D = 8 during final descent, including the drag from the original unblown flapped wing. The thrust coefficient of the two ATR-42 propellers during landing is 0.4, giving a velocity 18% higher than the freestream velocity covering 32% of the wing span. As the wing profile drag accounts for only 13% of the overall drag of the aircraft during landing, the change in drag due to the ATR-42 propeller blowing the wing is small (approximately 1% of the total aircraft drag) and can be ignored. The drag coefficient of the wing without distributed blowing is therefore taken as the unblown wing drag, with flaps deployed. The wing profile drag, with blowing, is extracted from the CFD simulation.

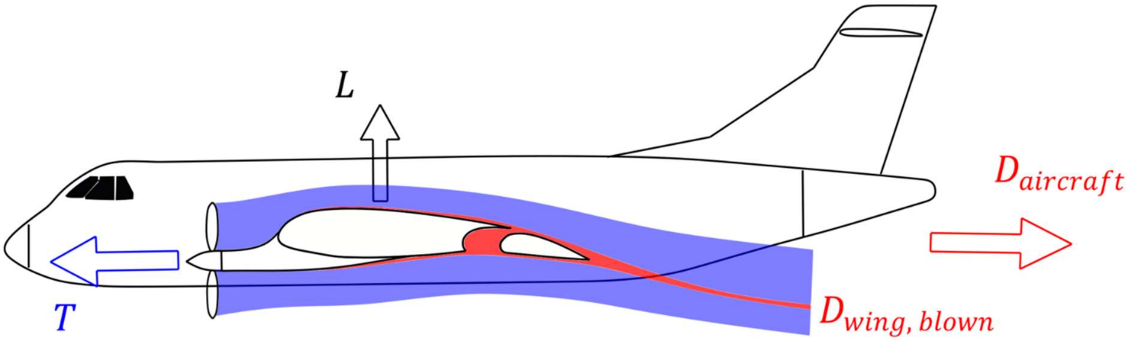

Figure 4.14: Forces on an aircraft fitted with a blown wing.

If we define an axial force coefficient,

$$C_x = \frac{T - D}{\frac{1}{2}\rho A_{wing} V_\infty^2} \quad , \quad (4.6)$$

we can calculate C_x for the aircraft with a blown wing from,

$$C_x = \frac{D_{wing,blown} - T}{\frac{1}{2}\rho A_{wing} V_\infty^2} - \frac{D_{wing,unblown}}{\frac{1}{2}\rho A_{wing} V_\infty^2} + \frac{D_{aircraft}}{\frac{1}{2}\rho A_{wing} V_\infty^2} \quad , \quad (4.7)$$

and this can be re-written as,

$$C_x = C_{x,wing\ blown} - C_{x,wing\ unblown}\frac{C_{L,wing\ blown}}{C_{L,wing\ unblown}} + \frac{C_{L,wing\ blown}}{L/D} \quad . \quad (4.8)$$

The two axial force coefficients $C_{x,wing\ blown}$ and $C_{x,wing\ unblown}$ can be easily extracted from CFD simulations of the wing and flap, with and without blowing.

Figure 4.15 (a) shows the construction of the operating space, incorporating the necessary constraints identified in this section, for an analytical model of a blown wing. The blown wing lift is modelled with Eq. 4.1 and a linear lift-flap polar $C_{L,unblown} = 3.8\phi + 0.52$ for the unblown wing, measured from the unblown wing CFD. The wing drag was neglected and the aircraft lift-to-drag ratio in landing was assumed to be 8, typical of many aircraft during final descent [46]. Blowing is assumed to cover the full wing span with a propeller diameter to chord ratio, $\overline{D_p}$/c =0.5. The span of the wing is fixed, and any reduction in wing area is achieved solely by decreasing the wing chord. This keeps the induced drag of the wing constant. Parameters for the model, based on the ATR-42, are tabulated in Table 3.2.

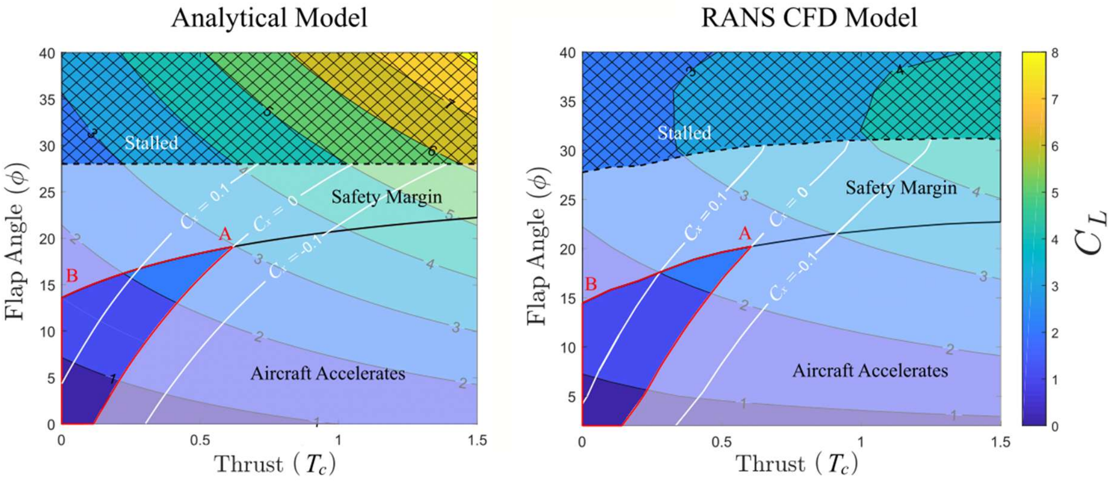

(a)

(b)

Figure 4.15: Effect of thrust and flap angle on the lift coefficient of a blown wing and the feasible blown wing operating space during landing. Analytical model shown in (a) and RANS CFD solutions in (b).

The analytical case, Fig. 4.15 (a) has a maximum blown lift coefficient of 8, shown in the right-hand top corner. However, as discussed, several regions of the plot are off-limits due to operating constraints. First, the stall flap angle provides a limit above which the pilot may not go without encountering control issues and wing buffeting, shown in the hatched out region.

This has been assumed constant at 28°, matching the unblown flap CFD simulations. The solid black line in Fig. 4.15 demarks the safety margin region of the blown wing operating space. The region of the operating plot between the stall line and the safe operating line is shaded out as usable only in emergency landings.

Plotted in white are contours of net axial force coefficient, C_x. The aircraft decelerates provided $C_x > 0$. This criterion enables a second region to be removed, to the right of $C_x = 0$, from the operating space as unfeasible at the point of landing. The remaining safe region (outlined in red) has two corners of interest, labelled A and B in the diagram. Point B is the maximum lift achieved by the original wing without any blowing, $C_{L,unblown}$=1.47 and point A is the maximum lift possible with the blown wing, $C_{L,blown}$, in this case equal to 3.

Figure 4.15 (b) shows the same geometry considered in Fig. 4.15 (a), but predicted by 2D RANS CFD simulations. The same process as above is applied to give a maximum feasible lift coefficient of 2.5. This is slightly lower that the analytically predicted lift coefficient of 3.0. This is due to the finite propeller diameter which reduces the lift for a given flap angle and thrust setting, compared to Eq. 4.1, and the stall angle varies with thrust, due to the changing local Reynolds number of the wing.

The constraint diagram approach described above is useful as it allows the competing effects of maximum lift coefficient and jet thrust to be quantified and compared. Figure 4.16 shows constraint diagrams for the two cases discussed so far in this thesis with y_p/c=0 and y_p/c=-0.2. The constraint diagram is able to identify the reducing stall angle with thrust, due to the adverse stall mechanism discussed previously, for y_p/c=0, and how this reduces the operating flap angle of the wing. Because the lift of the wing is small, the wing chord remains large. For a fixed non-dimensional propeller diameter $\overline{D_p}$/c=0.5, the physical size of the jets will also remain large and so the maximum operating thrust coefficient is low for a fixed thrust. Increasing the lift of the wing with blowing therefore has a ‘snowball effect’ as small increases in lift allow reductions in the dimensional size of the jet, allowing higher thrust coefficients and further increases in lift. This snowball effect is shown in Fig. 4.16 (b) for the actuator disk placed at y_p/c=-0.2. The operating lift coefficient of the wing is 2.75, nearly double the 1.55 of the blown wing with y_p/c=0. This high lift allows a thrust coefficient of 0.75 to be used, compared to 0.4 with y_p/c=0.

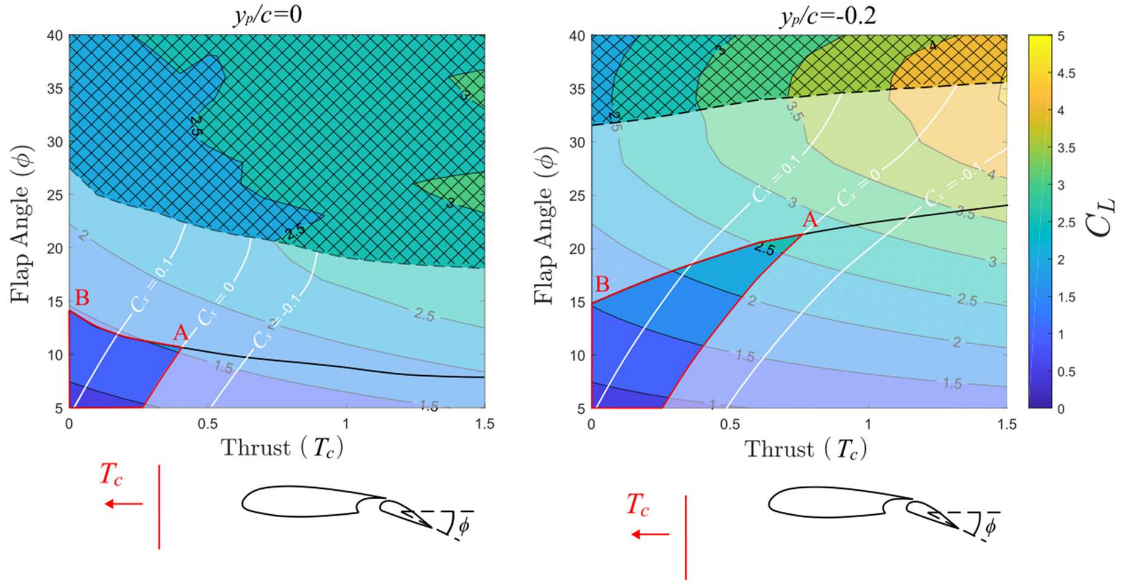

(a)

(b)

Figure 4.16: Effect of thrust and flap angle on the lift coefficient of a blown wing with two different propeller vertical offsets, y_p/c=0 and y_p/c=-0.2. Moving the propeller down below the wing centreline moves the blown operating point, marked as A, to higher thrust coefficients and flap angles, increasing the wing lift coefficient from 1.55 to 2.75.

4.6 The Blown Wing Design Space

Having established a method to assess the operation of different blown wing geometries, we now perform a sweep of the design space to look at how the predicted blown wing performance changes with different propeller locations and diameters. Figure 4.17 shows the design space mapped out in this section. Schematics of the real propeller geometries being modelled by the 2D actuator disk within this design sweep are shown in the four quadrants of the space. Moving to the left of Fig. 4.17 reduces the propeller diameter, leading to more, smaller propellers along the wingspan. Moving down within Fig. 4.17 leads to larger vertical offsets of the propeller below the wing centreline. The horizontal position of the propeller was also varied, although this is not shown in the figure.

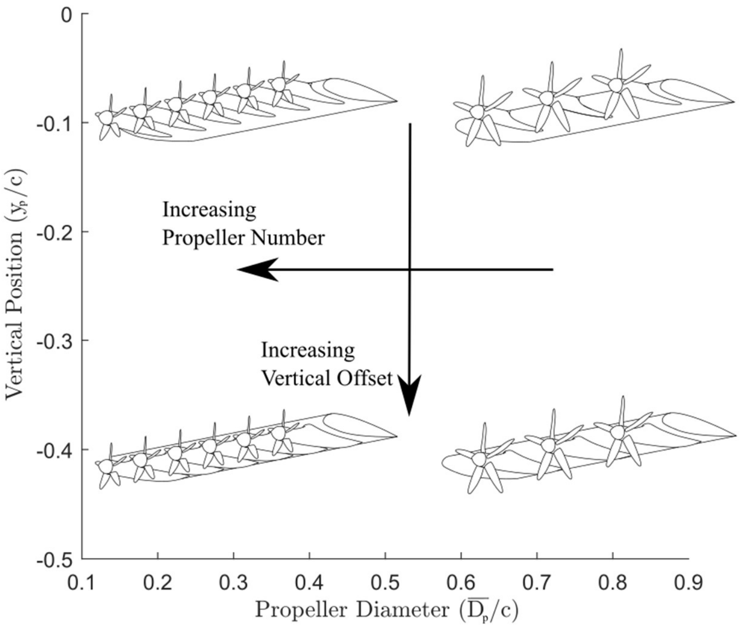

Figure 4.17: Mapping out the design space. The equivalent 3D geometries for the 2D design space under consideration are shown in each quadrant.

Figure 4.18 shows the effect of changing the propeller vertical position and size at two fixed axial locations upstream of the wing (x_p/c=-0.5 in Fig. 4.18 (a) and x_p/c=-0.25 in Fig. 4.18 (b)) on the blown lift. Plotted is the ratio of maximum possible blown lift (point A in Fig. 4.15) to unblown lift (point B). Because the thrust is fixed during landing, reducing the propeller size raises the jet velocity and the lift augmentation. The white lines in Fig. 4.18 show a constant value of the left hand side of Eq. 4.4. This represents the point beyond which the jet moves above the wing and the wing stalls. As the propeller is moved vertically downward, below the lowest white line, the peak lift coefficient achieved increases as the wing becomes immersed in the jet. Below a critical vertical offset of the actuator disk, the jet passes below the wing and flap at the operating point (point A) and the realisable lift drops.

For the case where x_p/c=-0.5 in Fig. 4.18 (a), the peak lift augmentation occurs when the propeller centre is 0.3 chords below the wing and when the propeller diameter is around 0.2 of the chord. This results in a maximum lift augmentation of 3.2. For the case where x_p/c=-0.25 in Fig. 4.18 (b), the peak lift augmentation occurs when the propeller centre is 0.21 chords below the wing and the propeller diameter is around 0.2 of the chord. This results in a maximum lift augmentation of 3.4. When the thrust is fixed, there is an advantage to having small propellers located below the wing.

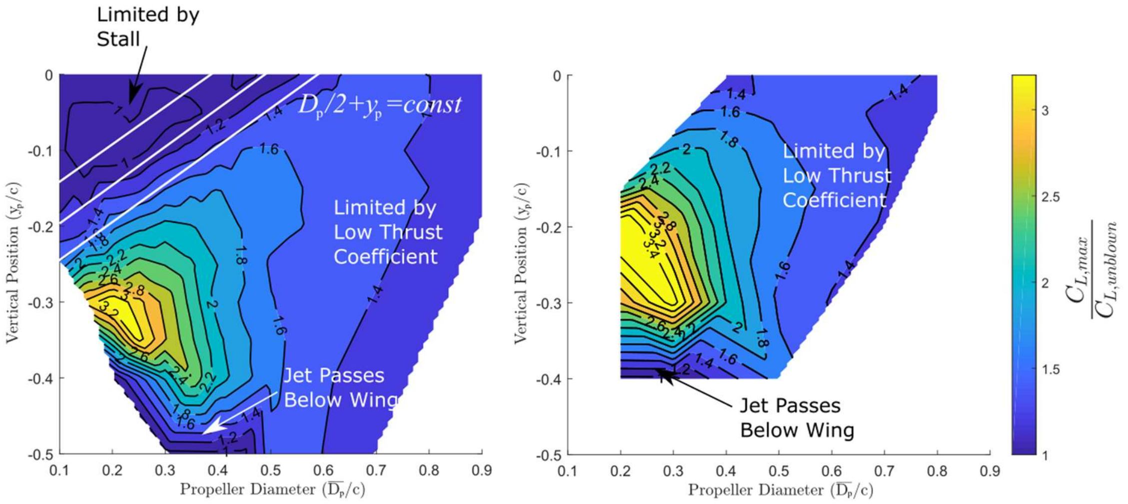

(a)

(b)

Figure 4.18: Plots of maximum achievable lift coefficient for blown wings with various combinations of propeller vertical offset y_p and propeller diameter, $\overline{D_p}$. Results for two streamwise positions of the propeller are shown x_p/c=-0.5 (a) and x_p/c=-0.25 (b).

The lift augmentation shown in Fig 4.18 will result in a reduction in wing size (and hence profile drag). Figure 4.19 shows the reduction in cruise profile drag for the two axial jet locations shown in Fig. 4.18 as a percentage of the cruise drag of the original unblown wing. It can be seen that in both cases the maximum cruise drag reduction of 50% is theoretically possible.

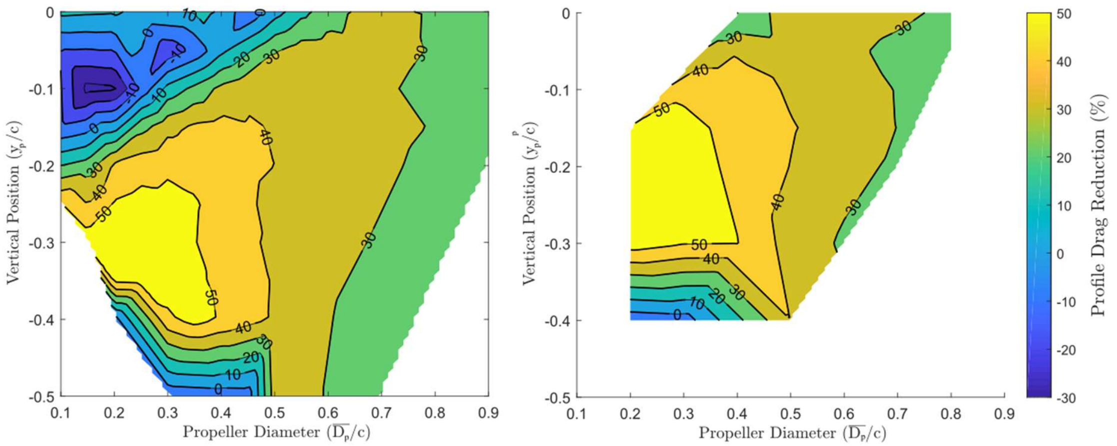

(a) (b)

Figure 4.19: Maximum wing profile drag reduction of a blown wing with varying jet size and location. Two actuator disk axial locations are shown: (a) x_p/c=-0.5 (a) and (b) x_p/c=-0.25.

4.7 Conclusions

The optimum blown wing geometry is shown in Fig. 4.20: the horizontal offset, x_p/c=-0.25, vertical offset y_p/c=-0.21, and mean propeller diameter $\overline{D_p}$/c=0.2. The use of a small propeller diameter allows fast jets to be used for a fixed landing thrust, increasing the lift augmentation. However, this chapter has identified that the wing must be fully immersed in the blowing jet to avoid premature stall. This is only possible by placing the propeller below the wing centreline, due to the up-wash of the wing. The maximum lift of a wing is increased by a factor of 3.4 when distributed blowing is employed along the wing leading edge, reducing the profile drag by 50%. The next 3 chapters aim to answer how much of this theoretical benefit is realisable for a practical blown wing system.

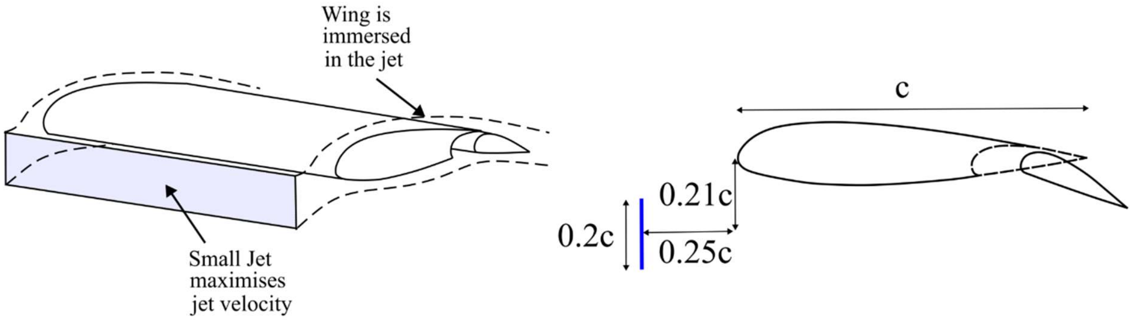

Figure 4.20: Schematic of the optimum geometry for blown lift. x_p/c=-0.25, y_p/c=-0.21 and $\overline{D_p}$/c=0.2.

5. Installation Drag

5.1 Introduction

The first question posed in this thesis is, by how much can the wing drag be reduced with a blown wing, and what geometry achieves this reduction? Chapter 4 showed that the best propeller jet to maximise lift, and minimise wing profile drag, is a small jet placed below the wing centreline. This does not account for the installation drag of the nacelles required to carry the propellers producing these jets, shown on the left of Fig. 5.1. In this chapter the effect of nacelle drag is quantified and it is shown that the nacelle drag, for the optimum geometry reported in Chapter 4, is substantial and offsets any benefit from incorporating a blown wing. A new optimum geometry is identified as a compromise between maximising the wing profile drag reduction, and minimising the nacelle drag, which does offer a net reduction in drag.

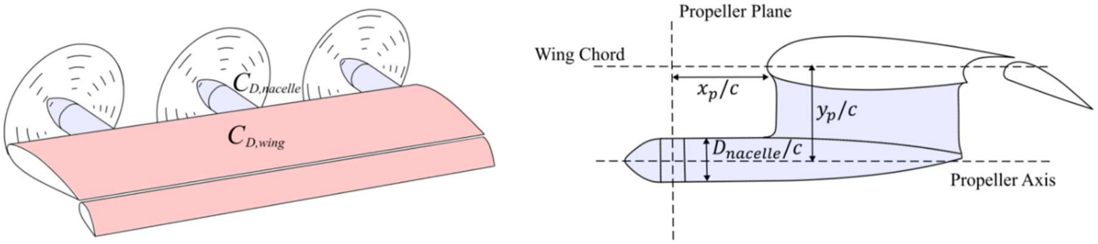

Figure 5.1: The contribution of the drag from blown wing nacelles is quantified in this chapter. The nacelle diameter, $D_{nacelle}$, horizontal offset of the nacelle, x_p and vertical offset, y_p are varied.

To quantify the nacelle drag contribution, an analytical drag build-up for each nacelle is developed. Experimental data is used to quantify the interference drag between the nacelle and wing which cannot be predicted from this analytical drag build-up. Three key nacelle geometry parameters are varied, the nacelle diameter, $D_{nacelle}$, horizontal offset of the nacelle, x_p and vertical offset, y_p as shown on the right of Fig. 5.1. The resulting model is used to quantify the nacelle drag contribution, and identify the new optimum geometry to minimise the total airframe drag, thereby answering the first question of this thesis.

5.2 The Impact of Installation Drag

In Chapter 4, we found that to maximise the performance of the blown wing, the jet should be small, and placed below the wing centreline. A graphical representation of the effect of moving in the design space on nacelle geometry is shown in Fig. 5.2. Moving left on the chart reduces the propeller size and therefore increases the number of propellers (and nacelles). This increases the total nacelle drag. Moving down on the chart moves the propeller below the wing, increasing the nacelle size. This also increases the total nacelle drag. The design for maximum lift (see previous chapter) and for minimum nacelle drag exist in opposite halves of the design space. A compromise geometry is required between these two extremes that minimises the system drag.

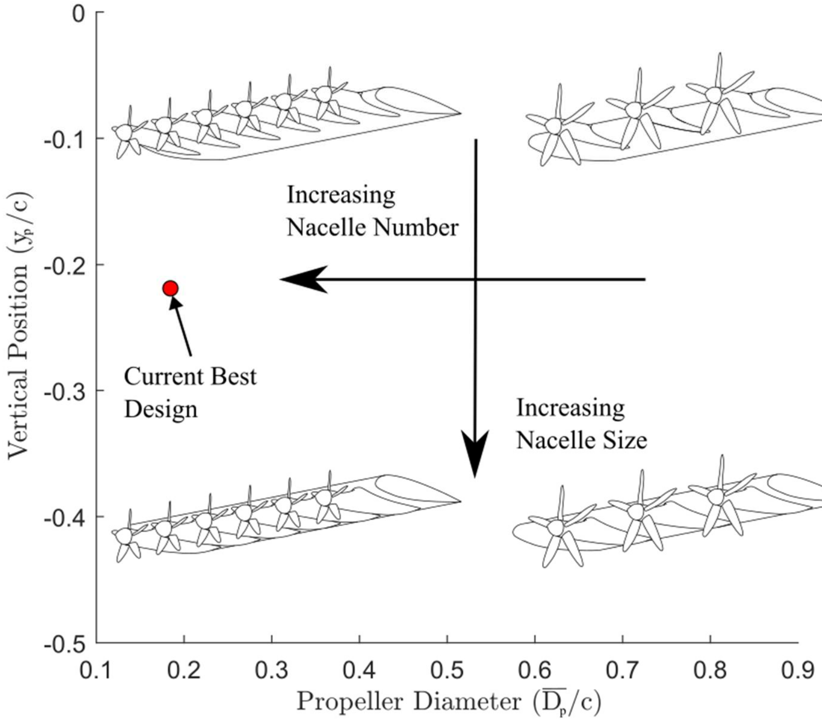

Figure 5.2: Blown wing geometries within the design space and their nacelle drags. The design for maximum lift, found in Chapter 4, coincides with a high nacelle drag region of the design space.

5.3 Experimental Nacelle Drag Measurements

To accurately measure the drag of each nacelle geometry, traverses were conducted with a rake traverse downstream of the wing within the experimental test rig. Details of the rake traverse, and the error analysis, are given in Chapter 3. Figure 5.3 shows the downstream wake total pressure measurements of the wing with nacelles fitted. Only half the wing span was measured.

Three cases are shown, a single nacelle mounted near the mid-span, three nacelles spread evenly over the span, and 6 nacelles mounted to the wing (the maximum number possible in the test rig). The section drag coefficient for each of these three cases is shown on the right of Fig. 5.3. The total drag coefficient of the nacelle and wing changes from 0.0284 to 0.0277 to 0.0270 as the number of nacelles is reduced, a 5% change which is within the experimental error of the measurement. The bottom two-thirds of the span, including the corner separation, was neglected in the analysis. Based on this result, it was deemed reasonable to measure a single nacelle wake when testing multiple nacelle geometries, and assume the nacelle-nacelle interaction is negligible. This was beneficial as it reduced, by a factor of 6, the cost of 3D printing the nacelles and time hand finishing and installing each one.

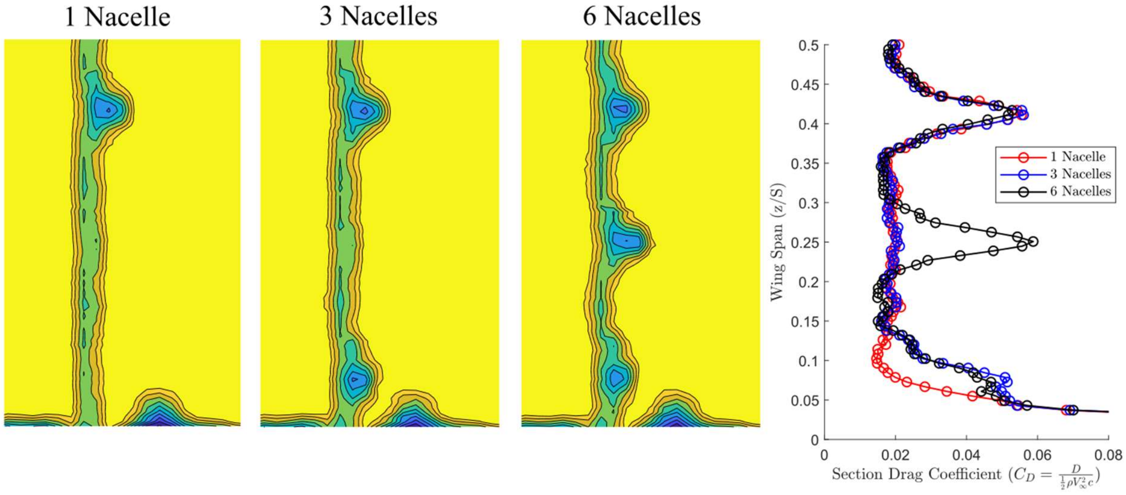

Figure 5.3: Measurements of the wake downstream of the wing for 1, 3 and 6 nacelles fitted to the wing. Half the span is shown. The nacelle geometry is x_p/c=-0.33, y_p/c=-0.1 and $D_{nacelle}$/c=0.146.

5.4 Nacelle Drag Analytical Build-up

The experimental test rig allows the drag coefficient of many nacelle geometries to be tested quickly. These results are presented in Sections 5.5 and 5.6. In order to understand the trends in this experimental drag data, and extend these trends to other designs not tested, an analytical drag build-up is first conducted in this section.

The total drag from the nacelles can be calculated as,

$$C_{D,nacelle} = N_P\left(C_{D,nacelle\ body} + C_{D,fairing} + C_{D,interference}\right) \quad , \quad (5.1)$$

where N_P is the number of propellers [37] and the drag terms are labelled in Fig. 5.4.

The drag from the nacelle can be split into three components, the drag of the nacelle body, the drag from the fairing and the interference drag. Interference drag exists between the nacelle body and the fairing, between the fairing and the wing, and between neighbouring nacelles. The nacelle body, whose geometry is dictated by both the horizontal position of the propeller, and the motor diameter, is treated as a body of revolution. The fairing, whose size is dictated by the propeller vertical offset, is modelled as a 2D extruded fairing section. The interference drag is unknown and will be measured experimentally in the next section [37].

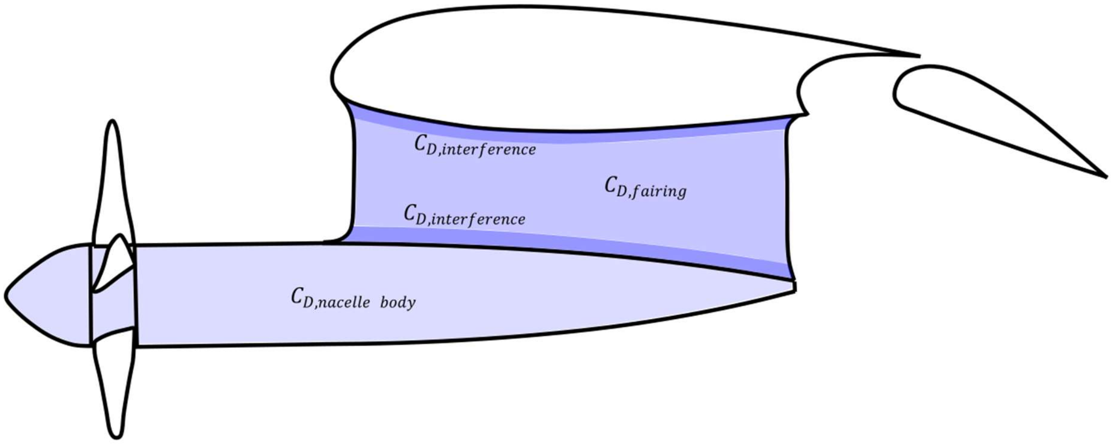

Figure 5.4: The sources of nacelle drag can be broken up into $C_{D,nacelle\ body}$, $C_{D,fairing}$ and $C_{D,interference}$ which accounts for distortion of the flow at the interface between components [37].

To model the nacelle body drag, a form factor drag model from Raymer [62] was used,

$$C_{D,nacelle\ body} = C_F FF_{body} \frac{S_{wet}}{S_{ref}} \quad , \quad (5.2)$$

where the form factor of each nacelle body is calculated from

$$FF_{body} = 1 + 0.0025(l/d) + \frac{60}{(l/d)^3} \quad . \quad (5.3)$$

In this calculation, S_{wet} is the wetted area of the nacelle body and S_{ref} is the wing area, A_{wing}. l/d is the aspect ratio of the body of rotation, in this case the nacelle length to diameter, $D_{nacelle}$ [37].

The second term in Eq. 5.1, the fairing drag, can be calculated from

$$C_{D,fairing} = C_{D,fairing,section} \frac{S_{wet,fairing}}{S_{ref}} \quad . \quad (5.4)$$

This drag contribution term arises from extending the nacelle to greater vertical offsets, y_p. Details of the fairing geometry used in this work are given in Appendix C, along with other parameters for the family of nacelle geometries used in this thesis. A constant, 2D, drag coefficient for the fairing section of $C_{D,fairing,section}$=0.026 was measured at the experimental Reynolds and Mach number. This coefficient can be scaled to other operating conditions by multiplying by the ratio of flat plate skin friction values, C_F, at the test rig and new operating points [37].

For nacelles far from the wing, as shown in Fig. 5.5 (a), the nacelle body wetted area can be calculated from

$$S_{wet,nacelle\ body} = \frac{\pi}{2\sqrt{2}} D_{nacelle}{}^2 + \pi D_{nacelle} x + \frac{\pi}{2} D_{nacelle} \sqrt{\frac{D_{nacelle}{}^2}{4} + c_{fairing}{}^2} \quad , \quad (5.5)$$

and the nacelle fairing wetted area can be calculated from

$$S_{wet,fairing} = \int (f(x) - y_{nacelle}) dx = c_{fairing} \bar{y} \quad , \quad (5.6)$$

where $f(x)$ defines the wing lower surface coordinates. For nacelles close to the wing, as shown in Fig. 5.5 (b), only a fraction of the nacelle surface area is exposed as the nacelle merges with the wing. For x-locations where the wing begins to merge with the nacelle, $y_{wing} < y_{nacelle}$, the fairing area is not calculated. The nacelle wetted area is then,

$$S_{wet,nacelle} = \int 2r(x) \cos^{-1}\left(\frac{f(x) - y}{r(x)}\right) dx \quad . \quad (5.7)$$

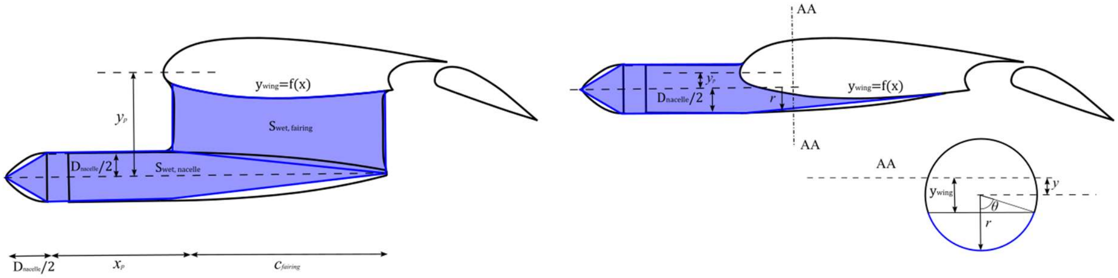

Figure 5.5: The geometry representation of the nacelle for calculating the nacelle body and fairing wetted areas.

A comparison between the real nacelle areas, measured from CAD drawings, and the modelled areas from Eq. 5.4-5.6 are shown in Fig. 5.6. The models are able to accurately capture the wetted area of the nacelles used in the experiment for different vertical offsets.

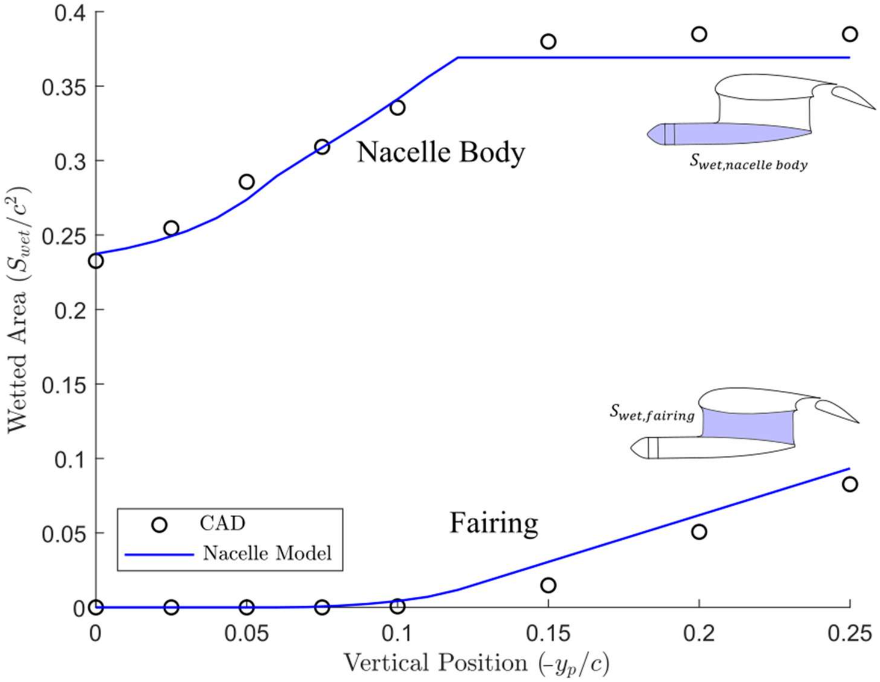

Figure 5.6: Nacelle wetted areas calculated from the low order model compared to the actual areas from CAD.

5.5 Experimental Prediction of Interference Drag

The previous section developed an analytical drag build-up of the nacelle body and fairing drag based on wetted areas and form factor models. We now consider the third term in Eq. 5.1, the interference drag. The interference drag is due to modifications of the flow-field at the nacelle-fairing-wing interfaces and cannot be easily predicted analytically. Through the use of CFD, Patterson [56] proposed the use of a factor of 1.3 to be applied to the nacelle body drag to account for the increased drag due to the modification of the flow field at the nacelle-wing interface. We are able to measure experimentally the drag contribution of the nacelle to the wake, ΔC_D. Figure 5.7 shows the experimentally measured nacelle drag (black line with circles), calculated nacelle body (dashed blue) and fairing drag (solid blue) for varying vertical offsets, y_p/c. The interference drag, shaded in blue, is the difference between the analytical drag build-up prediction, and the measured drag. The interference drag contributes 11.2% of the total drag at y_p/c=0 and 20.7% at y_p/c=-0.25.

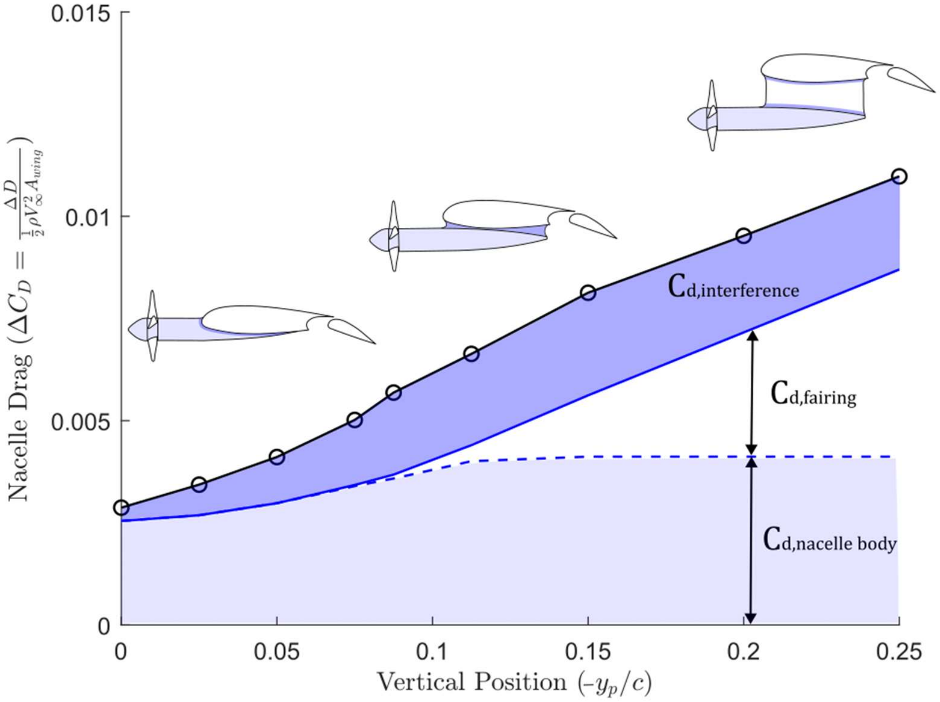

Figure 5.7: Drag decomposition for nacelles with different vertical positions, y_p/c, from the analytical drag build-up model of Section 5.4.

For small vertical offsets, the interference drag is purely due to the local change in flow-field around the nacelle body-wing joint, as there is no fairing. We assume the potential field of the wing is large compared to the nacelle body. As either the nacelle length increases, or the nacelle diameter increases, the reaction of the wing's potential field will therefore be negligible. However, the extra nacelle surface area leads to a greater boundary layer growth. It is this boundary layer which is distorted at the nacelle-wing interface. The interference drag for small vertical offsets of the nacelle will therefore scale with the drag of the nacelle body.

For large vertical offsets of the wing, beyond y_p/c=-0.08, the interference drag is constant, as seen from Fig. 5.7. The interference drag now consists of two terms: interaction at the wing-fairing joint, and interaction at the nacelle body-fairing joint. The fact that the interference drag remains constant for larger vertical offsets shows that the interference drag is not a function of the fairing's potential field, and the majority of the fairing experiences clean, 2D flow. Therefore, the drag at the nacelle-fairing joint will scale with the nacelle body drag as only the incoming boundary layer size changes the drag term. As the fairing is thin, we assume that the modification of the flow in the joint between the wing and fairing is small, and neglect the interference drag term here. If the fairing size was increased to be of a similar size and aspect ratio as the nacelle body in order to fit additional cabling, sensors, motor cooling systems etc., this assumption would not be valid.

Within the confines of the experiment, it is not possible to differentiate between the interference drag at the nacelle body and the interference drag at the wing, and so the assumption that the interference drag is proportional to the nacelle body drag is a necessary one to make progress with the low order model.

Figure 5.8 shows the measured interference drag for different vertical offsets for 3 different nacelle lengths, x_p/c=-0.33, -0.43 and -0.53 using the method shown in Fig. 5.7. The nacelle diameter, $D_{nacelle}/c$=0.142. Normalising the measured interference drag by the predicted nacelle body drag helps to collapse the data onto a single line, indicating the interference drag is primarily a function of nacelle body drag in each of the regions discussed.

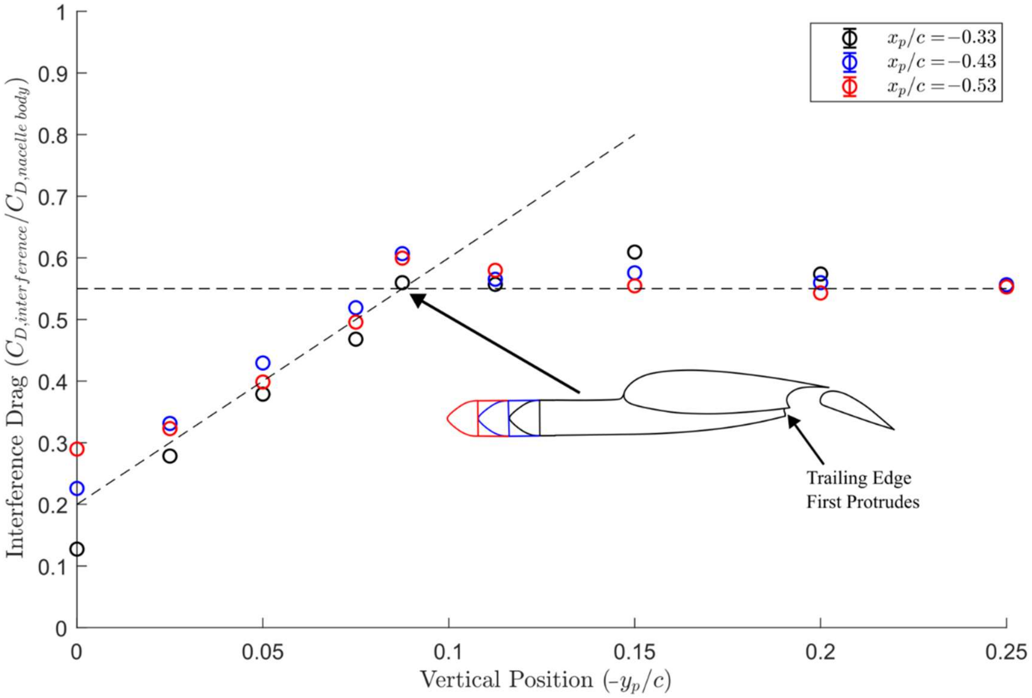

Figure 5.8: Interference drag prediction for 3 different nacelle lengths, x_p/c=-0.33, x_p/c=-0.43 and x_p/c=-0.53. For large vertical offsets, the interference drag is constant.

Two straight lines are found to fit through the measured data. For y_p/c<-0.875, the interference drag is 57% of the nacelle body drag with a root mean square error (RMSE) of 3.4%. For y_p/c>-0.875, a straight line, given by,

$$\frac{C_{interference}}{C_{D,nacelle\ body}} = \begin{cases} 4.23|y_p|/c + 0.2, & |y_p|/c < 0.0875 \\ 1.57, & |y_p|/c \geq 0.0875 \end{cases} \quad . \tag{5.8}$$

fits the data with a RMSE of 18%. The high error is caused by the spread in the data at y_p/c=0. If the data at y_p/c=0 is removed, the RMSE drops to 6.3%. The intersection at y_p/c=-0.875 coincides with the vertical position below which the nacelle trailing edge first protrudes from the wing. This is the point at which the nacelle fairing is first required. The flow-field in this transitional region between the two geometries is complex and the assumptions made to estimate the interference drag are likely to break down.

5.6 Nacelle Drag Model Prediction

Figure 5.9 shows the nacelle drag estimate using the method outlined in Eq. 5.1-5.8, and experimental traverse drag measurements for nacelles with 3 different nacelle lengths, x_p/c=-0.33, x_p/c=-0.43 and x_p/c=-0.53 at a range of vertical offsets, y_p/c. The diameter, $D_{nacelle}/c$=0.146. This data was used in the previous section to estimate the interference drag term. As a result, the model correctly predicts the drag over the full range of nacelles tested. Error bars for the drag measurements are included in the figure. Details of the error analysis can be found in Chapter 3.

Comparison of the predicted and experimental nacelle drag for three different nacelle diameters, $D_{nacelle}/c$=0.0731, $D_{nacelle}/c$=0.146 and $D_{nacelle}/c$=0.219 is shown in Fig. 5.10 for x_p/c=-0.33 and a range of vertical offsets. For the two smaller diameters, the model is able to correctly capture the change in nacelle drag, including the reduction in drag as the nacelle merges with the wing. For the larger nacelle diameter, $D_{nacelle}/c$=0.219, the model over-predicts the drag by up to 18%. This is to be expected as the assumptions made in the model that the nacelle aspect ratio is large and that the wing potential field is unaffected by the nacelle will break down. As the nacelle body moves away from the wing to y_p/c=-0.2, the error reduces to 4.6%, indicating that the bulk of the error is due to the change in potential field, impacting the interference drag, rather than a breakdown in Raymer's model for the form factor. An empirical drag model is presented in Appendix E for $D_{nacelle}/c$>0.146.

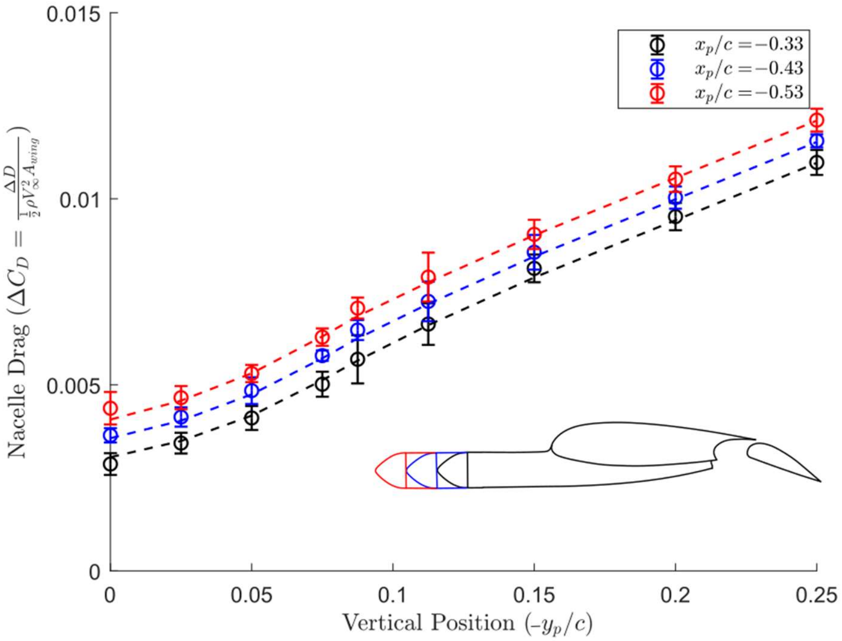

Figure 5.9: Nacelle drag predicted for 3 different nacelle lengths, x_p/c=-0.33, x_p/c=-0.43 and x_p/c=-0.53 over a range of vertical offsets y_p/c. The diameter, $D_{nacelle}/c$=0.146. Experimental data, including measured errors are overlaid.

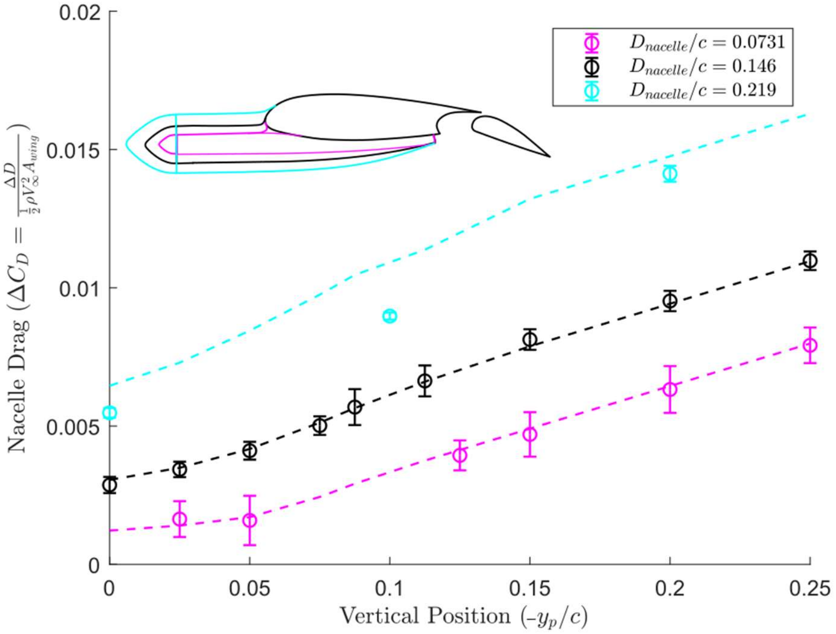

Figure 5.10: Nacelle drag predicted for 3 different nacelle dimeters, $D_{nacelle}/c$=0.0731, $D_{nacelle}/c$=0.146 and $D_{nacelle}/c$=0.219. x_p/c=-0.33. Experimental data, including measured errors are overlaid.

5.7 Effect of Nacelle Drag on the Design Space

In the previous sections, a model for the nacelle drag has been developed which can predict the nacelle drag contribution for different horizontal and vertical positions of the propeller $(x_p/c,\ y_p/c)$ and nacelle diameter, $D_{nacelle}/c$. In this section, we use this model to quantify the impact of nacelle drag for the blown wing design space explored in Chapter 4.

To determine the nacelle geometry at each point in the design space, we assume the diameter of the nacelle, $D_{nacelle}$, is taken as 20% larger than the minimum motor diameter required for blowing, to account for cooling and structural design. The motor power is estimated from the minimum induced loss propeller code, described in Chapter 3, which calculates the power requirements of each blowing propeller for the operating thrust coefficient and correlates this continuous power requirement with current motor technology [39] assuming a linear scaling for the power and torque with volume. Nacelle body lengths are estimated from the prescribed axial position of the propeller. The flat plate skin friction coefficient, C_F, is estimated from the aircraft cruise conditions included in Table 3.2. The nacelle number is calculated from the propeller diameter, D_p, taken from the 2D actuator disk jet height $\overline{D_p}$ using the method described in Chapter 6. The propellers are assumed to cover the full blown wing span with no gaps between propellers.

Figure 5.11 shows the blown wing design space plots of Chapter 4, with the nacelle drag contribution included in the total drag prediction. By including the nacelles, the drag reduction possible with a blown wing has dropped from 50% to 29.3%. For x_p/c=-0.5, shown in Fig. 5.11 (a), a single peak exists at y_p/c=0 and $\overline{D_p}/c$=0.7. The drag reduction is 22.4%. For x_p/c=-0.25, shown in Fig. 5.11 (b), a double peak exists at y_p/c=0 and -0.07 with mean jet diameters of $\overline{D_p}/c$=0.5 and 0.39 respectively; the drag reduction is 26.4% and 29.3%. The benefit of reduced wing area which is achieved by moving to the bottom left of the figure is greater than the penalty of increased nacelle drag in this region. For x_p/c=-0.25, the nacelle drag is lower as the nacelle is shorter, and the blowing benefit is greater as the wing is fully immersed in the jet up to higher incidences with smaller vertical offsets according to Eq. 4.3. Regions of the design space where the nacelle diameter, $D_{nacelle}/c$>0.146 have been faded out as the model is known to be less accurate in this region. These regions are not near the optimal operating points for either horizontal offset, so this does not impact the accuracy in this analysis.

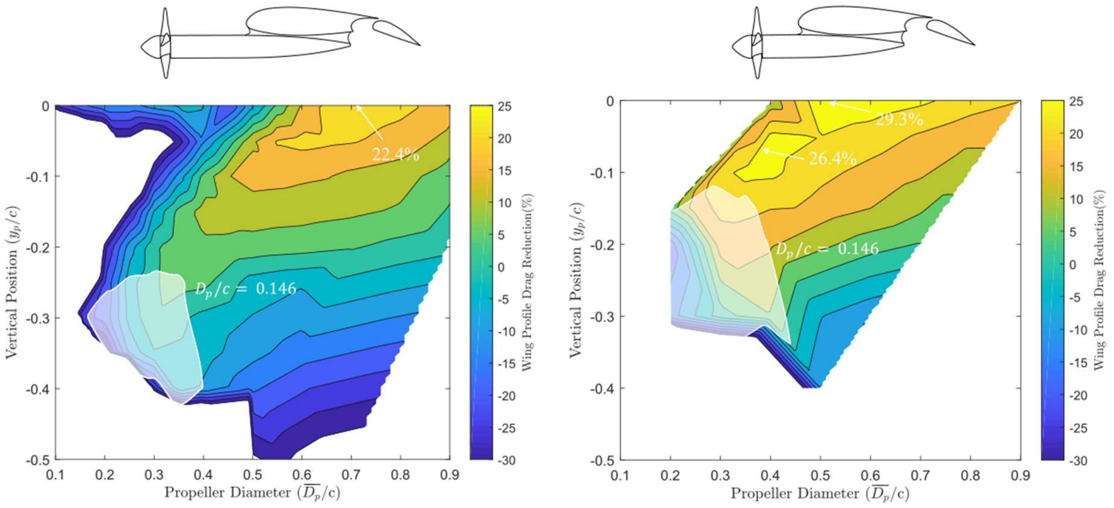

(a) (b)

Figure 5.11: Overall wing profile drag reductions possible with a blown wing including installation drag for x_p/c=-0.5 (a) and x_p/c=-0.25 (b). A 22.4% reduction in profile drag is possible for x_p/c=-0.5 and 29.3% for x_p/c=-0.25 due to the reduced wetted area of the nacelle.

This section shows that the optimum blown wing design to reduce wing drag, if you include the effect of the nacelle drag contribution, is a jet with a horizontal offset of x_p/c=-0.25, no vertical offset, y_p/c=0, and a jet height of $\overline{D_p}/c$=0.5. This geometry allows the non-linear reduction in nacelle drag for small offsets to be exploited, ensure the wing is still fully immersed in the jet to maximise wing lift, and reduce the nacelle horizontal offset, reducing its drag contribution. An average jet height of $\overline{D_p}/c$=0.5 gives a propeller diameter, D_p/c = 0.64 (see Chapter 6).

5.8 Off-Design Performance of the Nacelle

The nacelle drag model has been developed for an angle of attack of 0°. During operation the incidence onto the nacelle will vary. In practice this requires the drag of the nacelle to be independent of incidence up to 8°. This equates to wing lift increases of a factor of 2. In this section the angle of attack of the wing will be varied. Figure 5.12 shows the experimentally measured load cell lift and drag coefficients for the clean wing, and with 6 nacelles attached with geometries y_p/c=-0.05 and -0.2, x_p/c=-0.33 and $D_{nacelle}/c$=0.146. The drag plot, shown in Fig. 5.12 (b) confirms that it is appropriate to use the on-design nacelle drag model at incidences of up to 8°. Beyond this wing angle, the drag of the nacelle begins to rise.

For y_p/c=-0.05, the lift of the wing with nacelles attached, shown in Fig. 5.12 (a), is increased by 0.08 pre-stall. However, the stall of the wing is sharp and brought forward to a wing angle of 11° from the unblown wing stall angle of 17°. It is likely that small nacelle vertical offsets will be used for their low drag properties and this reduction in operational range is a penalty which the aircraft designer would need to consider. It is likely that the nacelle is acting as an additional lifting body, and stalls at 11°. In the range 11° to 15°, lift of the wing is approximately equal to the unblown case. Beyond this angle, the whole wing stalls.

For y_p/c=-0.2, the lift curve slope of the wing with nacelles attached is reduced, compared to the unblown wing, by 7.8%. However, the wing stall is delayed by 2.5° compared to the unblown wing, possibly due to the reduced circulation of the wing-nacelle combination. Beyond a wing angle of 7.5°, the nacelle drag for y_p/c=-0.05 is greater than that for y_p/c=-0.2, despite the nacelle having a lower wetted area, due to the adverse effects of the nacelle on the wing performance.

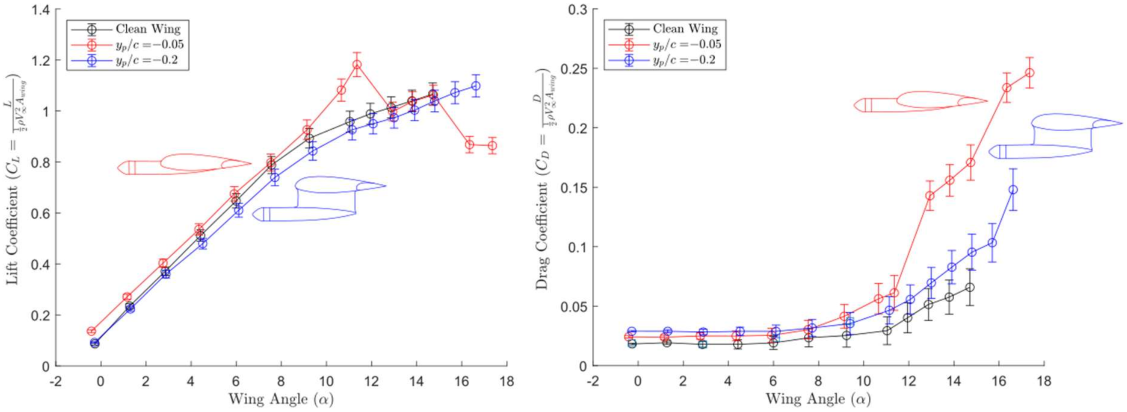

(a) (b)

Figure 5.12: Off-design performance of selected nacelles measured from load cells in the test rig. Geometries y_p/c=-0.05 (a) and y_p/c=-0.2 in (b). Moving the nacelle down below the wing centreline increases drag at low angles of attack but delays wing stall, decreasing the drag contribution at high angles of attack.

5.9 Conclusions

The optimum blown wing geometry for minimum drag, when the nacelle drag contribution is included, is a horizontal offset of the jet of x_p/c=-0.25, no vertical offset, y_p/c=0, and a jet height of $\overline{D_p}/c$=0.5. An average jet height of $\overline{D_p}/c$=0.5 gives a propeller diameter, $D_p/c = 0.64$. This geometry is shown in Fig. 5.13. This geometry is a compromise between the ideal geometry for minimum wing drag, found in Chapter 4, and the nacelle drag penalty of many small propellers placed far below the wing centreline. A 29.3% reduction in wing drag can be achieved with this blown wing geometry. The modelling in this chapter focuses on the aerodynamic drag increase due to the presence of the nacelles and does not account for weight changes of the airframe. Increasing the number of propulsors on the wing will likely increase the airframe weight (due to the installation of multiple motors and nacelles), and hence the overall drag of the aircraft due to the larger wing area required. Airframe weight penalties are considered in Chapter 8.7.

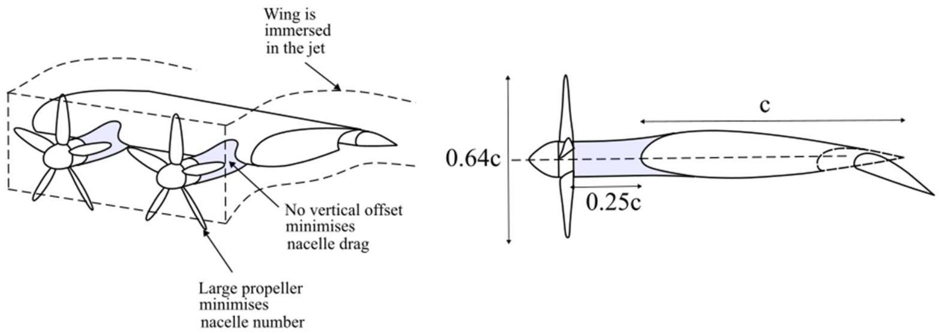

Figure 5.13: Modelling the nacelles changes the optimum design for minimum drag (note equivalent propellers shown instead of the 2D jet model). The impact of the nacelle drag leads to designs with smaller horizontal and vertical offsets of the propeller, with large diameters to reduce the number of nacelles.

6. Real Propulsor Effects On-Design

6.1 Introduction

In this chapter, we answer the question: what are the limitations of 2-dimensional actuator disk modelling for a blown wing and by how much does the performance prediction change as the blown wing model fidelity is systematically increased from 2D modelling to experiment? The results of Chapter 4 relied on the use of 2D actuator disk calculations. 2D actuator disk calculations allow the first order impact of propeller location and diameter to be quickly established; however, they assume that neighbouring jets merge upstream of the wing, ignore the effect of jet swirl and are unable to account for large propeller spacings. In this chapter, the effect of real propulsor jets and spacing is introduced into the modelling, as shown in Fig. 6.1. A combination of a 2D blown wing model, 3D actuator disk CFD, and the experimental test rig are used. We focus on the wing away from stall in this chapter. The stall behaviour is discussed in Chapter 7.

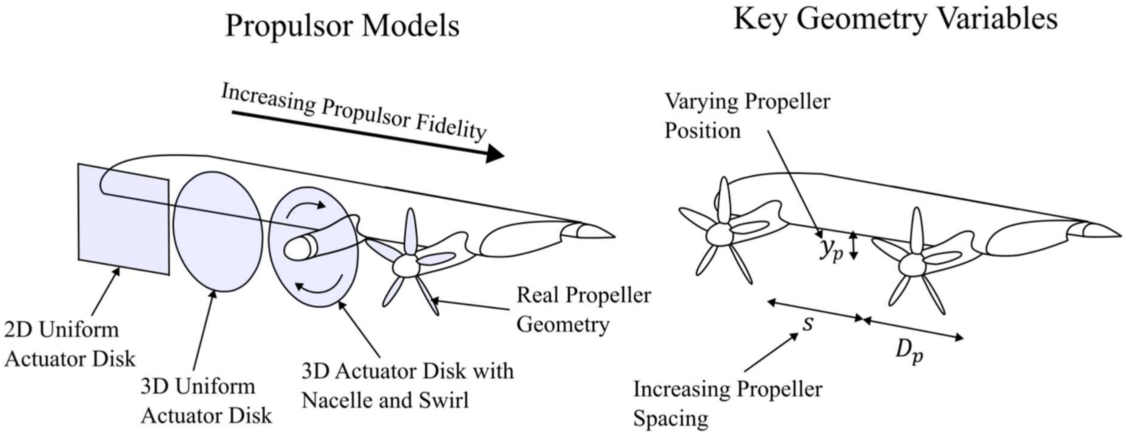

Figure 6.1: Model parameters studied in this chapter. The performance of the blown wing on-design is established using a combination of different fidelities of actuator disk modelling and an experimental test rig [37].

The results of Chapter 5 show that nacelle drag is significant for a blown wing. We are therefore motivated to find blown wing designs with high lift, but low nacelle drag impact. Increasing the spacing between adjacent propellers reduces the number of nacelles, and therefore reduces the nacelle drag contribution. Moving from a 2D actuator disk model to 3D modelling allows the effect of propeller spacing to be quantified. The second half of this chapter investigates the effect of propeller spacing and finds that high lift, and therefore low profile drag, can still be achieved with fewer, more highly loaded propellers.

6.2 Systematic Build-up of the Propulsor Model

In this first results section, the propulsor modelling is systematically built up from a circular jet to a swirling jet with a nacelle and finally a real propeller is tested in the experiment. Each of the 3D cases presented in this section has a propeller spacing, s/D_p =0.05. This was done due to meshing issues in the gap for the CFD modelling, and due to concerns of propeller tip contact in the experiment. Each 3D case is compared to the 2D actuator disk approach used in Chapters 4 and 5. To account for the small propeller spacing, a model is developed in Appendix F to account for the reduction in lift and drag with spacing when using 2D simulations. Use of the model requires the 2D calculation to have a jet height equal to,

$$\overline{D_p} = \frac{\pi}{4} D_p \ , \quad (6.1)$$

where D_p is the propeller diameter. This average jet diameter, $\overline{D_p}$, is called the mean jet height. The derivation of this mean jet height is included in Appendix F, and was used previously in Chapter 5 to calculate the propeller diameter for a given 2D Actuator disk calculation.

6.2.1 The Effect of Circular Jets

Figure 6.2 shows the variation in the spanwise wing loading with a uniform circular jet placed upstream of the wing, as well as the 2D model. The wing loading varies by 2.8% about the mean for the 3D actuator disk. It was shown in Chapter 4 that decreasing the jet height reduces the lift of the wing for a fixed thrust coefficient, due to the reduced momentum of the jet. A 2D view of the wing immersed in a circular jet suggests the wing loading should vary along the span, due to the changing jet height of the circular jet. In this case, variations of up to 71% (the difference between the mean lift and the unblown value) would be expected. The fact that the wing section lift varies by only 2.8% suggests the pressure field around the wing is unable to react to the spanwise variation in jet momentum, as the local jet height varies, and instead reacts to the averaged momentum of the jet, producing a “smeared” 2D loading on the wing surface.

The ability of the wing to locally react to the changing jet height will scale with D_p/c. In the limit as D_p/c becomes large, the wing will react to the “local jet height” momentum, varying between the 2D lift coefficient for $\overline{D_p}/c$=0.5 at the jet centre, and the unblown wing at the jet edge. The small variation in lift along the span suggests that the 3D problem can be modelled with a single 2D calculation with the correct choice of jet height.

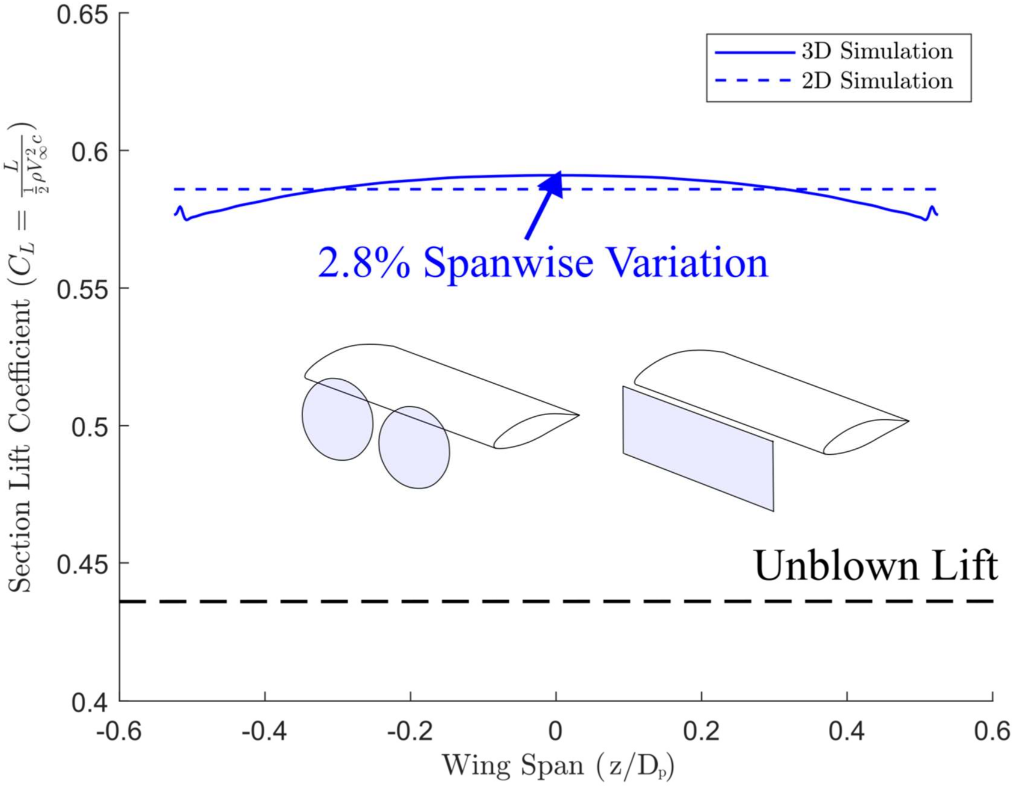

Figure 6.2: Comparison of the 3D spanwise loading, and the 2D approach to modelling the blown wing lift. The wing is at an angle of attack of 3°, the actuator disk is placed at x_p/c=-0.33, and y_p/c=-0.05. The diameter, D_p/c=0.5 and the thrust coefficient, T_c=1. A propeller spacing of s/D_p=0.05 has been used. The diameter of the 2D actuator model is $\overline{D_p}/c$=0.39.

Next we consider the spanwise variation in the drag coefficient. The drag has been calculated from integrating the pressure and shear stresses on the wing surface for the 3D simulation, and the thrust from the actuator disk is neglected. The results show the combined parasitic and induced drag contributions of each 2D section along the wing span to the total drag. The section drag coefficient is plotted in Fig. 6.3. When spanwise averaging the drag coefficient, we get a mean drag coefficient of 0.0398 for the 3D case, with a maximum 74% variation along the span. The largest variations from the mean occurs at the jet edge.

The 2D jet model of Chapter 4 does not include a correct model for the vorticity produced in the jet edge shear layer. For a 2D simulation, the vorticity consists of two semi-infinite planar sheets that pass above and below the wing. In 3D, the vorticity consists of cylindrical sheets, shown schematically at the top of Fig. 6.3. The wing stops the passage of these vorticity sheets downstream, leading to the production of secondary flows around the wing. A pair of vortices form which roll up at the intersection between neighbouring jets, both above and below the wing. Initially, the induced velocity fields of the vortices cause them to move towards one another in the spanwise direction, then upwards away from the wing surface. The large spanwise variations in wing drag occur because of the vorticity in the shear layer modifying the boundary layer.

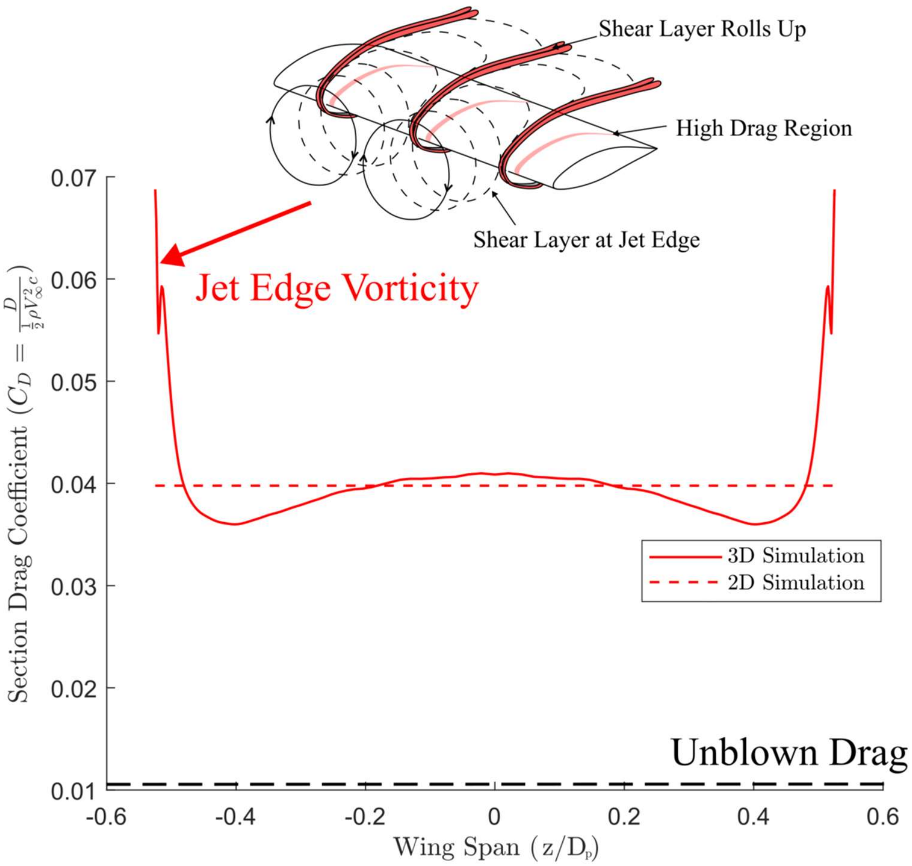

Figure 6.3: Comparison of the real 3D spanwise drag (both induced and profile drag contributions), and the 2D approach to modelling the blown wing drag. The wing is at an angle of attack of 3°, the actuator disk is placed at x_p/c=-0.33, and y_p/c=-0.05. The diameter, D_p/c=0.5 and the thrust coefficient, T_c=1. A propeller spacing of s$/D_p$=0.05 has been used. The diameter of the 2D actuator model is $\overline{D_p}/c$=0.39.

We next investigate the agreement between the 2D and 3D approaches over a range of incidences. The lift and drag plots for both 3D CFD simulations, and 2D CFD simulations, are shown for varying angles of attack and no flap deployed in Fig. 6.4. The thrust coefficient, T_c=1. The 3D diameter, D_p/c=0.5, spacing s/D_p=0.05 and horizontal offset, x_p/c=0.33. Two vertical offsets, y_p/c=-0.05 and y_p/c=-0.2 are plotted in red and blue respectively. The 2D mean jet height is $\overline{D_p}/c$=0.39.

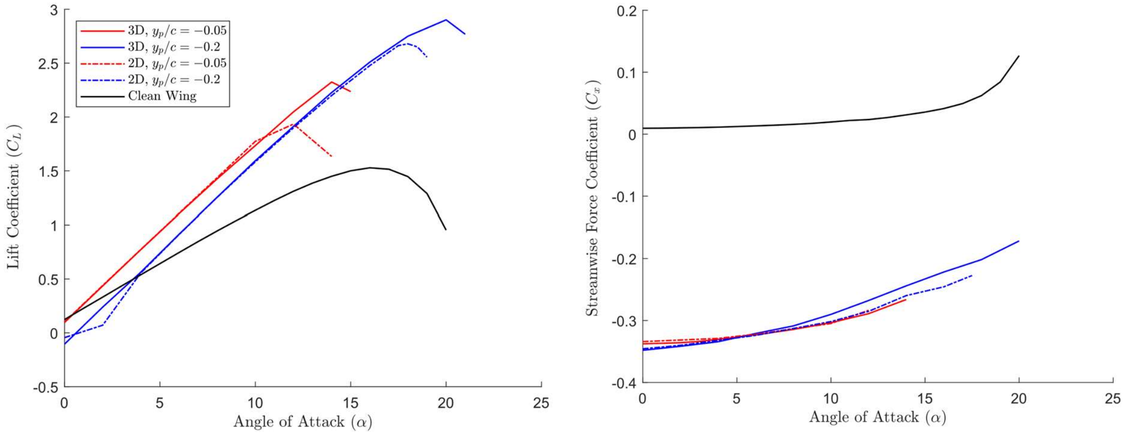

(a) (b)

Figure 6.4: Lift (a) and drag (b) polars for no flap deployment comparing the 2D and 3D approach to modelling the wing lift. Two vertical offsets, y_p/c=-0.05 and y_p/c=-0.2 are shown.

For the actuator disk positioned at y_p/c=-0.05, the lift coefficients agree to within 2.3% up to an angle of attack of 10°, and the streamwise force coefficients agree to within 0.46%. Whilst the drag is not well predicted by the 2D model, the streamwise forces are dominated by the actuator disk thrust which is equal between the simulations, leading to the small error. Beyond 10°, the 2D case begins to stall whilst the 3D case continues to generate lift up to 14°. For both the 2D and 3D cases, the wing stalls when the jet first passes above the wing suction surface. However, whilst the 2D case has a diameter of $\pi D_p/4$, the equivalent 3D jet height is greater than this value for 62% of the span. This greater jet height, as discussed in Chapter 4, enables the wing to remain un-stalled up to higher incidences. For the actuator disk positioned at y_p/c=-0.2, the lift at low angles of attack is poorly captured as the jet from the 2D case passes below the wing at these angles, whilst for 3D, the jet height at the centre of the disk is greater than the 2D average, meaning that some jet immersion is achieved. At 4° angle of attack, the 2D case has sufficient wing circulation to pull the jet over the wing suction surface, allowing better agreement between 2D and 3D to be achieved. Between angles of 4° and 17.5°, the lift coefficient agrees to within 1.3%. Up to an angle of 14°, the streamwise forces agree to within

6.6% but begin to diverge above this angle as the wing begins to stall. The key takeaway from Fig. 6.4 is that for on-design performance, the 2D mean diameter approach is accurate at predicting the averaged lift and drag coefficient of the wing.

We now consider the same wing and actuator disk geometries, but with a deployed flap. The wing angle for these cases is 3°. As with the no-flap case, the 2D simulation is able to predict the averaged lift and drag coefficient of the wing for different flap deployments, as shown in Fig. 6.5. Issues with mesh quality in the gap between the main wing and the flap lead to amplification of non-uniformities in the flow-field around the edge of the jet as it is convected downstream onto the flap. These non-uniformities lead to the kinks in the lift curves beyond ϕ=20° and a possible premature stall of the 3D cases. For the actuator disk positioned at y_p/c=-0.05, the lift coefficients agree to within 2.8% up to ϕ=20°, and the streamwise force coefficients agree to within 1.2%. For the actuator disk positioned at y_p/c=-0.2, the lift coefficients agree to within 4.4% and the streamwise force agrees to within 4.9%.

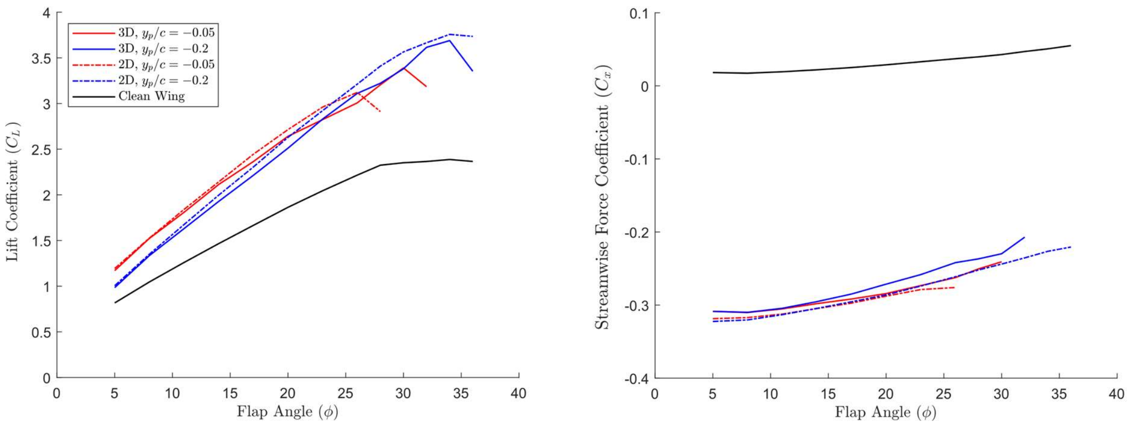

(a) (b)

Figure 6.5: Lift (a) and drag (b) polars for flap deployment comparing the 2D and 3D methodology. Two vertical offsets, y_p/c=-0.05 and y_p/c=-0.2 are shown.

Whilst the 2D model performs better with no flap deployment, for preliminary design, agreement to within 5% with flaps deployed is still useful to the designer for predicting performance.

6.2.2 The Effect of Jet Non-Uniformities

Thus far, we have only considered a uniformly loaded jet. In practice, the jet will have 3 sources of non-uniformity. First, there will be a non-uniform thrust profile along the propeller blade, with peak loading typically around 75% span, and no loading at the tip. Second, swirl will be imparted on the flow, assuming no flow straightening devices are used, and this will change the incidence locally onto the wing. Finally, as discussed extensively in Chapter 5, a nacelle is required to mount the propeller. The nacelle body will interact with the jet downstream of the propeller. In this section we examine how these 3D effects change the lift of the wing.

The input actuator disk body forces used in this section are described in Chapter 3. We consider three cases in this chapter, the uniform actuator disk with no nacelle, the uniform actuator disk with a nacelle, and a non-uniform co-rotating swirling actuator disk with a nacelle. Figure 6.6 shows the last of these 3 cases for an angle of attack of 4° and no flap deployment. Consider first the right of the figure. Plotted are the suction surface pressure and surface streamlines. With a nacelle, the actuator disk jet has two boundaries: the outer edge, and an inner edge at the nacelle where the disk loading drops to zero in the Goldstein model. The secondary flows due to the outer edge are labelled on the figure. Due to the presence of the swirl, the secondary flows migrate from the up-wash to the down-wash region. In addition to the secondary flow vortices due to the outer edge, vortices are generated at the inner edge near the nacelle wing junction. The main body of the jet rotates due to the swirl, producing another separation line on the wing surface which merges with the secondary flows at the jet inner edge.

The total pressure and pitch angle of the flow are plotted in the bottom left of Fig. 6.6 at a cut section with streamwise position x/c =-0.25. Regions of low total pressure exist at the centre of the jet due to the reduced thrust at the propeller hub. The average pitch angle is positive due to the upwash from the wing. The pitch angle varies about the average upwash angle by 25° along the span. Based on the lift curve slopes of Fig. 6.4, this variation in incidence should lead to a difference in spanwise lift coefficient of ~4. However, the spanwise lift coefficient actually varies between 0.64 and 0.86 about an average of 0.76, a difference of 0.22. This variation in lift coefficient would be explained by a difference in incidence along the span of 1.3°. As with the uniform jet, the pressure field of the wing is unable to react to the locally varying inlet conditions produced by the jet, and a "smeared" average wing loading is produced which only partially reacts to the spanwise distribution. The key determiner of the wing lift is still the bulk momentum of the jet, and not its local velocity distribution.

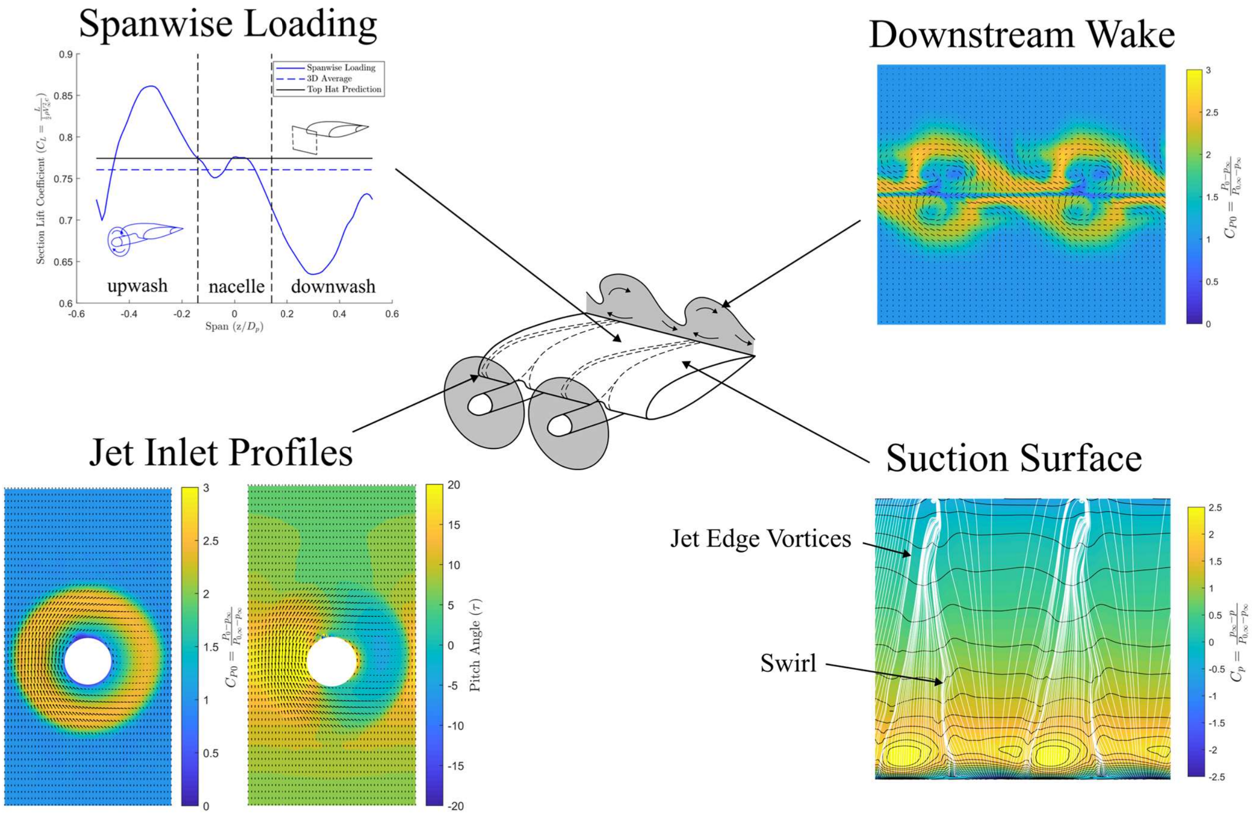

Figure 6.6: Plots of the flowfield upstream, downstream and on the surface of the wing for a swirling actuator disk jet. The spanwise loading is also plotted. The swirl of the jet leads to local areas of high and low wing loading. However, whilst the swirl varies by 20° between the upwash and downwash regions, the lift coefficient only varies by 29%, which would be caused by an angle of attack change of 1.3°.

The observation that the wing is unable to react to the local incidence of the swirling jet indicates that the 2D actuator model may also be applicable for these flows. The lift coefficients for y_p/c=-0.05 (Fig. 6.7 (a)) and y_p/c=-0.2 (Fig. 6.7 (b)) are shown overlaid for the different actuator disk inputs modelled in this section. We first consider the case y_p/c=-0.05. With the nacelle included in the model, the lift curve slope increases by 6.1%. This effect, where the nacelle acts as an additional lifting body, was observed in the previous chapter. Adding swirl to the jet further increases the lift curve slope by 5% up to an angle of attack of 10° before the graph kinks. In this initial linear region, the 2D model is able to capture the lift coefficient to within 0.1. Beyond this wing angle, the 2D model begins to stall. For y_p/c=-0.2, adding the nacelle reduces the lift coefficient of the wing by 0.08, but maintains the lift curve slope. Up to an angle of attack of 15°, the presence of swirl alters the lift coefficient by up to 0.06. For both vertical offsets, the presence of swirl extends the operating range of the wing. The additional incidence range due to swirl could not be explained and requires further research.

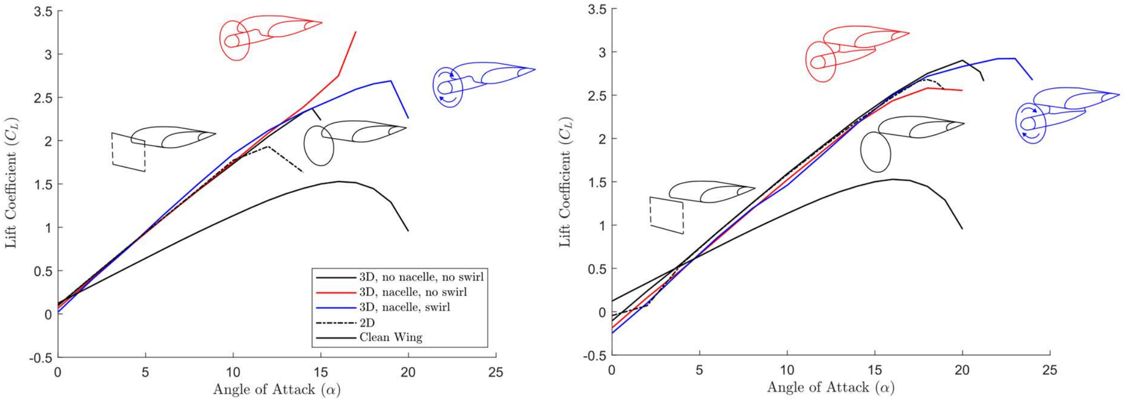

(a)

(b)

Figure 6.7: Lift coefficients for y_p/c=-0.05 (a) and for y_p/c=-0.2 (b) at different angles of attack for different fidelities of actuator disk modelling. The flap is not deployed in these simulations.

Fig 6.8 shows lift curves for different flap angles at y_p/c=-0.05 (Fig. 6.8 (a)) and y_p/c=-0.2 (Fig. 6.8 (b)). Again we first consider the case y_p/c=-0.05. The kinks in the curve due to mesh quality, observed for a 3D jet with no nacelle, also occurs for the case with a nacelle beyond a flap angle of 20°. Prior to this angle, the nacelle changes the lift coefficient by ±0.015, a 1.2% discrepancy at the smallest lift coefficient calculated. Adding swirl to the flow increases the lift coefficient by 0.06 and the 2D model is able to capture the 3D lift coefficient with swirl to within 0.018. For y_p/c=-0.2, adding the nacelle reduces the lift coefficient by 0.02, whilst the addition of swirl increases the lift by 0.08 up to a flap angle of 20°. The discrepancy between the 2D model and 3D CFD with swirl increases from 0.02 at 8° flap deployment to 0.12 at 20° flap deployment: errors of 1.5% and 4.8% respectively. As with the angle of attack sweeps shown in Fig. 6.8, the presence of swirl extends the incidence range of the flap for y_p/c=-0.2. The increase in maximum lift coefficient for the y_p/c=-0.2 geometry with swirl modelled is particularly noticeable. It is not known why the flap is able to be deployed to higher incidences without stalling, and requires further research. It is likely that the y_p/c=-0.2 geometry without swirl modelled is stalling prematurely due to the non-uniformities described in Section 6.2.1 and the increased stall angle of the swirl case compared to the 2D model can be partially explained by the greater maximum jet height in the 3D geometry.

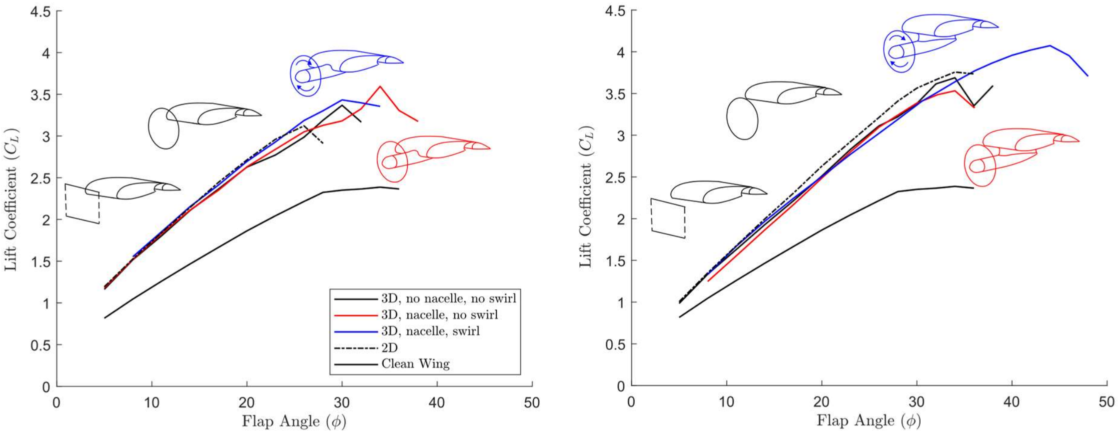

Figure 6.8: Lift coefficients for y_p/c=-0.05 (a) and for y_p/c=-0.2 (b) at different flap angles for different fidelities of actuator disk modelling. The wing angle of attack is 3°.

The key take-away from the build-up of CFD complexity is that the primary levers the designer can pull with blown wing design are the propeller jet location, size and thrust: topics explored already in Chapter 4. The profile of the jet, and the presence of obstructions such as the nacelle have only a second order effect on the on-design blown wing lift, the details of which can be delayed to the detailed design phase. For the preliminary design phase, a 2D model is sufficient.

6.2.3 The Effect of Real Propeller Geometry

To validate the 2D model for on-design performance, we compare the 2D model to experimental data from the test rig. For angle of attack sweeps, the test rig data is compared to 2D CFD predictions at the test rig Reynolds number. For flap angle sweeps, the test rig data is corrected for Reynolds number effects to the aircraft Reynolds number using the method outlined in Chapter 3. The 3D CFD with swirl is also shown for reference.

Good agreement between the 2D model and experiment is found for angle of attack sweeps, as shown in Fig. 6.9. For the case y_p/c=-0.05, the lift coefficient from the experiment is 0.1 greater than the 2D model at the same Reynolds number at 9°, a 6.5% error. Beyond this point the 2D wing begins to stall whilst both the 3D CFD simulation and experimental lift increase. The 2D model under predicts the 3D CFD with swirl by 0.07. For the case y_p/c=-0.2, the lift from the experiment is lower than the 2D model by 0.08 at an angle of 12°. At this angle, the 2D model over predicts the 3D CFD with swirl lift by 0.12. The difference between the experiment and the 2D model amounts to a less than 7% error across the design range. For larger angles of attack, the experimental lift no longer agrees with the CFD, possibly due to the greater thickening of the wing boundary layer in the experiment.

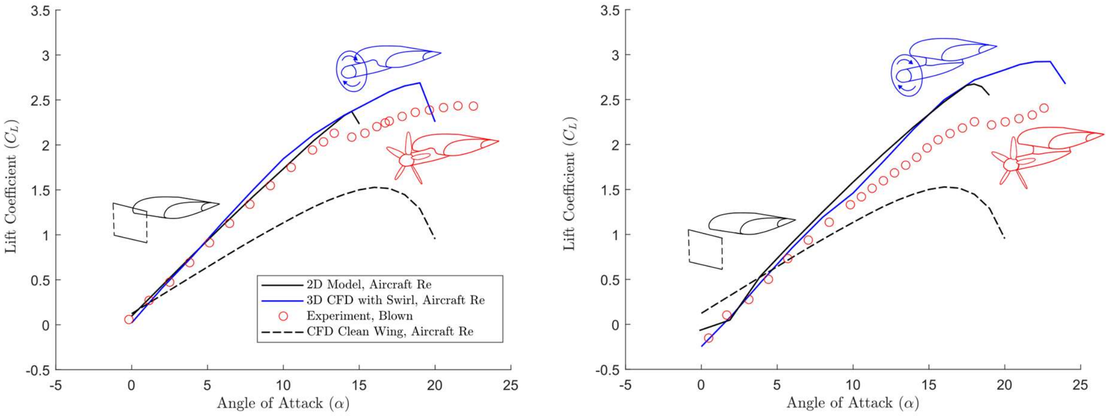

(a)

(b)

Figure 6.9: Lift coefficients for y_p/c=-0.05 (a) and y_p/c=-0.2 (b) at different angles of attack comparing actuator disk and experimental predictions. The flap is not deployed in these simulations.

Next, we consider the experimental lift curves for flap deployment, shown in Fig. 6.10. Once corrected for the effect of Reynolds number and the flap trip, the experimental lift curve slope matches the 3D CFD and 2D model for both y_p/c=-0.05 (to within ΔC_L=0.12) and y_p/c=-0.2 (to within ΔC_L=0.08) [37]. This range extends to ϕ=23°. For the case y_p/c=-0.05, the 2D model underpredicts the maximum lift coefficient of the wing, indictating that the reported drag reductions of Chapter 4 and 5 are underpredictions of the experimental value for smaller propeller vertical offsets. For the case y_p/c=-0.2, the maximum lift coefficient of the wing is overpredicted by 15% by the 2D model. This reduces the maximum safe operating lift coefficient from 3.17 to 2.67, giving a 16% increase in the area of the wing, and an increase in the wing profile drag. The consequences of the 2D model overpredicting the maximum lift coefficient of the blown wing are discussed further in Chapter 8.

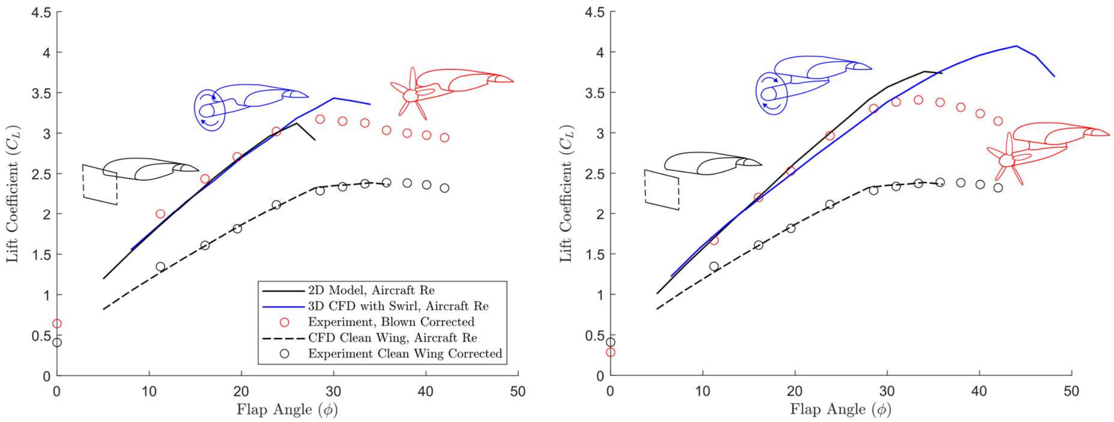

(a) (b)

Figure 6.10: Lift coefficients for y_p/c=-0.05 (a) and y_p/c=-0.2 (b) at different flap angles comparing actuator disk and experimental predictions [37]. The wing angle of attack is 3°.

Plots of streamwise force coefficient on the blown wing for angle of attack and flap angle sweeps are shown in Fig. 6.11. Higher angle of attack and flap angle drag data has not been plotted in some cases due to simulation convergence issues. The low Reynolds number of the wing increases the drag coefficient of the wing, however this delta in performance is negligible compared to the propeller thrust. As a result, for angle of attack sweeps, the agreement between the experimental data and CFD actuator disk simulations is within C_x=0.012. Beyond a wing angle of 14° for y_p/c=-0.05, the drag increases. This is due to a corner separation which was found to develop in the test rig at one of the end-walls at high angles of attack. The same separation occurs for y_p/c=-0.2 at a wing angle of 18°.

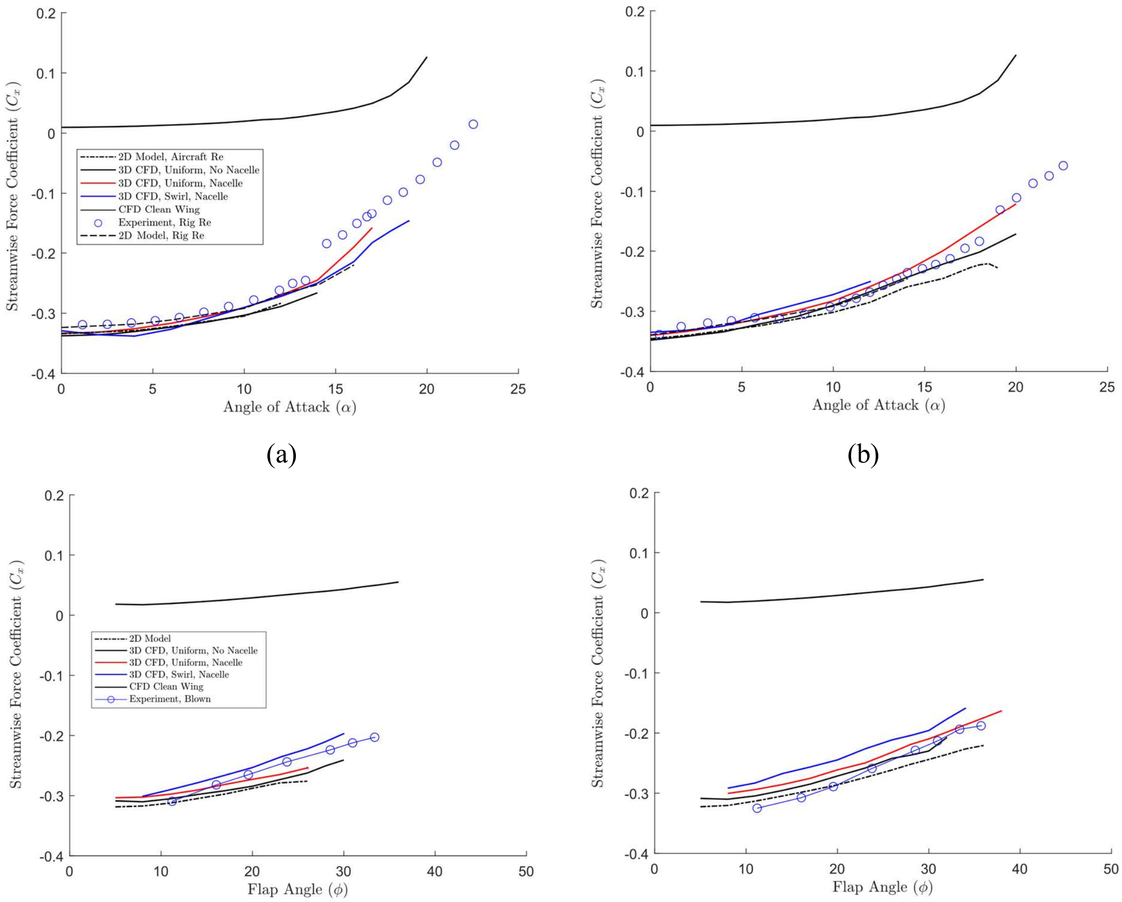

(a) (b)

(c) (d)

Figure 6.11: Streamwise force coefficients for y_p/c=-0.05 (a) and y_p/c=-0.2 (b) at different angles of attack and y_p/c=-0.05 (c) and y_p/c=-0.2 (d) at different flap angles comparing experiment and different fidelities of actuator disk modelling.

For sweeps of different flap angles the rate of increase in streamwise force with flap angle deployment is greater in the experiment and 3D simulations with swirl, and the drag with swirl is higher than the 2D model prediction by up to 0.05 at ϕ=30° for y_p/c=-0.05. At y_p/c=-0.2, the drag of the blown wing is lower in the experiment than the model, although there is some uncertainty in the effect of the propeller position on the propeller characteristic (which in this analysis is assumed to be unaffected by the presence of the wing). More work is required to understand the sources of drag on the blown wing with swirl when the flap is deployed. The flow-field, particularly around the wing cove, is complex and the induced drag will be modified due to the varying up-wash and downwash of the wing due to swirl. In addition, the drag due to the flap boundary layer trip may be contributing to the increased drag rise.

6.3 The Effect of Propeller Spacing

The results of the previous section have shown that all the modelling methods agree well away from stall, and that the 3D effects of the jet does not change the overall lift of the wing, for a given geometry, incidence and total thrust. In this section we investigate the other 3D geometry effect not considered in the 2D modelling of Chapter 4: the effect of propeller spacing.

6.3.1 Propeller Spacing with Real Propulsor Effects

Figure 6.12 shows plots of the lift coefficient measured in the experiment. Spacings of s/D_p=0.05 and s/D_p=1.1 were tested for two vertical offsets, y_p/c=-0.05 and y_p/c=-0.2. A range of propeller advance ratios were tested from which the thrust coefficients, T_c=1 and T_c=2 were interpolated for s/D_p=0.05 and 1.1 respectively. This ensured that the total streamwise thrust remained constant between the two propeller spacings.

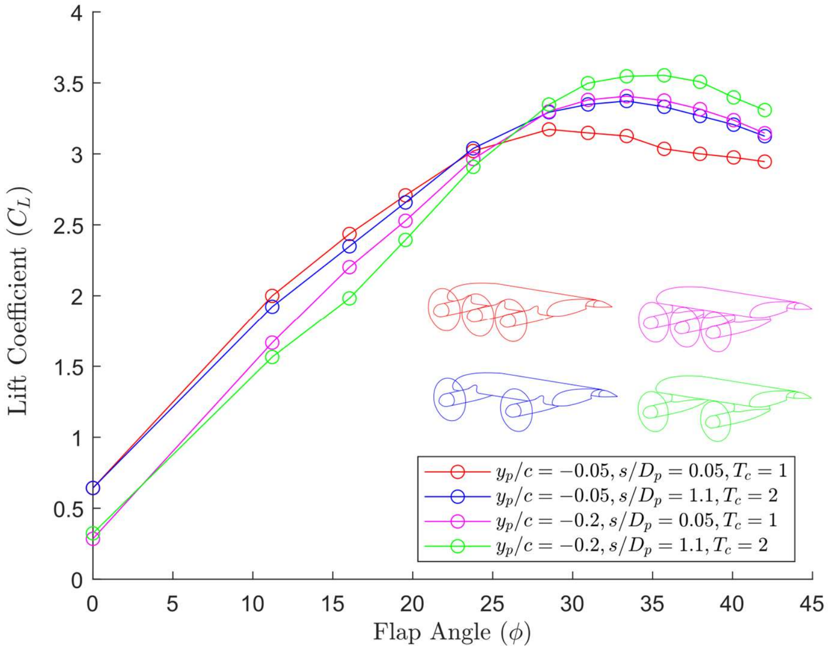

Figure 6.12: Measured lift coefficients for four different geometries, y_p/c=-0.05 and y_p/c=-0.2, s/D_p=0.05 and s/D_p=1.1. Thrust coefficients of T_c=2 were used for the wider spacing, and T_c=1 for the narrow spacing to ensure conservation of thrust.

For y_p/c=-0.05, increasing the spacing from s/D_p=0.05 to s/D_p=1.1 leads to a maximum 3.6% reduction in lift for the same total thrust. For y_p/c=-0.2, increasing the spacing from s/D_p=0.05 to s/D_p=1.1 leads to a maximum 11.1% reduction in lift for the same total thrust. These errors are calculated for on-design performance, which has been defined here as flap angles below ϕ=25°. Beyond this flap angle, the wing begins to stall. The stall point is delayed by spacing the propellers out, as seen in Fig. 6.12 and this is explored further in the next chapter. The key result from Fig. 6.12 is that the wing is still able to generate the same blown lift, to within 10%, with half the number of propellers blowing a faster jet over the wing surface.

6.3.2 Modelling the Effect of Propeller Spacing

In Appendix F, a top-hat model is presented for 2D actuator disk models used to predict the blown wing lift. The key result is,

$$\overline{C_x} = \frac{C_{x,blown} + C_{x,unblown}\frac{s}{D_p}}{1+\frac{s}{D_p}} \quad , \quad (6.2)$$

and,

$$\overline{C_L} = \frac{C_{L,blown} + C_{L,unblown}\frac{s}{D_p}}{1+\frac{s}{D_p}} \quad . \quad (6.3)$$

where C_{blown} is the aerodynamic coefficient predicted by the 2D Actuator disk calculation and $C_{unblown}$ the aerodynamic coefficient of the 2D wing without blowing. The top-hat model was found to accurately predict the on-design performance of the blown wing for small propeller offsets shown in the previous section. In this sub-section we explore the effect of increasing the propeller spacing, s, to test the validity of the top hat model at larger spacings.

Figure 6.13 shows plots of lift and streamwise force coefficient for a blown wing with an actuator disk vertical offset of y_p/c=-0.05 at 4 angles of attack: 3°, 6°, 9° and 12° for a range of actuator disk spacings, s. No flap is deployed. The top hat model is overlaid on to the 3D CFD simulations. The top hat model is able to capture the trends in lift and streamwise force coefficient for different spacings and angles of attack. Up to 9°, the model is able to predict the lift of blown wings with large spacing above s/D_p =1.1 to within 1.8%. The streamwise force is well captured by the model. At a wing angle of 12°, the 2D blown wing begins to stall whilst the 3D blown wing lift coefficient increases up to 14°. As a result, the model does not perform as well for off-design cases. Between s/D_p=0.1 and s/D_p=0.8, the 3D lift diverges from the model by up to 4%.

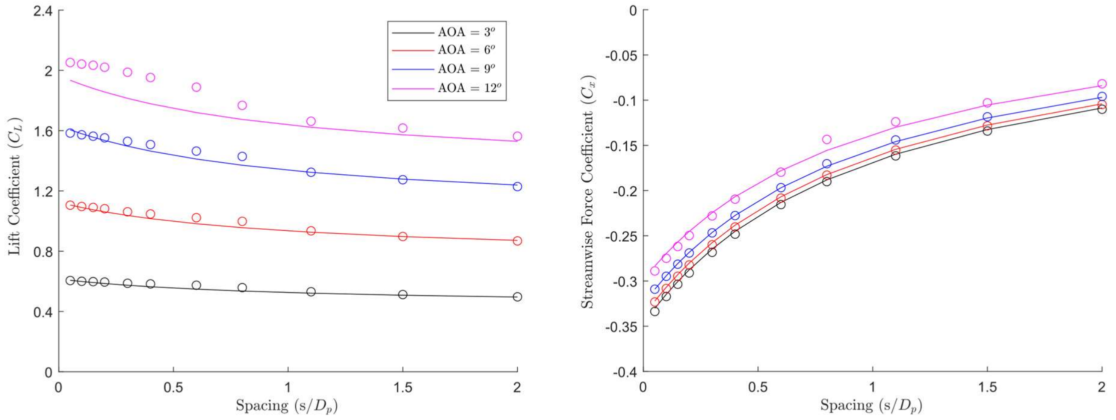

(a) (b)

Figure 6.13: Variation of lift and streamwise force coefficient with actuator disk spacing comparing 2D models to 3D uniform jet actuator disk simulations at different wing angles of attack.

Figure 6.14 shows plots of the wing surface pressure field with streamlines for s/D_p=0.05, 0.4, 0.8 and 1.1. As the jets are spaced out, both the maximum and minimum spanwise loading of the wing drops. Even though the jets are spaced out by more than one actuator disk diameter, the unblown section of the wing is more highly loaded than the clean wing at the same angle of attack. For s/D_p=0.1, the neighbouring jets merge by the trailing edge to produce a single continuous jet. As the jets convect downstream over the wing, the mutually-induced velocities of the secondary flows cause the secondary flow vortices to move towards each other over the wing surface and then away from the wing surface along the line of symmetry. This occurs up to s/D_p=0.8. Beyond this spacing, the neighbouring vortices do not meet before the wing trailing edge is reached. This yields a region on the wing surface that is unaffected by the presence of the jet, and the spanwise loading is constant, albeit higher than the unblown wing. The top-hat model is unable to capture the effect of the secondary flow passing along the wing surface, and typically under predicts the lift between s/D_p=0.1 and s/D_p=0.8 where this effect is significant. The model agreement for s/D_p=0.05 discussed previously is good because the secondary flows immediately move away from the wing when they are formed due to their close proximity, and there is minimal interaction with the wing.

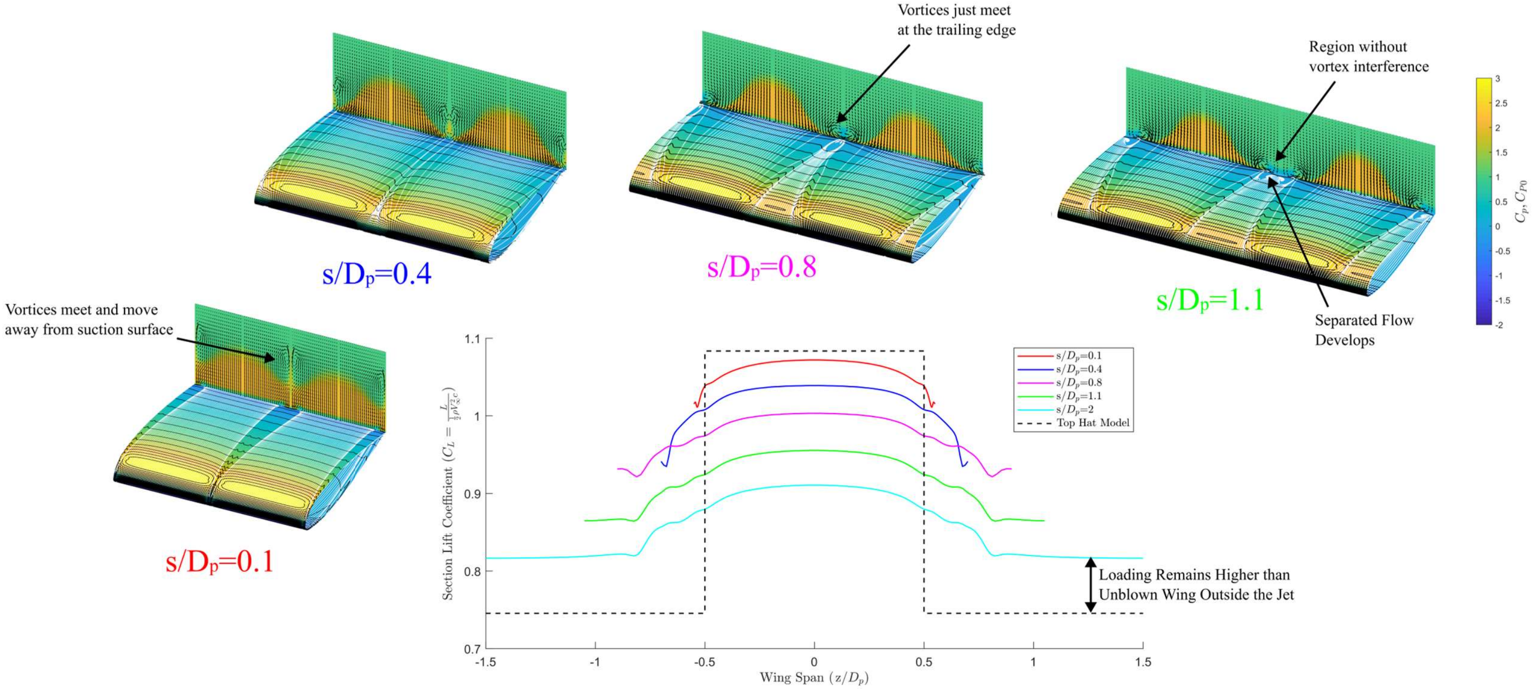

Figure 6.14: Spanwise section lift coefficient of the wing at 6° angle of attack for different actuator disk spacings. Wing static pressure, and trailing edge total pressure are plotted with wing surface streamlines for a selection of cases. The vortices generated by the roll up of the actuator disk jet meet in the gap between adjacent jets, modifying the wing loading. Beyond s/D_p=0.8, these vortices no longer meet before the wing trailing edge, and the lift remains constant in the gap between the jets.

6.3.3 Blown Wing Lift for a Fixed Total Thrust

The 2D model is able to correctly capture the trends in lift and streamwise force of the blown wing using single 2D CFD simulations for the blown, and unblown wing sections. The experimental results shown in Fig. 6.12 showed that the wing lift remains unaffected by the introduction of propeller spacing, provided the total thrust is held constant. This is explained in this sub-section. Ignoring finite jet effects and viscosity, the lift coefficient of the wing can be written as,

$$C_{L,blown} = (1 + T_c)C_{L,unblown}\,, \quad (6.4)$$

and the streamwise force coefficient can be calculated as,

$$C_{x,blown} = -\frac{\overline{D_p}}{c}T_c \;\; . \quad (6.5)$$

Making use of the inviscid assumption that $C_{x,unblown}$=0, Eq. 6.2 and 6.3 can be re-written as,

$$\overline{C_x} = -\frac{\overline{D_p}}{c}\frac{T_c}{1+\frac{s}{D_p}} \;\;, \quad (6.6)$$

and,

$$\frac{\overline{C_L}}{C_{L,unblown}} = 1 + \frac{T_c}{1+\frac{s}{D_p}} = 1 - \frac{\overline{C_x}}{\overline{D_p}/c} \;\; . \quad (6.7)$$

For a fixed streamwise force coefficient, the lift augmentation given by Eq. 6.7 should be independent of propeller spacing, as observed in Fig. 6.12 [37].

Figure 6.15 shows plots of lift and streamwise force coefficient at two thrust coefficients, T_c=1 and T_c=2. Results for an angle of attack of 6° are plotted using both 3D CFD simulations without swirl, and the top-hat model prediction. At a thrust coefficient of T_c=1 and spacing, s/D_p=0.05, the streamwise force coefficient is -0.323. Increasing both the spacing between propeller tips to s/D_p=1.1 and the thrust coefficient to T_c=2 conserves the total thrust of the system. The streamwise force coefficient drops to -0.325, a 0.6% decrease in streamwise force due to a change in the wing drag. Whilst the streamwise force is nearly constant, increasing both the spacing and actuator disk thrust drops the lift coefficient from 1.106 to 1.083, a 2.1% reduction. This reduction in lift is smaller than that predicted by the top hat model (5.0%

reduction from 1.1065 to 1.0535) due to deviation of the 3D CFD from the model caused by secondary flows [37].

Whilst the wing lift coefficient has dropped by only 2.1%, the number of nacelles has dropped by 50% when doubling the spacing. This reduction in nacelle number will lead to a significant reduction in the cruise drag, and complexity of the system. Increasing the propeller spacing yet further could yield even greater reductions in nacelle drag. However, the thrust coefficient will eventually be limited by the design and efficiency of the propeller [37]. The benefits of increasing propeller spacing to reduce nacelle drag, and the practical limits on increasing propeller spacing due to reduced propeller efficiency will be explored in Chapter 8.

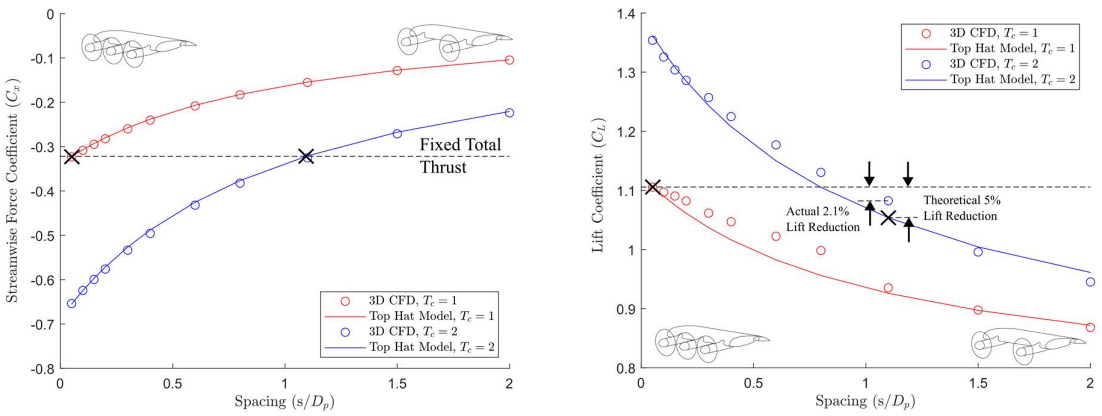

(a)

(b)

Figure 6.15: Streamwise force (a) and lift (b) for blown wings with variable spacing and thrust coefficients of T_c=1 and T_c=2 [37]. Increasing the spacing and thrust coefficient allows similar lift to be generated with a reduced number of propellers.

6.4 Conclusions

This chapter has shown that the lift of a blown wing is primarily driven by the thrust from the jet, and its position. 2D modelling of the blown wing is therefore able to capture the lift and drag without the need to use more complex models. This answers the second question posed in Chapter 2. The optimum design for a blown wing, found in Chapters 4 and 5 using 2D modelling, is therefore still valid, as shown in Fig. 6.16.

This chapter also introduced the other 3D geometry variable not considered so far: propeller spacing. It was found that the propeller spacing can be increased, with a minimal reduction in the blown lift, provided that the total thrust of the propellers remains constant. Increasing the propeller spacing reduces the number of nacelles, and therefore the nacelle drag. The optimal propeller spacing, and performance benefit will be shown in Chapter 8.

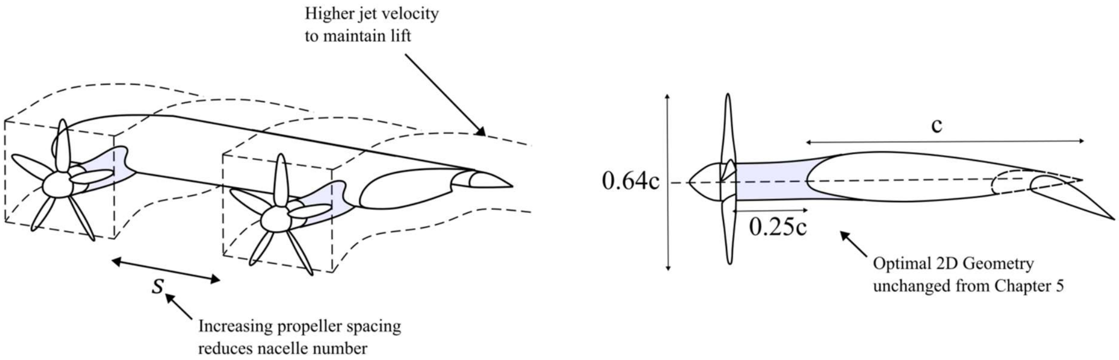

Figure 6.16. The 2D approach of Chapter 4 is able to capture the on-design performance of the blown wing with real propulsors. The optimum geometry found in Chapter 5 is still valid. Increased spacing can still achieve high lift, but with fewer nacelles, reducing drag.

7. Real Propulsor Effects Off-Design

7.1 Introduction

It was shown in the previous chapter that, away from the stall point, the performance of the blown wing is primarily a function of jet position and thrust, and can be well approximated by simplified 2D modelling. In this chapter, we look at the performance of the blown wing at the stall point in order to answer the questions posed in Chapter 2: What is the mechanism by which the flap of a blown wing stalls? How does the position of the propeller in relation to the wing affect the stall point? Can 2D modelling capture this behaviour? First, the mechanism by which the wing stalls when the flap is deployed is identified. Second, the effect of geometry, specifically propeller vertical position, y_p/c, and the spacing between propellers, s/D_p, on the stall mechanism and maximum lift coefficient are identified, as shown in Fig. 7.1. Finally the ability of 2D modelling to capture the stall point of the blown wing is discussed and it is found that the 2D model under-predicts the stall point of the wing.

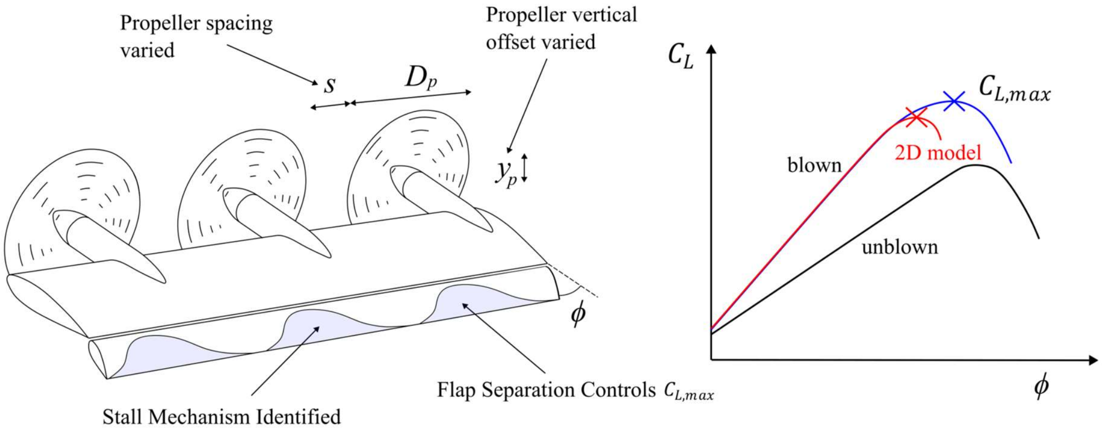

Figure 7.1: The effect of propeller vertical offset, y_p/c, and propeller spacing, s/D_p on the wing stall and maximum lift coefficient are studied in this chapter. The stall mechanism is identified and the predictive capabilities of 2D modelling near stall established.

7.2 Stall Mechanism for the Wing and Flap

For blown wings during landing, the maximum lift coefficient with the flap deployed is the key limit on performance. In this section, we study the stall mechanism of the wing with a flap deployed.

7.2.1 Validating the use of CFD to Study the Wing-Flap Stall Mechanism

First we compare the 3D actuator disk model with swirl to the experiment for off-design performance. The CFD gives us information about the wing surface pressure that the experiment cannot provide, and will help to explain the stall mechanism. Figure 7.2 shows plots of the trailing edge streamwise velocity field for both CFD and experimental measurements at a flap angle of 26°. The plots show the wing downstream of two propellers. Arrows with the in-plane flow velocity are also included.

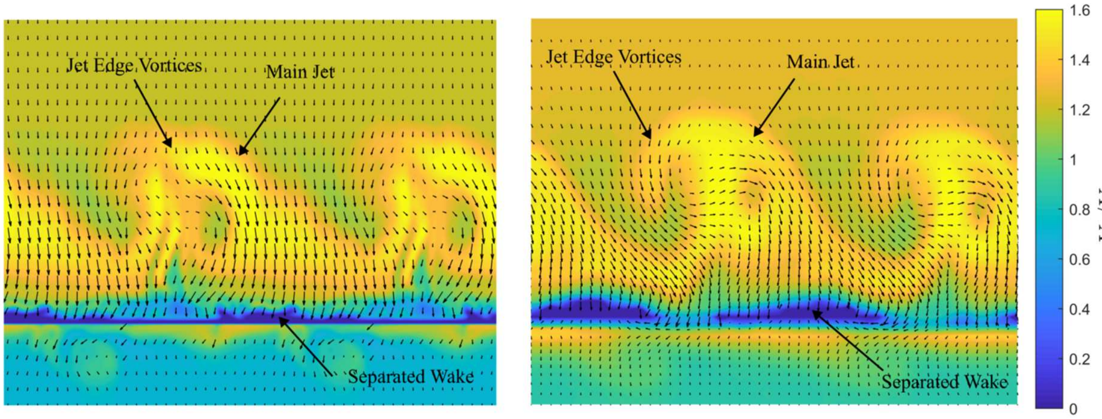

(a)

(b)

Figure 7.2: Trailing edge CFD (a) and experimental measurement (b) of the velocity field with the flap deployed at 26°. The angle of attack is 3°, the thrust coefficient, T_c=1, y_p/c=-0.05, s/D_p=0.05.

The CFD is able to capture the shape of the jet, and the location of the wing separation, seen by the dark blue areas of Fig. 7.2. The CFD also captures the roll up of the jet edge vortex with the swirling main jet. The low momentum at the centre of the jet due to the nacelle and low loading of the hub is also resolved. This indicates that the use of a 3D actuator disk with swirl can capture the key physics of the stall mechanism. There are discrepancies between the two plots. Discrepancies at the centre of the jet can be attributed to differences in the modelling between the 3D actuator disk model and the real propeller jet profile. The Goldstein jet model described in Appendix A is only able to model the propeller wake at its design point. The discrepancy in periodicity for the experiment is due to small variations in propeller rpm of up to 5% between neighbouring propellers. It is possible that the mixing in the CFD is under-predicting the experiment, as the CFD exhibits more clearly defined structures within the interacting vortex regions, such as the vortex roll-up downstream of the nacelle on the flap pressure side, and the vortex interactions on the suction surface. Both of these have mixed out in the experiment. This may be due to the use of steady RANS to model the unsteady propeller wakes. Further investigation of the correct turbulence modelling for blown wings, and the impact of unsteadiness on the flow-field is required.

Having established that the wing trailing edge velocity fields show acceptable agreement between the CFD and experiment, we next look at the wing suction surface. Figure 7.3 shows a comparison between a flow visualisation study of the wing in the experiment, and the surface streamlines within the CFD. Both the CFD and experiment are at a wing angle of 3°, a flap angle of 26° and a thrust coefficient of 1. Schematics have also been produced for each case, on the right of Fig. 7.3, with views from above of the wing and flap suction surface, to compare the two.

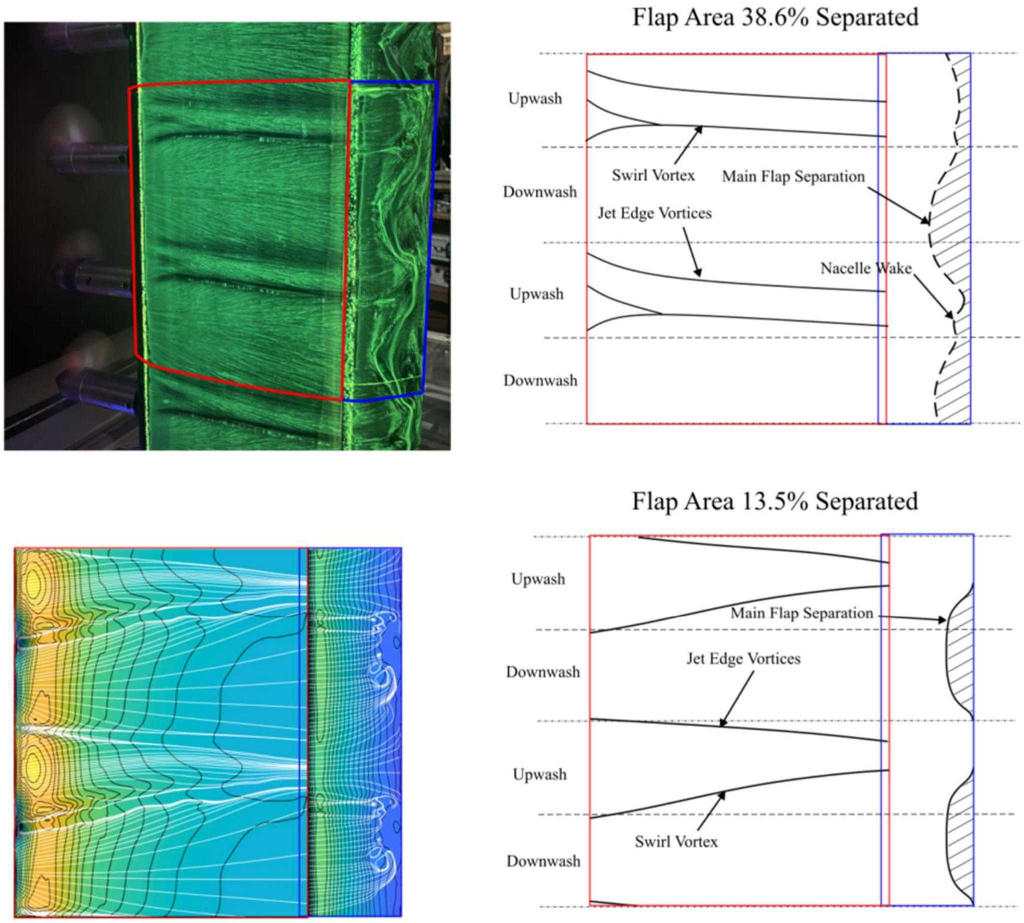

Figure 7.3: Flow visualisation and schematic separation lines for a wing angle of α=3°, a flap angle of ϕ=26° and a thrust coefficient of T_c=1 [37]. The propeller is positioned at y_p/c=-0.05 with a propeller spacing of s/D_p=0.05. Experiment shown at the top, CFD shown at the bottom.

Both the CFD and experiment show local regions of separation on the flap trailing edge. The location of the separation, on the downwash side of the propeller centreline matches between the two cases. The CFD separation line has been taken as the point where the x-component of shear stress drops below zero. This separated area under predicts the size of the separation (38.6% vs. 13.5% of the flap area for the experiment and CFD respectively). The lift of the wing will be shown in Section 7.5 to correlate closely with the separated flap area. The reduced separated area predicted by the CFD is the primary cause of the extended range, pre-stall, seen for the 3D actuator disk with swirl in Chapter 6.

Streamlines have been seeded at the wing leading edge to identify the jet edge and swirl separation lines. The CFD is able to capture the jet edge vortices seen in the experiment, as well as a central separation line emanating from the nacelle due to the bulk swirl of the main jet. The location and shape of the vortices is different between the two cases, possibly due to the differences between the actuator disk and real propeller jet profiles. The rate of spanwise migration of the vortex emanating from the nacelle is greater in the experiment indicating the upwash region is imbedded in an area of lower static pressure than the CFD. This spanwise migration increases the diffusion of the boundary layer in the downwash region (due to the expansion of the flow towards the upwash region) which may be contributing to the early stall of the flap when compared to the CFD.

7.2.2 Explanation of the Wing-Flap Stall Mechanism

In this section, we use the 3D CFD to identify the stall mechanism for a blown wing with flaps deployed. The wing downstream wake total pressure (a), and the wing suction surface pressure (d), are shown in Fig. 7.4 for a 3D Actuator disk simulation with swirl. Figure 7.4 (c) shows the location of the flap downstream plane in relation to the wing. The jet is positioned at y_p/c=-0.05 with a propeller spacing of s/D_p=0.05. The wing angle is 3°, the flap angle is 26° and the thrust coefficient is 1. Two spanwise locations, a separated location z/D_p=0 and an unseparated location z/D_p=-0.3, are considered. The propeller downwash region occurs beyond z/D_p>0 [37].

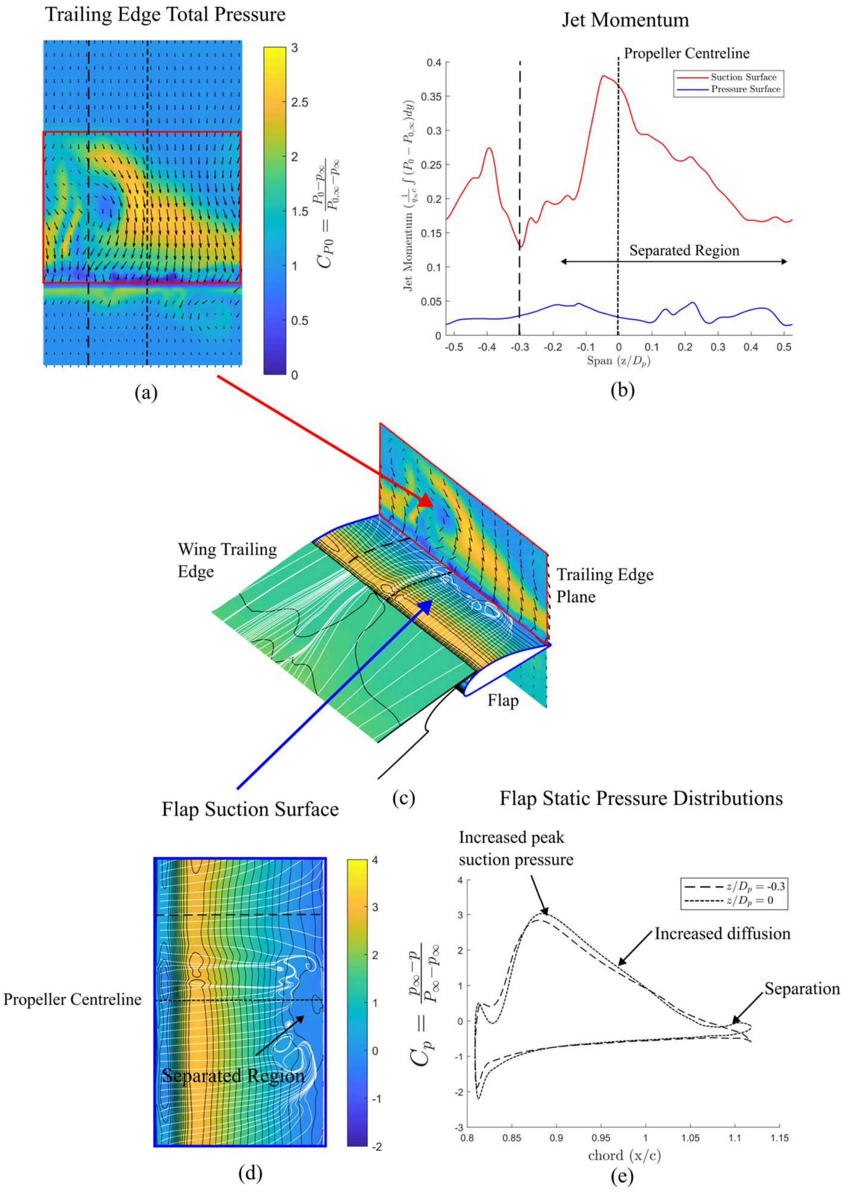

Figure 7.4: The CFD flow-field around the flap at stall [37]. The wing trailing edge total pressure field is plotted in (a) and integrated in (b) to give the spanwise variation in trailing edge jet momentum above and below the flap. The flap suction surface pressure and streamlines are shown in (d) and the pressure distribution is plotted in (e) for z/D_p=0 (the propeller centreline) and z/D_p=-0.3 (a point in the propeller upwash region). The location of the flap and trailing edge plane are shown in (c). The wing angle is 3°, flap angle ϕ=26°, thrust coefficient of T_c=1. The propeller is positioned at y_p/c=-0.05 with a propeller spacing of s/D_p=0.05.

The total pressure above and below the flap has been integrated in Fig. 7.4 (b) to show the momentum of the jet. Above the wing, the swirl from the actuator disk causes the main jet to move in the spanwise direction from the propeller upwash to the downwash side as it is convected in the streamwise direction, leading to high total pressure above the flap in the downwash region. The jet momentum is greatest at the propeller centreline, z/D_p=0, and in the downwash region z/D_p>0. The greater jet momentum in this region leads to an increased suction peak as shown by plots of static pressure coefficient, C_p, in Fig. 7.4 (e). The lower surface of the flap is unblown for z/D_p>0, as shown in Fig. 7.4 (a). This leads to a reduced trailing edge velocity, to maintain the Kutta condition, increasing the boundary layer diffusion.These two factors lead to separation in the downwash region first [37]. This is the same mechanism identified in Chapter 4 for 2D blown wing failure.

Moving the propeller upwards will cause the jet to move above the flap suction surface, increasing the momentum above the flap and reducing the momentum underneath the wing. This increases the diffusion of the boundary layer. The diffusion of the boundary layer also increases when the flap incidence increases. The total diffusion determines the health of the boundary layer. The separated area is a function of these two sources of diffusion,

$$Separated\ Area = f\{incidence - based\ diffusion, \qquad jet - based\ diffusion\}\ . (7.1)$$

Whilst incidence-based diffusion is uniform along the span, producing a straight separation line, jet-based diffusion varies along the span due to the jet swirl and spanwise varying jet height, leading to the wing separation originating at a point first. For a straight wing section, this point repeats periodically along the span, with the same offset as the propeller centre-lines. Although, the mechanism causing the flap stall is unchanged from 2D to 3D, the difference between the 2D and 3D cases is that because the separation grows from a single point, rather than a line along the span, the roll off in lift with flap incidence is more gradual than that predicted by the 2D model.

This section has shown that the wing will stall when the jet no longer immerses both the upper and lower surface of the flap and thus the design philosophy of Chapter 4, that the wing should be fully immersed in the jet, holds true. However, the separation of a wing with real propulsors upstream is 3D, and the loss of lift at high incidence occurs more gradually than the 2D equivalent case. As the wing stall is dependent on the position of the jet, we use the next two sections to explore how propeller position can be used to delay wing stall.

7.3 The Effect of Vertical Offset on Wing-Flap Stall

In this section we look at the effect of propeller vertical position and propeller spacing on the stall of the wing. Only the experimental data will be used in this section. Two methods will be used: flow visualisation, and 5-hole probe traverses. Two vertical offsets, y_p/c=-0.05 and y_p/c=-0.2, and two propeller offsets, s/D_p=0.05 and s/D_p=1.1 were tested, forming a matrix of four configurations. For each configuration, four flap angles were tested, ϕ=12°, 20°, 26° and 31°. For s/D_p=0.05, a propeller advance ratio of 0.83 was tested, equating to a thrust coefficient of 1. For s/D_p=1.1, an advance ratio of 0.71 was used, equating to a thrust coefficient of 1.6. Running the propellers for the duration of the probe traverse at an advance ratio of 0.64 (a thrust coefficient of 2) was likely to risk overheating the motors, hence the lower thrust coefficient was used for s/D_p=1.1.

7.3.1 Flow Visualisation

In this section, we use silicone-based flow visualisation paint to track the separated area of the flap. First we consider the case y_p/c=-0.05, s/D_p=0.05. Figure 7.5 shows photographs of the flow visualisation of the separated flap region at each flap angle. Also included is a schematic of each separation line overlaid onto a single plot of the wing and flap suction surface.

At the lower flap angle, ϕ=12°, there is no evidence of separation. Increasing the flap angle to 20° leads to a separation on the flap occupying 8.4% of the flap area. The separation consists of a region due to the jet, on the flap downwash side, and a “bump” at the trailing edge due to the nacelle wake. Increasing the flap angle further leads to a growth of the separated area. At ϕ=31°, the maximum upstream extent of the flap reaches the boundary layer trip, whilst the maximum downstream extent is 10% of the flap chord. This flap 3D stall structure will lead to large variations in the flap loading.

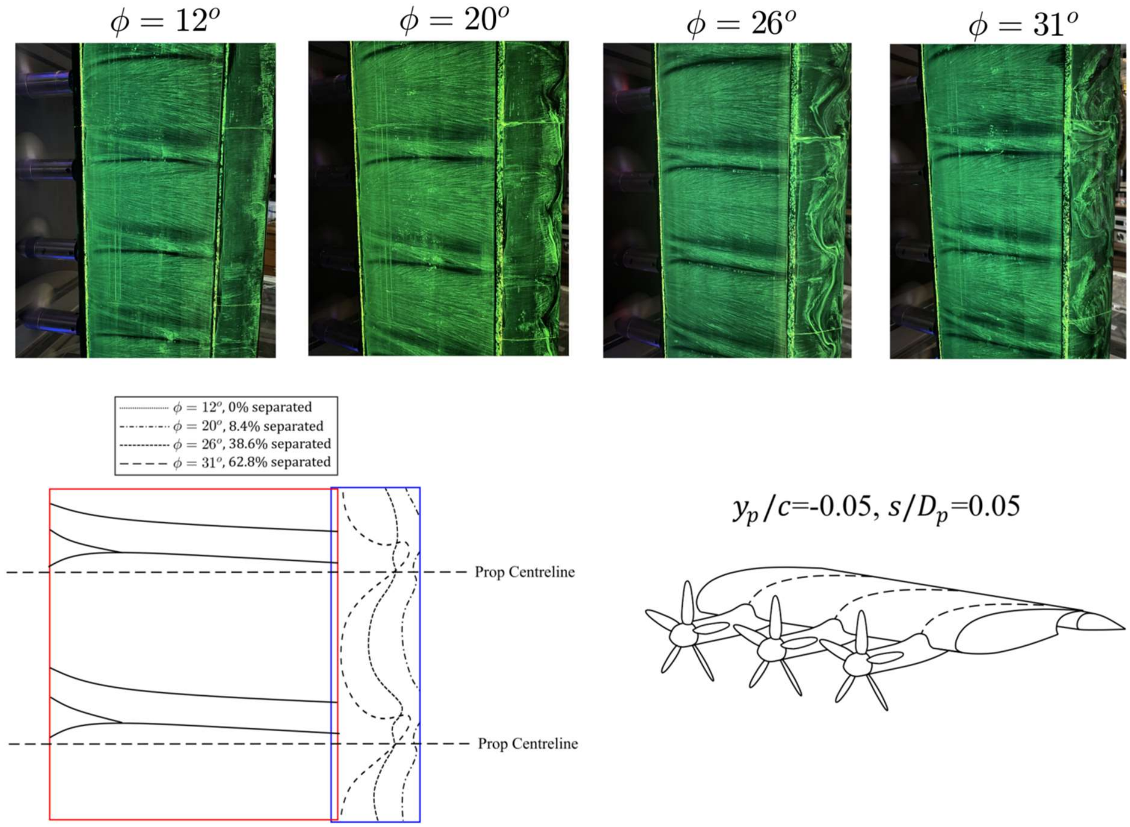

Figure 7.5: Photographs of flow visualisation results at four flap angles, ϕ=12°, 20°, 26° and 31° for the geometry y_p/c=-0.05, s/D_p=0.05 along with a schematic. The angle of attack is 3° and the thrust coefficient is T_c=1.

We now look at the effect of moving the propeller down to a vertical offset y_p/c=-0.2, as shown in Fig. 7.6. Again, at a flap angle ϕ=12°, the flap is not separated. Increasing the flap angle introduces the 3D stall structure observed previously for y_p/c=-0.05, however the separated area is lower at each flap angle than for y_p/c=-0.05. This explains why the lower vertical offset position leads to a greater flap angle range before stall, observed in Chapter 6.

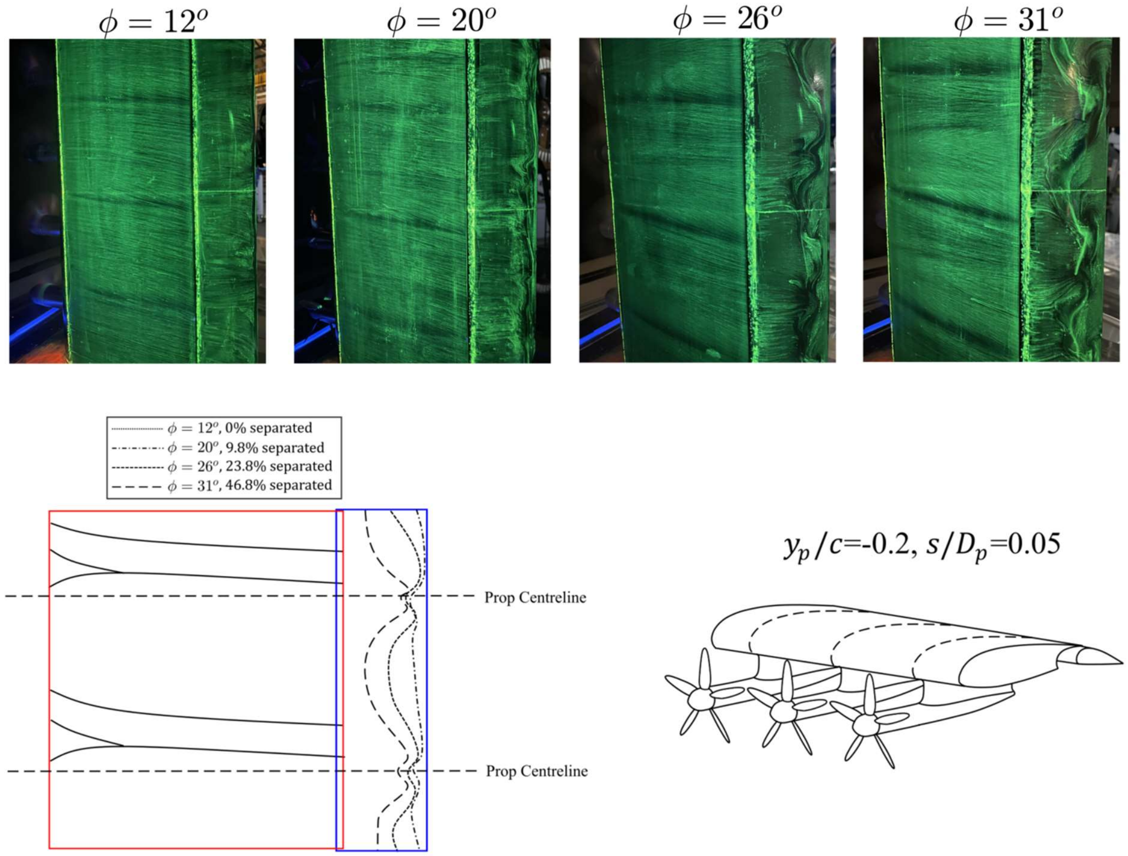

Figure 7.6: Photographs of flow visualisation results at four flap angles, ϕ=12°, 20°, 26° and 31° for the geometry y_p/c=-0.2, s/D_p=0.05 along with a schematic. The angle of attack is 3° and the thrust coefficient is T_c=1.

7.3.2 Area Traverses

It was shown in Section 7.2 that, along with the incidence of the wing, the shape of the jet at the trailing edge determines the location and size of the separation. In this section, we use 5-hole probe traverses downstream of the flap trailing edge to measure the velocity field.

Increasing the flap incidence causes the jet to move above the flap suction surface, as shown by the plots of trailing edge velocity field in Fig. 7.7. Moving the jet above the flap reduces the high velocity flow underneath the wing. At ϕ=20°, a region of the flap has no high momentum flow below it, and the flap begins to separate. Increasing the flap angle further causes the spanwise extent of the stalled region to grow, as the gap in the jet under the flap grows. The stalled area of the flap occurs first due to the jet-based diffusion at ϕ=20°, then grows further due to both incidence-based diffusion and the jet-based diffusion.

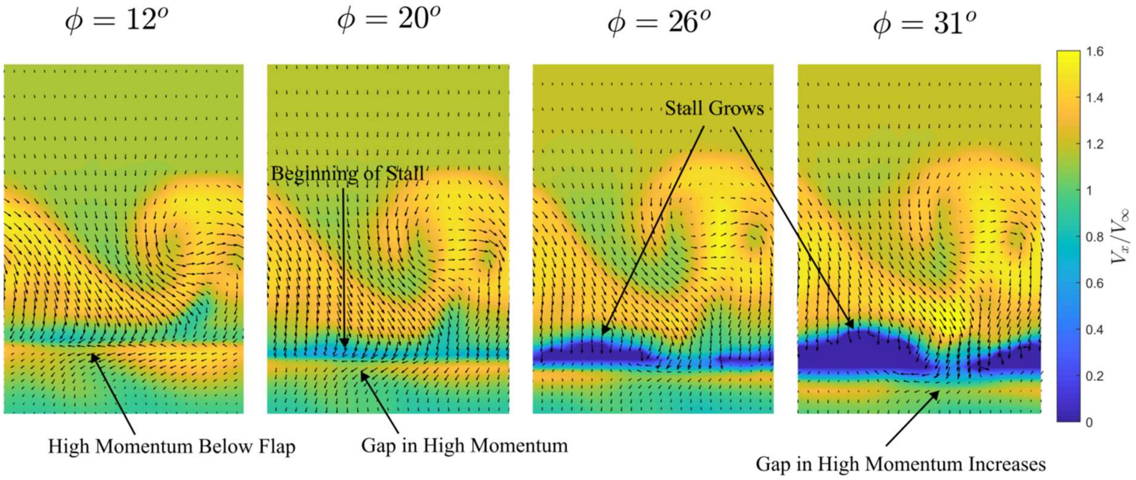

Figure 7.7: 5-hole probe traverses downstream of the flap at four flap angles, ϕ=12°, 20°, 26° and 31° for the geometry y_p/c=-0.05, s/D_p=0.05. The angle of attack is 3° and the thrust coefficient is T_c=1.

Next we consider moving the propeller down to y_p/c=-0.2, shown in Fig. 7.8. Comparing Fig. 7.7 with Fig. 7.8, moving the jet down has had the effect of covering the gaps in high momentum flow, at low incidence, on the flap pressure surface. This is due to the geometry of the jet, with the maximum jet width coinciding with the flap trailing edge near the operating point below ϕ=20°. Above a flap angle of 20°, the flap begins to stall despite there being high momentum below the flap, due to incidence-based diffusion. The stall pattern for ϕ=20° shown in Fig. 7.6 shows a predominantly 2D separation line, suggesting that for y_p/c=-0.2, the flap stalls first due to incidence-based diffusion. At the highest flap angle, ϕ=31°, the separated flap area is 16% lower for y_p/c=-0.2 compared to y_p/c=-0.05. By keeping the flap trailing edge immersed in the jet, the stalled area is reduced.

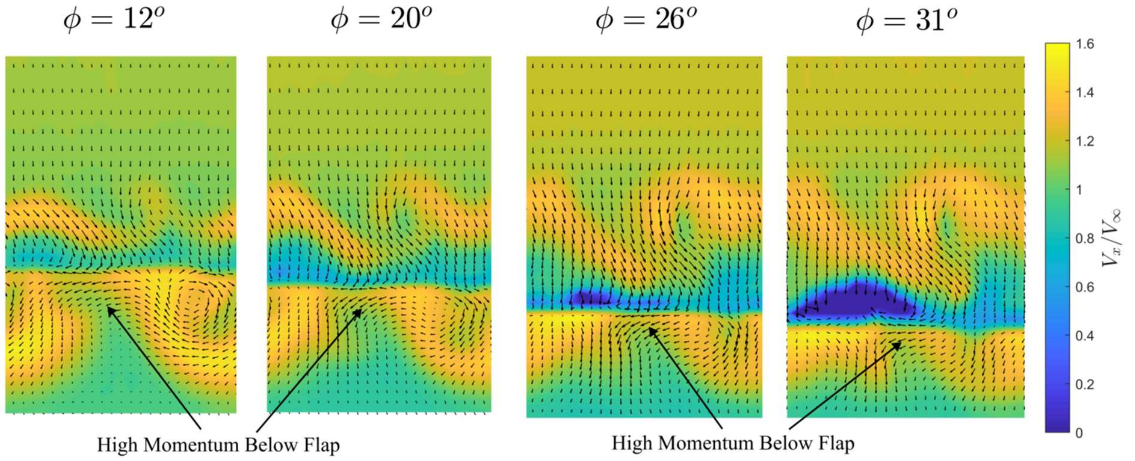

Figure 7.8: 5-hole probe traverses downstream of the flap at four flap angles, ϕ=12°, 20°, 26° and 31° for the geometry y_p/c=-0.2, s/D_p=0.05. The angle of attack is 3° and the thrust coefficient is T_c=1.

7.4 The Effect of Spacing on Wing-Flap Stall

Next we consider spacing the propellers out from s/D_p=0.05 to s/D_p=1.1.

7.4.1 Flow Visualisation

First we consider the small vertical offset case, y_p/c=-0.05. Figure 7.9 shows the flow visualisation plots for this study. The images are centred on the middle propeller in the test rig, however it was found that good periodicity could still be achieved either side of the outer propellers.

Removing the propellers to increase the spacing leads to a separated region on the flap at ϕ=12°. Up to ϕ=20°, the separated region is larger for the spaced out case than the tightly spaced case. This will be understood when we examine the area traverses downstream of the wing in the next section. For larger flap angles beyond ϕ=20°, the separated region is smaller, which explains the additional range achieved with widely spaced propellers seen in Chapter 6.

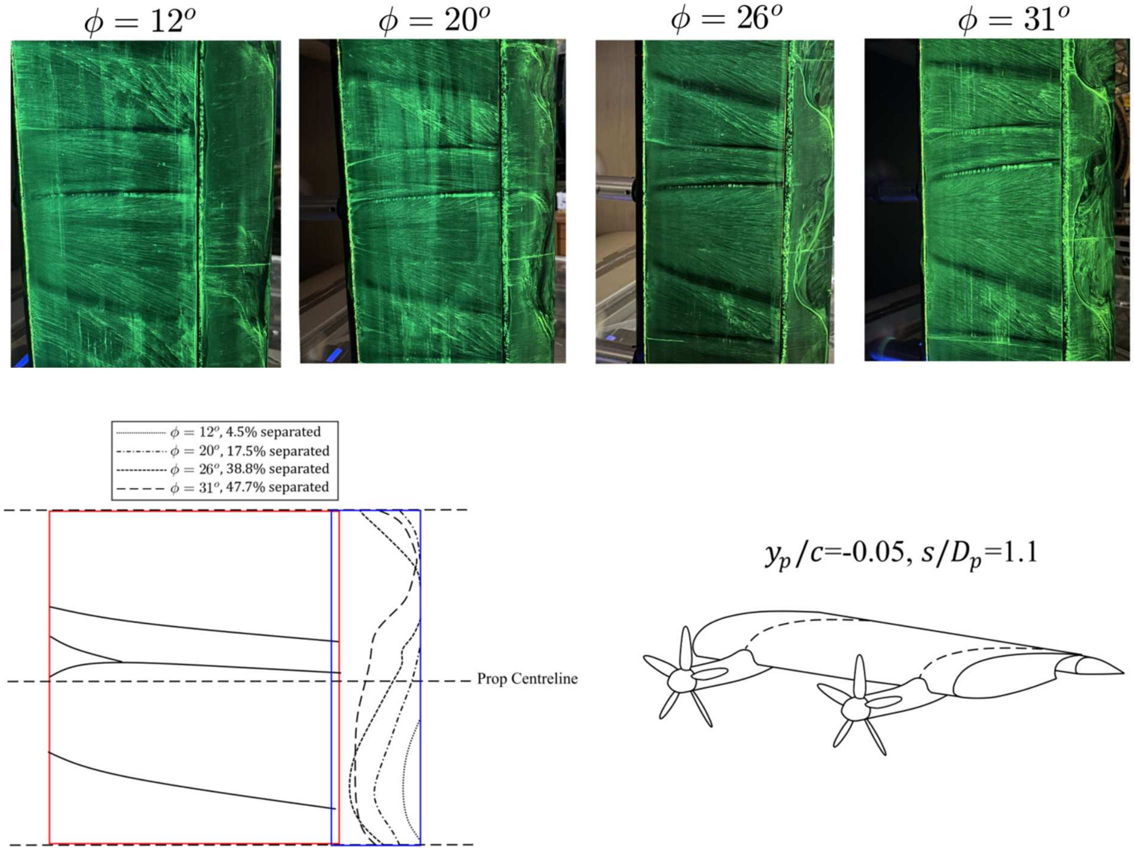

Figure 7.9: Photographs of flow visualisation results at four flap angles, ϕ=12°, 20°, 26° and 31° for the geometry y_p/c=-0.05, s/D_p=1.1 along with a schematic. The angle of attack is 3° and the thrust coefficient is T_c=1.6.

Figure 7.10 shows the final case tested, y_p/c=-0.2, s/D_p=1.1. This geometry has the most benign stall characteristic of the four tested, with only 40.9% of the flap stalled at a flap angle of ϕ=31°. However, at lower flap angles of ϕ=11° and 15°, the separated area is highest.

The effect of moving the propeller down is to reduce the size of the separated areas at a given flap angle. The effect of moving the propellers apart is to reduce the separated area at high flap angles at the expense of larger separated regions at low incidence. Even “on-design”, we can still expect to see regions of separated flow on the flap for spaced-out propeller geometries with s/D_p=1.1.

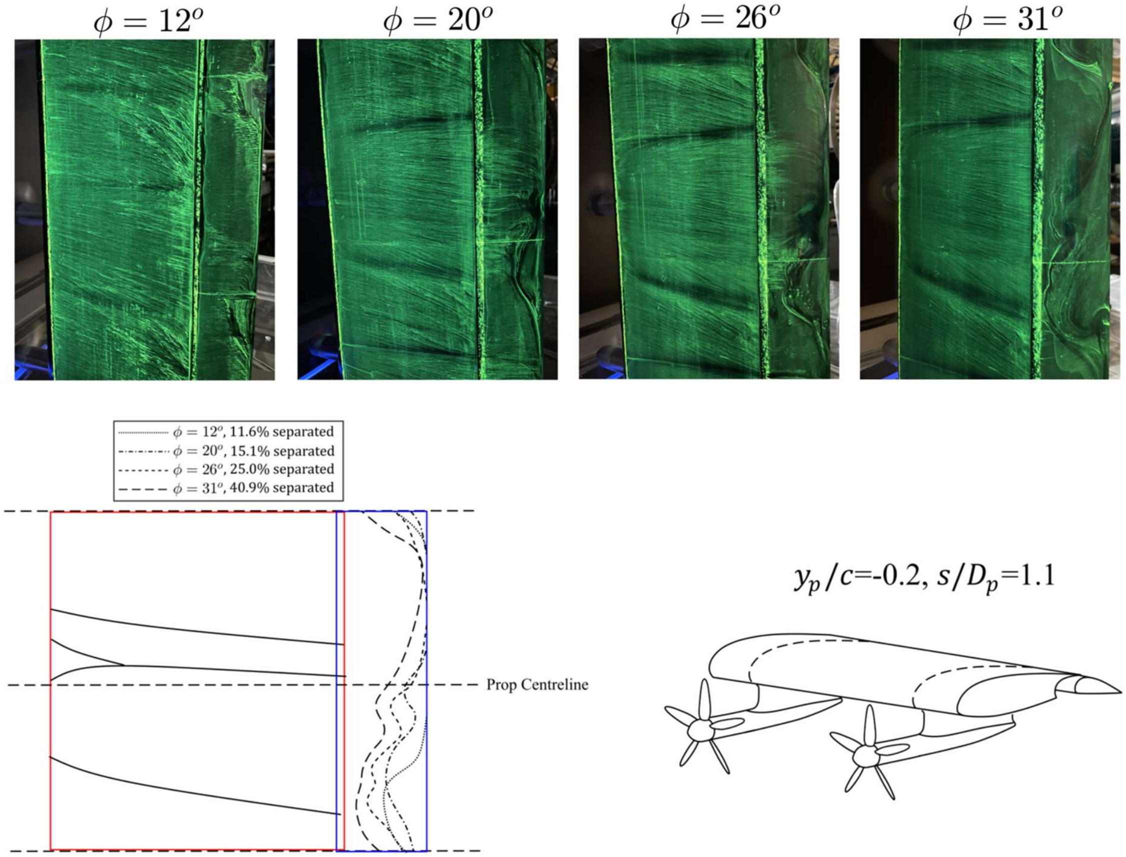

Figure 7.10: Photographs of flow visualisation results at four flap angles, ϕ=12°, 20°, 26° and 31° for the geometry y_p/c=-0.2, s/D_p=1.1. The angle of attack is 3° and the thrust coefficient is T_c=1.6.

7.4.2 Area Traverses

We now interpret the trends in flap separated area for spaced out propellers by examining the trailing edge velocity field. Figure 7.11 shows the trailing edge velocity field for a small vertical offset, y_p/c=-0.05, and spacing of s/D_p=1.1. In the previous section, the flow visualisation showed the flap began to stall as early as ϕ=12°. The mechanism for this early development of separated flow is due to spanwise movement of the main jet as it convects downstream, shown in the top-left of Fig. 7.11. This spanwise movement is due to the swirl imparted by the propellers, causing the bulk flow to move from the upwash to the downwash region on the suction surface, and vice versa on the pressure surface. Because there is no neighbouring propeller jets nearby, this spanwise movement of the jets leads to regions with high momentum flow passing only above the flap, and regions with high momentum flow passing only below the flap. In the region of the flap where the jet passes only above the flap, premature separation occurs, as seen for 2D jets in Chapter 4.

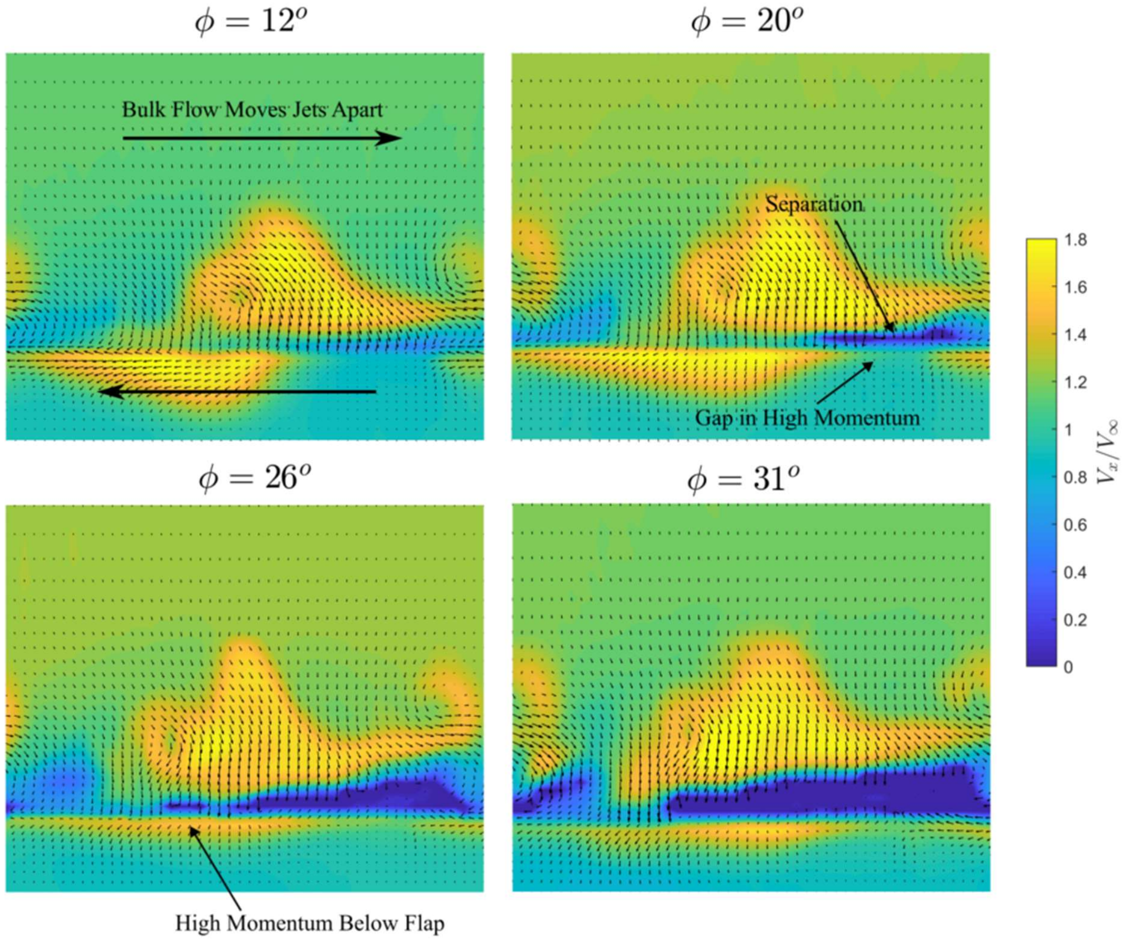

Figure 7.11: 5-hole probe traverses downstream of the flap at four flap angles, ϕ=12°, 20°, 26° and 31° for the geometry y_p/c=-0.05, s/D_p=1.1. The angle of attack is 3° and the thrust coefficient is T_c=1.6.

At higher incidences, the stalled region continues to grow due to a combination of incidence-based diffusion, and jet-based diffusion. The incidence-based diffusion arises from the extra turning of the flow, and increase of the peak suction surface pressure on the flap, The jet-based diffusion increases as higher flap incidences pull more of the jet over the top of the flap, exposing more of the flap to an unprotected trailing edge.

Whilst the stalled region of the flap grows with incidence, this growth rate is lower than for the tightly spaced propeller case. Regions of the flap remain largely attached, even at the highest flap angle tested of ϕ=31°, whilst the tightly spaced case is almost fully separated along the span. In the limit as the propeller spacing becomes very large, we expect the stall of the flap to approach that of the unblown wing which for this test is ϕ=34°. Spacing the propellers out therefore allows a greater proportion of the span to experience clean flow, delaying the stall angle.

Finally we consider the large vertical offset case, y_p/c=-0.2, and spacing of s/D_p=1.1. Again, the process of spacing the propellers out allows the jets to migrate along the span, giving rise to higher jet-based diffusion and early stall. However, as the incidence increases, the extent of the spanwise migration decreases. Because of the reduced spanwise migration, the wing is immersed in a straight jet at high incidence, with immersion on both sides of the flap. The jet-based diffusion reduces and the wing stalls primarily because of incidence-based diffusion.

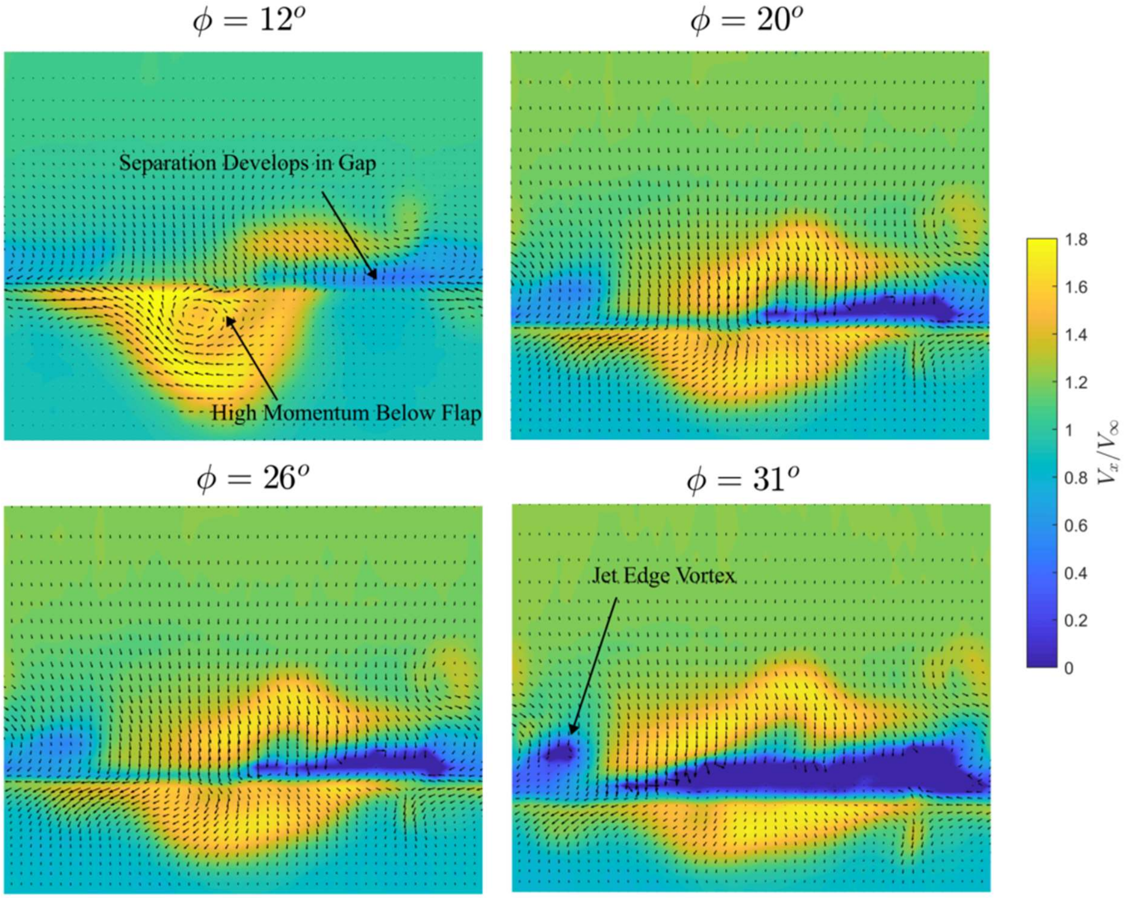

Figure 7.12: 5-hole probe traverses downstream of the flap at four flap angles, ϕ=12°, 20°, 26° and 31° for the geometry y_p/c=-0.2, s/D_p=1.1. The angle of attack is 3° and the thrust coefficient is T_c=1.6.

7.5 Comparing Separated Area to Maximum Lift Coefficient

This chapter has identified the mechanisms for blown wing flap stall, and found how the location, and spacing between propeller jets affects these mechanisms. The position of the jet affects the area of the flap that is separated. The lift coefficient measured from the load cell is plotted in Fig. 7.13 (a) with the point of maximum lift marked with a cross. The magnitude of the separated areas is summarised in Fig. 7.13 (b) for all the cases tested in this chapter. Increases in the separated area correlates with a reduction in the flap angle at which maximum lift coefficient, $C_{L,max}$ is generated. The y_p/c=-0.2, s/D_p=0.05 and y_p/c=-0.05, s/D_p=1.1 cases both have the same stalling flap angle, and the same separated flap areas at ϕ=31°. Whilst spacing the propellers out leads to early separation of the flap, the growth of the separated area is lower leading to extended range, similar to the range of the unblown wing.

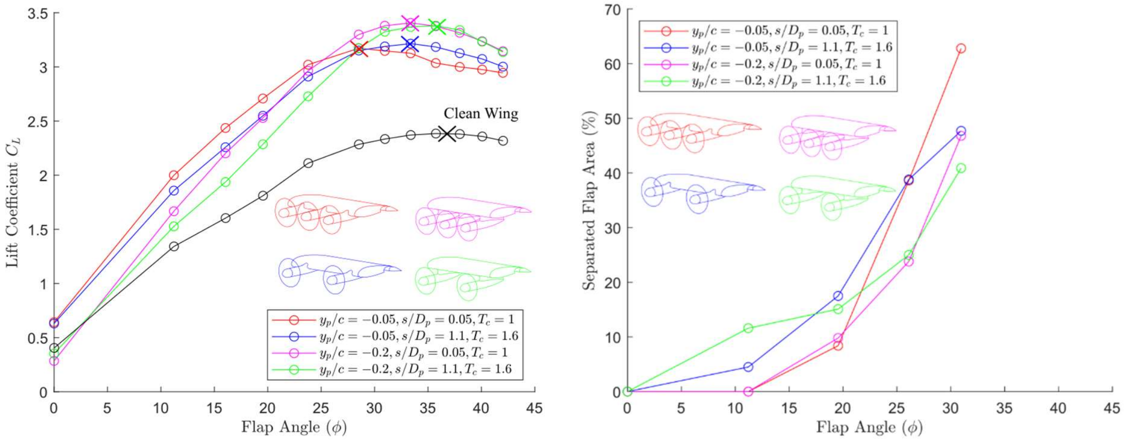

(a) (b)

Figure 7.13: Lift curve for the matrix of geometries tested in this chapter (a) and the separated flap area (b). The point of maximum lift is marked on the figure for each geometry in (a).

7.6 CFD and Experimental Predictions of Maximum Lift

7.6.1 Maximum Lift Prediction with Small Propeller Spacing

In this section, we look at the difference in the predicted maximum lift coefficient, $C_{L,max}$, between the different CFD fidelities and the experiment. The lift curves from Chapter 6 are shown in Fig. 7.14 for s/D_p=0.05.

First let us consider the cases y_p/c=-0.05, shown in Fig. 7.14 (a). The 2D model predicts a maximum lift coefficient of $C_{L,max}$=3.12. Introducing swirl increases the flap angle range by 4° compared to the 2D model and the maximum lift coefficient to $C_{L,max}$=3.43, 10% higher than the 2D model. The roll off in lift is now gradual, as the 3D separation with swirl is a trailing edge separation developing from a single point, as discussed in Section 7.2. The stall angle for the 3D case is delayed compared to the 2D model as the jet immersion criteria becomes the point at which the whole jet passes above the wing suction surface, which is dependent on the maximum diameter, D_p, rather than the 2D average diameter, $\overline{D_p}$. The average diameter is 21.5% smaller than the real jet diameter. The top hat model therefore under-predicts the 3D CFD stall point, and predicts a sharper stall than is observed in practice. The experimental maximum lift coefficient is 3.17. The 9.2% drop in lift from the 3D swirl case to the experimental lift is due to the under-prediction of the separated area by the CFD, as discussed previously in Section 7.2.1.

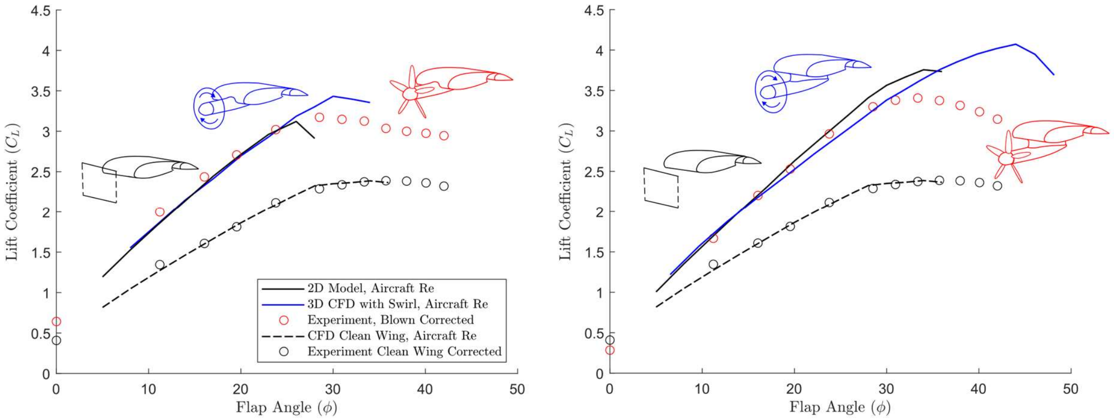

(a) (b)

Figure 7.14: Lift curve for the 2D and 3D actuator disk and experiment tested with s/D_p=0.05 [37]. A propeller vertical offset of y_p/c=-0.05 is shown in (a) and y_p/c=-0.2 is shown in (b).

Next we look at the case y_p/c=-0.2, shown in Fig. 7.14 (b). The top hat model predicts a maximum lift coefficient of $C_{L,max}$=3.76. Introducing swirl extends the flap angle range pre stall to ϕ=44°, an increase of 10°. This additional range increases $C_{L,max}$ to 4.07, an 8.2% increase from the top hat model. This percentage increase in lift coefficient is similar to that observed for the case y_p/c=-0.05, although the extension in the flap angle range is 2.5 times greater. The measured maximum lift coefficient in the experiment is $C_{L,max}$=3.4, a 10% drop compared to the 2D model and a 16.5% reduction compared to the 3D CFD with swirl [37]. The 3D CFD with swirl correctly captures the stall mechanism of the blown wing with a flap, but under-predicts the separated area.

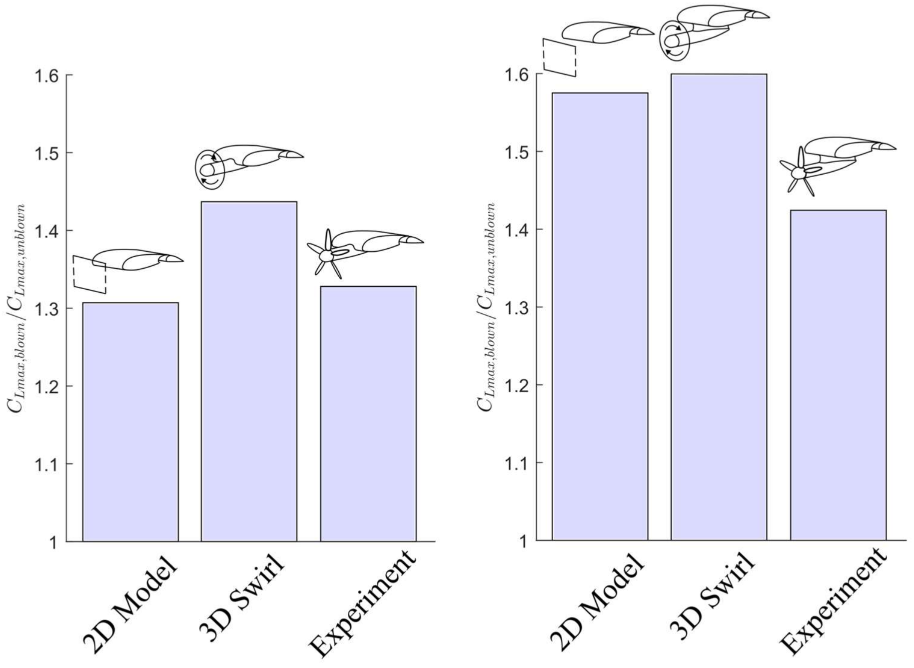

(a) (b)

Figure 7.15: Summary of the measured maximum lift coefficient with s/D_p=0.05. y_p/c=-0.05 in (a) and y_p/c=-0.2 is shown in (b). Values are normalised by the unblown wing maximum lift.

A summary of the maximum blown lift coefficient for the different propulsors models is shown in Fig. 7.15. The data has been normalised by the unblown lift coefficient of the wing. The key takeaway is that the 2D model is capable of capturing the trend in lift coefficient with vertical offset, but under predicts the 3D blown wing maximum lift coefficient from the CFD. The CFD under predicts the separated area for a given flap angle, leading to an increase in the maximum lift coefficient when compared to the experiment.

7.6.2 Maximum Lift Prediction with Large Propeller Spacing

We now look at the maximum lift coefficient prediction for large propeller spacing, in this case s/D_p=1.1. Figure 7.16 shows the predicted lift coefficient from the top hat model, and the experimentally measured lift coefficient with a spacing of s/D_p=1.1 and propeller thrust coefficients of T_c=1. The black lines show the CFD predicted value for the unblown section of the wing in the top hat model, derived from 2D CFD calculations.

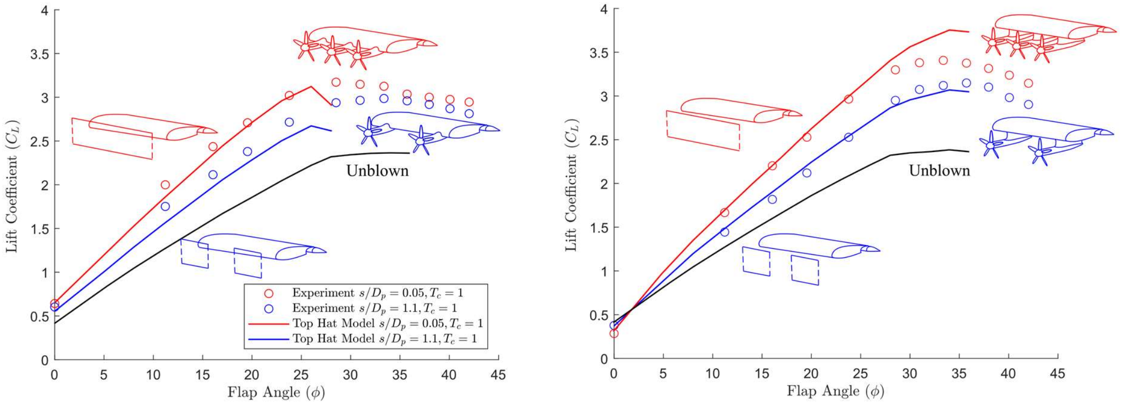

(a) (b)

Figure 7.16: Experiment and 2D actuator disk model predicted lift coefficients with s/D_p=0.05 and s/D_p=1.1 [37]. y_p/c=-0.05 is shown in (a) and y_p/c=-0.2 is shown in (b).

For y_p/c=-0.05, the model is able to capture the lift coefficient of the wing in the experiment to within 0.15 for the tightly spaced test, and to within 0.2 for the large spacing test away from stall. However, the top hat model is unable to predicted the extended un-stalled range of the flap with large spacing, an extra 0.4 to the maximum lift coefficient. Built into the model is the sharp drop in lift at ϕ=26° for the 2D CFD case, leading to a drop in the lift coefficient predicted by the model at this angle [37].

Moving to y_p/c=-0.2, the top hat model is able to capture the on-design lift coefficient well up to ϕ=30°, with an error of 0.13 for the tightly spaced case and 0.08 for the large spacing test [37]. Again, the top-hat model does not capture the extended range of the flap with spacing, this time an additional lift of 0.05.

7.7 Conclusions

This chapter has identified the mechanism by which a blown wing with a flap stalls, the effect of propeller vertical position and spacing on the point of stall, and the capability of 2D and 3D CFD models to predict the stall of the wing. It was shown that the flap stalls due to a combination of propeller jet and flap incidence-based boundary layer diffusion. The propeller jet-based diffusion is driven by spanwise discrepancies in the jet momentum, and regions of the span where the flap is not immersed in the jet on both the suction and pressure side. Moving the propeller down vertically increases the range of the wing, as the wing remains fully immersed in the jet up to higher flap angles. Increasing the propeller spacing leads to early separation, however the growth of the separation is slowed as less of the flap is affected by the jet.

The 2D modelling of the blown wing underpredicts the maximum lift coefficient of the wing at a low propeller vertical offset of y_p/c=-0.05 by 2% and overpredicts the maximum lift coefficient at y_p/c=-0.2 by 10% when compared to the experiment. Whilst the 2D modelling captures that the maximum lift coefficient increases when the propeller moves further below the wing centreline, this increase is overestimated compared to the experiment. The shortcomings of the 2D modelling in predicting the blown wing performance are discussed further in Chapter 8. The 3D Actuator disk model with swirl overpredicts the maximum lift coefficient of both the 2D model and the experiment for both propeller vertical offsets.

Whilst the optimum geometry predicted by the 2D model in Chapters 4 and 5 is valid for tightly spaced propellers, the increased maximum lift coefficient achievable with high spacing will be underpredicted by the 2D model for larger propeller offsets. In this study, the 2D method will get you to within a maximum lift coefficient of 0.4 of the measured value for a propeller offset of y_p/c=-0.05, and 0.05 for y_p/c=-0.2, each with a propeller spacing of s/D_p=1.1. However, this additional maximum lift due to increased propeller spacing has to be experimentally verified.

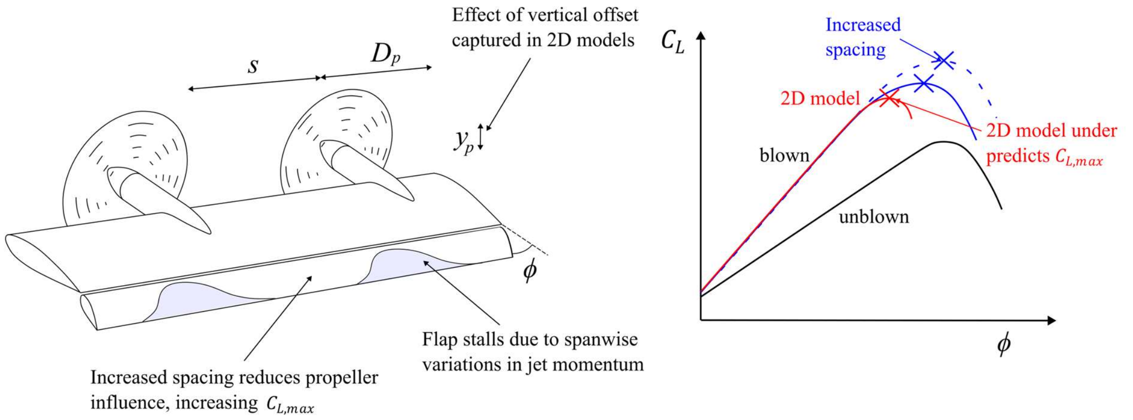

Figure 7.17: In this chapter, the mechanism of blown wing flap stall is identified, the effect of propeller position and spacing quantified, and 2D modelling is found to under-predict the real wing maximum lift coefficient.

8. Overall Aircraft Performance with a Blown Wing

8.1 Introduction

This chapter answers the final research question of Chapter 2: what is the overall benefit of fitting an aircraft with a blown wing using distributed propulsion? To do this, a power balance analysis [25] is conducted for the design space explored in Chapters 4 and 5. The power consumption in cruise of an aircraft fitted with blown wings is reported, relative to a baseline electric aircraft, designed in Section 8.3. The aircraft is assumed to have a fixed take-off weight, cruise speed and altitude, details of which are given in Table 3.2. The performance benefits presented in this chapter are those achieved by moving from a baseline electric aircraft with a conventional propulsion system, to a blown wing, and ignore the weight penalties associated with moving from a gas turbine to an electrical powertrain.

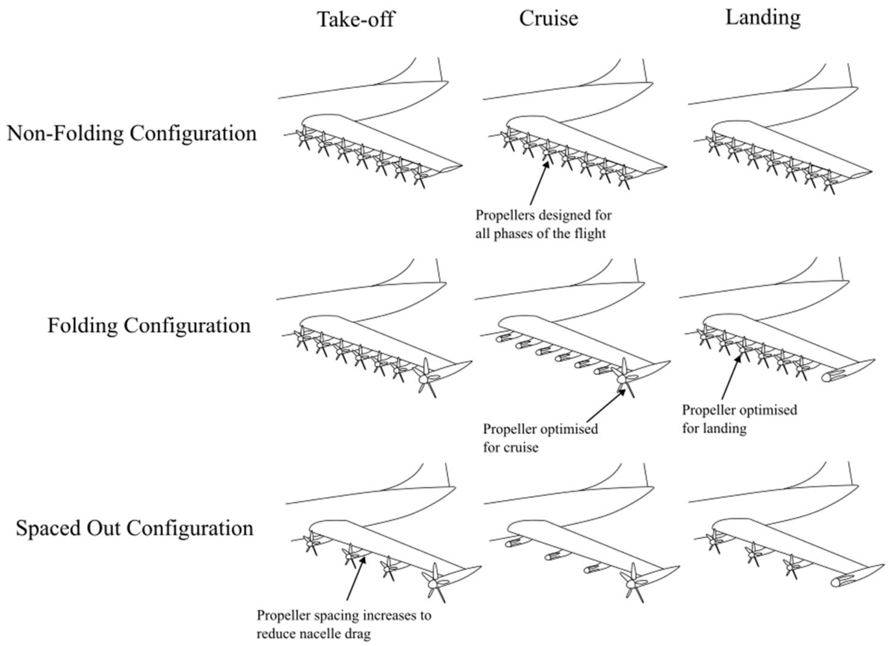

Figure 8.1: The final three design configurations investigated in this chapter: a non-folding propeller design, a design with leading edge propellers folded in cruise, and a design with fewer, spaced out propellers folded in cruise.

Three blown wing design philosophies are explored. The first design uses the leading edge propellers during all phases of the flight: take-off, cruise and landing. This requires the propellers to be efficient thrust producers in cruise whilst achieving useful wing drag reductions through blowing in landing and sufficient thrust in take-off. The second design folds the leading edge propellers away during cruise, with thrust provided by larger propellers mounted at the wing-tip. This allows leading edge propeller designs to be optimised for landing requirements and tip mounted propellers to be optimised for cruise requirements. The final design we investigate uses fewer folding propellers spaced out along the wing leading edge. This is only possible with a folding configuration in cruise as spaced out leading edge propellers would be unable to achieve efficient thrust production due to their higher disk loading. These approaches are shown in Fig. 8.1.

To calculate the overall performance of the blown wing in cruise, we draw upon both the numerical modelling, and experimental results of the previous four chapters. Chapter 4 developed a framework in which to compare different blown wing geometries, and quantify their benefit. A database of blown wing data using 2D models was generated, allowing the design space to be explored quickly. Chapter 6 showed that the 2D modelling used in Chapter 4 is representative of the on-design wing performance, even when real propeller effects such as circular jets and swirl are included. Chapter 7 showed that the 2D model under predicts the maximum lift coefficient of the blown wing, and so provides a safe under-estimate of the blown wing performance. In Chapter 5, the lift and drag impact of nacelles was quantified, and a low-order model developed to predict the nacelle drag for any nacelle geometry. The methods incorporated into this chapter are shown in Fig. 8.2.

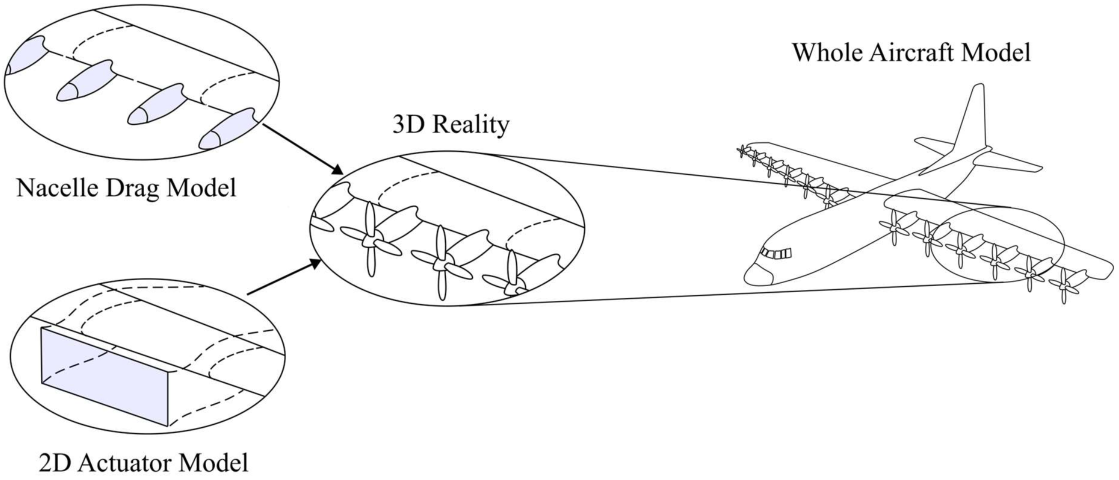

Figure 8.2: This chapter combines the 2D blown wing model from Chapter 4 and the nacelle drag model from Chapter 5 to establish the whole aircraft performance with blowing.

8.2 Aircraft Model Construction

The key sources of loss on the aircraft are shown in Fig. 8.3. Drela [25] developed a power balance method for aerodynamic flows which balances the work into the flow from the propulsors (in this case the shaft work from the propulsors, $P_{propulsor}$) with the losses and work done against the induced drag and gravity. This consists of the work done against the induced drag, $\dot{E}_{induced}$, work done against gravity, $W\dot{y}$, losses in the boundary layer, $\phi_{sufaces}$ and losses due to wasted kinetic energy in the propeller wake ϕ_{froude}.

The power balance can be expressed as,

$$\sum P_{propulsor} = \phi_{froude} + \dot{E}_{induced} + \sum \phi_{sufaces} + W\dot{y} \quad . \quad (8.1)$$

The required propeller thrust can be calculated from a force balance on the aircraft. The minimum induced loss propeller design code described in Appendix B calculates the propeller efficiency, and hence $P_{propulsor}$. In this section we look at the models developed for each of the terms in Fig. 8.3.

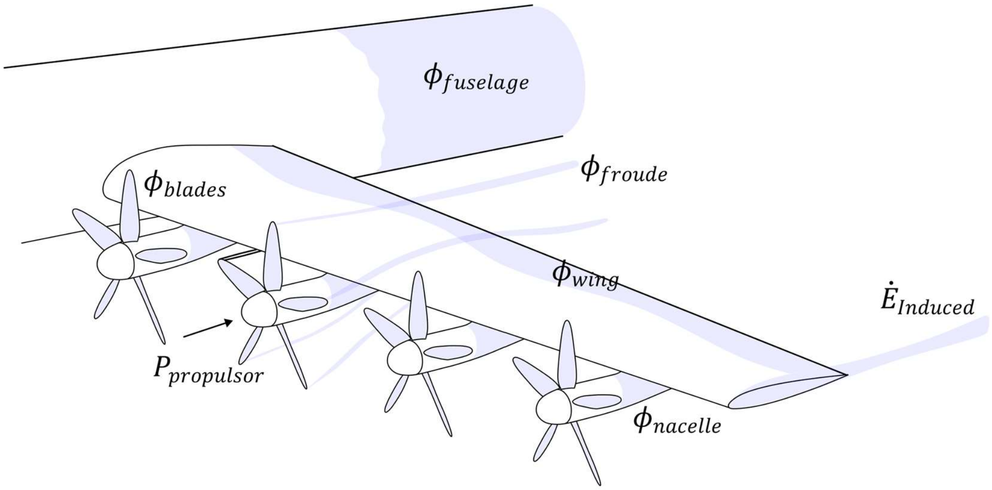

Figure 8.3: Work inputs to the flow from the propellers and the sources of loss modelled in this chapter when assessing the overall power requirements of the aircraft at cruise [37].

8.2.1 Viscous Drag Estimations

The viscous loss sources are split into five components,

1. Losses in the wing boundary layers, ϕ_{wing}.

2. Losses in the nacelle boundary layer, $\phi_{nacelle}$.
3. Losses in the fuselage boundary layer, $\phi_{fuselage}$.
4. Losses in the tail section boundary layer, $\phi_{empennage}$.
5. Losses in the propeller blade boundary layers, ϕ_{blades}.

Calculation of (1) consists of multiplying the predicted wing profile drag from Chapter 4 by the cruise velocity. The increased local velocity over the wing for the scenario where the wing remains blown in cruise is also accounted for when calculating the cruise lift coefficient. Loss (2) is modelled using the nacelle drag model developed in Chapter 5. The nacelle length and vertical offset is dependent on the blown wing geometry. Calculation of the nacelle diameter uses the same method discussed in Chapter 5 for the motor sizing. The model presented in Chapter 5 is inaccurate beyond $D_{nacelle}/c$=0.146. As spaced out propellers require these larger nacelle diameters, an additional empirical correction factor is developed in Appendix E to better fit the experimental data beyond this upper limit. Losses (3) on the fuselage are modelled using the same form factor model from Raymer used in Chapter 5 for rotated bodies. Losses on the empennage were taken as a fixed value of 27% of the fuselage drag. This was estimated from other calculations by Raymer for empennage drag and found to agree with the lift to drag ratio of the ATR-42. The fuselage and empennage is not modified in this thesis, so this approach was deemed sufficient. Propeller blade losses are modelled using the minimum induced loss (MIL) design code described in Appendix B.

8.2.2 Induced Drag Estimations

In the absence of propellers, the induced drag can be estimated as,

$$C_{D,Induced} = \frac{C_L^2}{\pi A_R e} \quad , \qquad (8.2)$$

where the span efficiency parameter, e, to take account of non-elliptically loaded wings, was taken as 0.85 in this study for cases without blowing. Stoll [72] predicted from RANS CFD that the span efficiency parameter can drop to 0.5 when the wing is immersed in the propeller wakes. This section aims to develop a better prediction for e in cruise with propellers blowing.

Miranda and Brennan [54] developed a method for calculating the modification to the induced drag due to blowing for low propeller disk loadings. The method assumes that the effect of the propeller jet is confined to the region within the jet area. The jet acts to modify the local up-wash onto the wing, as shown in Fig. 8.4, changing the tilt direction of the lift vector.

The perturbation velocities due to the propeller are calculated from the minimum induced loss design code at each blade section. The local upwash of the wing at a given span location is assumed equal to the propeller blade section exit conditions upstream of that location, with the propeller centred on the wing chord-line.

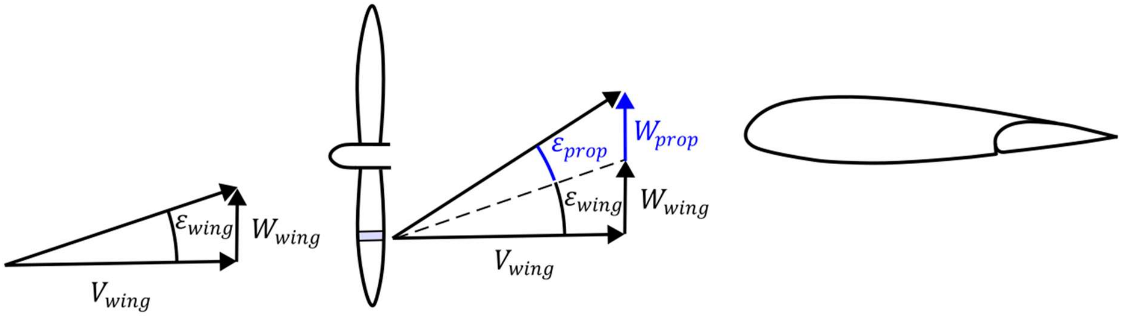

Figure 8.4: Model for calculating perturbations to the wing upwash angle due to the presence of propeller swirl The swirl angle increases the local upwash angle, and is modelled using blade element momentum theory.

The induced drag, due to the wing circulation, Γ_w, can be expressed as,

$$D_{induced} = \int_{-S/2}^{S/2} \rho V_\infty \Gamma_w \varepsilon_{wing} dz + \int_{-S/2}^{S/2} \rho V_\infty \Gamma_w \varepsilon_{prop} dz \quad . \quad (8.3)$$

The circulation of the wing is represented as a Fourier series,

$$\frac{\Gamma_w}{2V_\infty S} = \sum_{n=1}^{\infty} A_n \sin(n\varphi) \quad , \qquad (8.4)$$

with the spanwise coordinate, z represented parametrically as,

$$z = -\frac{S}{2}\cos(\varphi) \quad . \ (8.5)$$

The full derivation which substitutes Eq. 8.4 into the drag calculation, Eq. 8.3, can be found in Miranda and Brennan's work [54]. The key result is that when Eq. 8.3 is minimised, the minimum induced drag of the wing is,

$$C_{D,Induced}^{*} = \frac{C_L^2}{\pi ARe} - \frac{2{A_1}^{*} C_L}{e} - \pi AR \sum_{n=2}^{\infty} n({A_n}^{*})^2 \quad , \qquad (8.6)$$

with the coefficients, A_n, given by,

$$A_n^{\ *} = \frac{-1}{n\pi}\int_0^{\pi} \varepsilon_{prop}(\varphi)\sin(n\varphi)\sin(\varphi)\,d\varphi \quad . \quad (8.7)$$

The * prefix denotes that this is the minimum theoretical induced drag. In practice, the distribution of chord produced by this optimum may not be practical to design. This was partially accounted for by the introduction of the span efficiency parameter, e, taken as 0.85 in this study. The integration and summation of Eq. 8.6 and 8.7 were done numerically in MATLAB and found to converge for n >500.

To validate the use of this method, the model was applied to experimental data from Sinnige et al. [69]. Their test rig is shown in Fig. 8.5 (a). Experimental measurements of the difference in drag between placing the propeller at the wing mid-span, and at the tip, are reproduced from their work in Fig. 8.5 (b). For low thrust coefficients, up to C_T =0.04, the drag increases with wing-tip mounted propellers due to the presence of a corner separation at the nacelle-wing joint. The propeller geometry used was not specified in the paper, however it was possible to match the propeller characteristic presented in the work to an equivalent design using the minimum induced loss propeller code. This is shown in Fig. 8.6 (a).

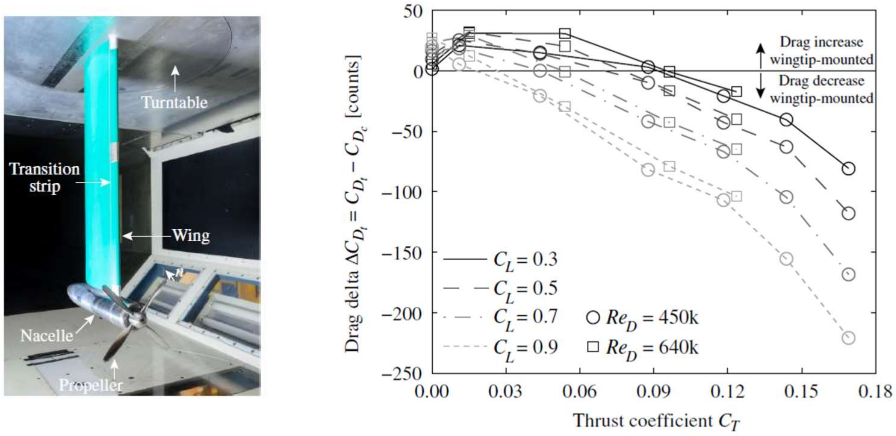

(a) (b)

Figure 8.5: Experimental work of Sinnige et al. used to validate the low-order induced drag model with upstream propellers [69]. Drag changes with tip propellers are reported for a range of wing lift coefficients and thrust settings.

Figure 8.6 (b) shows the comparison between the experimental drag data from Sinnige, and the low order model of Miranda and Brennen. The experimental drag values have been shifted such that the model and experiment agree at a thrust coefficient, C_T of 0.04. This was done in order to account for the viscous drag rise caused by the nacelle. Once this correction is made, the model is able to predict the induced drag change of the wing to within 15% across the tested range of lift and thrust coefficients, indicating that it can be used for quantifying the aircraft induced drag performance.

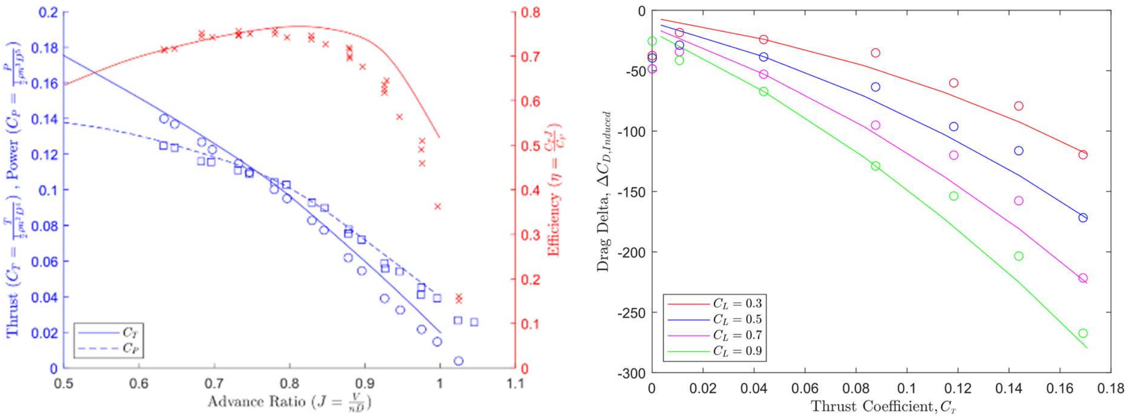

(a) (b)

Figure 8.6: Matching of the propeller data reported by Sinnige et al. [69] with the authors MIL design code (a) and comparison of the experimental data from Sinnige et al. [69] and the low-order model of Miranda and Brennen [54] (b).

8.2.3 Propeller Performance Estimations

The performance of the propellers is estimated using the minimum induced loss (MIL) design code presented in Appendix B. The hub diameter is determined iteratively from the diameter of the motor required. The tip diameter is determined by the specified blown wing diameter, D_p/c. The propeller number is set by the propeller diameter, wingspan and propeller spacing. The number of propeller blades was fixed at 5, and the tip Mach number, in all phases of the flight, was set to 0.8 [26]. This was done as an upper threshold for noise considerations. The MIL model does not account for compressible effects on the blade section lift and drag. However, the detailed design of high Mach number propellers is outside the scope of this work and it is assumed that the MIL code is able to correctly capture the trends in propeller performance even at high speed.

The propeller was assumed to be fixed pitch, a major benefit of electric propulsion as the efficiency of the motor does not vary significantly with rotation speed [56]. However, the propeller is required to operate throughout the flight envelope, and the propeller characteristic must be capable of producing the required thrust at each condition without exceeding the tip speed limit. Figure 8.7 shows an example propeller characteristic.

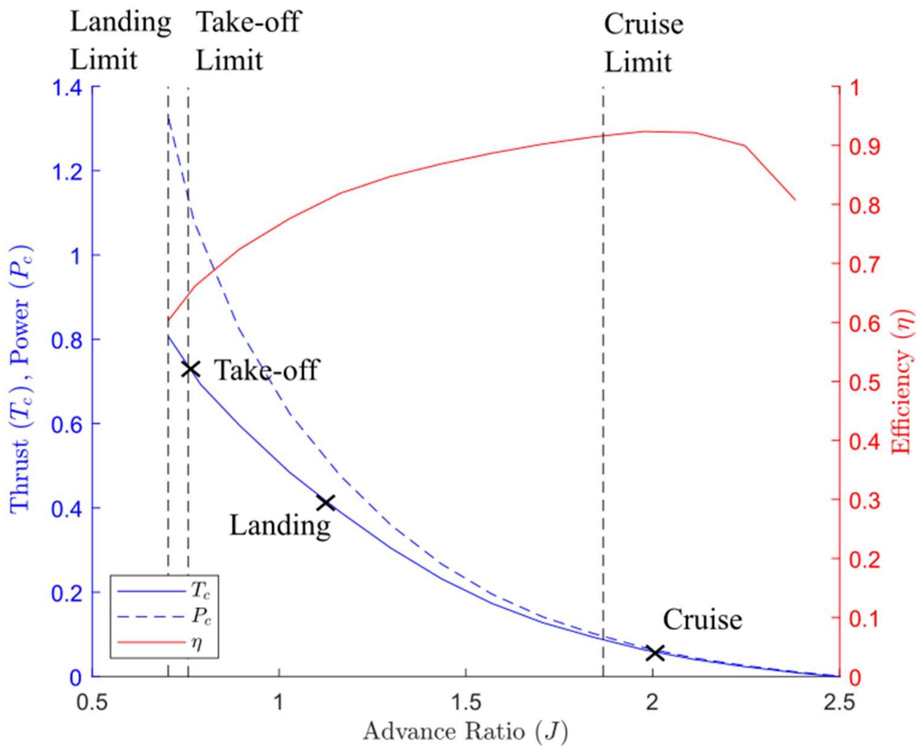

Figure 8.7: Propeller characteristic, solved with a minimum induced loss design code, identifying the thrust limits as the forward speed changes during phase of the flight due to propeller tip Mach number limits.

The different phases of the flight are labelled on the propeller characteristic. The advance ratio limit in take-off is lower than landing as the take-off speed is 8% higher than for landing (see Table 3.2). As the flight speed increases, the propeller advance ratio moves to a higher limit. The thrust coefficient required is highest at take-off. At cruise, the thrust coefficient is low due to the high cruise speed. The MATLAB code initially designs the propeller for optimum cruise performance, then solves the off-design take-off and landing cases to ensure the required thrust can be achieved, with the tip Mach numbers limited to 0.8. For aircraft configurations where the propellers are used in both takeoff, cruise and landing, the take-off thrust requirement was found to be the limiting case, and the design thrust coefficient was iteratively modified until the required thrust could be generated for all three cases within the propeller tip speed limits. For aircraft configurations with foldable propellers, the leading edge distributed propellers were sized for the landing thrust requirements, to minimise the nacelle diameters, and the tip propulsors were sized to meet the cruise thrust, and any deficit in take-off thrust requirement not supplied by the leading edge propellers during take-off. In all cases, it was found that the tip propellers could be sized for cruise, the leading edge propellers sized for landing, and both systems operating together could supply the required take-off thrust.

8.2.4 Aircraft Model Flow Diagram

Figure 8.8 shows the iterative scheme to size the aircraft.

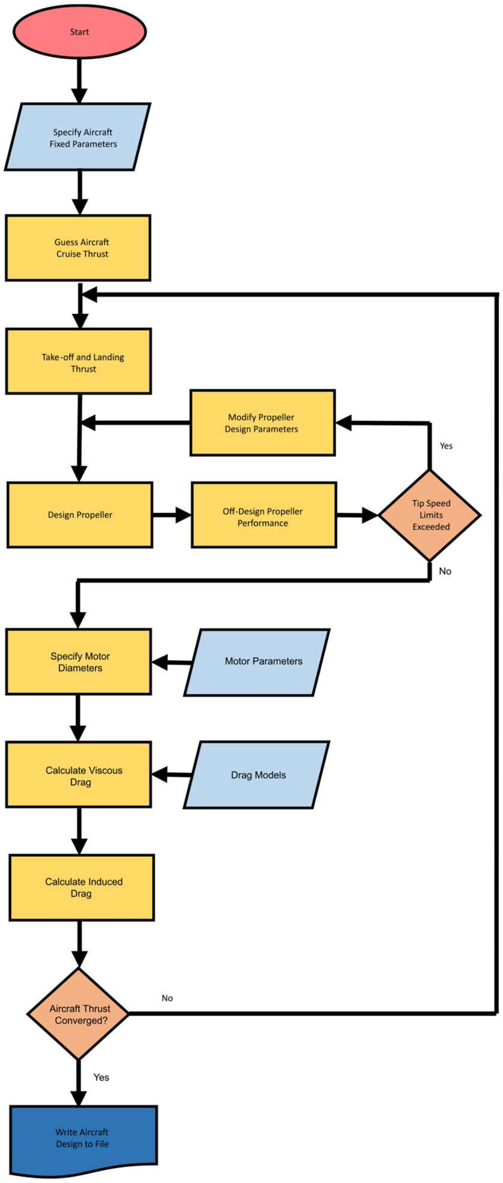

Figure 8.8: Aircraft solver used to model the aircraft performance in this chapter. Take-off and landing thrust limits are set by the design constraints described in Chapter 4. The propeller thrust and motor diameter is iteratively changed until the propeller thrust matches the airframe drag.

The aircraft weight is assumed constant, reducing the complexity of the analysis. This assumption is validated when weight is analysed later in this chapter. Fixed aircraft parameters, such as the blown wing non-dimensional geometry, cruise and take-off/landing conditions and the aircraft weight are specified. From the non-dimensional blown wing geometry, the analysis presented in Chapter 4 is applied to calculate the wing area.

The iterative scheme consists of an outer loop to converge the propeller thrust requirements, and an inner loop to ensure the propeller can operate within the full flight envelope. For each inner loop, the propeller is designed based on the current known thrust requirements, and the design point iteratively modified until the tip speeds do not exceed the imposed limits. Once this loop converges, the motor diameter is calculated, allowing the nacelle drag to be estimated using the models from Chapter 5. The gearbox needed to generate the required motor torque and rpm is also calculated. Other drag terms are calculated and the reduction in induced drag due to blowing is predicted from the method described in Section 8.2.2.

The wing profile drag is calculated using the landing constraint diagram and 2D CFD blown wing data presented in Chapter 4. Calculation of each of the drag terms allows the thrust for level flight in cruise to be calculated, and this is fed back into the input of the solver. The solver typically takes ~30 seconds to converge with sensible initial guesses for the aircraft thrust and propeller geometry. Each design is written to a file allowing subsequent post-processing.

Versions of the code with and without tip mounted propellers were developed, as well as cases with and without propellers folding in cruise.

8.3 Design of a Representative Reference Aircraft

The aircraft designed in this chapter are based on the ATR-42. Details for the baseline aircraft are included in Table 3.2. As the aim of this chapter is to assess the aerodynamic benefits of a blown wings, and not the full design of an electric aircraft, the maximum take-off weight of the aircraft is assumed constant and equal to that of the ATR-42, as well as the cruise speed and altitude. A fully electric aircraft of this maximum take-off weight would experience a significant penalty in either payload or range due to the weight of the batteries, however a hybrid-electric aircraft may only experience a small penalty, and still enable distributed propulsion on the aircraft [80]. The choice of powertrain is outside the scope of this work and the results from this section will deal only with the relative benefits of a blown wing compared to a conventional propulsor layout.

Whilst it is tempting to compare the blown wing aircraft with the ATR-42, this is an unfair comparison for assessing the aerodynamic benefits of blown wing technology. Improvements in aerodynamic performance can be made to the ATR-42 with electric power on board without distributed blowing. These improvements are first incorporated to design a more representative datum case to compare to aircraft with blown wings.

The new baseline aircraft maintains the ATR-42 architecture but retrofits the engine with electric motors. The nacelles housing these motors can be streamlined relative to the Pratt and Whitney PW100 turboprop used in the ATR-42. The same propeller diameter as the ATR-42 is used. The breakdown of the power consumption is shown in Fig. 8.9. An 8.8% reduction in the power consumption of the aircraft at cruise is possible with the slimmed down electric motors. The aspect ratio of the ATR-42 nacelle is 2.9. This is outside the accurate range of the form factor models reported in Chapter 5, and so it is likely the drag is being over-predicted. However, the aspect ratio of the electric ATR is 5.4, which is within the dataset tested to develop the form factor model. This allows us to use the electric ATR as a reference aircraft with confidence.

Also shown in Fig. 8.9 is a second, “radical design” of electric ATR, where the propellers are moved to the wing tips to reduce the induced drag of the wing. Whilst this design reduces the power consumption by 13.6% compared to the ATR-42, it is unlikely to be practical to implement. In the event of an engine out condition, due to the yawing moment of the propeller thrust vector, either the opposing tip propeller must also be shut down (it is predicted the pilot would have ~1.5 seconds to achieve this before the aircraft enters an unrecoverable spin), or the tail section is increased in size to provide sufficient rudder to oppose the yawing moment. The former is unacceptable and the later is likely to offset any drag reduction benefit from the tip propellers.

The analysis of this section assumes the maximum take-off weight of the aircraft, cruise altitude and cruise speed remain constant. With a hybrid-electric aircraft, these assumptions may be realisable in practise [80] however for a fully electric aircraft, the weight of the batteries will increase the empty weight, reducing either the payload or range of the aircraft. If the designer reduces the range, the cruise altitude may be reduced to decrease the time spent in climb. Reducing the cruise altitude will reduce the aircraft speed, to maintain the same Mach number and increase the design lift coefficient.

If instead the aircraft maximum take-off weight was allowed to grow to maintain the design payload and range, the wing area would need to grow in order to maintain the same take-off and landing speeds. With the same wing loading, the design altitude and speed would be kept constant. The fuselage drag may increase, depending on the volume of batteries used, and the empennage drag would increase due to the larger wing. In either case, the total drag (and power requirements) would increase due to the additional weight of the aircraft [86]. Detailed trajectory optimisation, and weight estimation of the electric propulsion system is outside the scope of this thesis but should be born in mind for more detailed analysis using the data of this chapter.

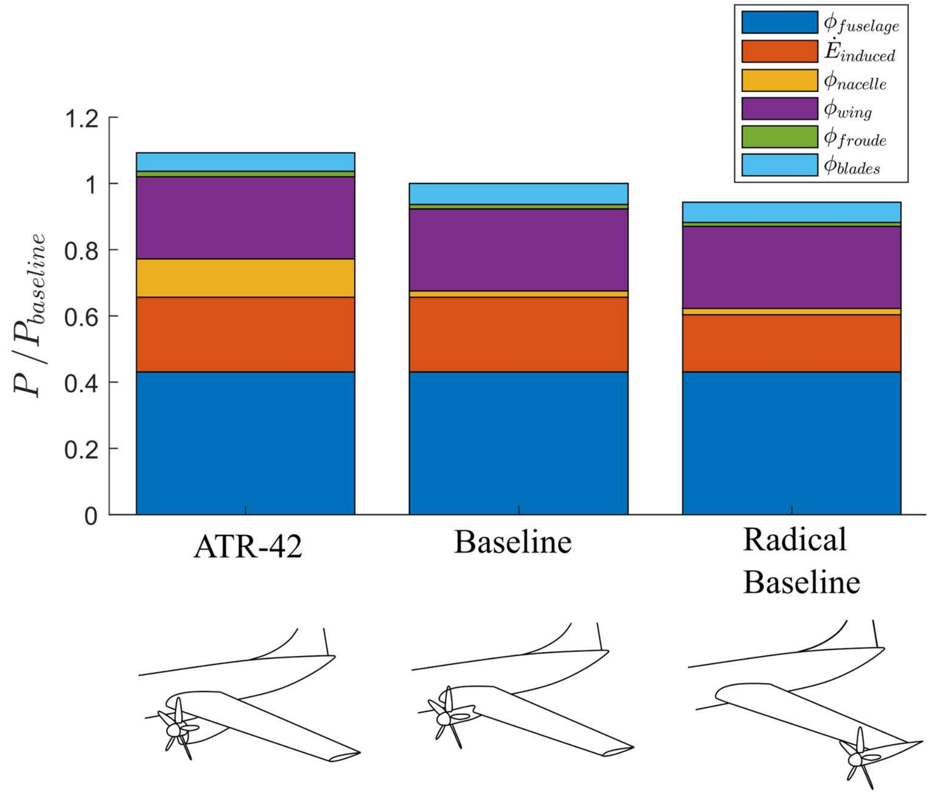

Figure 8.9: Cruise power consumption for different choices of reference aircraft. Both electric designs, shown on the right of the figure, offer a power saving compared to the ATR-42 baseline design. The radical baseline was not adopted due to its poor one-engine out performance.

8.4 Performance Benefits of the Blown Wing

In this section, the relative performance of an aircraft with a blown wing is calculated for the non-folding configuration, where the propellers are deployed in take-off, landing and cruise.

Although the induced drag reduction is maximised by placing propellers at the wing tips, some induced drag reduction is still achieved by placing the propellers along the full wing span. The variation in wing up-wash due to the leading edge propellers is modelled across the full wing span in order to calculate the induced drag reduction from Eq. 8.6. The propellers are assumed to be rotating up at the fuselage, down at the tip as this acts to reduce the induced drag term. The propellers are designed for efficient cruise performance. Each propeller has the same diameter to wing chord ratio, and non-dimensional position relative to the wing.

Figure 8.10 shows a map of the design space, using the 2D actuator disk simulations presented in Chapter 4, to calculate the blown wing benefit. The power requirement for the aircraft when fitted with leading edge propellers is plotted for different propeller sizes and positions. The 3D propeller diameter, D_p is plotted on the x-axis, rather than the average jet height $\overline{D_p}$. A fixed streamwise location of x_p/c=-0.25 is used in this chapter. It is possible to achieve a 10.5% reduction in the power consumption of the aircraft, relative to the baseline using leading edge blowing. This is achieved for a propeller positioned in line with the wing chord, and a propeller diameter to wing chord ratio D_p/c=0.9, giving 18 propellers along the wing span [37].

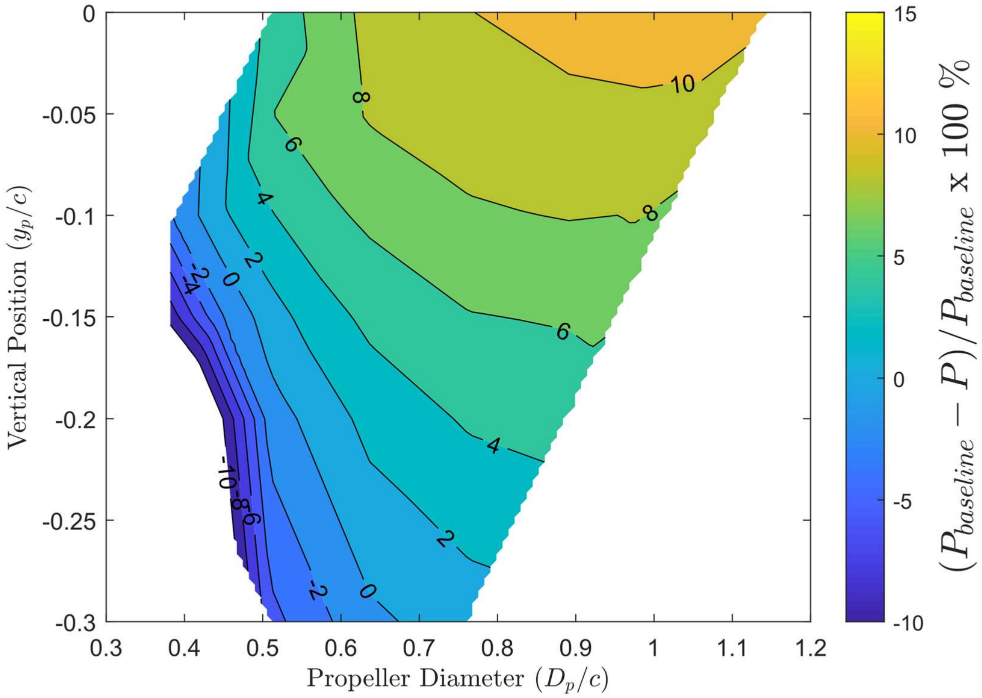

Figure 8.10: Cruise power consumption for different blown wing geometries with the propellers deployed in take-off, cruise and landing [37]. The propeller axial offset is x_p/c=-0.25. A maximum power reduction of 10.5% can be achieved with propellers positioned in line with the wing chord, and a propeller diameter to wing chord ratio D_p/c=0.9, giving 18 propellers.

The shape of the performance map consists of a trade-off between the drag of the airframe, and the propulsive efficiency of the aircraft. Figure 8.11 shows maps of the propeller efficiency at take-off and cruise.

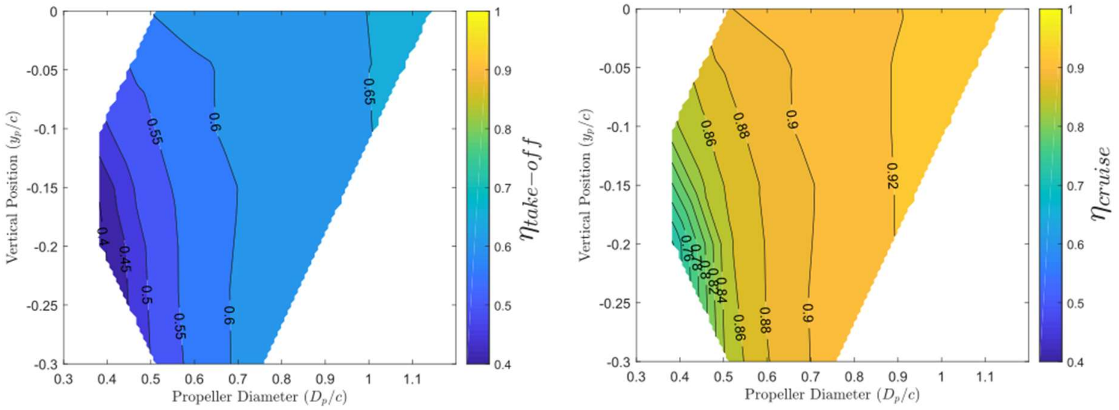

(a) (b)

Figure 8.11: Propeller efficiency for different propeller diameter and vertical offsets from the wing at take-off (a) and cruise (b). The take-off efficiency is low due to the high thrust requirements.

For the optimum design identified in Fig. 8.10, the efficiency of the propellers is 92.0% at cruise, and 64.1% during take-off. Reducing the propeller diameter increases the disk loading, reducing the propulsive efficiency and increasing the losses on the propeller blades. The efficiency is a weak function of propeller location as this affects the overall thrust requirements of the propellers.

The effect of moving within the design space on the profile drag of the wing and nacelles has been previously discussed in Chapters 4 and 5 and will not be repeated here. The induced drag reduction achieved with the blown wing is greatest for small fast jets. This is because the swirl from these jets is higher than the wider, slower jets and maximises the tilting of the wings lift vector. Bulkier motors are required for take-off due to the higher power requirements and lower propeller efficiencies, increasing the nacelle drag contribution and also favouring small vertical offsets [37].

For the non-folding blown wing design, the maximum power saving possible is a 10.5% reduction in cruise power consumption. This is achieved with propellers with a streamwise offset of x_p/c=-0.25, no vertical offset of the propeller axis from the wing chord-line, and a propeller diameter to wing chord ratio D_p/c=0.9. This design choice is a compromise between propeller efficiency, and increased blown lift coefficients.

8.5 Performance Benefits of Folding Propellers in Cruise

We now consider the configuration where the leading edge propellers are folded in cruise, and the cruise thrust is provided by additional, larger propulsors. This aircraft architecture is shown schematically in Fig. 8.12.

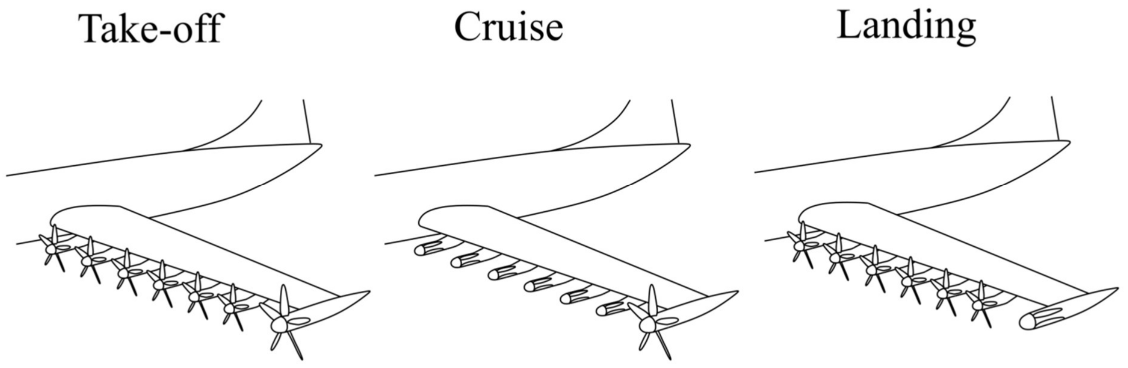

Figure 8.12: Aircraft configuration during different phases of flight for an aircraft fitted with folding propellers.

Whilst the tip propellers have been shown in Fig. 8.12 to stow away during landing, NASA [57] propose to windmill these tip propellers to increase drag and enable higher leading blowing. This is not modelled in this chapter and the region of the wing behind the tip propeller is assumed to be unblown.

As the design variables increase, there are a number of ways the designer may wish to deploy, and fold away, sources of thrust around the wing; too many to be tried exhaustively in this Chapter. For this work, the leading edge blowing propellers are sized for landing, and the tip-propellers are sized for cruise efficiency in the first instance. Checks are made to ensure the take-off climb rate can be achieved. It was found that the additional thrust from the leading edge propellers contributed between 40% and 60% of the total thrust in take-off, which was sufficient to allow the tip propellers to be optimised for cruise in most instances. The leading edge motors were always sized for landing, reducing the nacelle diameters and hence drag to a minimum. Therefore, the addition of the tip propellers gives the designer the freedom to decouple the take-off and landing motor requirements, optimising the sizing of both systems for reduced drag (and hence weight).

In order for the leading edge propellers to sit flush against the nacelles during cruise, the nacelle length must be greater than the folded propeller blade section. For this chapter, we assume the propeller blade section to be folded has a length equal to $r_{tip} - r_{hub}$ and pivots about the propeller centreline, positioned at x_p. A viable design requires that,

$$x_p > r_{tip} - r_{hub} \quad , \quad (8.8)$$

with the geometry parameters defined in Fig. 8.13.

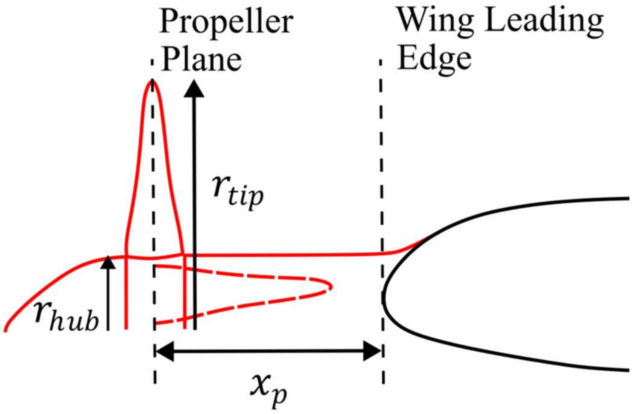

Figure 8.13: Folding designs require $x_p > r_{tip} - r_{hub}$ in order for the propeller blade to not interfere with the wing leading edge.

The performance map for the blown wing with folding propellers is shown in Fig. 8.14, with contours of required propeller offset, x_p/c overlaid onto the graph. Initially we consider the case of zero spacing, s/D_p=0. All the calculations in this chapter have used CFD data with a propeller horizontal offset of x_p/c=-0.25, however, as seen in the figure, larger horizontal offsets are required to stow away the largest propellers considered. To the right of x_p/c=-0.25 in the figure, the propeller diameter is too large to fold back against the nacelle during cruise, invalidating the analysis. By folding the propellers away in cruise and relying on tip propellers, the power consumption has decreased by 12.2% relatively to the conservative baseline, an additional 1.7% compared to the non-folding case. This is achieved at a smaller propeller diameter to chord ratio of D_p/c=0.64, with the propeller placed at x_p/c=-0.25, y_p/c=-0.05. There are 24 leading edge propellers along the full wing span and two tip propellers for this configuration [37].

Because the cruise and leading edge propellers are now optimised for their respective function, the tip propeller efficiency increases by 2.4% relative to the non-folding case. The additional leading edge nacelles increases the leading edge nacelle drag by 24% and the overall nacelle drag increases by 68% due to the additional nacelles of the tip motors. The induced drag increases by 6.3% as, whilst the jet is now concentrated at the wing tip where it is most effective, the propeller efficiency is higher than for the non-folding scenario analysed previously, reducing the amount of swirl to modify the wing up-wash. Decoupling the landing and cruise thrust production allows smaller jets to be used without incurring a propulsive efficiency penalty, decreasing the profile drag by 13% compared to the non-folding case [37].

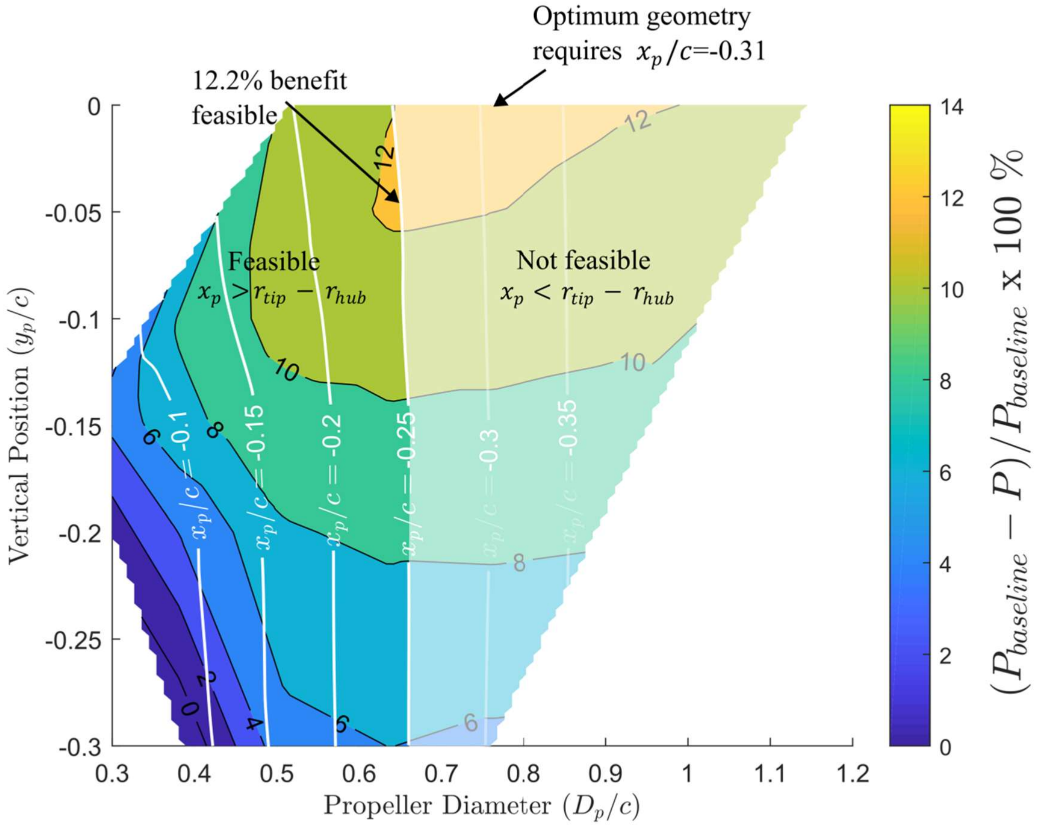

Figure 8.14: Power consumption in cruise for the folding propeller configuration for different blown wing geometries [37]. The propeller axial offset is x_p/c=-0.25. Non-feasible folding designs have been shaded out.The power consumption has decreased by 12.2% relatively to the baseline with a propeller diameter to chord ratio of D_p/c=0.64, with the propeller placed at x_p/c=-0.25, y_p/c=-0.05.

The map in Fig. 8.14 represents aircraft designed with a horizontal offset of x_p/c=-0.25. An additional 0.1% improvement in power consumption is achievable by moving to y_p/c=0,

D_p/c=0.76 in the design space map, however the nacelle length must be increased to x_p/c=-0.31 to allow this to happen. With this additional nacelle length, the power reduction of the configuration drops from 12.3% to 11.9%. Conversely, it is likely that reducing the nacelle horizontal offset further will reduce the nacelle drag further and produce an additional benefit, however further work is required to understand the close coupling of propellers and wings which may limit the closest proximity of the propeller to the wing.

8.6 Performance Benefits of Propeller Spacing

The top-hat model, developed in Chapter 6, allows the effect of spacing on the design space to be captured to a first order. As the optimum geometry for the non-folding architecture is heavily dependent on the propeller efficiency, increased propeller spacing will always lead to a reduction in performance due to the higher disk loading this creates. For the folding configuration, the de-coupling of the thrust production in landing and cruise opens up the possibility to space out the propellers. For this architecture, the variation of performance with spacing for four different propeller vertical offsets, y_p/c=-0.05, -0.1, -0.15 and -0.2 using the top-hat model is shown in Fig. 8.15. The propeller diameter is fixed at D_p/c=0.64, the optimum feasible diameter identified for the zero spacing case considered previously [37].

For the optimum design, increasing the leading edge propeller spacing to s/D_p=0.59 improves the performance by 0.5% to a 12.7% reduction in cruise power consumption over the baseline aircraft. For spacings greater than this value, the increase in the nacelle diameter (due to higher loading of the propellers), outweighs any benefit from reduced nacelle number, leading to a net increase in drag. The step changes in the graph are due to the integer, even propeller number required along the span. Off-design, the nacelle drag is more significant, due to the additional fairing drag (which does not scale with nacelle diameter). Greater performance benefits of 1.5% can be achieved with a higher spacings of s/D_p=0.59 for y_p/c=-0.2. Greater spacings than those shown in Fig. 8.15 could be used, however the thrust coefficient achievable will eventually be limited by the propeller design [37].

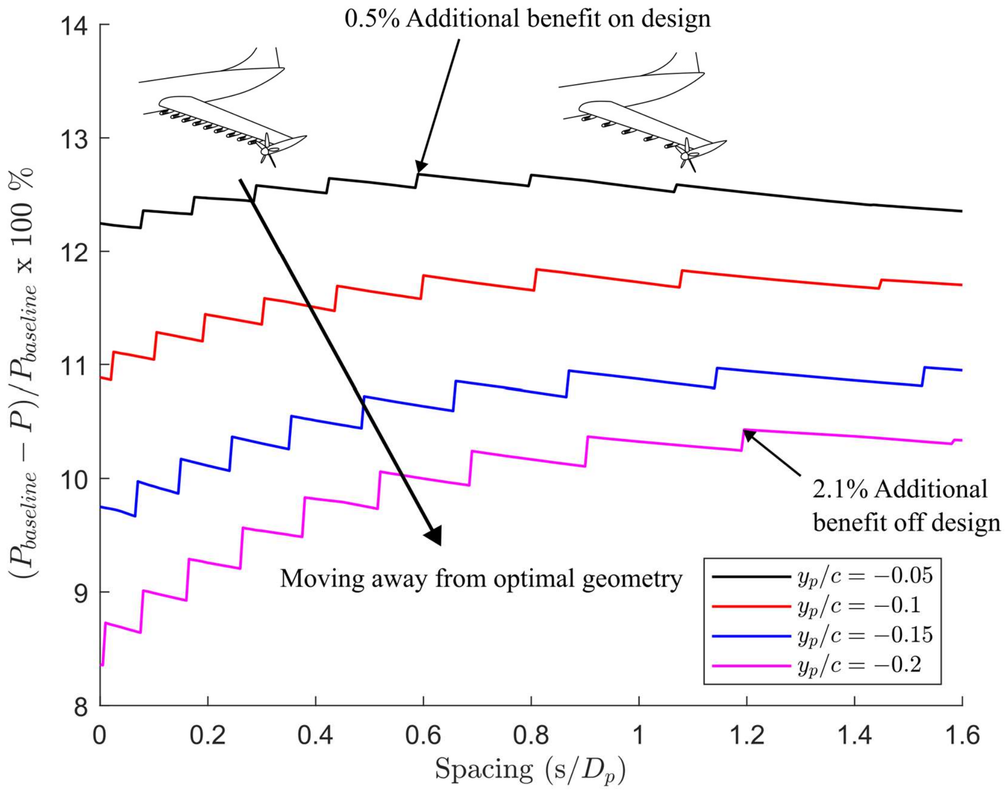

Figure 8.15: Power reduction in cruise achievable with varying propeller spacing s/D_p and vertical offset y_p/c [37]. For the optimum propeller vertical offset, an additional 0.5% power saving can be achieved by increasing the propeller spacing to s/D_p=0.59.

The calculated losses for the folding and non-folding optimum designs are shown relative to the baseline case in Fig. 8.16, along with the losses in the system for the optimum spaced out configuration. The fuselage and empennage account for 43.4% of the aircraft power consumption, and is equal for each configuration. Moving to distributed propulsion reduces the induced drag by 17.5% for the non-folding case and 12.3% with the folding configuration compared to the baseline. The nacelle drag increases for all the distributed propulsion technologies, a factor of 1.77 for the non-folding case, and 2.98 for the folding case. Spacing the propellers out reduces this factor to 2.48, a 16.8% reduction compared to the tightly spaced case. The profile drag of the wing is reduced by 28.8% and 38% for the folding, and non-folding cases respectively and 37.0% for the spaced out case. This is because folding the propellers allows for the optimal blowing configuration to be chosen, however the maximum lift is reduced marginally by spacing out the propellers. Whilst the folding and non-folding drags are identical to within 0.5%, the losses from the propellers is higher for the non-folding case, due to the reduced efficiency of the smaller leading edge propellers during cruise [37].

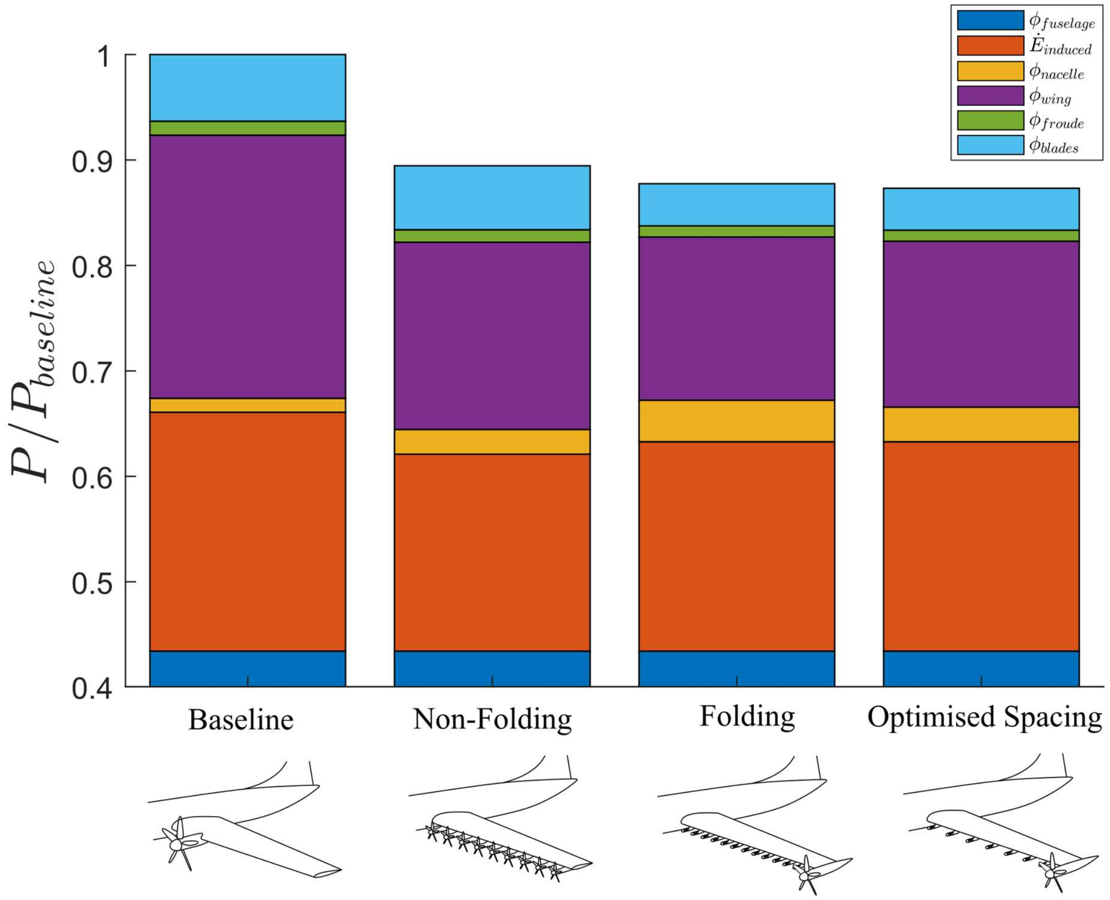

Figure 8.16: Power consumption during cruise for optimum folding and non-folding blown wing configurations [37]. A maximum 12.7% reduction in cruise power consumption can be achieved with a blown wing with folding propellers spaced out to s/D_p=0.59.

8.7 Uncertainty in the Estimated Power Consumption

The estimated power consumptions calculated in Section 8.6 for the different propulsion systems are subject to uncertainty due to the modelling methods used. In this section, uncertainties are estimated for each of the major sources of drag modelled: induced drag, nacelle drag and wing profile drag. To estimate the uncertainty, each drag estimate was perturbed to see the effect on the predicted performance.

Figure 8.17 shows the estimated power consumption benefit at cruise using both the 2D CFD data of Chapter 4, and the experimental lift and drag measurements of Chapter 6 for four different vertical offsets, y_p/c=-0.05, y_p/c=-0.1, y_p/c=-0.15 and y_p/c=-0.2. Two propeller spacings, s/D_p=0.05 and s/D_p=1.1 are plotted.

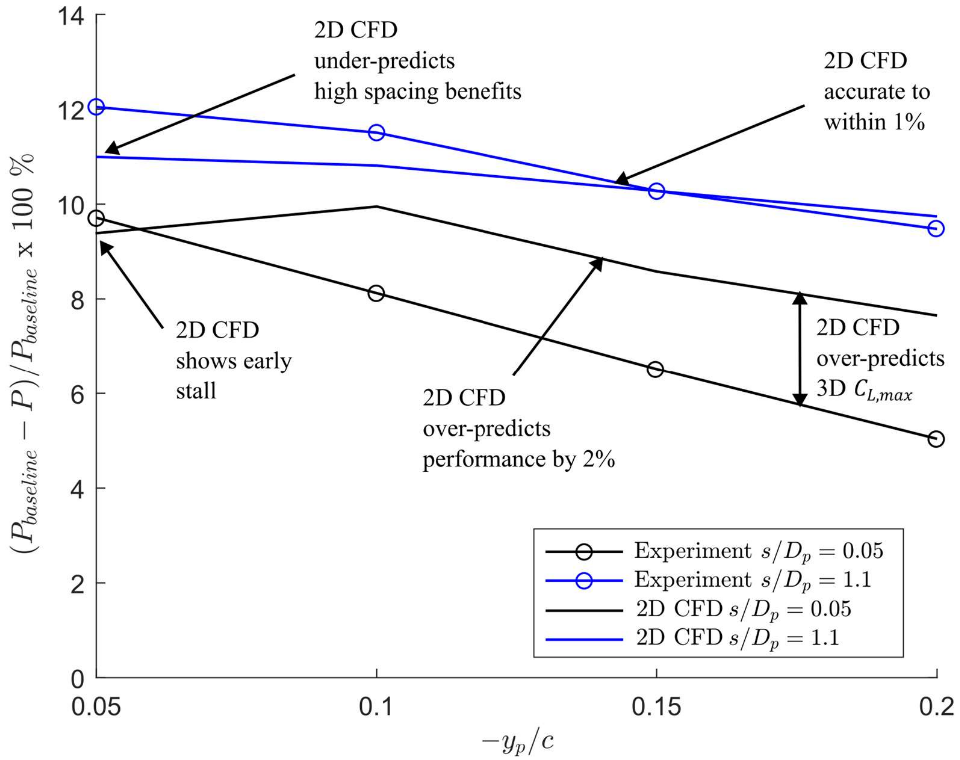

Figure 8.17: Power consumption during cruise predicted by both the 2D CFD model used elsewhere in Chapter 8, and the experimentally measured lift and drag presented in Chapter 6. 8 propeller positions are shown, y_p/c=-0.05, y_p/c=-0.1, y_p/c=-0.15 and y_p/c=-0.2 with s/D_p=0.05 and s/D_p=1.1.

The experiment predicts that for a small spacing of s/D_p=0.05, the maximum benefit is a 9.7% decrease in power consumption at cruise, using a small vertical offset of y_p/c=-0.05. For y_p/c=-0.05, the 2D calculation stalls prematurely leading to a 0.2% under prediction of the performance relative to the experiment. Increasing the vertical offset reduces the experimental benefit to a 5% improvement at y_p/c=-0.2, 2% lower than the 2D model prediction. The higher $C_{L,max}$ predicted in the CFD therefore leads to a 2% error in the predicted power reduction at cruise for tightly spaced propellers with s/D_p=0.05

Moving the propellers apart, from s/D_p=0.05 to s/D_p=1.1 achieves an additional 2.4% benefit in power saving at cruise for y_p/c=-0.05 and a 4.6% benefit for y_p/c=-0.2. For the higher spacings with s/D_p=1.1, the 2D model and experimental results agree to within 1% with the 2D model underpredicting the benefit at low propeller vertical offsets, due to the CFD being unable to predict the increase in $C_{L,max}$ seen in Chapter 7 for spaced out configurations. The results of Fig. 8.17 show that the estimated power consumption is overestimated by 2% by the 2D CFD model used in this chapter for small propeller spacings, but that the estimated power consumption is underestimated by 1% for larger propeller spacings of s/D_p=1.1. Both CFD and experiment predict the same reduction in performance with increased propeller vertical offset.

It was shown in Fig. 8.5 that the induced drag model can capture the reduction in drag due to propeller blowing to within 15%. By decreasing this predicted induced drag reduction by 15%, it was found that the power consumption predicted for the optimal non-folded geometry by the model decreased from 10.5% to 9.9%, a 0.6% reduction. This is to be expected, as the reduction in induced drag accounts for 3.5% of the power savings reported for the unfolded propeller case, and 15% of this saving gives 0.5%. The remaining 0.1% reduction in performance is due to the additional loss in the more highly loaded propellers. When the optimal folded geometry has its induced drag reduction decreased by 15%, the power saving drops from 12.2% to 11.8%. As the tip propeller is more efficient, and the induced drag decrease lower with the folding geometry, the effect of uncertainties in the induced drag modelling are less significant.

It was shown in Chapter 5, and Appendix E, that the nacelle drag model is able to accurately capture the nacelle drag estimate over a range of nacelle vertical and horizontal offsets and nacelle diameters. However, the nacelle diameter predicted in the aircraft model is determined by the predicted diameter of the motor. The motor used in the model has a power density of 16.5 kW/L [39] however there is some uncertainty in the achievable power densities of future electric motors. To account for this uncertainty, the power density was reduced by a factor of 2, increasing the motor diameter by 26%. For the optimal folding propeller geometry, increasing the motor diameter by 26% leads to an 11% reduction in power consumption at cruise, a drop of 1.2%. For the optimal non-folding propeller geometry, increasing the motor diameter by 26% reduces the power consumption benefit to 9.8%, a reduction of 0.7%.

The results of this uncertainty analysis suggest the predicted improvement in power consumption at cruise is most sensitive to the diameter of the motor for the folding propeller geometry, due to the high number of nacelles, and most sensitive to the induced drag prediction for the non-folding geometry.

8.8 Aircraft Weight Penalties

In the proceeding analysis, the aircraft weight has been assumed constant. Our reference aircraft is electrically powered, so the power source weight is assumed to be constant between the baseline and blown case (in practice the more efficient distributed blown wing should allow a smaller power plant to be fitted, reducing weight). However, the blown wing does produce additional weight penalties compared to the baseline aircraft. These consist of cable weights to deliver the electric power along the wing to the motors, weights of additional electric motors and epicyclic gearboxes, heat exchangers, nacelles and a structural re-design of the wing due to the increase in aspect ratio and weights of the nacelles and motors. In this section, the additional weight of the wing due to the increased aspect ratio is predicted, as well as the weight of the motors, gearbox and heat exchangers.

First we consider the weight of the wing box structure. A model was developed, shown in Fig. 8.18, for the structural design of the wing box section. The spar caps are treated as point masses, placed at 20% and 60% of chord respectively. The spar flange thicknesses and skin thickness were varied to reduce the total mass. Failure from buckling, and bending moment were both calculated. Engines were treated as point masses and the wing loading was assumed elliptical.

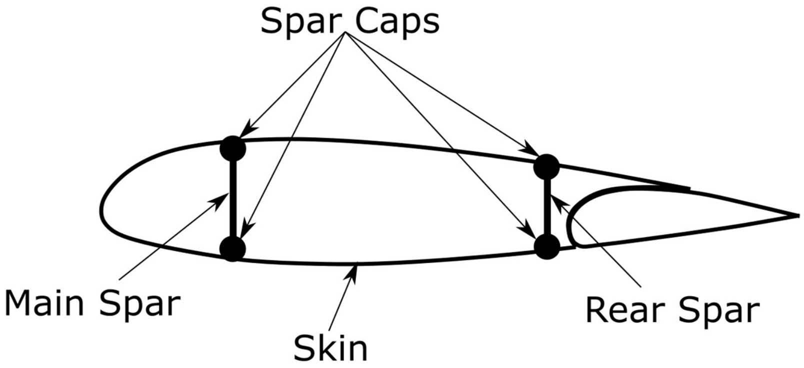

Figure 8.18: Simplified wing box model used to estimate changes to wing weight when re-sized with a blown wing. Spar caps are treated as point masses with spars at 20% and 60% of the wing chord.

Figure 8.19 shows the results of the analysis for a fixed span aircraft, with variable wing chord (as used in the modelling thus far), and a fixed area, variable span aircraft, which could aim to reduce induced drag through higher aspect ratio.

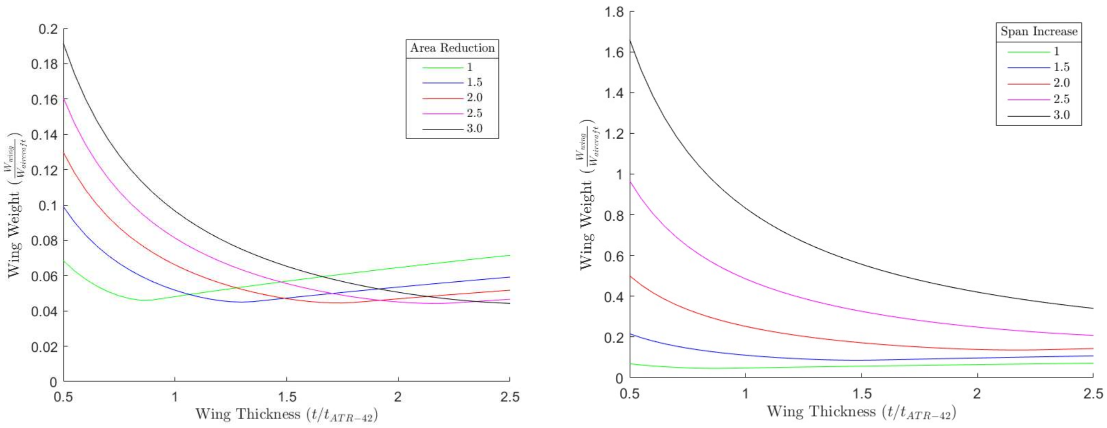

(a) (b)

Figure 8.19: Structural weight calculations for fixed span (a), and fixed area (b). The weight penalty of reducing wing chord to increase aspect ratio is an order of magnitude lower than increasing wing span.

The results show that there is nearly an order of magnitude reduction in the weight increase by using fixed span, variable chord, rather than fixed area, variable span to increase aspect ratio. The data is normalised by the ATR-42 design values, using the NACA-43018 section geometry. For no change to the wing geometry, the optimum structural thickness is around 85% of the actual design wing thickness, giving confidence that the wing box model is representative. For very thick wings, reducing the wing area is beneficial as the mass of the wing skin becomes more important than the wing box structure. The optimum designs identified in Section 8.4 and 8.5 are able to increase the wing lift coefficient by 50% during take-off and landing. For a wing thickness of half the ATR-42, the wing weight increases by 54%. However, for equal wing thicknesses, as modelled in this work, the weight change is negligible, around 0.5% of the aircraft take-off weight.

We next consider the motor, gearbox and heat exchanger mass. The mass of the motors (with integrated gearbox and heat exchanger) required for both folding and non-folding blown wing configurations is shown in Fig. 8.20. The motor mass (including an integrated gearbox and heat exchanger) was scaled from the data in [39], assuming a constant power density. The motor weight fraction for the baseline aircraft is 1.57%. As the power density of the motors is assumed constant, the total motor weight is a reflection of the worst case power usage of the aircraft in the flight cycle. The motor weight always increases with both the folding and non-folding configurations.

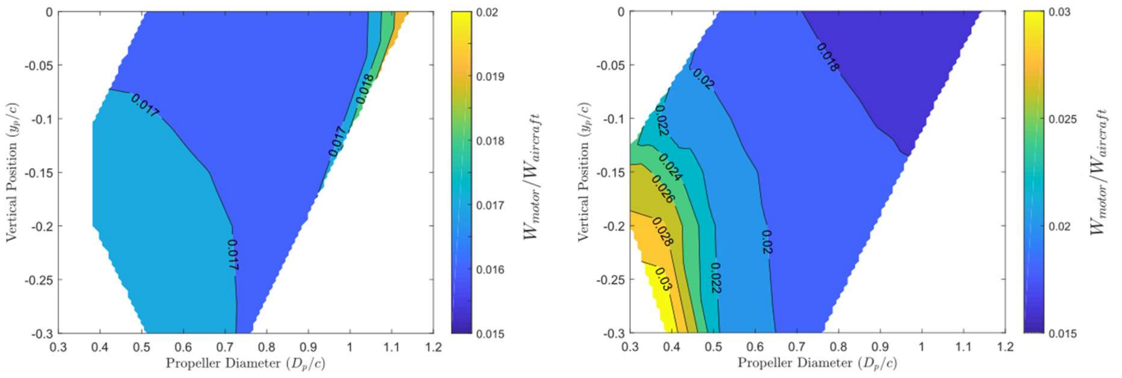

(a) (b)

Figure 8.20: Motor weights for non-folding (a) and folding (b) blown wing geometries. The motor weight fraction for the baseline aircraft is 1.57%. Folding propellers suffer from higher motor mass fractions, however these occur in regions of the design space with poor overall performance and the motor mass fraction is 0.06% higher than the baseline at the optimum design.

For the non-folding propeller design, the key design condition is take-off. The higher disk loading of the blown configuration in take-off compared to the folding scenario leads to reduced take-off efficiency of the propeller design, and hence extra motor weight. At the optimum design point for the non-folding configuration, the motor weight fraction is 1.63%, 0.06% higher than the baseline.

For folding propellers, the propeller efficiency decreases as the disk loading rises, which occurs for smaller propellers generating high thrust in the bottom left of Fig. 8.20 (b) during landing. There is also a component of weight contributed by the tip propeller motors, and this additional component leads to greater motor weight increases of up to a factor of 2 compared to the baseline. However, at the optimum tightly spaced design point, the motor weight fraction is 1.88%, an increase of 0.31% compared to the baseline. Spacing the propellers out increases this weight fraction by 0.15% to 2.03%.

The increased weight of the wing and motors can be compared to the reduced power consumption, predicted in Section 8.4 and 8.5, using the Brequet range equation for a fully electric aircraft [82],

$$R = \eta_{motors}\eta\left(\frac{L}{D}\right)\left(\frac{e_{battery}}{g}\right)\left(\frac{W_{battery}}{W_{aircraft}}\right), \quad (8.9)$$

where η_{motors} is the efficiency of the electric motors, η the efficiency of the propellers and $e_{battery}$ the specific energy of the battery.

Reducing the power consumption in cruise by 10.5% with the non-folding blown wing configuration and increasing the aircraft weight by 0.56% (the total additional weight of the motors and re-sized wing) leads to an 11.1% increase in range compared to the baseline aircraft, assuming the efficiency of the electric motors, specific energy of the battery, and battery weight remain fixed.

Reducing the power consumption in cruise by 12.2% with the folding blown wing configuration (with no propeller spacing, s/D_p=0), and an increase in the aircraft weight of 0.81% leads to a 12.9% increase in range compared to the baseline aircraft, assuming the efficiency of the electric motors, specific energy of the battery, and battery weight remain fixed. With the same assumptions, reducing the power consumption in cruise by 12.7% with the folding blown wing configuration (with optimal propeller spacing, s/D_p=0.59), and an increase in the aircraft weight of 0.96% leads to a 13.5% increase in range.

8.9 Other Blown Wing Benefits

This chapter has developed several models to assess the benefit of the blown wing on the airframe performance. There are a number of other potential benefits to a blown wing which are too complex to model fully in this chapter:

First, as the wing chord is reduced with re-sizing the wing, the moment of the main wing reduces approximately linearly. The chord, c is inversely proportional to C_L, and C_L is proportional to the wing moment coefficient C_M. However, the moment on the wing is proportional to $C_M c^2$. As a result, the moment is proportional to the wing chord. The moment of the blown wing, around the design points found in this chapter can be reduced by up to 30%. The advantage of reducing the wing moment is two-fold. First, the wing structure can be made lighter as less torsional stiffness is required. Second, the size of the rear tail on the aircraft can be reduced as the lift required for cruise stability is reduced. Neither of these effects has been modelled in the code.

Whilst the modelling presented in this thesis assumes that all blown wing lift benefit will be “cashed in” for reduced wing area, it is possible to maintain the same wing area (or some larger fraction of the original wing area) and use the increased lift available to take-off at lower runway speeds. Depending on the acceleration profile of the aircraft, the runway length can be reduced, opening up a wider range of airports for the aircraft to use. This is particularly relevant to smaller general aviation aircraft.

A major benefit of distributed propulsion is that the engine out failure case becomes a less significant sizing condition. For a jet engine powered aircraft, this requires the engine to be oversized by either 33% or 100% for 4 and 2 engine configurations. For the distributed propulsion system, between 18 and 24 leading edge propellers will be used, each with a motor running in parallel. An engine out condition would then represent only a 4-6% increase in thrust required by the other propulsors. The designer has the freedom to either shut down the equivalent propeller on the other semi-span, with no yaw moment, increasing the critical thrust requirement to 8-12% above design, or the propeller can remain operational and the tail designed to accommodate the yawing moment. As discussed previously, it is only by adding the leading-edge propellers to the aircraft that the tip propeller geometry can be safely implemented, giving another safety incentive for the use of leading-edge distributed blowing.

Finally, the large number of propellers introduces additional degrees of freedom for the pilot. Differential blowing between the two semi-spans, and along the span, could be used to manoeuvre the aircraft, reducing the size of the control surfaces required.

8.10 Conclusions

This chapter has developed a low-order whole aircraft model to establish the breakdown of loss at cruise and estimate total aircraft power consumption at cruise. The optimum blown wing designs, and their benefits are shown in Fig. 8.21. If the leading edge propellers are used in all phases of the flight, the maximum power reduction of the aircraft in cruise is 10.5% using a geometry with a horizontal offset of x_p/c=-0.25, no vertical offset of the propeller, y_p/c=0, and a propeller diameter, D_p/c=0.9. If the propellers are folded away in cruise, the power reduction possible increases to 12.2% with a geometry with a horizontal offset of x_p/c=-0.25, a vertical offset of the propeller, y_p/c=-0.05, and a propeller diameter, D_p/c=0.64. The weight of the aircraft increases by ~0.8% due to the structural weight of the wings, and motor masses, however this fraction is small compared to the predicted performance improvement. Around the optimum design, a further 0.5% reduction in power consumption is possible by spacing propellers out to s/D_p=0.59, giving a total power reduction in cruise of 12.7% with a blown wing.

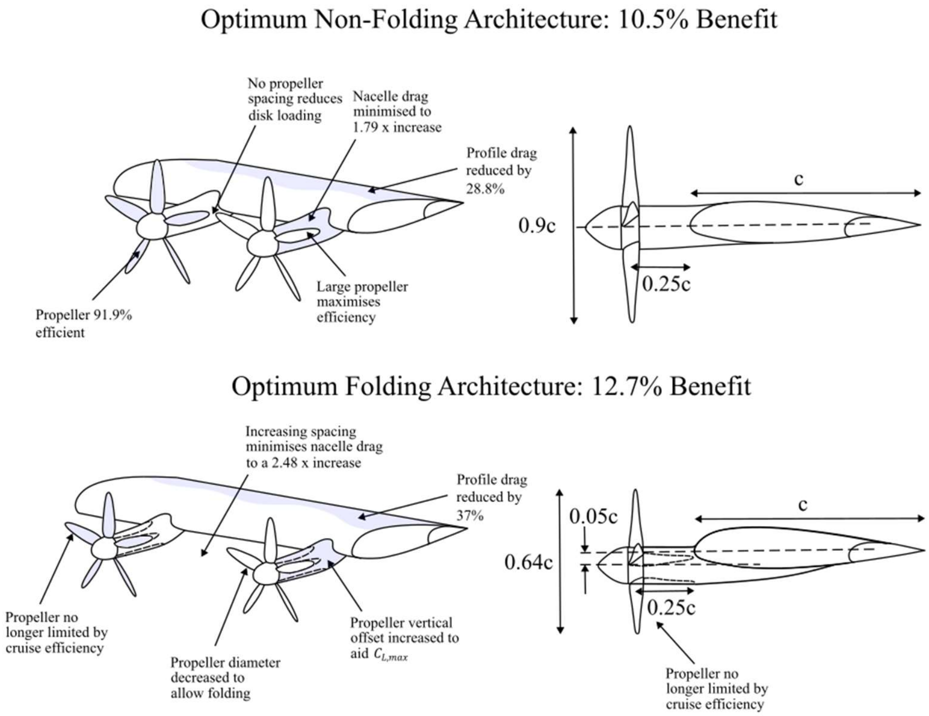

Figure 8.21: The optimum blown wing configurations found in this chapter. If propellers are not folded away in cruise, the optimum design is strongly influenced by the cruise efficiency of the propeller. If the propellers are foldable in cruise, the optimum blown wing design is determined by the maximum drag reduction of the wing and nacelles.

9. Conclusions

9.1 Introduction

This work set out to answer four questions:

1. What propeller position and diameter should be used to minimise the drag of a blown wing whilst constrained to still give adequate performance in landing, and by how much can the wing drag be reduced?
2. What are the limitations of 2D actuator disk modelling for a blown wing and by how much does the performance prediction change as the fidelity of the modelling is systematically increased from 2D modelling to experiment?
3. What is the mechanism by which the flap of a blown wing stalls, how does the position of the propeller in relation to the wing affect the stall point and can 2D modelling capture this behaviour?
4. What is the performance benefit of using distributed blowing over conventional propulsion layouts and how should the blown wing be configured to maximise this benefit?

A combination of experimental testing of a sub-scale model, simulations of the flow-field at real aircraft conditions, and low-order modelling of the whole aircraft system was used to answer these questions. The key results of this thesis are laid out in the next four sections.

9.2 Blown Wing Sizing for Minimum Drag

How should a blown wing with distributed propulsion be sized in order to minimise the drag of a real aircraft? Chapter 4 showed that the maximum lift of the blown wing (and hence minimum profile drag) is achieved with a small horizontal offset of x_p/c = -0.25, a large vertical offset of y_p/c = -0.21, and a mean jet diameter of $\overline{D_p}$/c = 0.2 for the wing geometry studied in this work. The profile drag can be reduced by 50%.

The optimal blown wing geometry for maximum lift is set by two criteria. First, the blown wing operation is limited by the aircraft landing thrust. As the aircraft makes its final approach, the thrust of the propellers cannot exceed the aircraft drag. In addition, the lift coefficient of the wing during landing is set to a safety factor below the maximum lift coefficient of the wing. To best use the available thrust for lift generation, the designer should use more, smaller propellers. This brings the jet closer to the wing surface, where its momentum is best deflected by the wing. However, a stall mechanism was found in Chapter 4 to exist for wings immersed in semi-infinite jets; when the jet goes from fully immersing the wing to passing above the wing suction surface, the boundary layer diffusion increases, causing stall. Therefore, the small propellers best suited for optimum lift increase should be positioned well below the wing centreline in order for the wing stagnation streamline to pass through the disk, ensuring the wing is always fully immersed in the jet.

In Chapter 5 it is shown that, when the installation drag of the propeller nacelles is included, the optimal geometry changes to a horizontal offset of the jet of x_p/c = -0.25, no vertical offset, y_p/c = 0, and a jet height of $\overline{D_p}/c$ = 0.5. This geometry is a compromise between the ideal geometry for minimum wing drag, found in Chapter 4, and the large nacelle drag contribution of many small propellers placed far below the wing centreline found in Chapter 5. With this new geometry, the maximum cruise drag reduction is 29.3%.

9.3 Simplified Modelling Techniques for Blown Wing Lift and Drag

Can a 2D model of the blown wing correctly predict the on-design and off-design performance of a blown wing? The 2D approach used in Chapters 4 and 5 allowed the spanwise variations in propeller jet to be ignored, capturing the main trends in wing lift with propeller position. Chapter 6 asked what the real propulsors' effects on the wing are and how closely can 2D modelling capture these effects. On-design, the 2D model can correctly capture the change to the lift curve slope due to blowing to within 6%. The lift along the span in 3D CFD varies by 2.8% due to the circular shape of the real propulsors' jet. The effect of swirl modifies the lift along the span by 29%. This is equivalent to a variation in swirl angle of 1.3°, much lower than the local maximum swirl angles (30°) produced in the propeller wake. This inability of the wing to locally react to the changing flow-field along the span means the primary levers controlling the wing lift and drag are the spanwise-average momentum, and average jet location, both of which are captured by the 2D model. The 2D model correctly capture the on-design performance with non-zero spacing between adjacent propellers and showed that, provided the total thrust of the system is constant, spacing leads to only a small drop in on-design blown lift at the same angle of attack. For the propeller spacing, s/D_p = 1.1, a 2.1% drop in wing lift was measured compared to s/D_p = 0.

9.4 Stall Mechanisms for Blown Wings

What is the mechanism by which a blown wing stalls, and how is the stall point affected by blown wing design? Chapter 4 found that when the jet goes from fully immersing the wing, to passing above the wing suction surface, the wing stalls. Chapter 7 showed that this mechanism still exists for real propulsors with circular jets and swirl, however the stall mechanism is 3-dimensional, with separation growing from a point on the flap trailing edge, before growing in the spanwise and chordwise directions. This growth in the separated region of the flap from a single point leads to a more gradual loss of lift near the flap stall point. Bringing the real propulsors' jet down, below the wing centreline, delayed wing stall by keeping the flap pressure surface immersed in the jet. Spacing the propellers out increases the stall angle of the flap. Although localised separations were found to occur at lower flap angles with the spaced-out propellers, due to spanwise movement of the jets, a greater proportion of the span is unaffected by the jet, increasing the maximum lift coefficient of the wing.

9.5 Overall Performance Benefits of a Blown Wing

What is the performance benefit of using distributed blowing over conventional propulsion layouts and how should the blown wing be configured to maximise this benefit? Chapter 8 incorporated the blown wing drag reductions data from Chapters 4 and 5 into a whole aircraft model using a blown wing. A trade-off exists between the optimum blown wing geometry to minimise wing profile drag, and the propeller diameter that maximises the propulsive efficiency in cruise. If the leading edge propellers are used in all phases of the flight, the maximum benefit possible is a 10.5% reduction in cruise power consumption compared to an aircraft fitted with conventional propulsion technology, assuming the aircraft mass remains constant. The propeller geometry to achieve this is a horizontal offset of x_p/c = -0.25, no vertical offset of the propeller, y_p/c = 0, and a propeller diameter, D_p/c = 0.9. If the propellers are folded away in cruise, the power reduction increases to 12.2% with a propeller geometry with a horizontal offset of x_p/c = -0.25, a vertical offset of the propeller, y_p/c = -0.05, and a propeller diameter, D_p/c = 0.64. For the optimum folding geometry, spacing propellers out to s/D_p = 0.59, increases the performance by a further 0.5% to a 12.7% reduction in cruise power consumption, however this metric does not include the additional benefits of spacing to delay the flap stall point found in Chapter 7.

9.6. Future Work

The work presented in this thesis leaves a number of areas for further exploration. Proposed future research has been subdivided into experimental testing, CFD simulations and whole aircraft modelling.

9.6.1 Experimental Testing

The sub-scale experimental facility developed as part of this work allowed the performance of the wing to be explored for different propeller vertical offsets and spacings. There are however several drawbacks to the test rig which should be addressed:

- Only two propeller spacings can be tested, as the location of the propellers is fixed along the span.
- A single propeller diameter was tested.
- Corner separations where the wing meets the end plates introduce uncertainty into the lift and drag measurement from the load-cells.
- Boundary layer trips on the flap increased the boundary layer thickness, reducing the wing lift.
- Wing surface measurements were limited to flow visualisation.
- The wing angle of attack requires corrections to account for tunnel jet deflection.

The experimental facility requires further developments to improve on these shortcomings. Flexible end-wall and propeller locations would allow a wider choice of propeller diameters and spacings to be tested, improving the available data on blown wing performance. To achieve this, it is proposed that a future wing be machined from aluminium, rather than 3D printed. Using stiffer tie rods, multiple aluminium wing sections could be machined precisely, in a variety of lengths, and slotted together to form the test-section. Different sections would allow variable propeller diameters and spacings to be achieved. Moveable end-walls would also be required to ensure periodicity. This would require either modification to the outer frame currently used in order to raise or lower one of the end-walls, or the introduction of internal dummy end-walls.

A major source of uncertainty, quantified in Chapter 3, in the experimental load-cell data was the presence of separations at the corners of the flap. To remove these effects, dummy wing sections, not connected to the load-cell, could be introduced covering the flap separations. The chordwise extend of the boundary layer trip, set to ensure the trip is effective over the full flap angle range, was thought to excessively increase the boundary layer thickness, affecting the lift measurement. To test this, narrower flap trips could be used for specific flap angles to calibrate the lift lost due to the trip.

9.6.2 Numerical Simulations

A series of fidelities of CFD simulation were presented in this thesis in order to quantify the effects of different real propulsor effects. The CFD modelling in each case was self-consistent, with the same turbulence modelling and near-wall modelling used. The Spalart-Allmaras turbulence model was employed due to its extensive use in external flows, and in turbo-machinery applications. A wall y+ value of 30 was used for the 2D simulations to reduce the computational expense, important when collecting the large data set used in Chapter 4. The y+ of 30 means the wall boundary layer is not fully resolved, and the prediction of wing stall is less accurate [7]. Having identified the critical nature of predicting the stall point, it would be advisable to run both the large 2D dataset, and selected 3D geometries using a y+ <1 to better predict the wing separation. This would allow better comparison between the CFD and experiment. Using narrower trips, the experiment could be used to validate the turbulence modelling of the CFD using the separated area measured by the experiment.

The modelling complexity could be increased in two ways within the CFD. First, the effect of 3D wing design, such as taper, sweep, and twist should be considered for isolated geometries in order to quantify the change in lift delta with blowing when global effects are considered. Second, URANS simulations should be used to model the propeller wing interaction as an extension to the model fidelity build-up of Chapter 6. It is likely that the performance of the propeller will be modified by the wing potential field. URANS simulations of the propeller would allow this effects to be quantified, and the minimum upstream spacing of the propeller to be determined. In addition, URANS simulations of the propeller at the wing tip would allow the induced drag modelling of Chapter 8 to be validated by other means than the single experimental data set of Sinnige et al. [69].

9.6.3 Low Order Modelling

The low order modelling of the aircraft needs further work to improve its accuracy. A number of assumptions were made:

- The cruise performance is reflective of the overall benefit to the aircraft power requirements.
- The thrust from the blowing propellers can equal the airframe drag just prior to landing.
- A fixed safety margin for the lift coefficient of the blown wing is permitted.
- The aircraft weight, cruise altitude and Mach number, fuselage design and empennage design remain fixed.
- The local 3D performance benefit of blown wings is reflective of the global benefit to the real wing.

The performance estimates of Chapter 8 assume that the performance of the aircraft at cruise is representative of the total benefit to the airframe. In practice, the take-off and landing portions of the flight need modelling in greater detail. The power consumption in these phases of flight was not modelled, and may be significant for short haul flights, such as those envisioned for battery-electric aircraft.

The landing model developed in Chapter 4 assumes that the thrust from the blowing propellers equals the airframe drag prior to touchdown. In practice, it is likely that some additional margin is required on the thrust of the propellers, with the propeller thrust acting to control the rate of decent. A sensitivity study is required to understand how the blown wing benefit is affected by the choice of design streamwise force coefficient on landing.

A number of aircraft parameters were held constant, in order to avoid long convergence times which would inhibit the exploration of the design space. This required a fixed aircraft weight, as well as a fixed fuselage design and empennage. It was discussed in Chapter 8 that blowing allows the empennage to be re-designed to account for smaller wing moments. This needs factoring into a future aircraft model. An additional outer loop for the airframe weight is also required, including a model for the power system weight and efficiency, as the current ATR-42 weight may not be optimal for the mission requirements with electric propulsion on board.

Chapter 8 attempted to capture the global three-dimensional effect of blowing on the wing induced drag. This model requires validation for distributed blown wings along the span, and further research is required to understand how the tip mounted propellers and wing leading edge propellers interact to modify induced drag, and how localised blowing in a real 3D wing with end effects translates to total lift and drag.

9.6.4 Future Research Questions

A number of proposed future research questions exist, based on the work presented in this thesis:

1. How well does the optimal blown wing design, found using 2D actuator models, perform in a sub-scale experiment?
2. How does 3D actuator disk modelling compare to RANS and URANS simulations with a real propeller geometry, and what is the upstream impact of the wing potential field on the propeller for small horizontal offsets and small propeller diameters compared to the wing chord?
3. Using 2D models for the blown wing lift, including 3D validation, can a whole aircraft model be developed to design a new aircraft with distributed blown wings that accounts for aircraft weight changes?
4. How does the design of blown wings change, when going from a local viewpoint of the wing as a 2D section, to a global viewpoint of the wing including end effects, wing taper, and other aircraft systems such as ailerons on the wing?

10. References

[1] Adkins, C. and Liebeck, R., “Design of Optimum Propellers”, 1994, Journal of Propulsion and Power, 10. 676-682. 10.2514/3.23779.

[2] Agostinelli, C., Allen, C., Simeone, S., Zhu, F. and Rampurawala, A., “A Fast Approach to Model the Effects of Propeller Slipstream on Wing Load Distribution”, 2015, 10.2514/6.2015-0028.

[3] Agrawal, D., As’ad, F., Berk, B., Long, T., Lubin, J., Courtin, C., Thomas, J., Drela, M., and Hansman, R. J., “Wind Tunnel Testing of a Blown Flap Wing”, 2019 Aviation Technology, Integration, and Operations Conference, 2019.

[4] Ahuja, V. and Litherland, B., “Comparison of Aerodynamic Analysis Tools Applied to a Propeller-Blown Wing”, 2023, 10.2514/6.2023-1753.

[5] Aminaei, H., Dehghan Manshadi, M. and Mostofizadeh, A., “Experimental Investigation of Propeller Slipstream Effects on the Wing Aerodynamics and Boundary Layer Treatment at low Reynolds Number”, 2018, Proceedings of the Institution of Mechanical Engineers, Part G: Journal of Aerospace Engineering. 095441001879370. 10.1177/0954410018793703.

[6] Ananda, G., Selig, M. and Deters, R., “Experiments of Propeller-Induced Flow Effects on a Low-Reynolds-Number Wing”, 2018, AIAA Journal. 56. 1-16. 10.2514/1.J056667.

[7] ANSYS Fluent 12.0 UDF Manual, Retrieved 1st May 2020, https://www.afs.enea.it/project/neptunius/docs/fluent/html/udf/main_pre.htm Pointwise

[8] Aref, P., Ghoreyshi, M., Jirasek, A., Satchell, M. and Bergeron, K., “Computational Study of Propeller–Wing Aerodynamic Interaction”, 2018, Aerospace. 5. 79. 10.3390/aerospace5030079.

[9] Barlow, J.B., Rae, W.H. and Pope, A., “Low Speed Wind Tunnel Testing”, 3rd Edition, John Wiley & Sons, New York, 1999.

[10] Barnhart, S., Narayanan, B. and Gunasekaran, S., “Blown Wing Aerodynamic Coefficient Predictions Using Traditional Machine Learning and Data Science Approaches”, 2021, 10.2514/6.2021-0616.

[11] Bohari, B., Bronz, M., Benard, E. and Borlon, Q., “Conceptual Design of Distributed Propeller Aircraft: Linear Aerodynamic Model Verification of Propeller-Wing Interaction”,

7th European Conference for Aeronautics and Aerospace Sciences (EUCAAS), Jul 2017, Milan, Italy. 10.13009/EUCASS2017-445. hal-01599301

[12] Borer, N., Derlaga, J., Deere, K., Carter, M., Viken, S., Patterson, M., Litherland, B. and Stoll, A., “Comparison of Aero-Propulsive Performance Predictions for Distributed Propulsion Configurations”, 2017, 10.2514/6.2017-0209.

[13] Braslow, A. L., Harris Jr, R. and Hicks, R. M., “Use of Grit-type Boundary-layer Transition Trips on Wind Tunnel Models”, Technical Note NASA TN D-3579, National Aeronautics and Space Administration, Sept. 1966.

[14] Brenckmann, M.E., “Experimental Investigation of the Aerodynamics of a Wing in a Slipstream”, UTIA Technical Note, No. 11. 1957.

[15] Butler, K., Huang, K.P. and Goland, L., “An Investigation of Propeller Slipstream Effects on V/STOL Aircraft Performance and Stability”, 1966, U.S Army Aviation Material Laboratories.

[16] Cambridge University Research Computing Services, https://www.hpc.cam.ac.uk/

[17] Cao, T., Bai, J., Feng, S., Qiu, Y. and Han, K., “Novel High-Precision and Efficient Momentum Source Method”, 2023, AIAA Journal. 61. 1-18. 10.2514/1.J063024.

[18] Casses, C., Courtin, C., Drela, M., Fitzgibbon, T., Runda, J., Skarysz, M., Spalart, P. and Wang, Q., “Impact of Propulsion Modeling Approach on High-Lift Force Prediction of Propeller-Blown Wings”, 2022, 10.2514/6.2022-3302.

[19] Castillo Pardo, A., Williams, T., Clark, C., Atkins, N. and Hall, C., “Rig 150 fan de-risk test”, Whittle Laboratory University of Cambridge, 2021, Internal Report.

[20] Clarke, M., Erhard, R., Smart, J. and Alonso, J., “Aerodynamic Optimization of Wing-Mounted Propeller Configurations for Distributed Electric Propulsion Architectures”, 2021, 10.2514/6.2021-2471.

[21] Cole, J., Maughmer, M., Kinzel, M. and Bramesfeld, G., “Higher-Order Free-Wake Method for Propeller–Wing Systems”, 2018, Journal of Aircraft. 56. 1-16. 10.2514/1.C034720.

[22] Courtin, C., Hansman, R. and Drela, M., “Flight Test Results of a Subscale Super-STOL Aircraft”, 2020

[23] Davies, H. and Smelt, R., “Estimation of increase in lift due to slipstream”, Technical Report, Aeronautical Research Committee, 1937.

[24] Deere, K., Viken, S., Carter, M., Viken, J., Derlaga, J. and Stoll, A., “Comparison of High-Fidelity Computational Tools for Wing Design of a Distributed Electric Propulsion Aircraft”, 2017, 10.2514/6.2017-3925.

[25] Drela, M., “Power Balance in Aerodynamic Flows”, 2009, AIAA Journal. 47. 1761-1771. 10.2514/1.42409.

[26] Dubs, F., “Aerodynamik der reinen Unterschallströmung”, 4th edition, 1979.

[27] Dunkley, M.J., “The Aerodynamics of Intermediate Pressure Turbines”, PhD Thesis, 1998.

[28] Fillingham, D., Private Correspondence.

[29] Flanagan, F., “Fundamental Configuration Optimisation with Electric Propulsion”, PhD Thesis, 2022.

[30] Gentry, G. L., Takallu, M. A. and Applin, Z. T., “Aerodynamic Characteristics of a Propeller-Powered High-Lift Semispan Wing”, Technical Memorandum 4541, NASA, 1994.

[31] Glauert, H., “Wind Tunnel Interference on Wings, Bodies and Airscrews”, A.R.C., R&M 1566, 1933.

[32] Goodson K. W., “Comparison of Wind-Tunnel and Flight Results of a Four-Propeller Tilt-Wing Configuration”, NASA Langley Research Centre, NASA AS-116, April 4-5 1966.

[33] Hassell, J. L. and Kirby, R. H., “Descent Capability of Two-Propeller Tilt-Wing Configurations”, NASA Langley Research Centre, NASA AS-116, April 4-5 1966.

[34] Hayes, William C., Jr., Kuhn, Richard E., and Sherman, Irving R., “Effects of Propeller Position and Overlap on the Slipstream Deflection Characteristics of a Wing-Propeller Configuration Equipped With a Sliding and Fowler Flap”, NACA TN 44043, 1958.

[35] Hawkswell, G.N., “Distributed Propulsion Aerodynamics”, Masters of Research Project Proposal Dissertation, Cambridge University Engineering Department, August 2019.

[36] Hawkswell, G.N., Miller, R.J. and Pullan, G., “Selection of Propeller-Wing Configuration for Blown Wing Aircraft”, AIAA Scitech, January 2022.

[37] Hawkswell, G.N., Miller, R.J. and Pullan, G., “The Effect of Propeller Spacing on the Performance of a Blown Wing Aircraft for an Electric Regional Aircraft”, AIAA Scitech, January 2024.

[38] Howe, G., “Optimization of 2-D Flap Geometry Using Matlab and Fun3D”, 2011, 10.2514/6.2011-823.

[39] HPDM-250 Datasheet v1.1 | 11-5-2020, https://www.h3x.tech.

[40] https://www.atr-aircraft.com/wp-content/uploads/2020/07/Factsheets_-_ATR_42-600.pdf, accessed July 31st, 2024.

[41] https://aviationweek.com/aerospace/manufacturing-supply-chain/flyzero-identifies-zero-emissions-opportunities-uk-industry, accessed 8th October 2023.

[42] https://indianexpress.com/article/technology/science/nasa-showcases-x-57-maxwell-its-first-electric-airplane-6112771/, accessed 8th October 2023.

[43] https://www.leonardo.com/en/news-and-stories-detail/-/detail/leonard-clea-aviation-programme/, accessed 8th October 2023.

[44] Jameson, A., “Analysis of Wing Slipstream Flow Interaction”, NASA CR-1632, August 1970.

[45] Jardine, L., Private Correspondence.

[46] Kock, B.M., Fulton, F.L. and Drinkwater, F.J., “Low-Lift-To-Drag-Ratio Approach and Landing Studies using a CV-990 Airplane”, NASA TN D-6732, March 1972.

[47] Kroo, I., “Propeller-Wing Integration for Minimum Induced Loss”, 1986, Journal of Aircraft - J AIRCRAFT. 23. 561-565. 10.2514/3.45344.

[48] Kuhn, R. E., “Semi-empirical Procedure for Estimating Lift and Drag Characteristics of Propeller-Wing-Flap Configurations for Vertical and Short-Take-Off-and-Landing Airplanes”, NASA Memorandum, 19980232082, 1959.

[49] Kulfan, B.M., “Universal parametric geometry representation method”, In AIAA Aerospace Sciences Meeting and Exhibit, AIAA 2007-0062, 8-11 Jan 2007, Reno, Nevada.

[50] Litherland, B. L., Patterson, M. D., Derlaga, J. M., and Borer, N. K., “A Method for Designing Conforming Folding Propellers”, AIAA AVIATION Forum, American Institute of Aeronautics and Astronautics, 2017. URL https://doi.org/10.2514/6. 12 2017-3781.

[51] Marinus, B. G., Lino, M. and Bosschaerts, W., “Propeller Installation Effects on a Semispan Wing”, International Journal of Aerospace Engineering, June 2010.

[52] Matlab r2019a, https://www.mathworks.com/.

[53] McKinney, M., Kirby, R. and Newsom, W., “Aerodynamic factors to be considered in the design of tilt-wing V/STOL airplanes”, Annals of the New York Academy of Sciences. 107. 221 - 248. 10.1111/j.1749-6632.1963.tb13279.x.

[54] Miranda, L.R., and Brennen, J.E., “Aerodynamic Effects of Wingtip-Mounted Propellers and Turbines”, AIAA 4th Applied Aerodynamics Conference, June 1986.

[55] Moore, M. D., Clarke, S., Stoll, A., Clark, A., MacAfee, S., and Foster, T., “Affordable Flight Testing of LEAPTech Distributed Electric Propulsion”, January 13-15 2015, NASA Aeronautics Research Mission Directorate 2015 LEARN/Seedling Technical Seminar

[56] Patterson, M. D., “Conceptual Design of High-Lift Propeller Systems for Small Electric Aircraft”, Ph.D. Dissertation, Georgia Inst. Technology, Atlanta, GA, 2016.

[57] Patterson, M. and Borer, N., “Approach Considerations in Aircraft with High-Lift Propeller Systems”, 2017, 10.2514/6.2017-3782.

[58] Patterson, M. D., Borer N. K. and German, B.,"A Simple Method for High-Lift Propeller Conceptual Design", in 54th AIAA Aerospace Sciences Meeting, American Institute of Aeronautics and Astronautics, AIAA 2016-0770.

[59] Patterson, M. D., Derlaga, J.M. and Borer, N.K., “High-Lift Propeller System Configuration Selection for NASA’s SCEPTOR Distributed Electric Propulsion Flight Demonstrator”, 16th AIAA Aviation Technology, Integration, and Operations Conference, 13-17 June 2016, Washington, D.C. AIAA 2016-3922

[60] Patterson, M. D. and German, B. J., “Simplified Aerodynamics Models to Predict the Effects of Upstream Propellers on Wing Lift”, 53rd AIAA Aerospace Sciences Meeting, Kissimmee, Florida, 5-9 January 2015, AIAA 2015-1673.

[61] Pointwise v18.3 User Manual

[62] Raymer, D. P., “Aircraft Design: A Conceptual Approach”, AIAA Education Series, AIAA, Reston VA, 2006.

[63] Reissner, H., “On the vortex theory of the screw propeller”, Journal of the Aeronautical Sciences, 5(1), pp.1-7, 1937.

[64] Rolls-Royce plc. Distributed Open Rotor Aircraft (DORA), image provided by Herve Morvan for Whittle Laboratory internal use only, property of Rolls-Royce plc.

[65] Roosenboom, E., Stürmer, A. and Schröder, A., “Advanced Experimental and Numerical Validation and Analysis of Propeller Slipstream Flows”, 2010, Journal of Aircraft. Vol. 47. 284-291. 10.2514/1.45961.

[66] Rudolph, P.K.C., “High Lift Systems on Commercial Subsonic Airliners”, NCR 4746, September 1996.

[67] Rudolph, P.K.C., “Mechanical Design of High Lift Systems for High Aspect Ratio Swept Wings”, NASA/CR-1998-196709.

[68] Seddon, J. and Newman, S., “Basic Helicopter Aerodynamics”, 2nd Edition, 2002.

[69] Sinnige, T., van Arnhem, N., Stokkermans, T., Eitelberg, G., and Veldhuis, L., “Wingtip-Mounted Propellers: Aerodynamic Analysis of Interaction Effects and Comparison with Conventional Layout”, Journal of Aircraft vol 56. No.1, February 2019.

[70] Smith, A.M.O., “High Lift Aerodynamics”, Journal of Aircraft Vol 12 No 6. 37th Wright Brothers Lecture. August 1974.

[71] Spalart, P. R. and Allmaras, S. R., "A One-Equation Turbulence Model for Aerodynamic Flows", 1992, AIAA Paper 92-0439.

[72] Stoll, A., “Comparison of CFD and Experimental Results of the LEAPTech Distributed Electric Propulsion Blown Wing”, 2015, 10.2514/6.2015-3188.

[73] Suranto, P. S., “ Numerical study of aerodynamic analysis on wing airfoil NACA 43018 with the addition of forward and rearward wingtip fence”, 2016, Proceedings of the International Mechanical Engineering and Engineering Education Conferences (IMEEEC 2016) AIP Conf.

[74] Svenning, E., “CFD with OpenSource software 2010. Implementation of an actuator disk in OpenFOAM”, Chalmers University of Technology. October 30th 2010.

[75] Taylor, R.T., “Wind-Tunnel Investigation of Effect of Ratio of Wing Chord to Propeller Diameter with Addition of Slats on the Aerodynamic Characteristics of Tilting-Wing VTOL Configurations in the Transition Speed Range”, NASA TN D-17, 1959.

[76] Ting, L., Liu, C. H., and Kleinstein, G., “Interference of Wing and Multi-propellers”, AIAA Journal, Vol. 10, No. 7, 1972, pp. 906–914.

[77] Veldhuis, L. L. M., “Review of Propeller Wing Aerodynamic Interference”, ICAS 2004, 24th international congress of the aeronautical sciences, 2004.

[78] Veldhuis, L. L. M., “Propeller Wing Aerodynamic Interference”, Ph.D. Thesis, Delft Univ. of Technology, Delft, The Netherlands, June 2005.

[79] de Vries, R., van Arnhem, N., Sinnige, T., Vos, R. and Veldhuis, L., “Aerodynamic interaction between propellers of a distributed-propulsion system in forward flight”, 2021, Aerospace Science and Technology. 118. 107009. 10.1016/j.ast.2021.107009.

[80] de Vries, R., Brown, M. and Vos, R., “Preliminary Sizing Method for Hybrid-Electric Distributed-Propulsion Aircraft”, 2019, Journal of Aircraft. 1-17. 10.2514/1.C035388.

[81] de Vries, R., Brown, M. and Vos, R., “A Preliminary Sizing Method for Hybrid-Electric Aircraft Including Aero-Propulsive Interaction Effects”, 2018, 10.2514/6.2018-4228.

[82] de Vries, R., Hoogreef, M. and Vos, R., “Range Equation for Hybrid-Electric Aircraft with Constant Power Split”, 2020, Journal of Aircraft. 57. 1-6. 10.2514/1.C035734.

[83] Wang, K., Zhou, Z., Zhu, X., and Xu, X., “Aerodynamic Design of Multi-Propeller/Wing Integration at Low Reynolds Numbers”, 2018, Aerospace Science and Technology. 84. 10.1016/j.ast.2018.07.023.

[84] Webb, J., “Urban Air Taxis”, Masters Thesis, Cambridge University Engineering Department., 2019.

[85] West, R.N., “Urban Air Taxis”, Masters Thesis, Cambridge University Engineering Department., 2019.

[86] Wolleswinkel, R., de Vries, R., Hoogreef, M. and Vos, R., “A New Perspective on Battery-Electric Aviation, Part I: Reassessment of Achievable Range”, 2024, 10.2514/6.2024-1489.

[87] Wood, A., “Probe Calibration for Aerodynamic Measurements”, Masters Thesis, Cambridge University Engineering Department, 2023.

[88] XFOIL, https://web.mit.edu/drela/Public/web/xfoil/, accessed 1st December 2019.

Appendix A: 3D Actuator Disk Model Inputs

The Goldstein approximations are used in this thesis to prescribe the input to the 3D actuator disk model with swirl. These functions produce an approximation to the radial distribution of thrust and torque for a minimum induced loss propeller design (see Appendix B) and allow the body forces to be specified analytically, reducing the computational cost of the actuator disk method.

Expressions for the variation of axial and tangential force with radius are given by:

$$F_a = Ar^*\sqrt{1-r^*} \quad , \quad (A.1)$$

and

$$F_\psi = B\frac{r^*\sqrt{1-r^*}}{r^*(1-r'_{hub})+r'_{hu}} \quad , \quad (A.2)$$

where

$$r' = \frac{r}{r_{tip}} \quad , \quad (A.3)$$

and

$$r^* = \frac{r'-r'_{hub}}{1-r'_{hub}} \quad . \quad (A.4)$$

The constants A and B may be calculated from integration of Eq. A.1 and A.2 to get a total desired axial force and torque. A derivation is provided in [74]. The resultant expressions are given as

$$A = \frac{105}{8}\frac{T}{\pi\Delta\left(3r_{hub}+4r_{tip}\right)\left(R_P-r_{hub}\right)} \quad , \quad (A.5)$$

and

$$B = \frac{105}{8}\frac{Q}{\pi\Delta R_P\left(4r_{hub}+3r_{tip}\right)\left(r_{tip}-r_{hub}\right)} \quad . \quad (A.6)$$

Here T and Q are total thrust and torque on the control volume due to the momentum source, r_{tip} is the Propeller Radius and r_{hub} the hub radius and Δ the thickness of the actuator disk.

Appendix B: Propeller Modelling Techniques

Extensive use is made throughout this thesis of Actuator Disk theory and Blade Element Momentum theory (BEM) for the prediction of propeller performance, and the design of the propellers used in the experiments. This appendix provides a summary of these methods.

A 1-Dimensional model, called Actuator Disk theory can be used as a good approximation for predicting the change in velocity of the flow through a propeller disk. Figure B.1, reproduced from [56], shows a diagram of the flow through such a disk. The propeller is modelled by a region in space, called an actuator disk, where the fluid passing through the disk experiences a step change in static pressure, Δp. The thrust is equal to the product of the pressure difference and the area of the actuator disk. Because continuity is maintained across the disk $\rho_2 V_2 = \rho_3 V_3$, and any density changes are assumed to be small, there is a step change in total pressure equal to the pressure difference, Δp.

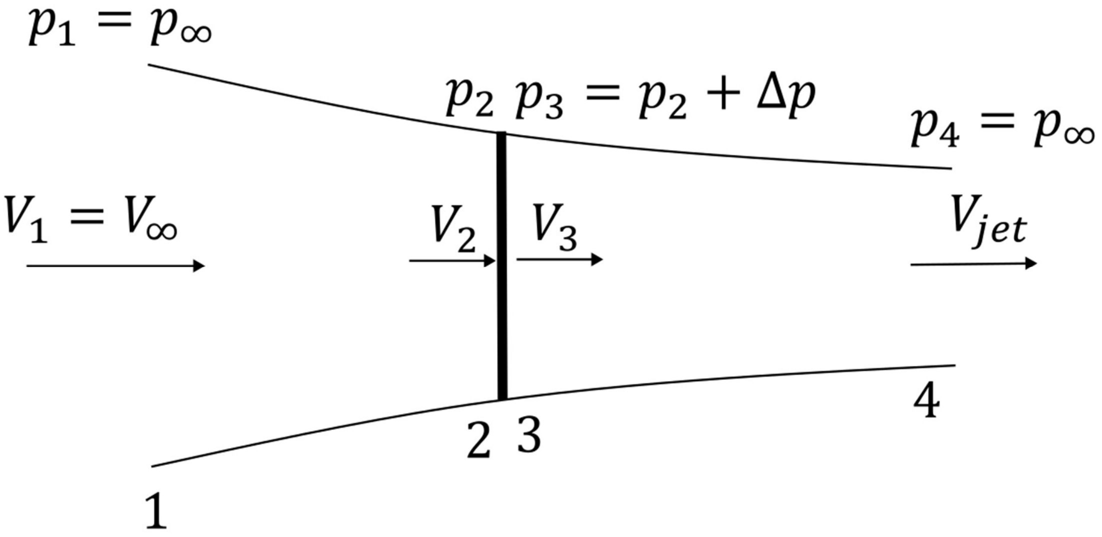

Figure B.1: Contraction of the jet stream-tube through an actuator disk. Adapted from [56].

Far away from the disk, the freestream pressure is atmospheric. The pressure decreases below static as the flow accelerates towards the disk, then increases as the pressure jumps across the disk. From Bernoulli, the velocity at station 2/3 is given by

$$p_\infty + \frac{1}{2}\rho V_\infty^2 = p_2 + \frac{1}{2}\rho V_2^2 \quad . \quad (B.1)$$

Just downstream of the disk,

$$p_2 + \Delta P + \frac{1}{2}\rho V_2^2 = p_\infty + \frac{1}{2}\rho V_{jet}^2 \quad . \quad (B.2)$$

Applying the steady flow momentum equation to the control volume shown in Fig. B.1, such that no flow leaves or enters through the upper and lower boundary,

$$T = \rho A V_2 \left(V_{jet} - V_\infty\right) \quad , \quad (B.3)$$

where A is the area of the disk and $\rho A V_2$ the mass flow rate through the control volume.

As mentioned, the thrust, T, can also be calculated from,

$$T = A\Delta p \quad . \quad (B.4)$$

Combining these equations,

$$\Delta p = \frac{1}{2}\rho\left(V_{jet}^2 - V_\infty^2\right) \quad , \quad (B.5)$$

$$V_2 = \frac{1}{2}\left(V_{jet} + V_\infty\right) \quad , \quad (B.6)$$

If

$$V_{jet} = V_\infty + \Delta V \quad , \quad (B.7)$$

then,

$$V_2 = V_\infty + \frac{\Delta V}{2} \quad , \quad (B.8)$$

showing that half the slipstream contraction occurs upstream of the propeller disk. A second useful equation from this analysis is,

$$\frac{V_{jet}}{V_\infty} = \sqrt{1 + \frac{T}{\frac{1}{2}\rho A V_\infty^2}} \quad . \quad (B.9)$$

The above analysis is an axial momentum theory and gives no detail about the design of the propeller required to achieve the pressure rise, Δp, of the actuator disk. This can be achieve with Blade Element Momentum Theory (BEM) which uses blade elements at radial location r and calculates the required distribution of blade chord and twist to achieve certain distributions of circulation for a given blade section, as shown in Fig. B.2. The slipstream contraction of the propeller wake is neglected and so the method is only accurate for moderate disk loadings, although reasonable agreement is achieved even for higher disk loading.

Diagram of the forces and flow angle definitions for a propeller blade section [1]. Removed for copyright reasons. Copyright holder is the American Institute of Aeronautics and Astronautics, Inc.

Figure B.2: Blade element model forces and flow at a given propeller radial station. Reproduced from [1].

Betz found that for a lightly loaded, frictionless propellers, optimum efficiency, defined by,

$$\eta = \frac{TV_\infty}{P} \quad , \quad (B.10)$$

is achieved when the vortex sheet shed from the propeller blades is a constant screw surface. This statement is analogous to the constant downwash velocity produced by elliptically loaded wings. Propellers designed according to this theory are called minimum induced loss propellers (MIL). This condition can be stated simply as

$$r \tan \psi_p = constant \quad , \quad (B.11)$$

The inflow angle ψ_p is defined above in Fig. B.2 along with the blade angle of attack α, axial induction factor a and radial induction factor a'. Note that the inflow angle is usually denoted by ϕ however this has been changed to avoid confusion with the flap angle, defined with the same symbol, in this thesis. The requirement for constant wake velocity provides a constraint which fixes the propeller design for given input geometry parameters, rotation rate and thrust coefficient. The value of $r \tan \psi_p$ is iterated such that the required thrust is produced by the propeller.

Constructing a control volume from far upstream to far downstream of the propeller disk passing through an infinitesimal ring of thickness dr, the thrust of this ring can be calculated with the steady flow momentum equation as

$$dT = 2\pi r \rho V_\infty (1 + a) \cdot 2 V_\infty a F \quad , \quad (B.12)$$

where the first term on the right hand side is the mass flow rate through the control volume, and the second term the change in velocity of the fluid. A similar expression can be produced for the torque on the ring,

$$dQ/r = 2\pi r \rho V_\infty (1+a) \cdot 2\Omega r a' F \quad . \quad (B.13)$$

Both equations above include a factor F, known as the Prandtl tip loss correction factor which accounts for the effect of a finite number of blades,

$$F = \frac{2}{\pi} \cos^{-1} e^{\frac{-B}{2} \frac{r_{tip}-r}{R \sin \psi_{p,tip}}} \quad , \quad (B.14)$$

where r_{tip} is the tip radius of the propeller, and $\psi_{p,tip}$ the inflow angle at the tip. This correction is required to model the vortex losses at the tip of the propeller due to the equalisation of pressure about the blade tip and accounts for the reduction in slipstream velocity near the tip. This correction only becomes significant very near the tip of the propeller, or when a low propeller blade count is used. For most simulations in this thesis, a 5 bladed propeller is modelled.

For a known aerofoil section, the lift and drag coefficients for a given angle of attack α and Reynolds number, defined by,

$$Re = \frac{\rho W_p c}{\mu} \quad , \quad (B.15)$$

can be calculated at each radial station, through a look up table of aerofoil section data. Typical solution procedures either fix the lift coefficient as uniform along the span (most robust method), or optimise each radial station to give the incidence with highest lift-to-drag ratio (highest efficiency). In this thesis, a fixed lift coefficient of 0.7 was always used.

Elemental thrust and torque contributions are given by

$$dT = \frac{1}{2} \rho {W_p}^2 B_p c \left(C_L \cos \psi_p - C_D \sin \psi_p \right) \quad , \quad (B.16)$$

and,

$$\frac{dQ}{r} = \frac{1}{2} \rho {W_p}^2 B_p c \left(C_L \sin \psi_p + C_D \cos \psi_p \right) \quad . \quad (B.17)$$

Eq. B.16 and B.12 can be equated (as can B.17 and B.13). This system of equations can then be iterated to fix the blade twist, β and local chord length c at each radial station.

Adkins and Liebick [1] present a commonly used method for MIL propellers that enables moderate and high disk loading propeller geometries to be designed. This method utilises the blade element theory calculations in Eq. B.11 to Eq. B.17 and was incorporated into a MATLAB design routine in this thesis that quickly calculated the performance of a given propeller geometry. The input parameters were the propeller hub and tip radius, blade number (set as 5 for all calculations unless stated otherwise), blade section aerodynamic data, rotation rate, fluid properties and desired thrust coefficient. The flow through the propeller was assumed incompressible in all calculations.

The NACA 4415 was used to provide the aerodynamic blade section data for use with all propellers in this thesis. The section was chosen as it was also used by Adkins and Liebick [1] in their studies of minimum induced loss propellers. Once the propeller design is fixed at an operating point, off-design performance can also be calculated by re-solving Eq. B.11 to B.17 at the specified rotation rate..

Appendix C: Nacelle Geometry Parameterisation

This appendix gives details of the family of nacelle geometries tested in this thesis. Figure C.1 gives the geometry representation.

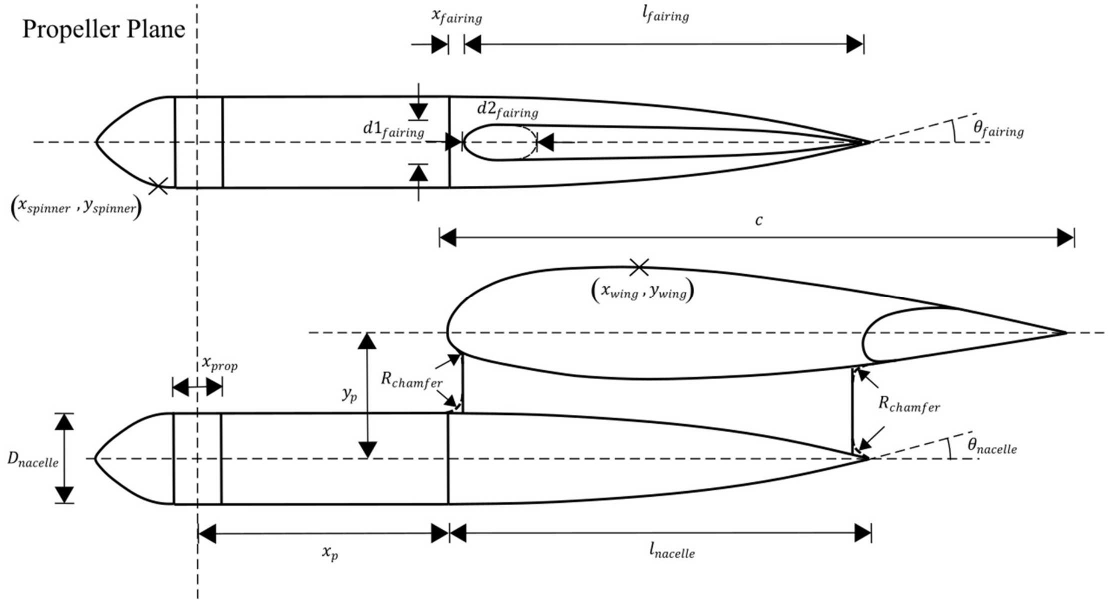

Figure C.1: Nacelle geometry parameterisation [37].

The key parameters varied in this work are the nacelle diameter, $D_{nacelle}$, horizontal offset of the nacelle, x_p and vertical offset, y_p. The other parameters, shown in Fig. C.1, are tabulated below.

c (mm)	212
x_{prop} (mm)	16
$l_{nacelle}$ (mm)	144.5
$l_{fairing}$ (mm)	135
$R_{chamfer}$ (mm)	4
$\theta_{nacelle}$ (°)	15
$x_{fairing}$ (mm)	5
$d1_{fairing}$ (mm)	12
$d2_{fairing}$ (mm)	24
$\theta_{fairing}$ (°)	10

Table C.1: Nacelle geometric parameters [37].

The nacelle body was modelled as a solid body of revolution, with a profile defined as a spline in CREO with a boat tail angle, $\theta_{nacelle}$ and a condition of no curvature in line with the wing leading edge. The fairing was modelled with an elliptical leading edge, and a spline for the trailing employing the same methodology [37]. The wing geometry, (x_{wing}, y_{wing}) is the NACA 43018 section. The spinner geometry, $(x_{spinner}, y_{spinner})$ was copied from the geometry used by [50] for their studies of blown wings with folding propellers. Shape space [49] was used to define the spinner profile. Shape space is able to vary the location and radius of the spinner leading edge while maintaining continuity of gradient and curvature at the leading and trailing edge of the curve. The shape space function, S, is defined as:

$$\hat{S}(\hat{\psi}) = \frac{\zeta(\hat{\psi}) - \hat{\psi}\zeta_{TE}}{\sqrt{\hat{\psi}}(1-\hat{\psi})} \quad , \quad (C.1)$$

where:

$$\hat{\psi} = \frac{x}{c} \qquad and \quad \hat{\zeta} = \frac{y}{c} \quad , \quad (C.2)$$

In the limit as $\hat{\psi} \rightarrow 0$, S is equal to the non-dimensional leading edge radius of the spinner. It can be shown that, as $\hat{\psi} \rightarrow 1$,

$$\hat{S}(1) = \hat{\zeta}_{TE} - \hat{\zeta}'(1) \quad , \quad (C.3)$$

and

$$\hat{S}'(1) = -\frac{1}{2}\left(\hat{S}(1) + \hat{\zeta}''(1)\right) \quad , \quad (C.4)$$

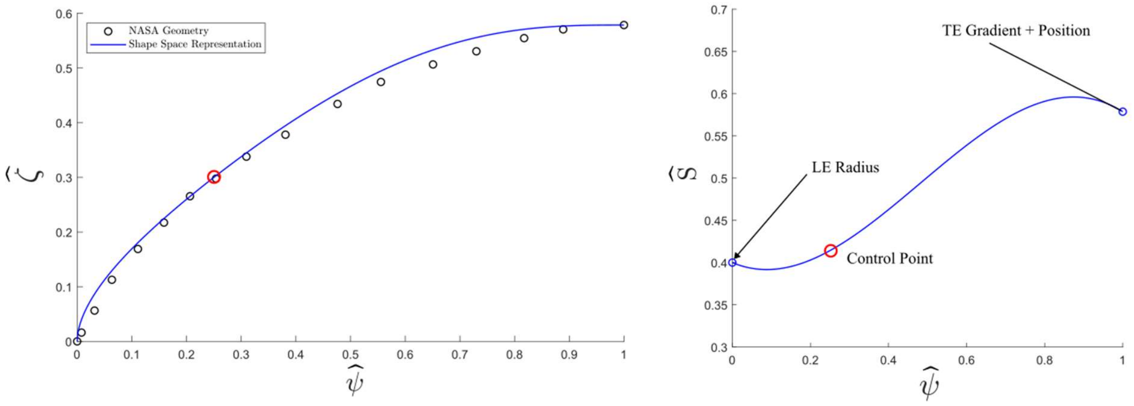

Figure C.2: Shape space representation of the spinner geometry from [50].

Figure C.2 shows the spinner geometry created using shape space. The shape space curve, was defined as a third order polynomial by

$$\hat{S} = -0.8408\hat{\psi}^3 + 1.2136\hat{\psi}^2 - 0.1941\hat{\psi} + 0.4 \quad . \quad (C.5)$$

The leading edge radius was set to 8% of the spinner chord length and the trailing edge diameter was sized from the NASA profile.

Appendix D: Safety Factors for Blown Wings in Landing

Patterson and Borer [57] studied changes to Part 23 FAA regulations for General Aviation class aircraft to account for the new development of DEP aircraft. In the previous Part 23 regulations, the stall speed of the aircraft was defined as that with the engines idle. This has been subsequently modified to take into account DEP systems where the engines, in this case motors, need to operate in order to blow the wing in landing. The regulations defined the approach speed of the aircraft to be 30% higher than the stall speed of the aircraft. This can be equated to an equivalent lift coefficient safety margin by,

$$\Delta C_L = \left(1 - \left(\frac{V_{stall}}{V_{approach}}\right)^2\right) C_{L,max} = 0.41 C_{L,max} \quad , \quad (D.1)$$

as the lift of the wing, and wing area are fixed in both approach and stall scenarios. Patterson and Borer used the new FAA regulations to argue that the lift of the blown wing can be split into an incidence contribution (either through flap deployment or angle of attack change) and a blowing contribution,

$$C_L = C_{L,incidence} + C_{L,blowing} \quad . \quad (D.2)$$

Patterson and Borer argue that the safety factor for a wing without blowing is effectively an angle of attack safety factor. If high lift generated through blowing can increase the lift of the wing by a factor of 2, a safety factor, ΔC_L, of 0.8, typical of conventional aircraft, would increase to a value of 1.6, greater than the lift of many conventional wings. To apply this safety factor to blown wings would considerably reduce the potential lift increase available from blown wings and, in the view of Patterson and Borer, the angle of attack safety factor on the wing would be unnecessarily high (in this example, doubled).

Figure D.1 shows the two possible methodologies available to calculate the maximum safe lift coefficient of the blown wing, $C_{L,safe}$. Use of the old FAA requirements lead to an increase of the angle of attack safety margin required, and only a small increase in the lift of the blown wing. Use of the new approach, taken from Patterson and Borer, uses a fixed safety margin for the blown wing, irrespective of the maximum lift coefficient (the authors recommend a value in the range 0.61 to 0.82, equal to the unblown wing safety margin) which maintains the safety factor for the incidence component of the lift coefficient, but leaves no safety margin for the blowing component. Provided the lift coefficient with blowing is lower than the maximum lift coefficient without blowing, the case of a full system power failure of the blown wing will still allow the aircraft to land at the design speed. As the probability of a full power failure is incredibly small [56], and this criteria limits blowing benefits to a 69.5% increase in lift coefficient, it is likely this criteria will be discarded. This limit was not applied in this thesis, but should be kept in mind when lift coefficient increases of over 69.5% are reported.

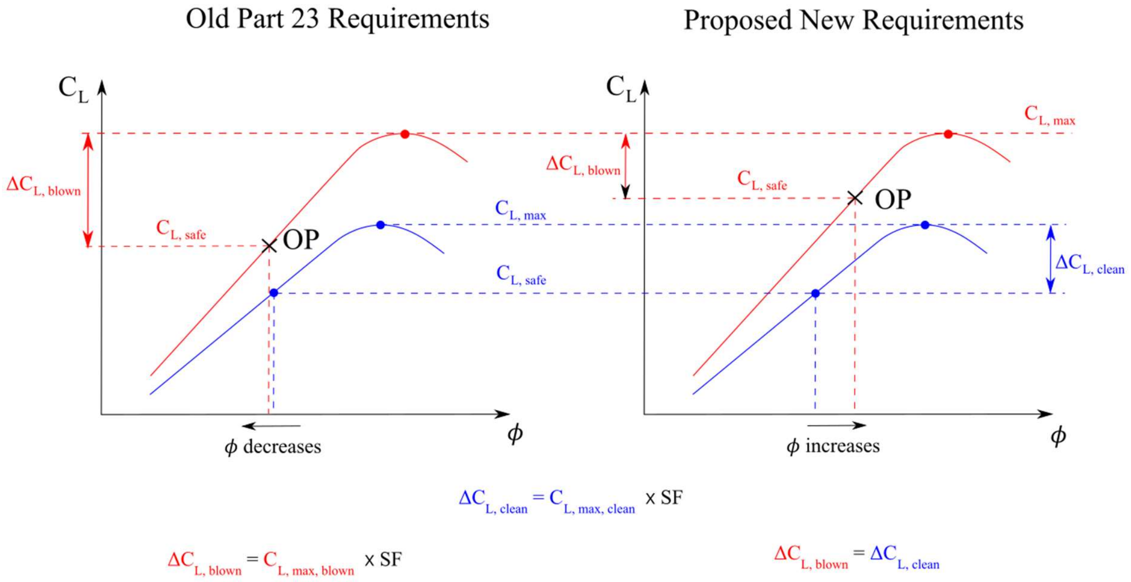

(a) (b)

Figure D.1: Comparison of the old Part 23 FAA regulations with Patterson and Borer's [57] interpretation of the safety factors applied to blown lift. In (a) the lift safety margin scales with the maximum lift coefficient, meaning the maximum safe angle of the wing or flap reduces with blowing. In (b) the safety margin is fixed, and blowing the wing allows the wing or flap angle to be safely increased.

Appendix E: Modified Nacelle Drag Model

Chapter 5 presents a model for the nacelle drag. For larger motor diameters, beyond $D_{nacelle}/c$=0.146, the model broke down due to the interference drag being over-predicted. Nacelles with diameters greater than this limit are predicted for cases with large propeller spacing (as the motor diameter increases due to the higher power requirements). To provide a better fit to the experimental data for larger nacelles, an empirical model,

$$IF = \begin{cases} 1.43 + 1.69\left|y_p/c\right| \quad , & \left|y_p/c\right| < \dfrac{D_{nacelle}}{2c} + \left|y_{wing}/c\right| \\ \left|1.43 + 1.69\left(\dfrac{D_{nacelle}}{2c} + \left|y_{wing}/c\right|\right)\right| , & \left|y_p\right| \geq \dfrac{D_{nacelle}}{2c} + \left|y_{wing}/c\right| \end{cases} , \qquad (E.1)$$

$$C_{D,interference} = IF \times C_{D,nacelle\,body} + 9.05C_f\left(13.68\frac{D_{nacelle}}{c} - 2\right)\frac{0.525c^2}{S_{Ref}} , \qquad (E.2)$$

is applied for nacelles with a diameter $D_{nacelle}/c > 0.146$ [37]. Note in Eq. E.2, the final term on the right of the equation was equal to 1 for the experimental measurements, however as the spacing between adjacent nacelles increases (and hence the reference area increases), the additional drag accounted for by this correction should also decrease inversely.

Figure E.1 shows the fit between the experimental data and new model applied to each diameter and horizontal offset tested.

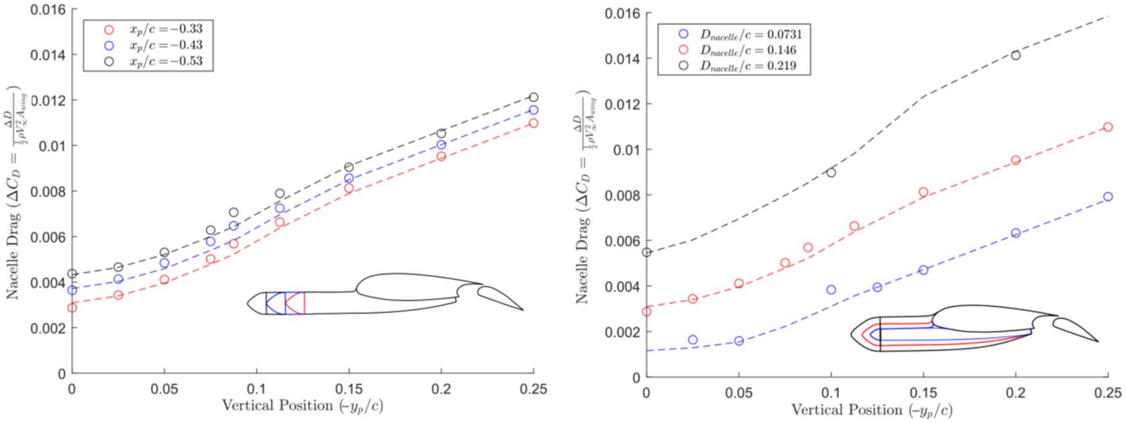

(a) (b)

Figure E.1: Drag due to nacelles on a wing at a wing angle of 0° for a single nacelle [37]. Nacelle length (a) and diameter (b) were both varied. Experimental data is shown in circles, the empirical model of Eq. E.1 and E.2 are shown in the dotted lines.

Appendix F: Modelling the 3D Blown Wing using 2D Simulations

In this appendix, we derive the effective jet height, and the corrections for spacing in order to use 2D actuator disk results to predict 3D aerodynamic coefficients with blowing.

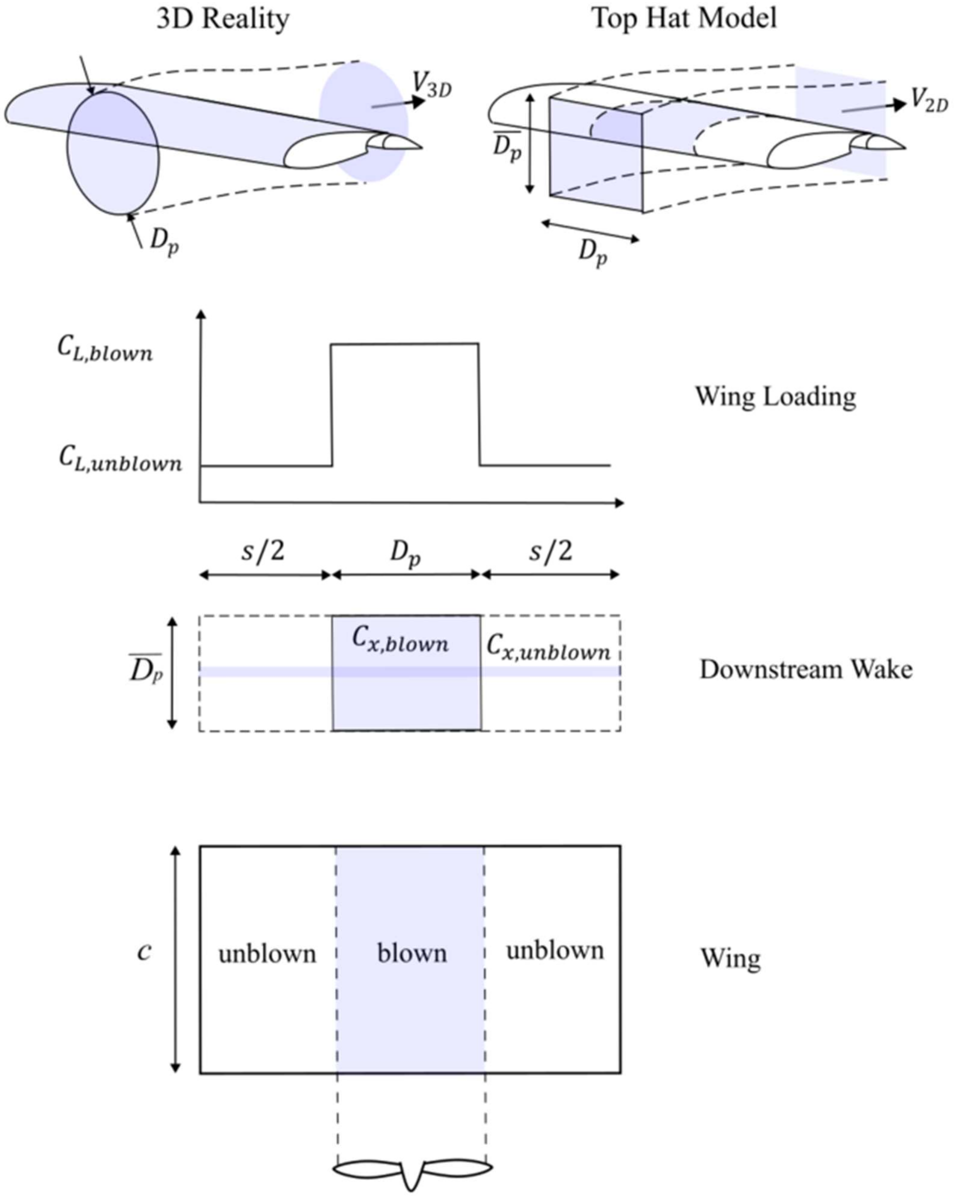

Figure F.1: Top hat model for a blown wing [37]. The model splits the wing into blown and unblown wing sections and assumes the jet is of uniform height in the blown section. 2D CFD models can predict the lift of the blown section.

Figure F.1 shows the construction of a "top-hat" model for the wing lift and thrust. The wing is separated into two sections: a blown portion, with a width of the jet diameter (this ignores any jet contraction) and an unblown portion for cases with non-zero spacing between jets. Both sections are at the same angle of attack, and flap angle if a flap is deployed. The lift and drag in the unblown section is uniform and equal to that of the 2D unblown wing. This value is extracted from CFD. The lift and drag in the blown section is also uniform, and neglects any variations due to jet height or swirl. This value is also extracted from a single 2D CFD calculation. The total thrust is conserved provided a suitable choice of 2D actuator height and thrust is made.

Agrawal et al. [3], uses an effective jet height, $\overline{D_p}$, given in Eq. F.3, when analysing 2D blown wing geometries to predict the average blown lift and drag. To derive this, we first analyse only the blown portion of the wing.

Assuming the jet contraction is negligible, conservation of mass and momentum require that

$$V_{2D}\overline{D_p}D_p = V_{3D}\frac{\pi {D_p}^2}{4} \;, \quad (F.1)$$

and,

$$ {V_{2D}}^2\overline{D_p}D_p = {V_{3D}}^2\frac{\pi {D_p}^2}{4} \;. \quad (F.2)$$

where V_{2D} is the velocity at the actuator disk in 2-dimensions, and V_{3D} the velocity at the actuator disk in 3-dimensions. In order to satisfy both of these equations, V_{2D}=V_{3D}. Applying actuator theory, this is only possible if the thrust coefficient, T_c is also equal [37]. If V_{2D}=V_{3D} then,

$$\overline{D_p} = \frac{\pi}{4}D_p \;. \quad (F.3)$$

This mean jet height is used throughout this thesis when predicting the blown wing performance from 2D simulations.

This mean jet height approach allows the performance of the blown section of the wing to be calculated from a single 2D calculation. The mean streamwise force on the wing for any spacing can then be predicted from the summation of the blown and unblown sections in Fig. F.1,

$$\overline{C_x} = \frac{C_{x,blown}D_p c + C_{x,unblown}sc}{D_p c + sc} = \frac{C_{x,blown} + C_{x,unblown}\frac{s}{D_p}}{1 + \frac{s}{D_p}} \quad . \quad (F.4)$$

This equation captures both the contribution of thrust and drag to the streamwise force on the wing. The mean lift coefficient is calculated as

$$\overline{C_L} = \frac{C_{L,blown}D_p c + C_{L,unblown}sc}{D_p c + sc} = \frac{C_{L,blown} + C_{L,unblown}\frac{s}{D_p}}{1 + \frac{s}{D_p}} \quad . \quad (F.5)$$

where s is the spacing between adjacent jets [37].